LIÈGE université
Sciences Appliquées

Characterization of solid–liquid flow in a stirred tank bioreactor designed for mesenchymal stem cell culture

A thesis submitted in partial fulfillment of the requirements for the degree of Doctor of Philosophy (PhD) in Engineering Science

by

Mohamad MADANI

Supervisor: Dominique TOYE
Co-supervisor: Sébastien CALVO

DOCTORAL COLLEGE IN CHEMICAL ENGINEERING
April 2026

Jury

Pr. Tristan Gilet	University of Liège, Belgium	President
Pr. Dominique Toye	University of Liège, Belgium	Thesis supervisor
Dr. Sébastien Calvo	University of Liège, Belgium	Member
Pr. Thomas Andrianne	University of Liège, Belgium	Member
Pr. Eric Olmos	University of Lorraine, France	Member
Dr. Marie-Laure Collignon	Cytiva, Belgium	Member

To the lost souls of the world

Acknowledgements

I would like to express my gratitude to all those who contributed to this journey. It would not have been possible without their help, encouragement, and support, especially during difficult moments.

I would like to sincerely thank my supervisor, Pr. Dominique Toye, for her continuous guidance and support. In addition to her feedback and discussions that helped me improve this work and stay on track, she was always available to listen and help through challenging moments, in ups and downs, and in times where things felt uncertain. Her contributions are beyond what I can express, both academically and personally. I would also like to thank my co-supervisors, Dr. Angélique Delafosse and Dr. Sébastien Calvo, for their assistance and direction. They not only taught me to develop strong technical skills, which often comes with huge cost, but also shared many moments of laughter, along with some French corrections, that made the journey much lighter. I truly appreciate this team, for their comments and instructions, their trust in my work and, above all, their time and effort. I am grateful to have shared this chapter of my life with you.

I appreciate the support of the committee members, Pr. Vincent Terrapon and Pr. Eric Olmos, for their valuable discussions and constructive remarks throughout my doctoral studies. I would like to thank as well Pr. Tristan Gilet, Pr. Thomas Andrianne, and Dr. Marie-Laure Collignon for agreeing to be part of the jury and taking the time to review this work.

Special thanks to LRGP lab, Biopromo team members, particularly Pr. Eric Olmos again and Dr. Celine Loubière, for their hospitality and friendly environment they provided during my stay. I truly appreciate the facility visit and the rich discussions and exchanges we had.

Evidently, a warm expression of gratitude to the Chemical Engineering department members and labs at the University of Liège, including NCE, PEPs, LCA, and la HALLE. From professors, researchers, and PhD students, to technicians and secretaries. I am thankful to Thierry Salmon and Christian Szykula for their practical help with the experiments and endless jokes and humour in the lab. I also would like to thank my lab mates Sergio, Ezgi,

Marc, Hajer, and Rana for the endless pictures and for putting up with my many requests. It was also a pleasure sharing the office in such an enjoyable environment: who else could it be but Jean-Luc the pranks' victim, Natalia whose daily life could easily qualify as a series, Francois the man of infinite facial expressions, Ali with whom I always had the "quietest & calmest" conversations, and finally Dr. Klara—well, thanks for the office desk. Many thanks as well to the rest of NCE, LCA, and Carbon-Capture friends. I am lucky to have met you all.

I would like to acknowledge the financial support from FNRS through the research grant (OptiReac4MSC project) and the FSA for their extension contract that made this work possible.

I would like to express my deepest gratitude to my fiancée, Mathilde Cuvelier, for being there for me throughout every step of this journey. In depressing and happy moments, and in anger and calm times, she stood by me with patience and strength. Her belief in me and her constant support are beyond words. I hope you know that you are part of this work. I would like to also thank Mathilde's family for their continuous encouragement.

Although I cannot name everyone, I would like to take a moment to appreciate the support, encouragement, and countless laughs of my friends in Lebanon, France, and Belgium.

Last but not least, I am deeply grateful to my family for their unconditional love and support. To my mom, my brothers, and sisters, I have no words to express how thankful I am to have you in my life. You have always been my strength and this would not have been possible without you. To my late uncle, the funniest soul on earth and to my cousin, who we lost in the war, this is for you.

Abstract

Mesenchymal stem cells MSCs are widely considered as the basis of next medical revolution in the field of tissue engineering and cell therapy, thanks to their differentiation capacities and immuno-regular properties. Unfortunately, the quantities derived from umbilical cords, bone marrows or adipose tissues are insufficient for the uses in therapeutic treatments. In order to reach high cells quantities for clinical applications, an expansion step is necessary, and several studies are underway to culture these cells in a scalable system. To manage cells culturing in such step, attention is drawn to the medium as it appears that cells are anchorage-dependent and adhesion to a surface for expansion process is fundamental. Studies have showed good results in terms of cells growth and attachment using plastic spherical microbeads, referred to as microcarriers of micrometer size range (e.g., Cytodex-1, plasticplus, etc.). The most promising system for cultivation of MSCs is a closed and controlled stirred tank type bioreactors STR, in which microcarriers are suspended in the culture medium up to $2-3$ v% volume fractions, allowing cell reproduction and preventing cell-to-cell bridging, i.e., aggregation.

The applicability of such an approach has been demonstrated. However, attention is paid to the bioreactor operating conditions and design to insure high MSCs production while retaining their quality and functionality. To avoid cell detachments, deaths, and aggregations, limiting hydromechanical stresses in the medium is a key-factor in optimizing the expansion process while operating at optimal suspension state (just suspension). These stresses experienced by cells are basically due to liquid-solid interactions (shear and normal stresses) forced by liquid displacement on one side, and solid-solid interactions between the microcarriers and between microcarriers and the walls of the system on the other side.

To better understand the stresses encountered in microcarrier-based MSC expansion in stirred-tank bioreactors, the development and validation of a detailed two-phase hydrodynamic model is at the core of this framework. Thus, CFD and numerical tools are extensively used to try and attempt to optimize models, but the need for experimental data and validation is paramount. Particle image velocimetry PIV—a commonly used technique for single phase flow—is set to characterize the solid–liquid flow for mean and turbulent quantities, while Particle Tracking Velocimetry PTV is used to track the trajectories of

particles.

The presence of the microcarriers (e.g., Cytodex-1) in the stirred tank adds a layer of complexity for flow characterization using visualization techniques. Because these techniques require high optical clarity, the translucent or opaque nature of microcarriers can obstruct the optical path. This leads to signal attenuation and "shadowing" effects that obscure the flow-tracking tracers used to map the fluid velocity. Given the optical issue caused by traditional microcarriers, there is a clear necessity to transition toward refractive index matched (RIM) solid–liquid systems. To this end, a system is chosen to closely replicate the physical behaviour of commercial microcarrier setups (suitability to mimic the original solid–liquid properties), while ensuring the optical transparency required for successful flow measurements. Consequently, the substitute RIM system is experimentally used to quantify and characterize the two-phase flow behaviour inside the stirred tank using PIV and PTV techniques for turbulence, interfacial interactions, and collisions with the effect of increasing volume fractions of the solid phase at a constant homogeneous agitation speed.

Notes related to this work:

i. All the relevant experiments attained are performed in steady state only.

ii. Cell culture experiments were not performed. Biological performances and assessments are therefore intentionally beyond scope and discussed only in the sense that they contextualize the engineering analysis of the dedicated stirred tank.

Résumé

Les cellules souches mésenchymateuses (MSCs) sont généralement considérées comme la base de la prochaine révolution médicale dans le domaine de l'ingénierie tissulaire et de la thérapie cellulaire, grâce à leurs capacités de différenciation et leurs propriétés immunomodulatrices. Malheureusement, les quantités dérivées des cordons ombilicaux, de la moelle osseuse ou des tissus adipeux sont insuffisantes pour envisager leur utilisation dans les traitements thérapeutiques. Afin d'atteindre de grandes quantités de cellules pour des applications cliniques, une étape d'expansion est nécessaire. Plusieurs études sont en cours pour cultiver ces cellules dansdes dispositifs utilisables à plus grande échelle. Dans ce cadre, la maîtrise des cultures cellulaires implique de bien contrôler leur environnement car les cellules sont dites "anchorage dependant" c'est à dire qu'elles doivent se fixer à un surface solide pour pouvoir se multiplier. Des études ont montré de bons résultats en termes de croissance cellulaire et d'attachement en utilisant des microbilles sphériques en plastique de taille micrométrique, appelées microporteurs (e.g., Cytodex-1, plasticplus, etc.). Par ailleurs, le système le plus prometteur pour la culture des MSCs est celui des bioréacteurs à cuve agitée fermés et contrôlés, dans lesquels les microporteurs sont mis en suspension dans le milieu de culture. Des fractions volumiques de $2 - 3$ v% permettent l'adhésion et la croissance cellulaire et tout en empêchant l'agrégation des microporteurs, due à des pontages cellule-à-cellule.

L'applicabilité d'une telle approche a été démontrée. Cependant, une attention particulière est portée aux conditions de fonctionnement et à la conception du bioréacteur afin d'assurer une production élevée de MSCs tout en préservant leur qualité et leur fonctionnalité. Un facteur clé dans l'optimisation du processus d'expansion est d'éviter le détachement des cellules, leur mort et l'agrégation des microporteurs. Il faut donc limiter les contraintes hydromécaniques dans le milieu, tout en opérant dans un état de suspension optimal (juste suspension). Les contraintes subies par les cellules sont essentiellement dues aux interactions liquide-solide (contraintes de cisaillement et contraintes normales) imposées par le déplacement du liquide d'un côté, et aux interactions solide-solide entre les microporteurs ainsi qu'entre les microporteurs et les parois du système d'autre part.

Afin de mieux comprendre les contraintes rencontrées lors de l'expansion de MSCs sur

microporteurs dans des bioréacteurs à cuve agitée, le développement et la validation d'un modèle hydrodynamique diphasique détaillé est au cœur de ce cadre de travail. Ainsi, En effet, même si la CFD et les outils numériques sont largement utilisés pour tenter d'optimiser les modèles, les données expérimentales sont indispensables pour leur validation. La vélocimétrie par image de particules PIV—une technique couramment utilisée pour les écoulements monophasique—est utilisée pour caractériser l'écoulement solide–liquide en termes de quantités moyennes et turbulentes, tandis que la vélocimétrie par suivi de particules PTV est utilisée pour suivre les trajectoires des particules.

La présence des microporteurs (e.g., Cytodex-1) dans la cuve agitée ajoute une couche de complexité à la caractérisation de l'écoulement par des techniques de visualisation. Étant donné que ces techniques nécessitent une grande transparence optique, alors que la nature translucide ou opaque des microporteurs peut empêcher la transmission de la lumière. Cela conduit à une atténuation du signal et à des effets d'« ombrage » qui masquent les particules de traceurs utilisées pour suivre l'écoulement et accéder à la distribution spatiale de la vitesse du fluide. Compte tenu de ce problème optique lié aux microporteurs traditionnels, un système solide–liquide "modèle", dont les constituants ont le même indice de réfraction (RIM) a dû être utilisé. Le système modèle a été choisi pour mimer le système solide–liquide original et donc reproduire fidèlement le comportement physique de la suspension de microporteurs commerciaux dans le milieu de culture, tout en assurant la transparence optique requise pour les mesures d'écoulement. Le système modèle RIM est utilisé pour quantifier et caractériser expérimentalement l'écoulement diphasique dans la cuve agitée à l'aide des techniques PIV et PTV. Les mesures permettent d'accéder aux grandeurs liées à la turbulence, aux interactions interfaciales et aux collisions, en fonction de la fraction volumique de solide, pour à une vitesse d'agitation constante.

Notes relatives à ce travail :

i. Toutes les expériences sont réalisées à l'état stationnaire, avec une suspension homogèen du solide.

ii. Aucune culture cellulaire n'a été réalisée. Les performances des cultures cellulaires et la qualité des cellules qui en sont issues sont donc volontairement excluent du champ d'application du présent travail. Elles ne seront évoquées que dans la mesure où elles contextualisent le choix du design et des conditions opératoires du bioréacteur étudié.

Foreword

This thesis is organized into five chapters; two of them have already been published and one is ready for publication (to be submitted). These three chapters are preceded by an introduction chapter and followed by a conclusion and perspective chapter.

Chapter one is an introduction which deals with limitations, solutions, and materials & methods of the current stirred tank configuration for MSC culture. It provides a quick overview of current cell culturing systems and the inherent limitations in these environments for visualization techniques, while exploring the relevant literature on potential RIM candidates by evaluating their advantages and disadvantages. Finally, a PMMA/NH_4SCN solid–liquid substitute is analysed, characterized, and proposed for different experimental measurements.

Based on the selected RIM system and the adopted measurement strategy, the remainder of the thesis is structured as follows, each chapter addressing a specific experimental and methodological aspect of this work.

Chapter two quantifies the effect of adding microparticles on the liquid-phase mean flow and turbulence using one-phase PIV (one-phase: liquid). Accordingly, the relevant studies concerning the turbulence modulation of the liquid phase were heavily discussed. This chapter has been published in *Fluids*, entitled *RIM-PIV Measurements of Solid–Liquid Flow in a Stirred Tank Used for Mesenchymal Stem Cell Culture*: https://doi.org/10.3390/fluids10100272.

Chapter three extends the analysis to two-phase PIV to simultaneously characterize both solid and liquid flow behaviour and to examine interfacial interactions (two-phase: solid & liquid). The challenges and techniques of measuring multiphase flows were explored. This chapter has been published in *Fluids*, entitled *Solid–Liquid Flow Analysis Using Simultaneous Two-Phase PIV in a Stirred Tank Bioreactor*: https://doi.org/10.3390/fluids11010017.

Chapter four uses time-resolved PTV to quantify particle trajectories of larger size and particle–particle interactions (one-phase: solid). For the first time, collision events are detected and processed to statistically evaluate collision rate, frequency, and intensity

metrics for this type of stirred tanks. The bibliography on the relevant solid–solid interactions was addressed. This chapter is ready for publication (to be submitted in *Chemical Engineering Science* journal).

Finally, chapter five lists the concluding remarks of this work and opens the door to exploring more ideas for flow characterization in the stirred tank.

Nomenclature

The following Nomenclature, abbreviations, and Greek letters are used in this manuscript:

CARPT	Computer automated radioactive particle tracking
CFD	Computational fluid dynamics
DOF	Depth of field
ERT	Electrical resistance tomography
IA	Interrogating area
KE	Kinetic energy
LDA	Laser Doppler anemometry
LDV	Laser doppler velocimetry
MSC	Mesenchymal stem cell
PBT	Pitched blade turbine
PEPT	positron emission particle tracking
PIV	Particle image velocimetry
PTV	Particle tracking velocimetry
RI	Refractive index
RIM	Refractive index matching
rms	Root mean square
SF	Scale factor
RT	Rushton turbine
TCS	turbulent collision severity
TKE	Turbulent kinetic energy
WHO	World health organization

α_p	Particle volume fraction, –
ε	Energy dissipation rate, m^2/s^3
μ	Dynamic viscosity, Pa.s
ν	Kinematic viscosity, m^2/s
ρ	Density, kg/m^3
λ	Taylor length scale, m

η	Kolmogorov length scale, m
τ	Time scale, s
θ	trajectory angle, $^\circ$

C	Impeller clearance, m
D	Impeller diameter, m
d_p	Particle diameter, m
F	Force, N/m^3
f	Collision frequency, s^{-1}
H	Liquid height, m
J	Impulse, g.cm/s
k	Turbulent kinetic energy, m^2/s^2
k^*	Non-dimensional turbulent kinetic energy, –
L	Integral length scale, m
M	Mean velocity magnitude, m/s
M^*	Non-dimensional mean velocity magnitude, –
N	Impeller speed, rpm
T	Tank diameter, m
P	Power input, W
P_0	Power number, –
R	Radial coordinate, m
r	Collision rate, s^{-1}
$\overline{U}$	Mean velocity, m/s
u	Instantaneous velocity, m/s
u'	Fluctuating velocity, m/s
V	Fluid volume, m^3
w	laser thickness, m
Z	Axial coordinate, m
Re	Reynolds number, –
St	Stokes number, –

Contents

Chapter 1

Toward a Refractive Index Matched System: Introduction, Materials & Methods

Abstract

Microcarrier-based MSC expansion in stirred-tank bioreactors requires operating conditions that ensure adequate suspension while limiting hydromechanical stresses. Quantifying these stresses and the underlying two-phase hydrodynamics requires experimental measurements for model development and validation. Optical velocimetry methods such as PIV and PTV are attractive for this purpose, but conventional microcarriers are translucent or opaque and introduce light scattering, attenuation, and shadowing that can prevent reliable measurements. This Introduction chapter summarizes the main configurations used for culturing cells and outlines the limitations of optical measurement techniques in the presence of microcarriers. It then explores the use of refractive index matched solid–liquid systems by reviewing candidate RIM solutions reported in the literature. Finally, the substitute solid–liquid system selected for this thesis is defined, and its key properties are presented and quantified to support its use for subsequent PIV and PTV measurements.

1.1 A Quick Biological Overview

A contemporary view of cells and stem cells originates from early microscopy and the formulation of cell theory. From single-lens instruments that revealed unicellular life by Van Leeuwenhoek [1], through the propositions of Schleiden and Schwann that all organisms are cellular and that cells grow and divide [2], to the affirmation by Virchow that every cell arises from a pre-existing cell [3]. These insights established cells as the fundamental units that self-organize into tissues via coordinated division and differentiation. Within this framework, "stem" cells function as precursors for maintenance, repair, and

disease modelling throughout the lifespan.

Boveri and Haecker set forth a first insight into self-renewal and the capacity to generate multiple cell types [4], while Gordon witnessed, by doing nuclear transfer experiments, that differentiated nuclei retain the information required to produce an adult organism. This means that differentiation can be reversible in principle [5]. Another breakthrough was pioneered by Friedenstein and his team as they discovered that marrow stromal precursors formed adherent fibroblast colonies in monolayer culture (i.e., growing on plastic). The terminology of stem cells subsequently evolved from "osteogenic stem cells" [6] and "marrow stromal stem cells" [7] to the widely adopted "mesenchymal stem cells (MSCs)" in the early 1990s by Caplan [8].

Functionally, MSCs are considered as multipotent: they are biased towards specific lineage families and support tissue maintenance and repair [9]. Sources have been identified in several tissues, notably bone marrow (BM), adipose tissue (AT), and umbilical cord (UC) [10]. Each source exhibits meaningful physiological and practical differences from the other, the biological aspects of such are found in the review of Jimenez-Puerta et al. [11].

Therapies using MSCs are positioned as advanced therapy medical products against leading global diseases; of the top 5 WHO 2016 causes of death, only lower respiratory infections had no MSC trial at the time [12]. Clinical trials are on the rise to date, as by January 2025, there were 1511 trials registered globally [13]. Inflammatory, degenerative and repair fields are targeted, with examples including: Crohn's disease [14], retinal degeneration [15], spinal cord injuries, and type II diabetes [16].

1.2 Expansion Process

MSC expansion platforms are grouped by energy delivery to the medium: static planar vs dynamic systems, where the latter could be subdivided to mechanically or hydraulically driven form. The classifications are summarized in Figure 1.1.

- Static planar culture - no mechanical input: simple, disposable, adhesion-based formats for screening or clinical trial expansion; however, limited growth area, manual handling and passaging, bulk at scale, and higher contamination risk [17].
- Dynamic culture:
  - Mechanical mixing: cells adhere to 100 – 400 µm microcarriers that are suspended and mixed—except for the rotating beds; enables better monitoring, control, homogenization, and convective mass and energy transfer, typically producing more cells per batch despite higher R&D demand [18, 19].
    - External agitation – body-moved – microcarrier system:

· Orbital shaking: microcarriers kept near just-suspended state; 5 – 10 times higher growth than spinner flasks in 7 days; operations typically limited to small volumes [20, 21].

· Wave-mixing bioreactor – rocking bags: a validated culture resulted in 15.7 – 16.3 times cell growth in 7 days in a 0.5 L volume; another one yielded 6.6 times cell growth in 9 days in a 1.5 L volume; however, cell-aggregates surfed after day 3 [22, 23].

∗ External agitation – body-moved – microcarrier free:

· Rotating bed bioreactor: integrated bed of polycarbonate plates with a cell culture surface area up to 0.6 m^2; a representative run reported 39 times cells expansion in 9 days [24].

∗ Internal agitation – impeller driven – microcarrier system:

· Stirred tank reactor (STR): dominant microcarrier platform from spinner flasks (small-scale; $\leq$ 0.2 L) to instrumented and well-equipped STR (high production; 1 – 5 L)[25]; offers scale-up potentials to 43 times cells expansion in 11 days in a 50 L [26].

– Hydraulic control: power input is generated by pumps; fixed plates/surface area, i.e., microcarrier free; continuous flow/perfusion.

∗ Parallel plate bioreactors: low shear with radial-flow geometries promote a more uniform environment and slow-flow regions at the growth surface; however, direct cell monitoring is inaccessible; total surface area 2.125 – 12.24 m^2 [27]; typical cell expansion factors range between 10 – 25 in 7 – 11 days [28].

∗ Hollow fiber bioreactor: low and uniform shear with 3D environment for cells; However, cell harvesting is a major drawback; yields of 15 – 22 expansion factor in 8 days with working surfaces of 2.1 – 2.5 m^2 [29, 30, 31].

∗ Fixed bed bioreactor: immobilized on a stationary packed matrix and nutrients are circulated in an internal loop; area of the matrices ranges between 2.5 – 7 m^2/L (per unit volume of the reactor) with 9.2 times cells expansion in 9 days [32, 33].

From the mentioned systems, stirred tanks offer one of the best viable and reliable choices for cell culture due to: ability to control and monitor the process (pH, temperature, nutrients needs over time, etc.), high surface area provided by microcarriers, and most importantly the scalability potential [26]. With these prospectives, attention is drawn to understand and

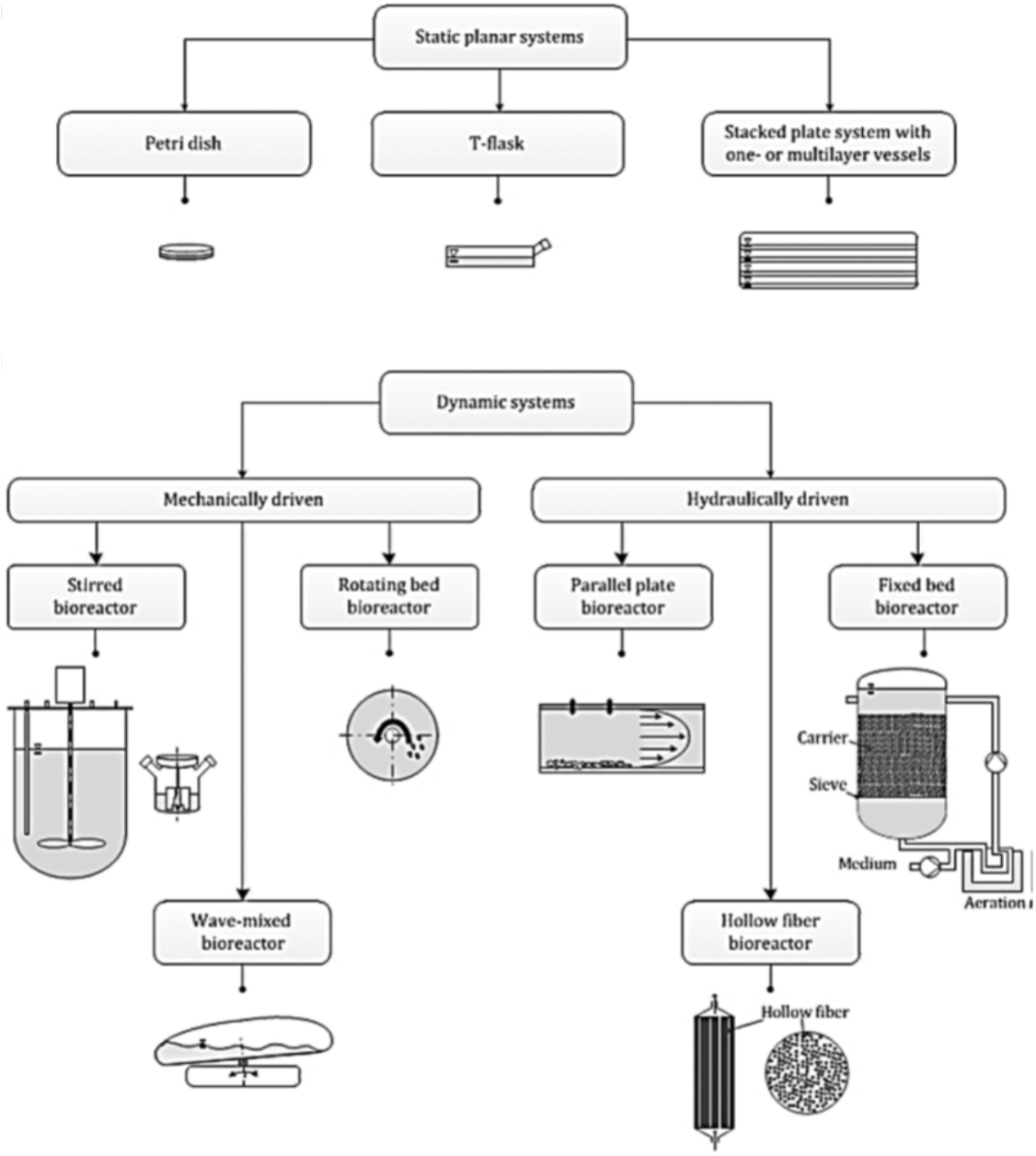

Figure 1.1: Types of systems available for cell expansion. Figure adapted from Jossen et al. [34].

enhance the performance of prior scale-ups: mixing time, mass transfer, impeller speed, and power input, to name a few.

As mentioned above, stirred tanks are microcarrier-based which means that the addition of such spherical particles is essential for growth. Based on their naming, the sizes of such particles vary between 90 and 400 µm and the term carrier is simply because they allow cells to adhere and expand [18]. Today, microcarriers are widely commercialized with variety of types, core materials, and porosities. An overview of the commercially available microcarriers for MSC culture is presented in Table 1.1.

For comprehensive treatments of MSC culture under related operating conditions (MSC adhesion to microcarriers, growth, quality, differentiation, signalling, etc.), the reader is referred to the dedicated works of Loubière [35] and Maillot [36], in the state-of-the-art section. Based on that, Cytodex-1 has been proven to be a reliable and excellent microcarrier in MSC culture within a stirred tank system. Thus, Cytodex-1 microparticles suspended in salinated water were chosen to study the two-phase flow behavior and hydrodynamics in such an agitated set-up.

Although agitation is required to ensure the mixing of nutrients and the suspension of microcarriers in the tank, and while speeds are tuned to just-enough to suspend particles (N_{js}), it represents the source of hydromechanical stresses that potentially damage cells adhered to the surfaces of the particles. The presence of microcarriers is a double-edged sword: in addition to the uses discussed, it adds an extra layer of complexity to the flow, promoting further interactions with the fluid and themselves. Hence, understanding the hydrodynamics of the multiphase flow is key to an optimized culture process and the scaling procedure. In this context, numerical tools such as CFD play an important role for the characterization of the flow; however, to choose or develop a model carefully, experimental data are a must, as they further support and validate the model used.

Table 1.1: Characteristics of commercial microcarriers used in cell expansion. Table adapted from Jossen et al. [34]

Type	**Diameter** µm	**Density** kg/m^3	**Surface area** cm^2/g	**Porosity**	**Core material**
Cultispher-G	130-380	1020	-	Macro-porous	Gelatin
Cultispher-S	130-380	1020	-	Macro-porous	Gelatin
Cytodex I	147-248	1030	4400	Micro-porous	Cross-linked dextran
Cytodex III	141-211	1040	2700	Micro-porous	Cross-linked dextran
Collagen	90-150 / 125-212	1020	480 / 360	-	Cross-linked polystyrene
FACT III	90-150 / 125-212	1020 / 1040	480 / 360	-	Cross-linked polystyrene
Hillex II	160-180	1110	515	-	Modified polystyrene
Hillex-CT	150-180	1110	515	-	Modified polystyrene
Plastic	90-150 / 125-212	1020 / 1040	480 / 360	-	Cross-linked polystyrene
Plastic Plus	90-150 / 125-212	1020 / 1040	480 / 360	-	Cross-linked polystyrene
ProNectin F	90-150 / 125-212	1020 / 1040	480 / 360	-	Cross-linked polystyrene
Star-plus	125-212	1020 / 1040	480 / 360	-	Cross-linked polystyrene

1.3 Problematic: Optical Issues

Particle image velocimetry PIV and particle tracking velocimetry PTV are laser-based techniques that are often used in research to experimentally quantify velocities and interactions in a certain flow. More details on the experimental techniques are presented in the Introduction of Chapter three (3.1). These tools are typically intended for single-phase flows, using tracers of size <20 µm that are effectively inertialess. This small scale ensures they precisely follow the streamlines of the continuous carrier phase, whether it is a gas or a liquid. In the case of multiphase flows, the dispersed-phase represents a crucial challenge. Since PIV and PTV are optical techniques, they necessitate fully transparent systems—including both the container and its contents. Without careful treatment, the dispersed phase elevates noise and obstructs the optical path, resulting in the loss of tracer information. As one may guess, the core problem lies in the optical properties of the microcarriers, as their optical nature scatters the laser sheet and induces extreme noise and attenuation to the light, where the image quality is completely deteriorated. In other words, the scattering and distortion of the laser light is a result of the translucent[1] (e.g. Cytodex) or opaque behaviour (e.g. Plastic Plus) of the microcarriers where some light passes through and changes direction. Note that optical distortions and intensity variations can arise either from differing refractive indices (between both phases), i.e. translucent materials, or from the lack of optical clarity of the dispersed particle phase, which absorbs and blocks light, i.e. opaque materials.

To emphasize this, a preliminary test is performed with PIV using Cytodex-1 microcarriers ($d_p \approx 160$ µm; $\rho_p \approx 1020$ kg/m^3) which is, as mentioned before, a robust candidate for cell culture (see Table 1.1), suspended in a stirred tank (V = 1 L) at a rotation speed N = 200 rpm. The stirred tank has a hemispherical bottom shape, equipped with an HTPG down-pumping axial impeller, and placed inside an aquarium. The full details and geometry of the stirred tank are reported in Chapter two (section 2.2.2). The solid volume fractions reached $\alpha_p = 0.5$ v%, which is low compared to typical microcarrier volume fraction used in MSCs culture (2 – 3 v%). Though as seen in Figure 1.2, the images taken were blurred, as microcarriers tend to scatter or diffuse the laser light, i.e., shadow effect, even with low particle volume fractions, resulting in issues to extract the necessary data (velocity maps). An optimal image is rather obtained by having bright white spots that represent the tracers, which is clearly not the case here (gray blurry image).

[1] Translucency is an inherent property which is related to the internal structure of the material and not only defined by differing refractive indices.

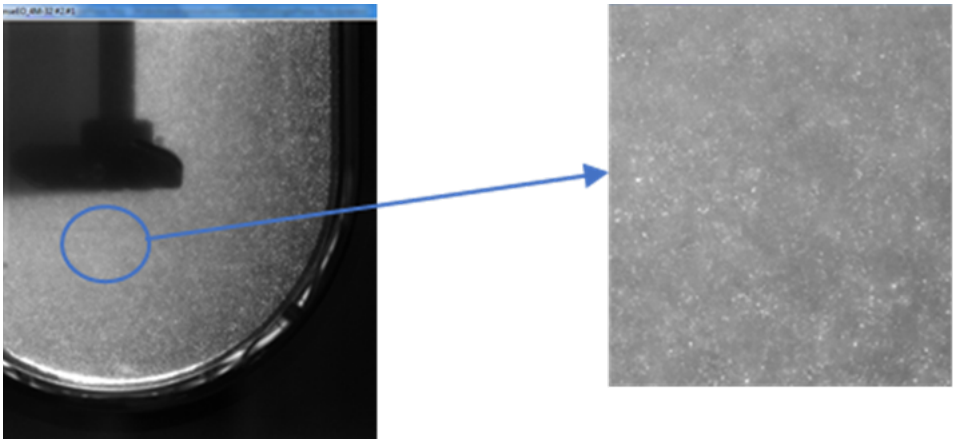

Figure 1.2: Liquid phase PIV raw image in presence of Cytodex-1 at $\alpha_p = 0.5$ v%. **(Left)**: full view of the tank. **(Right)**: zoomed-in view at the bulk.

1.4 Refractive Index Matched RIM Systems

Henceforth, to address visibility challenges in experimental laser-based techniques, it is essential to use optically clear (transparent) materials which could be fundamentally matched with the refractive index RI of a liquid candidate. This approach, known as Refractive Index Matching (RIM), makes the solid particles practically invisible to the camera, eliminating light scattering and optical distortions from the solid–liquid interfaces.

Beyond RI, properties like density, viscosity, interfacial tension, and surface wettability can be simultaneously tuned using liquid mixtures and additives, which is vital for achieving flow similarity with real-world applications. Intensive predictions of the properties listed could be found in the book of Poling et al. [37].

So, in the case of MSC culture, the challenge is to find a suitable solid–liquid system that not only has matching optical properties but also accurately mimics the physical characteristics of the original system. This includes ensuring that the density difference/ratio and viscosity remain within the same range as the original system. By preserving these properties, the hydromechanical stresses and fluid dynamics can be accurately reproduced and measured, allowing for a realistic study of the behaviour of the system.

Based on the literature summarized below and taking into account the advantages and disadvantages of candidates, it is found that PMMA acting as solid particles matched with the refractive index of Ammonium Thiocyanate NH_4SCN would be a perfect substitute for microcarriers (Cytodex-1, plastic plus, etc.) and water system, originally used in MSC culture. This is simply because the density ratio between both phases is highly close between the original and the substitute ($\rho_f/\rho_p \approx 1$), with viscosity also being within the range (low viscosity). Note that the microcarriers are practically suspended with Phosphate buffer saline solution PBS which has slightly higher density than distilled water ($\rho_f \approx 1000$

kg/m^3 [38]), but is referred to as water for simplicity.

In Table 1.2 below, a list of candidates for solid–liquid systems that have similar refractive indices, reported with their corresponding densities and viscosities. The table is adapted from the excellent review by Wright et al. [39], which also covers crucial aspects such as safety, toxicity, material compatibility, and the influence of temperature for more extensive data on solid–liquid and liquid–liquid systems. For interested readers, a detailed version of this table is found there.

Table 1.2: List of solid–liquid refractive index matched RIM systems with properties and references (adapted from Wright et al. [39]). Properties provided are at ambient laboratory temperatures 20 – 25 °C.

Solid (RI; ρ_p kg/m^3)	**Liquid candidate(s) (RI; ρ_f kg/m^3; μ mPa.s)**	**References**
FEP ($n \approx 1.338$; $\rho_p \approx 2150$)	Water ($n \approx 1.333$; $\rho_f \approx 998$; $\mu \approx 1.0$)	Satake et al. [40]
PVA ($n \approx 1.467$; $\rho_p \approx 1190$)	UCON oil + TBE ($n \approx 1.467$; $\rho_f \approx 1139$; $\mu \approx 2460$)	Karnis et al. [41]
PMMA ($n \approx 1.489$–1.491; $\rho_p \approx 1180$)	NaI (60 – 65 wt%; $n \approx 1.485$–1.491; $\rho_f \approx 1770$; $\mu \approx 1.9$)	Mehta et al. [42]; Soranna et al. [43];
	NH_4SCN, tunable with glycerol ($n \approx 1.485$–1.503; e.g. 62.6 wt% NH_4SCN: $\rho_f \approx 1140$; $\mu \approx 1.9$)	Bailey & Yoda [44]; Borrero-Echeverry & Morrison [45]
	KSCN–water (42 wt%; $n \approx 1.460$; $\rho_f \approx 1320$; $\mu \approx 2.0$)	Reddy et al. [46]
	Triton X-100 ($n \approx 1.489$; $\rho_f \approx 1070$; $\mu \approx 240$ at 23 °C)	Dijksman et al. [47]
	Turpentine + tetralin (69/31; $n \approx 1.489$; $\rho_f \approx 894$; $\mu \approx 1.53$)	Tindal et al. [48]

Table 1.2: List of solid–liquid refractive index matched RIM systems with properties and references (adapted from Wright et al. [39]). Properties provided are at ambient laboratory temperatures 20 – 25 °C.

Solid (RI; ρ_p kg/m^3)	**Liquid candidate(s) (RI; ρ_f kg/m^3; μ mPa.s)**	**References**
Nylon ($n \approx 1.514$; $\rho_p \approx 1150$)	Pale-4 oil + TBE ($n \approx 1.514$; $\rho_f \approx 1138$; $\mu \approx 1360$)	Karnis et al. [41]
Silicone rubber ($n \approx 1.410$–1.440; $\rho_p \approx 970$–1100)	Glycerol + water (50 wt% glycerol: $n \approx 1.41$; $\rho_f = 1130$; $\mu = 6.7$; 56 wt% glycerol: $\rho_f = 1140$; $\mu = 8.3$)	Duncan et al. [49]; Perktold et al. [50]; Hopkins et al. [51];
Urethane rubber ($n \approx 1.490$; $\rho_p \approx 1200$)	NaI + glycerol ($n \approx 1.490$; $\rho_f \approx 1780$; $\mu \approx 17.8$)	Le et al. [52]
Fused quartz ($n \approx 1.450$–1.460; $\rho_p \approx 2200$)	Mineral oils (e.g. Drakeol #5, $n \approx 1.459$; $\rho_f \approx 870$–890; $\mu \approx 25$–30)	Stoots et al. [53]; McIlroy et al. [54]
Borosilicate glass ($n \approx 1.470$–1.474; $\rho_p \approx 2230$)	NaI (60 wt%; $n \approx 1.470$; $\rho_f \approx 1770$; $\mu \approx 1.8$);	Jacobs et al. [55]
	KSCN (42 wt%; $n \approx 1.460$; $\rho_f \approx 1320$; $\mu \approx 2.0$);	Reddy et al. [46]
	Turpentine+tetralin (68/32 wt%; $n \approx 1.467$; $\rho_f \approx 915$; $\mu \approx 1.20$)	Reddy et al. [46]
Soda-lime glass ($n \approx 1.50$–1.52; $\rho_p \approx 2520$)	Diethyl phthalate ($n \approx 1.504$; $\rho_f \approx 1180$; $\mu \approx 12$);	Hassan & Dominguez-Ontiveros [56]

Table 1.2: List of solid–liquid refractive index matched RIM systems with properties and references (adapted from Wright et al. [39]). Properties provided are at ambient laboratory temperatures 20 – 25 °C.

Solid (RI; ρ_p kg/m^3)	**Liquid candidate(s) (RI; ρ_f kg/m^3; μ mPa.s)**	**References**
	Tetraline + silicone oil (28/72 wt%; $n \approx 1.5$; $\rho_f \approx 975$; $\mu \approx 19.62$)	Mikami et al. [57]
Silica gel / SiO_2 ($n \approx 1.452$; $\rho_p \approx 2210$)	Chloroform + water ($n \approx 1.452$; $\rho_f \approx 1489$; $\mu \approx 0.57$)	Abbas & Crowe [58]

continued from previous page.

Note that the refractive indices of fluids are not only highly sensitive to temperature variations, requiring precise control to maintain matching conditions [59], but also wavelength-dependent, which can lead to optical distortion or dispersion errors [60].

From the systems mentioned above, Fluorinated Ethylene Propylene FEP is extensively used as a RIM solid with water due to their close refractive indices. Satake et al. [40] conducted holographic PTV measurements in a sphere-packed pipe using an FEP pipe and Mexeflon resin spheres with water as the test fluid. It is worth-noting that FEP is in essence translucent rather than clear. Poly(methyl methacrylate) PMMA, also known as Perspex, Plexiglas or acrylic glass, is the most commonly employed solid in RIM experiments due to its optical clarity and ease of machining. Examples include highly concentrated spherical suspensions in a shear-induced Couette flow [61], motion and turbulence of suspended particles in stirred tanks [62], and velocity profiles in an axial turbo-pump [63]. Silicone and urethane rubbers are particularly useful for compliant models of flows through flexible structures, such as models for blood-flow experiments [50, 64] and aortic bifurcation [49]. While fused quartz, a high-purity silicon oxide in an amorphous form, has been employed for flow studies around complex geometries. For instance, a study of turbulent flow in a gas-cooled reactor part, made of fused quartz, was performed using PIV [54]. Last but not least, Borosilicate glass, also known as Pyrex or Duran glass, is a common solid in RIM experiments, second only to PMMA in terms of use according to literature [39]. Investigations include solid–liquid fluidized bed measurements using PIV [46], and horizontal liquid–liquid flow estimations in pipes built from borosilicate glass [65].

As mentioned, it is relevant to shed light on some of the advantages and disadvantages of the materials specifically in terms of safety and compatibility, which also helps in the selection process:

- Advantages:
  - FEP: good chemical resistance; RI is close to that of water, making it easier to utilize (directly used with water); non-toxic and non-volatile.
  - PMMA: optically clear and easily machined; readily available and affordable (easily manufactured into various shapes and sizes); no signs of water absorption.
  - Silicone and Urethane rubbers: flexible (useful for compliant models and complex structures); chemically inert [66].
  - Fused quartz: optically transparent with good chemical resistance; withstands higher stresses (pressure); thermally stable.
  - Borosilicate glass: optically transparent with good chemical resistance; withstands higher stresses (pressure); tolerates significantly higher laser powers than plastics [67].
  - Soda-lime glass: a lower cost compared to both borosilicate and fused quartz;
- Disadvantages:
  - FEP: hydrophobic fluoropolymer; translucent rather than clear (good images can still be taken through FEP walls a few mm thick [39]); sourcing in reasonable quantities and cost can prove difficult, especially for large systems [68].
  - PMMA: brittle and prone to cracking (although cracks could be dealt with during processing); it can be attacked by a number of chemicals (especially alcohols and some oils. A list of chemicals is shown in the Appendix in Table A.1.1)
  - Nylon: translucent (like FEP); rarely been used in RIM experiments according to literature [39], hence no specific information on safety in such uses.
  - Silicone and Urethane rubbers: known for liquid absorption and swelling [66]; effects of mixing and curing on silicone rubbers can result in RI variations [51]; influenced by temperature.
  - Fused quartz: its purity makes it more expensive; not as easily machined and is typically more brittle than plastics;
  - Borosilicate glass: not as easily machined and is typically more brittle than plastics; different batches of beads can have RI variations [47].
  - Soda-lime glass: more brittle than both borosilicate and fused quartz; exact composition and RI vary depending on the manufacturing process.
  - Silica gel: highly hydroscopic (high liquid absorption).

It merits attention that the resistance of solids to liquid absorption (swelling effect) was also a decisive step in choosing the candidate, so that the size of the particles does not change with time. Furthermore, some remarks should be mentioned for NH_4SCN: (i) it is toxic if inhaled or digested and may cause skin irritation, so careful handling and protective clothing are required (99% salt purity is used). Because it is an aqueous solution, it is easier to store and dispose than tertiary and organic oil mixtures. (ii) The use of salts can increase the risk of corrosion. According to Borrero-Echeverry and Morrison [45], NH_4SCN solution is compatible with 6061 aluminium alloy, anodized aluminium, 316 stainless steel, common plastics, and glass, but it can corrode plain steel and 304 stainless steel. A test of the effect of NH_4SCN on plain steel is reported in the Appendix in Figure A.1.1. In the set-up used for the experiments, the agitator was replaced by a 3D printed version made from plastic and thus no corrosion behaviour was noticed (no colour change of NH_4SCN solution).

As a final remark in this section, alternative liquid systems, including tertiary mixtures and oils, are in principle available to achieve refractive index matching with PMMA (tunable to achieve desired viscosity). However, in the present work, aqueous solutions were deliberately prioritized. Beyond their straightforward preparation and experimental accessibility, aqueous systems offer clear advantages over organic liquids in terms of safety during handling, operation, and potential leakage scenarios. In contrast, oil-based systems raise additional concerns related to flammability hazards as well as the long-term chemical stability of PMMA, since prolonged contact with such medium has been reported to compromise its service life (microcracks) [39, 47].

1.5 Experimental Set-up

As previously stated, general RIM systems require temperature control to maintain matching conditions due to the temperature dependence of fluid refractive indices. All the experimental measurements that follow in the upcoming chapters (using PIV/PTV), are performed in the desired operational room with an air conditioner which controls the temperature inside. Since the experimental set-up is not equipped with a dedicated temperature regulator, it is installed in the room at least one day prior to the experiments to allow thermal stabilization. The system is thus in thermal equilibrium with the room temperature, which remained approximately constant during the measurements.

The room is shown in Figure 1.3, where the stirred tank is installed inside an aquarium made of acrylic material and filled with paraffin oil (RI = 1.468; Fauth). The Aquarium helps minimize the distortions to the laser sheet due to the curvature of tank bottom (hemispherical). The transparent system, including the materials and the characterized two-phase flow itself, made it possible to acquire high-quality images. In addition, agitation

is provided by a shaft and a motor with adjustable values, while the cameras are installed on a separate stable rig. Due to laser intensity, a curtain is also available to split the room as well as a special user goggles with a cut-off filter (570 nm) to protect the eyes. Finally, the measurements are obtained with room lights turned off (full darkness, except for the laser) and a red led, mounted outside, is turned on to alert "prohibited entrance".

Figure 1.3: Experimental set-up installed in a special room.

1.6 PMMA/NH_4SCN Characterization

1.6.1 Refractive Index

The refractive index RI of NH_4SCN solution is measured with an Abbe refractometer and matched, according to the literature, with the PMMA particles, as it is not possible to assess them within such a device. The device is able to measure the RI of solids in general, but must fit as an entity within the measuring plate, which is not the case with particles. The working principle of Abbe refractometer could be find in this book [69]. It is also relevant to state that the precision is in the order of 0.001, beyond which it becomes tricky to designate/assign the exact value. An example of a measurement reading is shown in the Appendix (Figure A.1.2).

Two main concentrations are initially examined, 55 wt% and 61 wt% NH_4SCN salt solution

with results compared to those of Borrero-Echeverry & Morrison [45], who specifically studied NH_4SCN. Estimates can be found in Table 1.3 which shows good agreement between the experimental measurements done with the Abbe refractometer and the model developed by Borrero-Echeverry & Morrison. The idea of the two concentrations is to attempt and have the best scenario for PIV by tuning the concentration, with the fact that experimental refractive index of PMMA particles is unknown. A perfect refractive index matching set-up is much easier with other shapes (e.g. rods) or particles of millimeter size at the least. Ultimately, the focus is on enhancing the optical clarity of the solid–liquid system, while the slight mismatches between both phases are capitalized on and deliberately exploited in Chapters three and four.

Table 1.3: RI measurements for NH_4SCN solution at different concentrations and temperatures.

Concentration wt%	T °C	$RI_{exp} \pm 0.005$	$RI_{Borrero-Echeverry} \pm 0.004$
55	21 - 22	1.4742	1.4727
	22 - 23	1.4737	1.4725
61	21 - 22	1.4913	1.4928
	22 - 23	1.4910	1.4925

Based on the initial screening of some PIV tests, the best image quality is reached at 61 wt% NH_4SCN. A comparison between the effect of the addition of PMMA microparticles (α_p= 0.5 v%) on the image quality of the liquid phase is reported in Figure 1.4 below. As can be seen, tracers representing the liquid phase are best detected with a clearer capture in the 61 wt% NH_4SCN case (Right). The tracers appear as small white spots in the raw images, despite the presence of the dispersed phase (PMMA particles) thanks to the RIM effect. The difference is more evident in the impeller region and the bulk. Note that only tracers are detected in these images and not PMMA microparticles (dispersed phase). As a reminder, the image quality in this context means that the tracers representing the liquid phase are still detected with increasing volume fractions of PMMA particles (limiting the blur effect and noise generated). Another note is that a simple visual assessment of both concentrations would not make a clear distinguish since the particles are of micrometer size, so a practical test with PIV is rather adequate. Thus, 61 wt% of NH_4SCN is considered as a better matching option for PMMA (at 22 – 23 °C), at which particle volume fractions could reach the desired range (α_p = 2 – 3 v%), while acquiring information on the behaviour of the fluid phase.

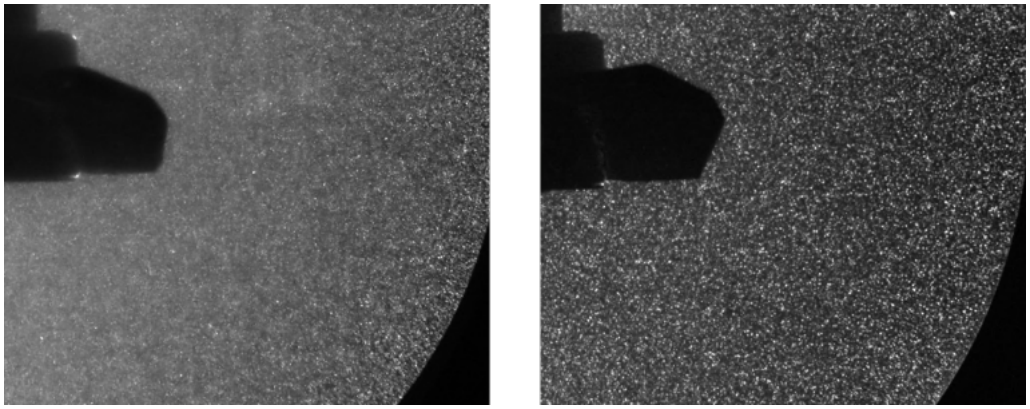

Figure 1.4: A comparison of the quality of liquid phase PIV raw images in presence of PMMA at α_p = 0.5 v%. **(Left)**: 55 wt% NH_4SCN solution. **(Right)**: 61 wt% NH_4SCN solution.

1.6.2 Density and Viscosity

NH_4SCN Solution

Since 61 wt% NH_4SCN solution is chosen as the option to go for the experiments, it is henceforth established for any characterization. Viscosity μ_f and density ρ_f are evaluated using Lovis 2000 M/ME a highly accurate rolling-ball viscometer widely used in R&D, pharmaceutical and chemical industries (Figure 1.5), equipped with a digital density meter DMA module. The density is determined based on the oscillating U-tube principle, where a U-shaped glass tube filled with 61 wt% NH_4SCN solution is set into vibration, and the oscillation period shifts according to the mass of the fluid. By precisely measuring this period, with corrections for temperature, the device converts it into an accurate density value. As for viscosity, it is based on Hoeppler's falling ball principle, which measures the time required for a ball to fall under gravity through the tube, which is inclined at an angle and filled with the same solution. The device applies different angles to calculate the average time that would be finally used with the manually entered density to obtain the viscosity of the fluid sample (works with Newtonian fluids). The desired temperature is also adjusted with attention paid to the filling process of the liquid into the device, as bubbles should not be presented inside the measuring tubes (density and viscosity).

For each prepared solution (61 wt%), the measurements are repeated multiple times to ensure consistency; this procedure is performed for each batch prepared to verify the composition of the solution and ensure precision across preparations (i.e., at least three times before every PIV/PTV experiment). On average, the density and viscosity evaluated for 61 wt% NH_4SCN, at 22 – 23 °C temperature, are ρ_f= 1139.2 ± 0.1 kg/m^3 and μ_f= 1.94 ±0.01 mPa.s, respectively. It should be noted that these values agree with the work of Borrero-Echeverry & Morrison [45] which further validate the accuracy of the device used.

Figure 1.5: Lovis 2000 M/ME device

PMMA Microparticles

Regarding the density of PMMA particles (Cospheric), ρ_p is estimated with the aid of a 5-ml volumetric Pycnometer (Figure A.1.3 in the Appendix). It is simple to use and handle, yet special consideration is placed on the temperature control. The challenge is that no temperature control is equipped with the device; hence it is maintained in a pre-heated water bath at a constant desired temperature.

Initially, the mass of the pycnometer is measured in a clean, dry state. This is followed by measuring the mass of the pycnometer completely filled with water up to the capillary, using water of known density (or any liquid of known density). These measurements are used to determine the volume of the pycnometer. Subsequently, the PMMA particles are placed in the dry pycnometer and the total mass is recorded. The pycnometer is then filled with water and the final mass of the system (pycnometer, particles, and water) is measured. From these measurements, the density of the particles is determined by dividing their mass by the volume in which they occupy. Note that some PMMA particles tend to float in water as a result of the formation of air bubbles between the particles (not fully hydrophilic). Therefore, before measurements and to avoid this issue, a few drops of a surfactant (commercial soap) are added to the water to improve wetting.

Several measurements were taken at different temperature levels, as can be seen in Figure 1.6, for more converged results. The average value was around $\rho_p = 1185$ kg/m^3 for temperatures ranging between 22 – 23°C.

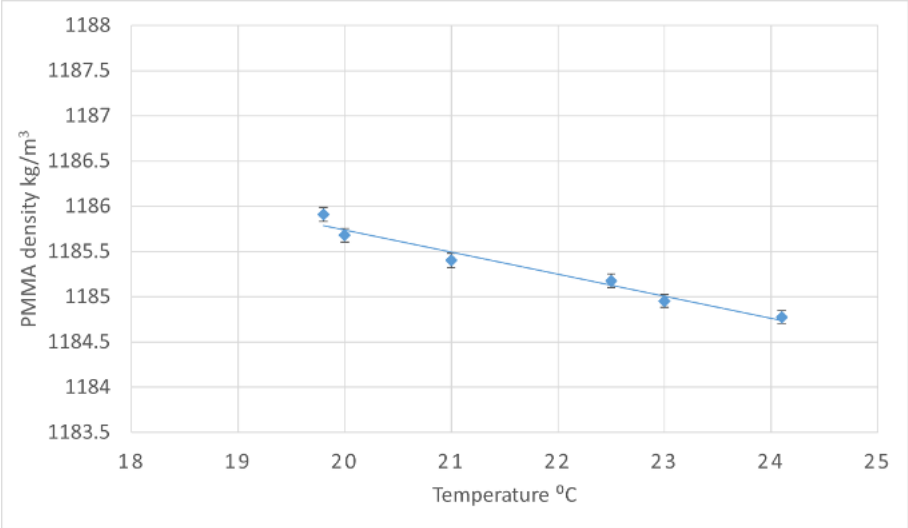

Figure 1.6: PMMA density (kg/m^3) recordings as a function of temperature °C.

1.6.3 PMMA Size

Regarding particle size, an optical microscope is used with the aid of Zenith software to capture high-resolution images of the particles (Figure 1.7). The process consists of visualizing the particles deposited on a lens in the presence of water by adjusting the focus for sharp and clear images. Recording a good number of images is also essential to provide a more accurate and representative evaluation (counted particles > 1000). A 5 times zoom lens (×5) was chosen to capture the images.

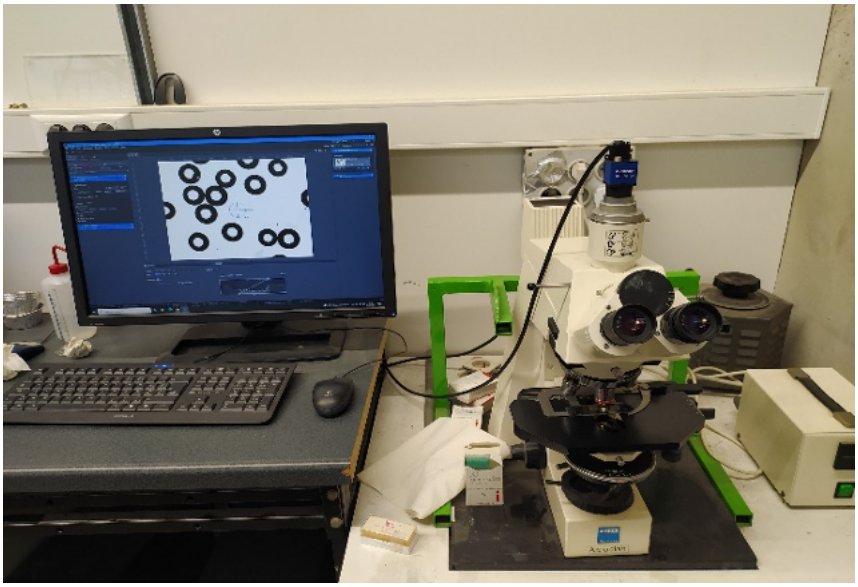

Figure 1.7: Microscope associated with Zenith software to register images.

The collected images are treated with a MATLAB script by transforming them into binary data type, eliminating any noise interference that may affect the detection, and finally resolving the particle size. Since PMMA are perfectly spherical, the script is able to

evaluate the diameter of each detected particle. A dashed blue line is over-plotted around the circumference of the particles in the raw images, indicating a successful detection, as can be seen in Figure 1.8.

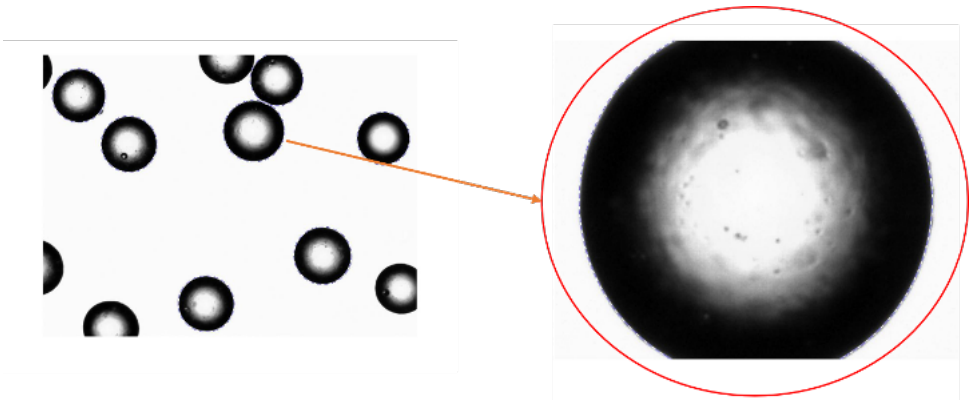

Figure 1.8: Raw image of PMMA particles and the corresponding diameter detected in MATLAB, zoom level ×5. Dashed blue lines on the circumference of the particles is shown as a successful detection.

The results in Figure 1.9 represent the distribution, in fractions, of the estimated diameter of PMMA particles for a total of 1100 measurements (1100 particle count). It is evident that the majority of the distribution, around 0.7 in fraction (70%), is heavily concentrated between 160 µm and 180 µm. The manufacturer (Cospheric) highlights that the range of these particles varies between 150 – 180 µm, which means that the sieving process is bounded within these norms and hence explains this distribution. The mean calculated diameter is then d_p = 168 µm with a standard deviation of ±9.33 µm.

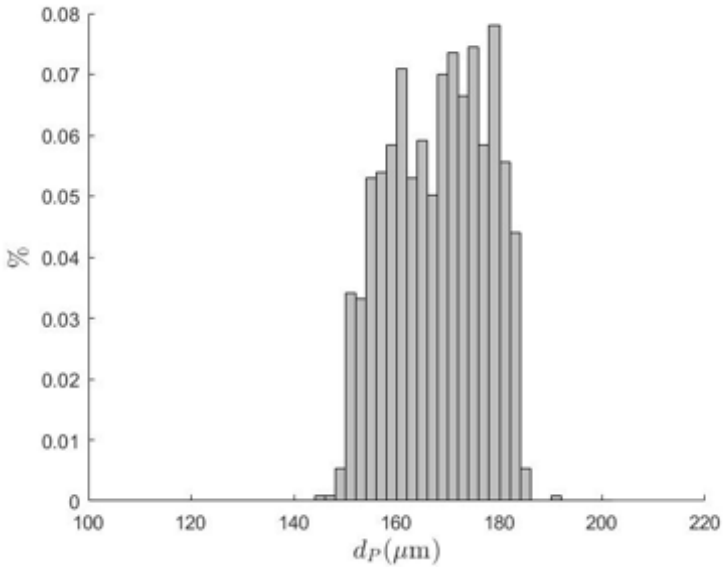

Figure 1.9: The distribution, in fractions (-), of the detected diameter of PMMA particles (d_p µm) for a total of 1100 particle count.

1.7 Summary

Using the aforementioned techniques and methods, the relevant model properties were rigorously evaluated to ensure that all the applicable aspects were verified before starting the experimental campaign. As a summary, Table 1.4 concludes the different properties of the alternative PMMA/NH_4SCN system compared to Cytodex/water, with a provisional estimation of the useful characteristic numbers for flow characterization including Reynolds ($Re \approx 5000$) and Stokes ($St \approx 0.08$). To emphasize the comparability between PMMA/NH_4SCN and Cytodex/water, other theoretical assumptions were evaluated using a model previously established by Loubiere et al. [70]. The geometric configurations of the stirred tank used for the model is the same as the one used in the experiments of this work. For the just suspended speed N_{js}, the solid volume fraction considered is α_p= 10 v%. Although the settling/terminal velocity of the substitute system is approximately three times higher than that of the original system, the Stokes regime is still attained. The Stokes law here refers to the estimation of the settling velocity of spherical particles in a quiescent fluid, which was also validated by Delafosse et al. [38] on this type of solid–liquid properties.

Moreover, another RIM example candidate is added in the table in the last column (PMMA with turpentine and tetralin mixture) to emphasize the importance of density matching and further validate the chosen PMMA/NH_4SCN system. This additional case is included as a contrast example to explore the effect of a larger density mismatch on the behaviour of settling and suspension; other candidates in the literature might have a better density ratio compared to $\rho_f/\rho_p \approx 0.76$, but were not retained due to practical limitations, as explained earlier (i.e. safety). As may be observed, the settling velocity jumps by more than one order of magnitude compared to the original Cytodex-1/PMMA which imply that this is beyond the Stokes law. The estimated just suspended speed is also far beyond the transitional flow being fully turbulent (Re > 10000), which further contradicts the principle of suspending microcarriers at the lowest energy required. Hence, RIM solid–liquid candidates with $\rho_f/\rho_p < 0.95$ are not suitable to represent the relevant flow of MSC culture.

Table 1.4: Comparison of relevant properties between PMMA/CH_4SCN, Cytodex-1/Water, and PMMA/(Turpentine + tetralin) systems at α_p = 10 v%. Models used are adapted from [70].

	Properties	PMMA/CH_4SCN	Cytodex-1/Water	PMMA/(Turpentine + tetralin)
	ρ_f/ρ_p (-)	$\approx 0.95 - 0.96$	≈ 0.97	≈ 0.76
	μ_f (mPa.s)	$\approx 1.5 - 1.9$	1	≈ 1.5
	Particles size d_p (µm)	≈ 168	≈ 160	≈ 168
	Terminal velocity (10^{-4} m/s)	$\approx 5.5 - 6.5$	≈ 2.4	≈ 30
Model by [70]	Stokes law	✓	✓	X
→	Just suspended N_{js} (rpm)	≈ 118	≈ 85	≈ 230
	Reynolds number Re	≈ 4000	4000	10500
	Stokes number St	0.056	0.04	0.2

Accordingly, the PMMA/NH_4SCN system was chosen as the most suitable RIM candidate for this thesis, with its relevant properties established and verified to be representative of the original Cytodex-1/water system.

Bibliography

[1] L. Yount, *Antoni van Leeuwenhoek: first to see microscopic life*. Enslow Publishers, Inc., 2009.

[2] D. Ribatti, "An historical note on the cell theory," *Experimental cell research*, vol. 364, no. 1, pp. 1–4, 2018.

[3] R. Virchow, "As based upon physiological and pathological histology," *Nutrition reviews*, vol. 47, no. 1, pp. 23–25, 1989.

[4] A.-H. Maehle, "Ambiguous cells: the emergence of the stem cell concept in the nineteenth and twentieth centuries," *Notes and Records of the Royal Society*, vol. 65, no. 4, pp. 359–378, 2011.

[5] J. B. Gurdon, "The developmental capacity of nuclei taken from differentiating endoderm cells of xenopus laevis," *Development*, vol. 8, no. 4, pp. 505–526, 1960.

[6] A. Friedenstein, R. Chailakhyan, and U. Gerasimov, "Bone marrow osteogenic stem cells: in vitro cultivation and transplantation in diffusion chambers," *Cell proliferation*, vol. 20, no. 3, pp. 263–272, 1987.

[7] M. Owen, "Marrow stromal stem cells," *Journal of cell science*, vol. 1988, no. Supplement_10, pp. 63–76, 1988.

[8] A. I. Caplan, "Mesenchymal stem cells," *Journal of orthopaedic research*, vol. 9, no. 5, pp. 641–650, 1991.

[9] R. Berebichez-Fridman and P. R. Montero-Olvera, "Sources and clinical applications of mesenchymal stem cells: state-of-the-art review," *Sultan Qaboos University Medical Journal*, vol. 18, no. 3, p. e264, 2018.

[10] I. Ullah, R. B. Subbarao, and G. J. Rho, "Human mesenchymal stem cells-current trends and future prospective," *Bioscience reports*, vol. 35, no. 2, p. e00191, 2015.

[11] G. J. Jimenez-Puerta, J. A. Marchal, E. López-Ruiz, and P. Gálvez-Martín, "Role of mesenchymal stromal cells as therapeutic agents: potential mechanisms of action and implications in their clinical use," *Journal of clinical medicine*, vol. 9, no. 2, p. 445, 2020.

[12] "World health statistics, disease burden and mortality estimates," *World Health Organisation*, 2020.

[13] Y. Chen, X. Li, J. Zhang, J. Peng, F. Huang, J. Bao, Y. Fan, and S. Huang, "Global clinical trials on stem cell therapy for autoimmune diseases: trends and future directions," *Frontiers in Immunology*, vol. 16, p. 1616231, 2025.

[14] J. Panés, D. García-Olmo, G. Van Assche, J. F. Colombel, W. Reinisch, D. C. Baumgart, A. Dignass, M. Nachury, M. Ferrante, L. Kazemi-Shirazi, *et al.*, "Expanded allogeneic adipose-derived mesenchymal stem cells (cx601) for complex perianal fistulas in crohn's disease: a phase 3 randomised, double-blind controlled trial," *The Lancet*, vol. 388, no. 10051, pp. 1281–1290, 2016.

[15] E. Özmert and U. Arslan, "Management of retinitis pigmentosa by wharton's jelly-derived mesenchymal stem cells: prospective analysis of 1-year results," *Stem cell research & therapy*, vol. 11, no. 1, p. 353, 2020.

[16] D. Jovic, Y. Yu, D. Wang, K. Wang, H. Li, F. Xu, C. Liu, J. Liu, and Y. Luo, "A brief overview of global trends in msc-based cell therapy," *Stem cell reviews and reports*, vol. 18, no. 5, pp. 1525–1545, 2022.

[17] D. Eibl, R. Eibl, and R. Pörtner, "Mammalian cell culture technology: An emerging field," in *Cell and Tissue Reaction Engineering: With a Contribution by Martin Fussenegger and Wilfried Weber*, pp. 3–11, Springer, 2009.

[18] A. v. van Wezel, "Growth of cell-strains and primary cells on micro-carriers in homogeneous culture," *Nature*, vol. 216, no. 5110, pp. 64–65, 1967.

[19] A. S. Simaria, S. Hassan, H. Varadaraju, J. Rowley, K. Warren, P. Vanek, and S. S. Farid, "Allogeneic cell therapy bioprocess economics and optimization: Single-use cell expansion technologies," *Biotechnology and bioengineering*, vol. 111, no. 1, pp. 69–83, 2014.

[20] X. Zhang, M. Stettler, D. De Sanctis, M. Perrone, N. Parolini, M. Discacciati, M. De Jesus, D. Hacker, A. Quarteroni, and F. Wurm, "Use of orbital shaken disposable bioreactors for mammalian cell cultures from the milliliter-scale to the 1,000-liter scale," in *Disposable bioreactors*, pp. 33–53, Springer, 2009.

[21] K. Y. Tan, K. L. Teo, J. F. Lim, A. K. Chen, S. Reuveny, and S. K. Oh, "Serum-free media formulations are cell line–specific and require optimization for microcarrier culture," *Cytotherapy*, vol. 17, no. 8, pp. 1152–1165, 2015.

[22] N. Timmins, M. Kiel, M. Günther, C. Heazlewood, M. Doran, G. Brooke, and K. Atkinson, "Closed system isolation and scalable expansion of human placental mesenchymal stem cells," *Biotechnology and bioengineering*, vol. 109, no. 7, pp. 1817–1826, 2012.

[23] V. Jossen, C. Schirmer, D. Mostafa Sindi, R. Eibl, M. Kraume, R. Pörtner, and D. Eibl, "Theoretical and practical issues that are relevant when scaling up hmsc microcarrier production processes," *Stem cells international*, vol. 2016, no. 1, p. 4760414, 2016.

[24] A. Reichardt, B. Polchow, M. Shakibaei, W. Henrich, R. Hetzer, and C. Lueders, "Large scale expansion of human umbilical cord cells in a rotating bed system bioreactor for cardiovascular tissue engineering applications," *The Open Biomedical Engineering Journal*, vol. 7, p. 50, 2013.

[25] Q. A. Rafiq, K. M. Brosnan, K. Coopman, A. W. Nienow, and C. J. Hewitt, "Culture of human mesenchymal stem cells on microcarriers in a 5 l stirred-tank bioreactor," *Biotechnology letters*, vol. 35, no. 8, pp. 1233–1245, 2013.

[26] T. Lawson, D. E. Kehoe, A. C. Schnitzler, P. J. Rapiejko, K. A. Der, K. Philbrick, S. Punreddy, S. Rigby, R. Smith, Q. Feng, *et al.*, "Process development for expansion of human mesenchymal stromal cells in a 50 l single-use stirred tank bioreactor," *Biochemical engineering journal*, vol. 120, pp. 49–62, 2017.

[27] Y. Shyu, K. Stratheam, and R. M. Eglen, "Large-scale expansion of stem cells for therapy and screening," *Drug Discov World Winter*, vol. 2013, no. Winter, pp. 35–9, 2013.

[28] J. Thorbow, A. Strauch, V. Pfening, J.-P. Klee, P. Brücher, B. Boshof, F. Petry, P. Czermak, M. B. Herrera Sanchez, and D. Salzig, "Large-scale expansion of human liver stem cells using two different bioreactor systems," *Bioengineering*, vol. 11, no. 7, p. 692, 2024.

[29] W. G. Whitford, J. C. Hardy, and J. J. Cadwell, "Single-use, continuous processing of primary stem cells," *BioProcess Int*, vol. 12, no. 3, pp. 26–32, 2014.

[30] J. E. Hambor, "Bioreactor design and bioprocess controls for industrialized cell processing," *BioProcess Int*, vol. 10, no. 6, pp. 22–33, 2012.

[31] B. Vang, N. Frank, M. Jones, B. Nankervis, and C. Coeshott, "Expansion and cellular characterization of primary human adherent cells in the quantum® cell expansion system, a hollow-fiber bioreactor system," *Journal of Biological Methods*, vol. 7, no. 2, pp. e130–e130, 2020.

[32] J. Warnock, K. Bratch, and M. Al-Rubeai, "Packed bed bioreactors," in *Bioreactors for Tissue Engineering: Principles, Design and Operation*, pp. 87–113, Springer, 2005.

[33] A.-C. Tsai, Y. Liu, and T. Ma, "Expansion of human mesenchymal stem cells in fibrous bed bioreactor," *Biochemical Engineering Journal*, vol. 108, pp. 51–57, 2016.

[34] V. Jossen, R. Pörtner, S. C. Kaiser, M. Kraume, D. Eibl, and R. Eibl, "Mass production of mesenchymal stem cells of bioreactor design and flow conditions on," *Cells and biomaterials in regenerative medicine*, p. 119, 2014.

[35] C. Loubière, *Characterization and impact of the hydrodynamics on the performance of umbilical-cord derived stem cells culture in stirred tank bioreactors*. PhD thesis, Université de Lorraine, 2018.

[36] C. Maillot, *Quantification and impact of microcarrier collisions during mesenchymal stem cell culture in bioreactors*. PhD thesis, Université de Lorraine; Université de Liège (Belgique), 2022.

[37] B. E. Poling, J. M. Prausnitz, O. John Paul, and R. C. Reid, *The properties of gases and liquids*, vol. 5. Mcgraw-hill New York, 2001.

[38] A. Delafosse, C. Loubière, S. Calvo, D. Toye, and E. Olmos, "Solid-liquid suspension of microcarriers in stirred tank bioreactor–experimental and numerical analysis," *Chemical Engineering Science*, vol. 180, pp. 52–63, 2018.

[39] S. F. Wright, I. Zadrazil, and C. N. Markides, "A review of solid–fluid selection options for optical-based measurements in single-phase liquid, two-phase liquid–liquid and multiphase solid–liquid flows," *Experiments in Fluids*, vol. 58, no. 9, p. 108, 2017.

[40] S.-i. Satake, Y. Aoyagi, N. Unno, K. Yuki, Y. Seki, and M. Enoeda, "Three-dimensional flow measurement of a water flow in a sphere-packed pipe by digital holographic ptv," *Fusion Engineering and Design*, vol. 98, pp. 1864–1867, 2015.

[41] A. Karnis, H. Goldsmith, and S. Mason, "The kinetics of flowing dispersions: I. concentrated suspensions of rigid particles," *Journal of colloid and interface science*, vol. 22, no. 6, pp. 531–553, 1966.

[42] M. Mehta, J. Kadambi, S. Sastry, J. Sankovic, M. Wernet, G. Addie, and R. Visintainer, "Particle velocities in the rotating impeller of a slurry pump," in *Fluids Engineering Division Summer Meeting*, vol. 42886, pp. 369–378, 2007.

[43] F. Soranna, Y.-C. Chow, O. Uzol, and J. Katz, "Turbulence within a turbomachine rotor wake subject to nonuniform contraction," *AIAA journal*, vol. 46, no. 11, pp. 2687–2702, 2008.

[44] B. Bailey and M. Yoda, "An aqueous low-viscosity density-and refractive index-matched suspension system," *Experiments in fluids*, vol. 35, no. 1, pp. 1–3, 2003.

[45] D. Borrero-Echeverry and B. C. Morrison, "Aqueous ammonium thiocyanate solutions as refractive index-matching fluids with low density and viscosity," *Experiments in Fluids*, vol. 57, no. 7, p. 123, 2016.

[46] R. Reddy, M. Sathe, J. Joshi, K. Nandakumar, and G. Evans, "Recent developments in experimental (piv) and numerical (dns) investigation of solid–liquid fluidized beds," *Chemical Engineering Science*, vol. 92, pp. 1–12, 2013.

[47] J. A. Dijksman, F. Rietz, K. A. Lőrincz, M. Van Hecke, and W. Losert, "Invited article: Refractive index matched scanning of dense granular materials," *Review of Scientific Instruments*, vol. 83, no. 1, 2012.

[48] M. Tindal, R. Cheung, and M. Yianneskis, "Velocity characteristics of steady flows through engine inlet ports and cylinders," tech. rep., SAE Technical Paper, 1988.

[49] D. Duncan, C. Bargeron, S. Borchardt, O. Deters, S. Gearhart, F. Mark, and M. Friedman, "The effect of compliance on wall shear in casts of a human aortic bifurcation," *Journal of biomechanical engineering*, vol. 112, no. 2, pp. 183–188, 1990.

[50] K. Perktold, M. Hofer, G. Rappitsch, M. Loew, B. Kuban, and M. Friedman, "Validated computation of physiologic flow in a realistic coronary artery branch," *Journal of biomechanics*, vol. 31, no. 3, pp. 217–228, 1997.

[51] L. Hopkins, J. Kelly, A. Wexler, and A. Prasad, "Particle image velocimetry measurements in complex geometries," *Experiments in Fluids*, vol. 29, no. 1, pp. 91–95, 2000.

[52] T. B. Le, D. R. Troolin, D. Amatya, E. K. Longmire, and F. Sotiropoulos, "Vortex phenomena in sidewall aneurysm hemodynamics: experiment and numerical simulation," *Annals of biomedical engineering*, vol. 41, no. 10, pp. 2157–2170, 2013.

[53] C. Stoots, S. Becker, K. Condie, F. Durst, and D. McEligot, "A large-scale matched index of refraction flow facility for lda studies around complex geometries," *Experiments in fluids*, vol. 30, no. 4, pp. 391–398, 2001.

[54] H. M. McIlroy Jr, D. M. McEligot, and R. J. Pink, "Measurement of turbulent flow phenomena for the lower plenum of a prismatic gas-cooled reactor," *Nuclear engineering and design*, vol. 240, no. 2, pp. 416–428, 2010.

[55] D. A. Jacobs, C. W. Jacobs, and C. D. Andereck, "Biological scattering particles for laser doppler velocimetry," *The Physics of fluids*, vol. 31, no. 12, pp. 3457–3461, 1988.

[56] Y. A. Hassan and E. Dominguez-Ontiveros, "Flow visualization in a pebble bed reactor experiment using piv and refractive index matching techniques," *Nuclear Engineering and Design*, vol. 238, no. 11, pp. 3080–3085, 2008.

[57] F. Mikami, B. Chen, and N. Nishikawa, "Visualization and ptv study of natural convection in particle suspensions (simultaneous measurements of velocity, temperature and interface between particle-free fluid and suspension)," *JSME International Journal Series B Fluids and Thermal Engineering*, vol. 44, no. 1, pp. 30–37, 2001.

[58] M. Abbas and C. Crowe, "Experimental study of the flow properties of a homogenous slurry near transitional reynolds numbers," *International journal of multiphase flow*, vol. 13, no. 3, pp. 357–364, 1987.

[59] L. Mondy, A. Graham, A. Majumdar, and L. Bryant Jr, "Techniques of measuring particle motions in concentrated suspensions," *International journal of multiphase flow*, vol. 12, no. 3, pp. 497–502, 1986.

[60] V. A. Patil and J. A. Liburdy, "Optical measurement uncertainties due to refractive index mismatch for flow in porous media," *Experiments in fluids*, vol. 53, no. 5, pp. 1453–1468, 2012.

[61] V. Breedveld, D. van den Ende, A. Tripathi, and A. Acrivos, "The measurement of the shear-induced particle and fluid tracer diffusivities in concentrated suspensions by a novel method," *Journal of Fluid Mechanics*, vol. 375, pp. 297–318, 1998.

[62] J. Nouri, J. Whitelaw, and M. Yianneskis, "Particle motion and turbulence in dense two-phase flows," *International journal of multiphase flow*, vol. 13, no. 6, pp. 729–739, 1987.

[63] O. Uzol, D. Brzozowski, Y.-C. Chow, J. Katz, and C. Meneveau, "A database of piv measurements within a turbomachinery stage and sample comparisons with unsteady rans," *Journal of Turbulence*, no. 8, p. N10, 2007.

[64] S. Burgmann, S. Große, W. Schröder, J. Roggenkamp, S. Jansen, F. Gräf, and M. Büsen, "A refractive index-matched facility for fluid–structure interaction studies of pulsatile and oscillating flow in elastic vessels of adjustable compliance," *Experiments in fluids*, vol. 47, no. 4, pp. 865–881, 2009.

[65] R. G. Morgan, C. N. Markides, I. Zadrazil, and G. F. Hewitt, "Characteristics of horizontal liquid–liquid flows in a circular pipe using simultaneous high-speed laser-induced fluorescence and particle velocimetry," *International journal of multiphase flow*, vol. 49, pp. 99–118, 2013.

[66] I. Burdett, D. Webb, and G. Davies, "A new technique for studying dispersion flow, holdup and axial mixing in packed extraction columns," *Chemical Engineering Science*, vol. 36, no. 12, pp. 1915–1919, 1981.

[67] D. Hirsch, E. C. Graff, F. Pereira, and M. Gharib, "Influence of common transparent materials on the accuracy of image-based velocimetry," *Measurement Science and Technology*, vol. 26, no. 8, p. 087002, 2015.

[68] R. Saksena, K. T. Christensen, and A. J. Pearlstein, "Surrogate immiscible liquid pairs with refractive indexes matchable over a wide range of density and viscosity ratios," *Physics of Fluids*, vol. 27, no. 8, 2015.

[69] K. S. Potter and J. H. Simmons, *Optical Materials*. Elsevier, 2021.

[70] C. Loubière, A. Delafosse, E. Guedon, I. Chevalot, D. Toye, and E. Olmos, "Dimensional analysis and cfd simulations of microcarrier 'just-suspended'state in mesenchymal stromal cells bioreactors," *Chemical Engineering Science*, vol. 203, pp. 464–474, 2019.

Appendix

Chemical	20 °C	50 °C	Chemical	20 °C	50 °C
Acetaldehyde (Ethanal)	C	D	Acetamide	B	D
Acetic Acid, anhydrous	D	D	Acetone	D	D
Acetonitrile	D	D	Acrylonitrile	B	D
Adipic Acid	B	B	Alanine	A	na
Aluminum Chloride, 10%	A	B	Ammonia, aqueous 25%	A	D
Ammonium Nitrate, 10%	A	D	Aniline	D	D
Antimony Trichloride	C	D	Aqua Regia	D	D
Barium Carbonate	A	na	Barium Chloride, 10%	A	A
Barium Hydroxide	A	D	Benzaldehyde	C	D
Benzene (Benzol)	D	D	Benzoic Acid	A	C
Benzoyl Chloride	D	D	Benzyl Alcohol (Phenyl-methanol)	D	D
Bromine Gas	D	D	Bromobenzene	D	D
Butane Gas	A	na	Butanol (1-Butyl Alcohol)	C	D
Calcium Acetate	C	D	Calcium Carbonate	A	A
Calcium Chloride, 10%	B	B	Calcium Hydroxide, 10%	A	A
Calcium Nitrate	A	D	Calcium Sulfate, 10%	A	D
Carbon Disulfide	D	D	Carbon Tetrachloride	C	D
Chromic Acid, 50%	D	D	Citric Acid, 20%	C	D
Chlorobenzene	D	D	Chloroform	D	D
Copper Nitrate	A	na	Copper Sulfate, 5%	A	A
Cyclohexane	C	D	Cyclohexanone	D	D
Dichloroacetic Acid	D	D	Dichloromethane	D	D
Diethyl Ether	D	D	Diethyl Ketone	D	D
Dimethyl Formamide (DMF)	D	D	Dimethyl Sulfoxide (DMSO)	C	D
Dioxane (1,4-Dioxane)	D	D	Diphenyl Ether	D	D
Ethanol (Ethyl Alcohol), 30%	D	D	Ethyl Acetate	D	D
Ethyl Benzene	D	D	Ethylene Glycol	A	A
Ethylene Oxide Gas (EtO)	D	D	Ethylenediamine	D	D
Ferric Chloride	B	D	Ferric Sulfate	B	D
Ferrous Chloride, 10%	A	na	Ferrous Sulfate	A	na
Fluorohydric Acid (HF)	D	D	Formaldehyde, 40%	B	C

Table A.1.1: PMMA — General chemical compatibility (major/common chemicals). Ratings at 20 °C and 50 °C. A = Excellent; B = Good - minor effect, slight corrosion or discolouration; C = Fair - Moderate (use not recommended); D = Severe (not recommended for ANY use). "na" = not available. Table adapted from Industrial Specialties Mfg. (ISM). Full classification could be found at www.industrialspec.com.

continued from previous page.

Chemical	**20 °C**	**50 °C**	**Chemical**	**20 °C**	**50 °C**
Formic Acid, 98–100%	D	D	Furfural	D	D
Gallic Acid, 5%	A	na	Gasoline	D	D
Glutaraldehyde	B	na	Glycerine (Glycerol)	A	A
Glycine	C	D	Glycolic Acid	C	D
Heptane	C	D	Hexafluorosilicic Acid	C	D
Hexane	C	C	Hexanoic Acid	A	na
Hydrazine Hydrate	C	D	Hydrochloric Acid, 35%	C	D
Hydrofluoric Acid, 40%	C	D	Hydrogen Peroxide, 30%	C	D
Hydrogen Sulfide, aqueous	A	D	Hydroquinone	A	na
Iodine	A	D	Iodine Tincture, 5%	D	D
Iron Perchloride	D	D	Isobutanol (Isobutyl Alcohol)	C	D
Isopropanol (2-Propanol)	B	D	Isopropyl Ether	C	D
Kerosene	A	C	Lactic Acid, 85%	B	C
Lead Acetate	B	D	Lithium Chloride	A	na
Lugol Solution	A	na	Magnesium Nitrate	B	D
Magnesium Sulfate	C	D	Maleic Acid	C	D
Mercuric Chloride	A	A	Methanol, 100%	C	D
Methyl Ethyl Ketone (MEK)	D	D	Methyl Isobutyl Ketone (MIBK)	D	D
Methylene Chloride (DCM)	D	D	Nickel Sulfate	A	na
Nitric Acid, 70%+	D	D	Nitrobenzene	D	D
Nitromethane	D	D	Nitrilotriethanol	A	na
Oxalic Acid	B	B	Oxalic Acid, 10%	A	A
Oleic Acid	C	D	Oxirane (Ethylene Oxide)	D	D
Ozone Gas	A	C	Perchloric Acid	C	D
Perchloroethylene	C	D	Phenol (Carbolic Acid)	D	D
Phosphoric Acid, 85%	D	D	Phosphorus Trichloride	D	D
Potassium Hydroxide, 30%	A	D	Potassium Nitrate, 10%	A	na
Potassium Permanganate	B	B	Propanol (1-Propanol)	B	D
Propylene Glycol	B	C	Propylene Oxide	C	D
Pyridine	D	D	Resorcinol	C	D
Salicylic Acid	B	D	Silver Nitrate	A	A

Table A.1.1: PMMA — General chemical compatibility (major/common chemicals). Ratings at 20 °C and 50 °C. A = Excellent; B = Good - minor effect, slight corrosion or discolouration; C = Fair - Moderate (use not recommended); D = Severe (not recommended for ANY use). "na" = not available. Table adapted from Industrial Specialties Mfg. (ISM). Full classification could be found at www.industrialspec.com.

continued from previous page.

Chemical	**20 °C**	**50 °C**	**Chemical**	**20 °C**	**50 °C**
Sodium Carbonate (Soda Ash)	B	D	Sodium Hydroxide, 10%	A	A
Sodium Hydroxide, >50%	A	D	Sodium Hypochlorite, 15%	A	A
Sodium Nitrate, 50%	A	na	Sodium Sulfite	A	na
Styrene	D	D	Sulfuric Acid, 98%	D	D
Sulfuric Acid, 60%	D	D	Sulfuric Acid, 6%	A	A
Tannic Acid	D	D	Tartaric Acid	C	C
Tetrachloroethylene	D	D	Tetrahydrofuran (THF)	D	D
Thionyl Chloride	D	D	Toluene	D	D
Trichloroacetic Acid	C	D	Trichloroethylene	D	D
Vinyl Acetate	D	D	Vinyl Chloride (Chloroethylene)	D	D
Water (general)	A	na	Xylene (Xylol)	D	D
Zinc Chloride, 10%	B	B	Zinc Sulfate, 10%	B	C

Table A.1.1: PMMA — General chemical compatibility (major/common chemicals). Ratings at 20 °C and 50 °C. A = Excellent; B = Good - minor effect, slight corrosion or discolouration; C = Fair - Moderate (use not recommended); D = Severe (not recommended for ANY use). "na" = not available. Table adapted from Industrial Specialties Mfg. (ISM). Full classification could be found at www.industrialspec.com.

Figure A.1.1: Corrosion effect of NH_4SCN in contact with plain steel. Duration: 3 - 4 days.

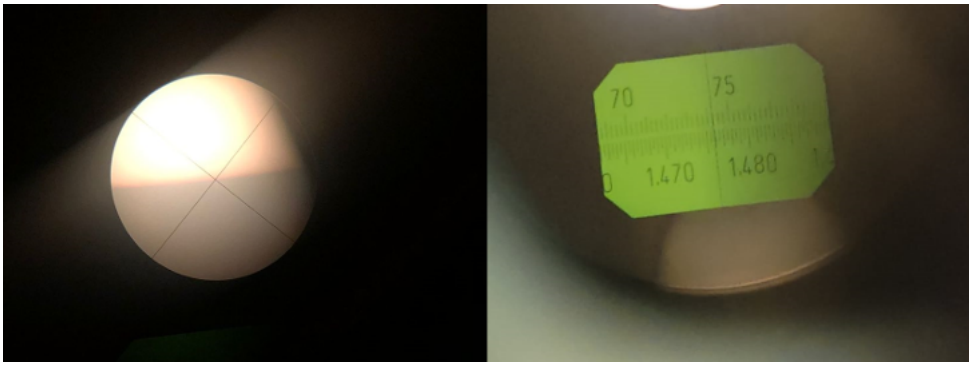

Figure A.1.2: A reading example of Abbe refractometer for 55 wt% NH_4SCN solution at 21 – 22 °C.

Figure A.1.3: 5–mL volumetric Pycnometer filled with PMMA particles and water

Chapter 2

Impact of PMMA Microparticles Addition on Liquid-Phase Flow Behaviour: One-Phase PIV

Abstract

Mesenchymal stem cells are widely cultivated in stirred tank bioreactors. Due to their adhesion properties, they are attached to small spheres called microcarriers. To understand the hydromechanical stresses encountered by the cells, it is essential to characterize the flow using the PIV technique. However, the usual solid–liquid system used in cell cultures has poor optical properties. Thus, shifting to one with better optical properties, while respecting the physical characteristics, is mandatory to achieve a relevant representation. PMMA microparticles suspended with 61 wt% ammonium thiocyanate solution NH_4SCN were found to be a robust candidate. The refractive index (RI) of both sides is of the order of 1.491 with a density ratio of $\rho_f/\rho_p \approx 0.96$, and particle size averaged around 168 µm. Using the RIM-PIV (refractive index matched particle image velocimetry) technique for a 0.7 L volume stirred tank equipped with an HTPG down-pumping axial impeller and operating at full homogeneous speed N = 150 rpm, mean and turbulence quantities of the liquid phase were measured as a function of PMMA particle volume fractions α_p, which ranged from 0.5 to 3 v%. This corresponds to a particle number density of n = 12 particles/mm^3, which is considered original and challenging for the PIV technique. At 3 v%, the addition of particles dampened the turbulent kinetic energy (TKE) of the liquid phase locally by 20% near the impeller. This impact became trivial (<10%) at the local-average level. The structure and direction of the recirculation loop also shifted.

2.1 Introduction

Over the past few years, mesenchymal stem cells (MSCs) have become promising in the fields of regenerative medicine, tissue engineering, and therapeutics, targeting a wide range of intractable diseases [1]. In vitro expansion processes are essential to meet the demand [2]. The biological nature of MSCs is anchorage-dependent, as they inherently rely on surface attachment for optimal function. A stirred tank bioreactor is one promising process for cell expansion, using small spheres called microcarriers as a support [3, 4, 5]. It is thus important to suspend the microcarriers to ensure enough mixing, maximize the adherence surface, and limit the cell aggregation. However, mechanical stirring will generate hydromechanical stresses in the medium that can lead to cell damage [6, 7]. The density of the microcarriers is close to that of the liquid medium ($\rho_f/\rho_p \approx 1$) to guarantee complete suspension at low agitation rates. Nonetheless, damage to cells can still be an issue in the form of interactions with turbulent eddies, shear stresses, and collisions [8].

To optimize the production process, developing and validating hydrodynamic models are crucial. Many authors have attempted to characterize bioreactors in terms of design and geometry [9, 10, 11], operating conditions [12, 13, 14], and microcarrier impact and critical suspension [15, 16, 17, 18], both experimentally and numerically. Although few experimental studies have been conducted to characterize the interactions between the continuous liquid phase and particles such as microcarriers, with a small diameter (in the $150 - -300$ µm range) and a density close to the liquid phase, there is still insufficient knowledge to propose robust design and extrapolation models. As such, there is a strong need to collect extensive experimental data to characterize this particular solid–liquid system, and Particle Image Velocimetry (PIV) appears to be an ideal tool for this goal.

PIV, commonly used for characterizing single-phase flows, is a non-intrusive, laser-based optical imaging technique for the evaluation of mean and fluctuating velocities. Solid–liquid systems present a complex domain for PIV due to the opacity of the multiphase flow as a result of the solid phase presence. In the case of MSC culture, commercial microcarriers, such as dextran-based Cytodex-1 or polystyrene Star-Plus, are typically used at volume fractions of $\alpha_p = 2 - 3$ v% [19] and exhibit poor optical properties. When PIV is applied directly to suspensions of commercial microcarriers, the latter cause significant perturbations and scatter the laser sheet, resulting in blurred raw images that are challenging to analyze reliably.

To account for the optical issues, a refractive index matching (RIM) technique between the dispersed and continuous phases could be a powerful tool, minimizing distortions to the laser sheet. An earlier attempt to use the RIM-PIV method was made by Northrup et al. [20] to measure the velocity vectors of the flow of heterogeneous porous media in a

fluidized bed using PMMA particles of d_p= 9.4 mm. Another interesting study by Hopkins et al. [21] characterized the flow in a complex geometry: a model of the human nasal cavity made of clear silicone. Additionally, Morgan et al. [22] described the behavior of liquid–liquid flow in a horizontal circular tube by matching Exxsol D80 oil and a glycerol solution. A more recent application of RIM-PIV by Bluestein and Bohl [23] investigated particle-laden flow in a T-shaped geometry by matching hydrogel particles in water.

On the other hand, few authors have examined the solid–liquid flow characteristics in stirred tanks using PIV, particularly the impact of the solid phase on the liquid phase. To our knowledge, the first study was reported by Virdung and Rasmuson [24], where they used glass beads 1 mm in diameter that matched the refractive index of a benzyl alcohol/ethanol mixture up to 1.5 v% loading, suspended by means of a pitched-blade impeller with a corresponding Reynolds number of Re= 7500. They noticed an increase in the r.m.s. velocities with the increase in particle concentration. Unadkat et al. [25] also used glass spheres with a size of 1 mm, which were, however, suspended in water without matching the refractive index, reaching a dilute volumetric fraction of 0.5 v%. The two phases were then separated using a phase discrimination technique. The application of a fully turbulent regime of Re= 30 800 resulted in the suppression of the turbulence levels in the continuous phase for particle concentrations above 0.2 v%, as indicated by the turbulent kinetic energy TKE and the dissipation rate ε; the suppression level remained stable up to 0.5 v%. Gabriele et al. [26] used RIM-PIV for a small, high-throughput-scale tank with a 45 mm diameter. PMMA spheres of a relatively large 1.5 mm size were suspended in p-cymene solution up to 5 v%, at a speed below the critical suspension speed of N_{js} at Re= 9300. The TKE levels in the impeller region were dampened by 40% and the dissipation rate ε by 30 – 50% of the liquid flow. Note that the estimation of the dissipation rate by the two mentioned authors was based on the Smagorinsky subgrid-scale (SGS) method [27]. The work by Montante et al. [28] covered the dilute suspension of 0.2 v% glass particles, which were 115 and 774 µm in diameter, without RIM for the liquid phase at Re= 88 000, corresponding to a fully turbulent system. They found that the smaller particles moderately reduced turbulent fluctuations while enhancing the levels of the larger ones. Another recent paper featuring RIM-PIV by Li et al. [29] discussed the effect of 7 mm diameter silica glass spheres of 8 v% concentration on the continuous phase represented by phenyl silicone oil at Re= 10 000. Within the partially suspended state, the presence of particles attenuated the peak levels of TKE by around 41%.

Laser Doppler Anemometry (LDA) is yet another laser-imaging technique for capturing the flow, which is also widely used in research. Studies that addressed particle-laden flow inside stirred tanks and used this technique side-by-side with the RIM method include those by Nouri and Whitelaw [30], Kohnen and Bohnet [31], Micheletti and Yianneskis [32], and Virdung and Rasmuson [33]. Phase Doppler Anemometry (PDA) was used by Guiraud et

al. [34] for the investigation of dilute solid–liquid suspension in stirred tanks. Nouri and Whitelaw [30] used a mixture of tetralin and turpentine oil to match the refractive index of Diakon particles up to 2.5 v% concentration with sizes ranging from 590 to 730 µm. The experiments were applied to different geometric setups and Re numbers using a large tank volume (≈ 20 L). Overall, they found that the particles led the bulk fluid in down-flow motion and lagged it in up-flow regions compared with single-phase flow. The particle turbulence levels were lower by 15% in the impeller stream and 10% in the wall jet than those of the single-phase flow. Note that the fluid velocities in the presence of particles could not be measured due to the appearance of gas inclusions (bubbles or voids) inside the particles. A similar approach was followed later by Micheletti and Yianneskis [32], using the RIM method to suspend styrene/divinylbenzene particles of 186 µm size into a tertiary organic mixture at volumetric concentrations up to 2 v%, at Re= 20 000. Suppression of the radial component of both the mean and the r.m.s. liquid velocities in the impeller plane was observed, the latter by around 50% compared to single-phase values. This attenuation in turbulence levels was noticed at low concentrations of 0.2 v% and did not drop further after 1 v%.

So far, limited attention has been paid to the density-matching criterion between the carrier and the particle states ($\rho_f/\rho_p \approx 1$), the range of particle sizes (100 − 300 µm), and the impact of a relatively moderate Reynolds number on the flow. Most of the studies mentioned were carried out at large density differences ($\rho_f/\rho_p \ll 1$), except for the work of Micheletti and Yianneskis [32], which was conducted at a high Reynolds number. Few studies considered particle sizes in the µm range (microparticles), whereas the agitation was provided by either a Rushton turbine or a pitched-blade turbine impeller. Furthermore, it is important to note that among the authors cited, those who reported the Stokes number found it to be greater than unity ($St > 1$) under the relevant operating conditions.

The literature on the effect of particle addition on fluid turbulence at low Stokes numbers ($St < 1$) is even more limited. A very recent study by Sommer et al. [35] which covered a range of density ratios, particle diameters, and solid volume fractions, revealed that polyethylene particles of 150 − 180 µm in size up to 0.1 v% concentration and ρ_f/ρ_p= 0.91 dampened the fluid turbulent fluctuations for Stokes numbers as low as St= 0.019. Ferrante and Elghobashi [36] previously showed, using DNS data for a particle-laden suspension, that the trajectories of microparticles of St≪1 and a size of 63 µm at α_p= 0.1 v% with ρ_f/ρ_p= 0.001 were almost aligned with those of fluid points, allowing vortical structures to be retained for a longer time and increasing the turbulent kinetic energy and viscous dissipation rate compared to single-phase turbulence.

Table 2.1 below summarizes the main experimental research carried out in stirred tanks with solid–liquid flows, along with the technique used to measure the flow and the characteristics

of the experimental setup. In addition, it further highlights the scarcity of experiments dedicated to revealing the effect of the addition of particles on the behavior of the liquid phase.

Table 2.1: Side-by-side comparison of solid–liquid multiphase flow studies in stirred tanks. Particle number density n is not reported for the mentioned works and is estimated based on the given data.

Study	Technique	Agitator	d_p (μm)	α_p (v%)	ρ_f/ρ_p	Re	$n_{\max}$ (mm^{-3})
Nouri & Whitelaw [30]	LDA	RT	590/730	2.5	0.75	54 000	0.233
Virdung & Rasmuson [24]	PIV	PBT	1000	1.5	0.40	7 500	0.0286
Micheletti & Yianneskis [32]	LDA	RT	186	2.0	0.99	20 000	5.936
Unadkat et al. [25]	PIV	PBT	1000	0.5	0.40	30 800	0.0096
Montante et al. [28]	PIV	RT	115/774	0.2	0.40	88 000	2.512
Li et al. [29]	PIV	PBT	7000	8.0	0.45	10 000	0.00045
This work	PIV	HTPGD	168	3.0	0.96	5000	12

The main goal of this work is to characterize the influence of the presence of microparticles on the liquid phase flow under conditions as close as possible to those encountered in MSC culture. As the optical properties of commercial microcarriers are not ideal, the first step is to establish a substitute RIM solid–liquid system (PMMA particles suspended in ammonium thiocyanate NH_4SCN solution). The challenge lies in meeting the original model properties, including matched densities of both phases, microparticle size range, low viscosity of the liquid phase, and intermediate Reynolds and low Stokes ($St < 1$) numbers for a valid representation of the original system. The PIV technique is then used to evaluate the influence of particle addition at various volume fractions ($0.5 < \alpha_p < 3$ v%) on the hydrodynamics of the liquid phase alone. The volume fractions reached not only represent the relevant condition in which the MSCs are cultured, but also correspond to a particle number density $n = 12$ particle/mm^3, which creates a dense field of particle-–fluid interfaces, making conventional PIV subject to multiple scattering and laser sheet distortion. RIM is therefore essential to preserve tracers and recover reliable velocity fields at such concentrations.

2.2 Materials and methods

2.2.1 Solid–Liquid System Properties

Previous studies characterized microcarrier suspensions, both experimentally and numerically, using Cytodex-1 (d_p= 170 µm and ρ_p= 1020 kg/m^3) suspended in a phosphate-buffered saline (PBS) solution of 1 v% concentration (ρ_f= 1000 kg/m^3) to control the microcarrier diameter [16, 14]. Because this liquid phase is a dilute saline solution, it is hereafter referred to as "water" for simplicity. Unlike many commercial plastic microcarriers, Cytodex-1 microcarriers are partially translucent, and PIV measurements were attempted with this solid–liquid system. However, the refractive indices of the solid and liquid phases were not perfectly matched, limiting measurements to very low solid volume fractions (<0.5 v%), which are far from the actual ones used in cell cultures.

In this work, the system is composed of PMMA particles (Cospheric) of d_p= 168 µm and ρ_p= 1185 kg/m^3 and ammonium thiocyanate NH_4SCN solution of 61 wt% (weight percent) corresponding to ρ_f= 1139.2 ± 0.1 kg/m^3 and μ_f= 1.94 ±0.01 mPa.s. Table 2.2 compares the properties with those of Cytodex-1/Water. The solid–liquid system is refractive index matched for RI=1.491 ±0.005 at T≈ 22 − 23 °C, measured using an Abbé refractometer, with no signs of water absorption [37]. Since direct measurement of the RI of the solid particles was not possible, it was assessed via a microscope in the presence of NH_4SCN solution and by referring to the literature [38, 39]. The difference between Cytodex-1/water and PMMA/NH_4SCN systems can be noticed in the microscope images (see Figure 2.1) with ×5 magnification. PMMA microparticles match the light background when immersed in 61 wt% NH_4SCN solution, whereas the opaque Cytodex-1 particles exhibit black contours/circumferences. It is important to note that the PMMA/NH_4SCN system is used solely in this work as an optical substitute and is not intended for MSC culture.

Table 2.2: Properties of alternative and original systems: PMMA/NH_4SCN and Cytodex-1/Water.

Properties	**Cytodex-1/Water**	**PMMA/NH_4SCN**
ρ_f/ρ_p (-)	≈ 0.97	≈ 0.96
μ_f (mPa.s)	1	1.94
d_p (µm)	170	168

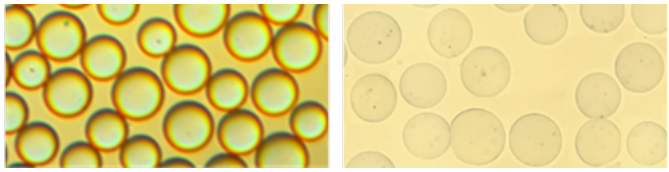

Figure 2.1: LEFT: Cytodex-1 in water, RIGHT: PMMA inside 61 wt% NH_4SCN.

2.2.2 Stirred Tank and PIV Setup

The tank (see Figure 2.2) used for the experiments is made of borosilicate glass with a hemispherical bottom shape and is equipped with a three-bladed axial down-pumping HTPGD impeller (Pierre Guerin). For geometrical concerns, it was operated with C/T=D/T= 0.5, where C is the off-bottom clearance, D is the impeller diameter, and T is the tank diameter, with T= 0.12 m. The working volume is V= 0.7 L, corresponding to a liquid height of H= 0.082 m (H/T= 0.68). The tank is unbaffled but equipped with four dip tubes housing the necessary sensors (temperature, pH, etc.), which play the same role as baffles and prevent the swirling phenomenon. This configuration differs from previous studies conducted by our team, but was chosen to replicate as closely as possible recent studies on MSC cultures [40].

Moreover, the stirred tank is held in an aquarium filled with paraffin oil (RI≈ 1.468; Fauth) to match the RI of the tank wall and thus limit the diffraction in the laser sheet due to the curvature of the wall. It is also worth noting that the temperature is controlled by means of an air conditioner inside the operating room.

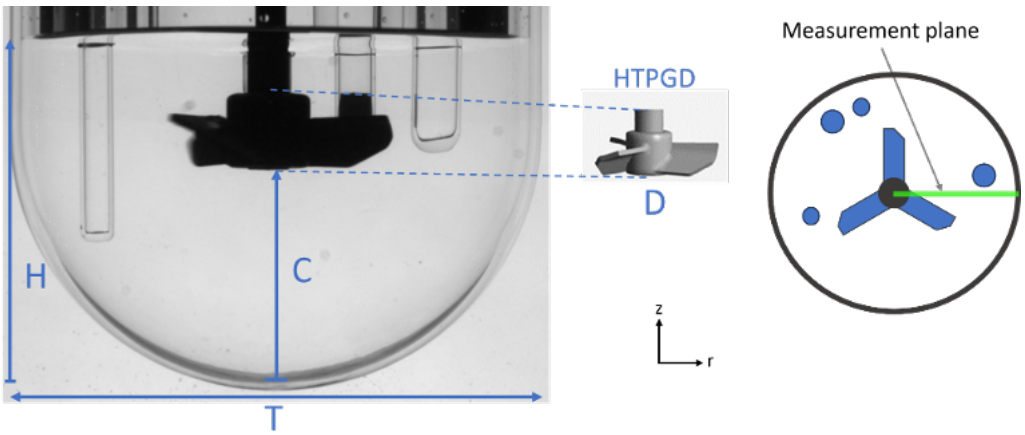

Figure 2.2: (**left**): Geometrical configuration of the stirred tank used. (**right**): Top view of the measurement plane.

Using the configuration described above, the experiments were carried out using ensemble-averaged PIV to characterize the flow in terms of mean and fluctuating velocities (see Figure 2.3). The idea is to evaluate the effect of particle loading α_p on the liquid phase

up to the desired 3 v%, which is ideal in MSC culturing. This corresponds to an average total number of particles of 8.5 million. To put this into perspective, that would give 12 particles in a 1 mm^3 volume (particle number density), which is impractical to utilize with PIV without RIM. To investigate the effect of particle addition, the rotation speed was fixed at a constant N = 150 rpm (Re ≈ 5000), which was sufficient to maintain a homogeneous suspension of the particles and to avoid air-bubble entrapment from the surface.

The PMMA/NH_4SCN multiphase flow was seeded with 20 µL Rhodamine-coated PMMA fluorescent tracers (Initial concentration = 0.25 g/mL, Dantec Dynamics), with an emission wavelength of 584 nm, size distribution of 1–20 µm, and density of ρ= 1190 kg/m^3. These tracers are neutrally buoyant in the 61 wt% NH_4SCN solution and their density closely matches that of the PMMA particles, as they are PMMA-based. The addition of seeding particles to the medium was thoroughly controlled to avoid any shift in the RI of the suspension, which could diminish its transparency [41].

The required PIV illumination was provided by a Nd:YAG double-pulse laser of 532 nm wavelength operating at 50 mJ. Image pairs were captured by a single CMOS camera (FlowSense EO 4 M), with a maximum acquisition frequency of 16 Hz and a resolution of 2048 × 2048 pixels. It was mounted with a 570 nm high-pass filter lens to remove any unwanted emissions and reflections. The spatial resolution determined from the calibration was 1.1625 mm. The acquisition setup enabled the synchronization between the camera and the laser with a time interval between pulses of Δt = 1000 − 1200 µs. The latter was chosen to ensure that the maximum displacement of tracer particles between pulses was one quarter of the length of the interrogation area L_{IA} [42], according to Equation (2.1).

$$\Delta t < \frac{L_{IA} M_u}{4 V_{tip}} \tag{2.1}$$

where M_u is the image magnification and V_{tip} is the tangential velocity at the blade tip (V_{tip}=πND). To ensure statistical convergence of the mean velocities and turbulence statistics, and to sample multiple impeller-blade passages, 1000 image pairs were acquired per measurement at an acquisition rate of 15.8 Hz (see Appendix, Figures A.2.1–A.2.4).

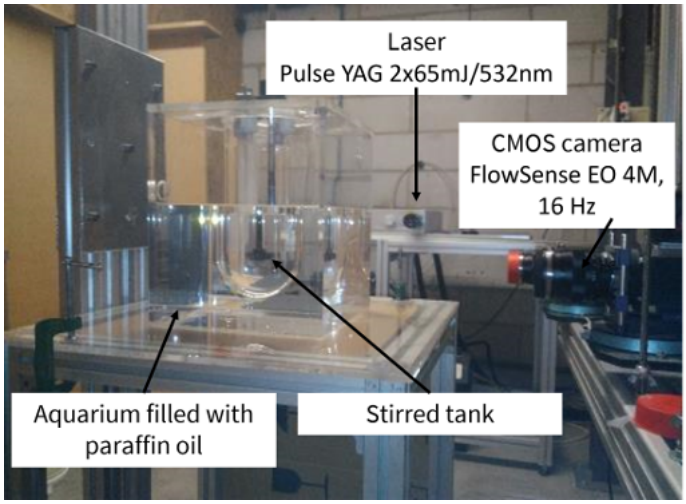

Figure 2.3: PIV setup.

2.2.3 Flow Properties

Kolmogorov's 1941 theory states that at the Kolmogorov scales, energy dissipates as heat due to the fluid's dynamic viscosity. Resolving the dissipation rate therefore requires an applicable spatial resolution down to these smallest length scales. Within the achieved PIV calibration, only turbulent structures above the measurement resolution could be observed. Therefore, one way to estimate the energy dissipation is to evaluate the mean energy dissipation ε in the domain based on the power number equation P_0:

$$\bar{\varepsilon} = \frac{P}{\rho_f V}, \quad P = P_0 \rho_f N^3 D^5 \tag{2.2}$$

where V is the fluid volume and $P_0 = 0.67$ is the corresponding impeller power number [43]. This estimation is a key for evaluating several scales of the domain. One such scale is the Taylor microscale λ, which is not straightforward to obtain and typically requires derivations of the correlation functions of the flow [44]. It was then estimated as:

$$\lambda = \sqrt{10\nu\frac{k}{\varepsilon}} \tag{2.3}$$

This scale provides not only information on the transition from large energy-containing eddies to small dissipative eddies, but also a benchmark for the PIV resolution required to accurately capture an adequately broad turbulence spectrum.

Following an approach used by Simon et al. [45], the turbulent kinetic energy k was used *a posteriori* to estimate the averaged Taylor microscale, λ. This yielded $\lambda \approx 3.3$ mm ($0.055D$), about three times larger than the spatial resolution used ($L_{IA}/\lambda \approx 0.35$), which can thus be considered acceptable.

A brief remark on the average Kolmogorov length scale η evaluated in Equation (2.4) reaffirms that the PIV spatial resolution is not accurate enough to capture the local dissipation rate at the lowest length scales. The estimated $\eta \approx 140$ µm ($0.0023D$), corresponding to $L_{IA}/\eta \approx 8.5$, would capture only approximately 50–60% of the true dissipation rate, whereas a ratio of $L_{IA}/\eta \approx 2$ is typically needed to achieve 90% accuracy in the energy dissipation measurement [46, 47].

$$\eta = \left(\frac{\nu^3}{\varepsilon}\right)^{1/4} \tag{2.4}$$

The average Kolmogorov time scale is another dissipation rate scale-dependent, obtained from dimensionless analysis:

$$\tau_\eta = \left(\frac{\nu}{\varepsilon}\right)^{1/2} \tag{2.5}$$

The ratio between the particle settling velocity and the Kolmogorov time scale, well known as the Stokes number $St = \tau_p/\tau_\eta$, characterizes the behavior of particles evolving within the carrier flow [48, 49]. For $St < 1$, particles follow the streamlines and are easily suspended, while for $St > 1$, particles do not have time to adjust to sudden changes in the flow and may separate from the carrier flow. A value of St= 0.078 was estimated in the present study and is further discussed in the results and discussions section. Note that particle-settling experiments were followed as in [16], to determine the particle relaxation time τ_p:

$$\tau_p = \frac{\rho_p d_p^2}{18\mu_f} \tag{2.6}$$

2.2.4 PIV Treatment and Post-Processing

The raw images recorded were processed in Dantec Dynamics software v7.3, first by a mask to hide the impeller, the dip tubes, and the external background. A low-pass filter was then applied to the images to eliminate part of the noise due to the presence of PMMA particles. The image pretreatment method used was based on generating a background by computing the minimum power mean grayscale values from the series of images (also known as the generalized mean) and then subsequently subtracting this background from each image.

The vector map of instantaneous velocities was obtained by applying an adaptive correlation scheme (Adaptive PIV) with a final window size of 32 × 32 pixels and a 50% overlap, corresponding to a final spatial resolution of 1.1625 mm. Finally, an N·σ validation step was included for the elimination of spurious velocity vectors resulting from the vector map treatment. The N·σ method simply computes the mean and r.m.s. (σ) values from the

vector-map series and subsequently rejects all vectors lying more than $3 \cdot \sigma$ from the mean (N = 3), so that the highly deviated ones are disposed. The addition of particles up to 3 v% did not increase the fraction of invalid vectors, the number of which remained rather stable and very low. On average, one rejected vector was found in every three images through all our measurements, corresponding to a validation of more than 99%, indicating a good vector map quality. For more information on vector validation and PIV reliability, the readers are invited to check the work by Scharnowski and Kähler [50]. The obtained results were then post-processed in MATLAB (R2023b) for further analysis.

Using the time-averaged and instantaneous flow fields, $\overline{U}$ and u respectively, and by means of the Reynolds decomposition $u = u' + \overline{U}$, the fluctuating velocity u' terms were evaluated. However, it is well known that close to the impeller, the fluctuations contain periodic and turbulent modes. The former is an organized motion generated by the impeller-blade rotation (impeller passage), in contrast to the principle of chaotic and irregular turbulent motions. Thus, synchronization of the data acquisition with the blade position can be used to separate periodic and turbulent fluctuations in what is often called an angle-resolved approach. This method is widely used in PIV systems, especially in the cases where the energy dissipation rate is estimated [51, 52]. Nevertheless, in the event that such a tool is inaccessible, it was shown that close to the impeller, there is a strong transfer of kinetic energy between periodic kinetic energy within the trailing vortices and turbulence, which then dissipates it at viscous scales. It was also shown that the dissipation rates of the mean and periodic kinetic energy were negligible compared to the dissipation rate of turbulent kinetic energy [53]. Hence, the classical Reynolds decomposition between the mean and fluctuating velocity components was considered sufficient. From the mean quantities, the time-averaged magnitude M of the flow was thus determined:

$$M = \sqrt{\overline{U_r}^2 + \overline{U_z}^2} \tag{2.7}$$

where $\overline{U_r}$ and $\overline{U_z}$ are the mean velocities in the radial and axial directions, denoted by subscripts r and z respectively. The determination of turbulent kinetic energy theoretically requires resolving all of the fluctuating velocities. Since the measurements were in a 2D coordinate system, the third unknown component was estimated assuming pseudo-isotropy, and the turbulent kinetic energy TKE was computed using Equation (2.8) [54, 55].

$$k = \frac{3}{4}\left(\overline{u_r'^2} + \overline{u_z'^2}\right) \tag{2.8}$$

The velocities and turbulent kinetic energy data were scaled by (ND) and $(ND)^2$, respec-

tively. The non-dimensional variables are:

$$M^* = \frac{M}{ND}, \quad k^* = \frac{k}{(ND)^2} \tag{2.9}$$

2.3 Results and Discussions

2.3.1 PIV Treatment Assessment

Despite the use of a RIM solid–liquid system, the presence of PMMA particles influences the PIV raw images as shown in Figure 2.4, where raw images taken without (a) and with particles at a concentration of 3 v% (b) are presented. The brightness of the background increases due to additional noise in the images as particle concentration increases. The use of RIM-PIV becomes highly demanding when the number of particle–fluid interfaces increases significantly: each interface introduces a slight refractive-index mismatch that can accumulate and cause image deformation [41]. In addition, at a given solid concentration, the interface number or surface area becomes more crucial when dealing with particles with µm sizes compared to much larger particles. Of course, the decreasing quality of raw images is not as marked compared to that observed when using the original solid–liquid system (Cytodex-1/Water). Figure 2.5a,b compares the maximum volume fraction reached by Cytodex-1/water α_p = 0.5 v% with that of PMMA/NH_4SCN, respectively. It is evident that the presence of Cytodex-1 significantly deteriorates image quality, underscoring the need to find an alternative system, even at a concentration as low as α_p = 0.5 v%. The high noise generated by scattering of the laser sheet makes tracer tracking impossible, unlike in the PMMA system, in which the tracking of the seeding particles is preserved. The brightness increase in images due to the PMMA particle addition can be addressed with the image treatment used to eliminate noise (minimum power mean filter), as seen in Figure 2.4c,d where PIV images after applying the noise filter are presented without particles and with 3 v% particles, respectively. The use of the filter without particles does not significantly influence the quality of the original raw images, as expected. On the other hand, applying this filter to images with PMMA particles significantly enhances the contrast between the seeding particles and the background. Nevertheless, a drop in the seeding particle number is noticed, especially under the impeller region, as a corollary of the diffraction of the laser sheet passing through the medium. However, this drop is not significant enough to alter the PIV detection algorithm, and the number of particles detected is still sufficient to ensure robust results.

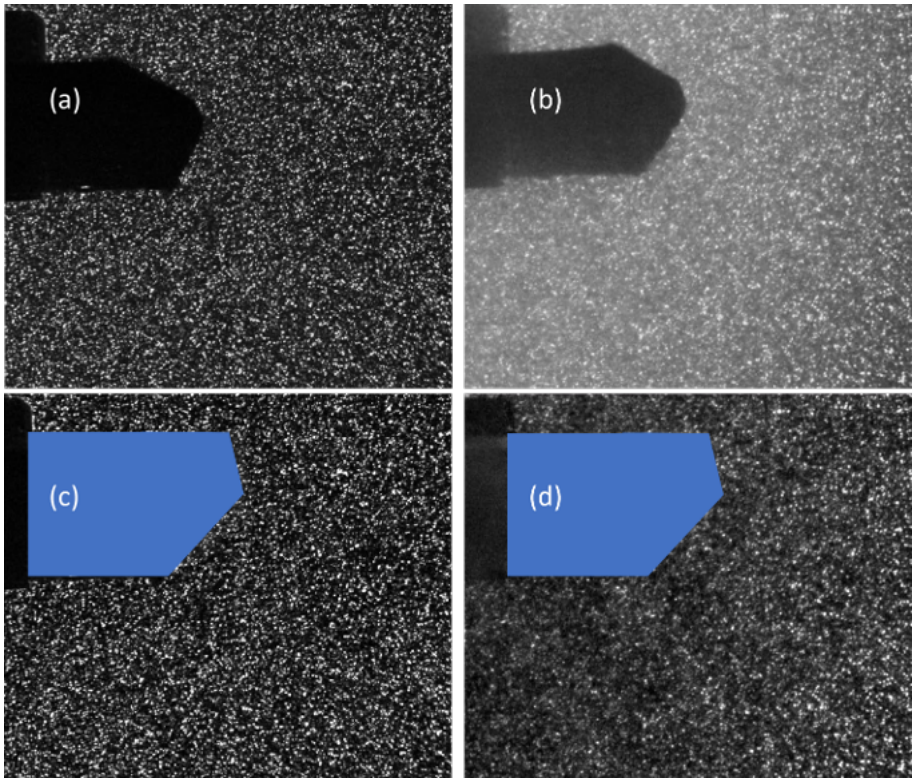

Figure 2.4: PIV raw images (**a**): 61 wt% NH_4SCN solution only (**b**): α_p = 3 v% PMMA/NH_4SCN (**c**): 61 wt% NH_4SCN solution only—with filter (d): α_p= 3 v% PMMA/NH_4SCN—with filter.

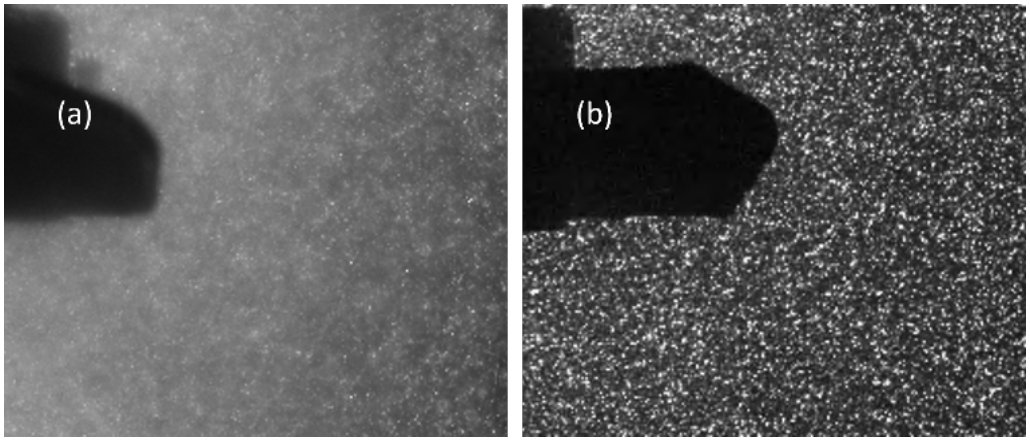

Figure 2.5: PIV raw images at α_p= 0.5 v% for (**a**) Cytodex-1/water (**b**): PMMA/NH_4SCN.

2.3.2 Flow Analysis

To achieve rigorous results analysis and consistency, the experiments were repeated three times for each solid concentration. Each time, the particles were recovered and the solution was disposed for a newly prepared one. The standard deviation between locally measured quantities (velocity and TKE) in successive experiments was used to evaluate the experimental error. Note that this experimental error, determined from replicates, is not limited to an assessment of the repeatability of the PIV technique (for a given experiment).

It is in fact an experimental error that takes into account all potential sources of error: liquid solution composition, solid concentration, laser alignment, camera focus, loss of seeding particles, to name but a few.

On average, the experimental error is around 0.025–0.027 ND $\approx$ 0.008–0.009V_{tip} for velocity magnitude and 0.006–0.008 $(ND)^2 \approx$ 6.1–8.1 $\times$ $10^{-4}V_{tip}^2$ for turbulent kinetic energy of α_p = 0 v% and 3 v% respectively. Figure 2.6a,b shows the differences in local experimental error between the single-liquid phase and the solid concentration of α_p = 3 v% for mean velocity magnitude, while Figure 2.6c,d shows those for TKE, respectively. For both quantities (velocity and TKE), one may observe a slight expansion (around 10%) of error regions in the contour plot for the α_p = 3 v% system. These regions are mainly below the impeller where off-plane tangential velocities are dominant and above the impeller at the end of the recirculation loop. The expansion observed near the impeller blade tip is more likely due to laser light reflection.

To firmly investigate the effect of the addition of PMMA microparticles on the fluid flow turbulence, PIV results are presented and analyzed in two manners. First, 2D velocity magnitude and turbulent kinetic energy profiles are plotted along two axial (vertical) and one horizontal lines. On all plots, the center of the tank floor, just below the agitator axis, is the origin of the axes. The axial and radial profiles are located at:

- r/T= 0.226, which cuts through the impeller tip to cover the beginning of the discharge flow and the ending phase of the recirculation loop;
- r/T= 0.452, near the wall, which covers the other half of the loop;
- z/H= 0.780, above the impeller, which covers the top of the recirculation loop.

For the sake of clarity, the profiles are presented only for the two extreme cases: single-phase flow (without PMMA particles) and two-phase flow (with PMMA particles) at α_p = 3 v%.

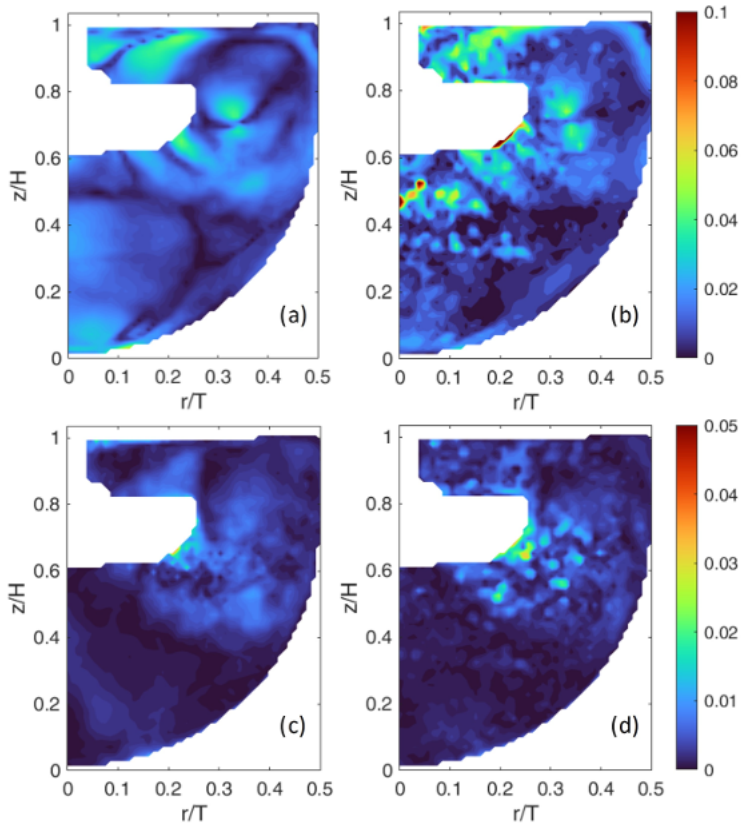

Figure 2.6: Experimental error contours (-). First row: error on non-dimensional velocity (**a**) single-phase and (**b**) PMMA α_p= 3 v%. Second row: error on non-dimensional TKE (**c**) single-phase and (**d**) PMMA α_p= 3 v%.

The second way is to use the locally averaged quantities, allowing comparison of velocity magnitude and TKE in two areas of interest of 1 × 1 cm^2. One area is located in the impeller-blade region and the second near the wall, denoted as box_1 and box_2, respectively. The selection was based not only on areas with low uncertainty but, more importantly, on regions where any differences were reported in profile plots between single-phase and α_p = 3 v% in order to inspect their extent.

The locations of the profiles and the averaging areas are depicted in Figure 2.7. Local standard deviations computed from three replicates are shown as error bars on the profiles and on the plots of local averages.

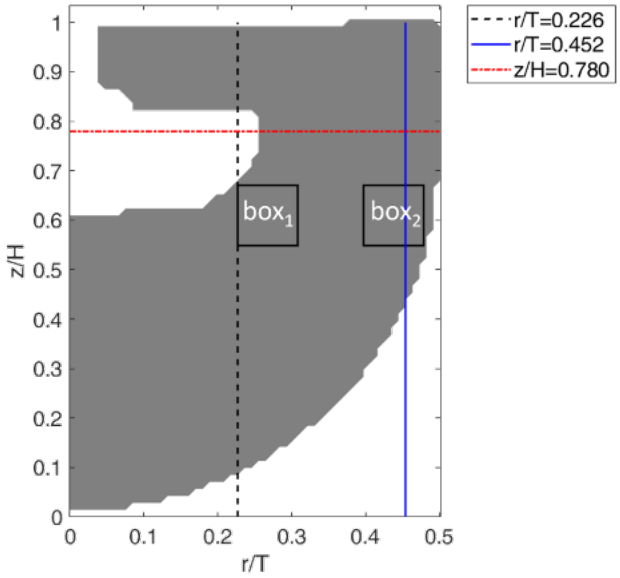

Figure 2.7: Visualization scheme showing the areas of analysis.

Mean Velocity Magnitude

The non-dimensional mean velocity magnitude M^* from Equation (2.9) is represented in Figure 2.8 alongside the corresponding mean velocity vectors for the single-phase flow (a) and two-phase flow at α_p = 3 v% (b). It shows the classical structure associated with a down-pumping axial impeller, featuring the recirculation of the liquid phase. The recirculation loop extends almost to the free surface, ensuring sufficiently homogeneous mixing while avoiding air-bubble capture. Under the impeller, there is a region of almost stagnant flow, whereas a slow flow is recognized at the bottom-right as a result of the imposed impeller mode and the asymmetric placement of the dip tubes in the tank. The maximum velocity magnitude in the impeller discharge is around $1.1ND = 0.35V_{tip}$.

When comparing the two mean velocity contour maps, without (Figure 2.8a) and with PMMA particles at α_p = 3 v% (Figure 2.8b), only slight differences are detected at the end of the recirculation loop, on top of the impeller, and at the beginning of the ascending movement near the wall, but they are nearly imperceptible in the contour plot. Additionally, a slight shift in the position of the center/vortex of the recirculation loop is observed between both cases: the center shifts modestly upward from z/H = 0.7 (single-phase) to z/H = 0.725 (α_p = 3 v%) at r/T = 0.35.

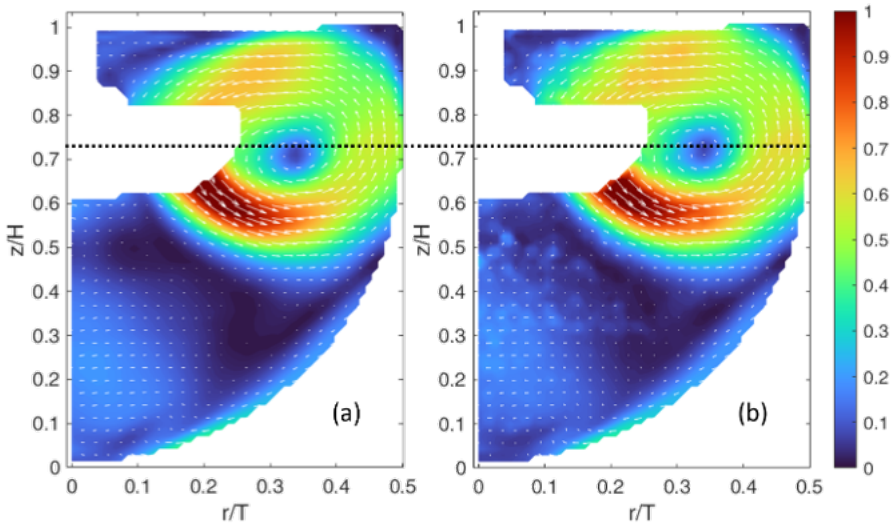

Figure 2.8: Non-dimensional (by (ND)) time-averaged flow magnitude: (**a**) single-phase α_p = 0 v% (**b**) α_p = 3 v% PMMA. The corresponding mean velocity vectors are added to each contour plot. The horizontal dashed line is added as a reference to compare the position of the center of the recirculation loop between both cases.

Figure 2.9a–c shows the non-dimensional mean velocity magnitude M^* along the z-axis at the locations r/T = 0.226 and r/T = 0.452 and along the r-axis at z/H= 0.78, respectively. Recall that in these profiles, non-dimensional velocity values larger than one are observed because the scaling factor is ND rather than $V_{tip} = \pi ND$.

In the vicinity of the blade, at r/T = 0.226 (Figure 2.9a), the two velocity profiles without particles and with 3 v% particles overlap almost perfectly, except near the surface for z/H > 0.9 where the experimental errors are high.

Near the wall, at r/T = 0.452 (Figure 2.9b), a higher velocity in the presence of PMMA particles is observed between z/H = 0.6 and 0.9, corresponding to the upward part of the recirculation loop. The maximum difference between the mean velocity without particles and with 3 v% particles reaches 10%, which exceeds the experimental error in this area (<0.02ND $\approx 0.006V_{tip}$). This trend is most pronounced near the wall for 3 v%.

Looking at the radial profile (Figure 2.9c), higher velocities are partially perceptible in the presence of particles for r/T > 0.4. On the other hand, in the descending part of the loop (r/T < 0.4), lower velocities are observed in the presence of PMMA particles. It is clear that the experimental errors are also slightly higher in this zone ($\approx 0.04ND \approx 0.013V_{tip}$).

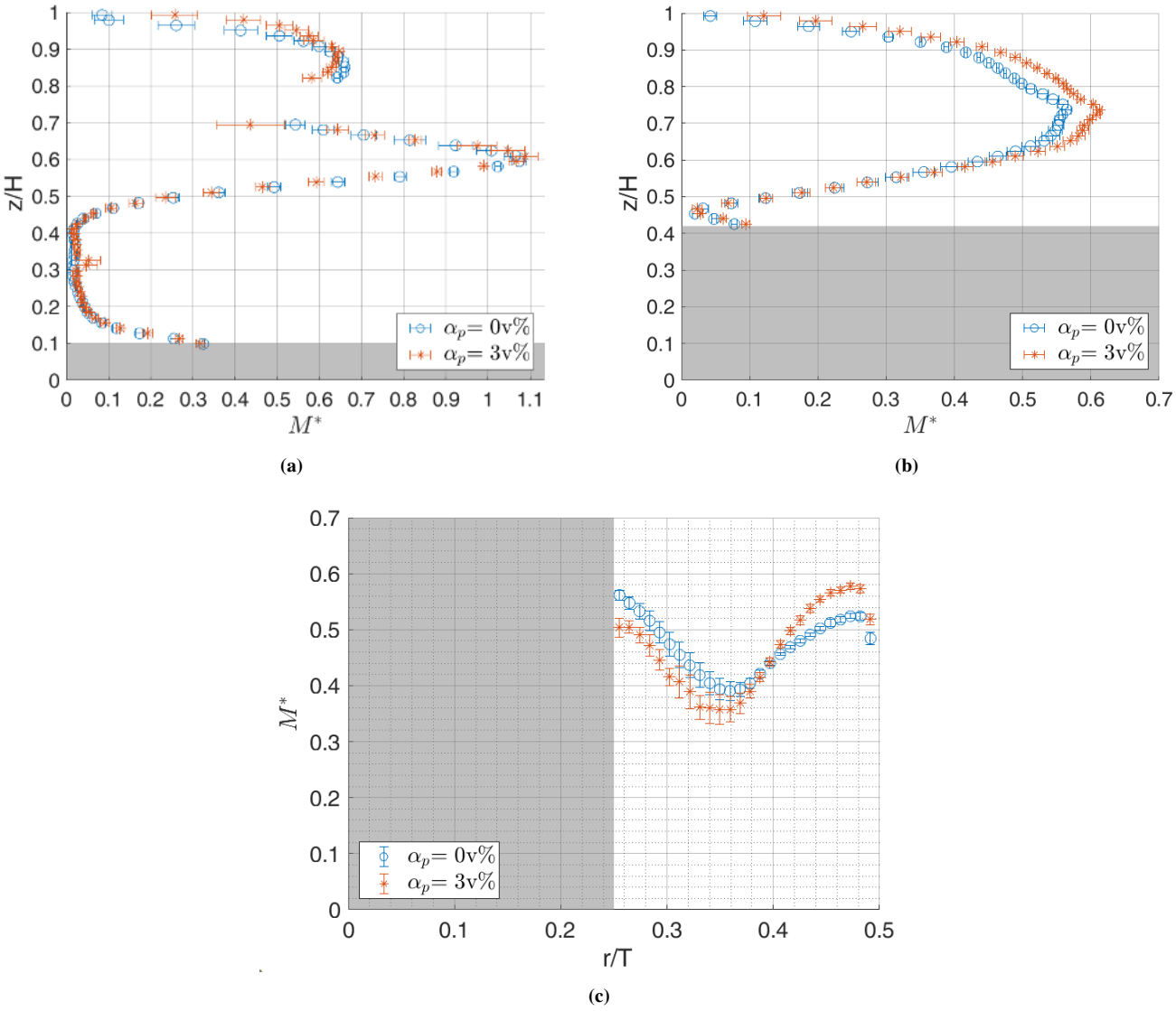

Figure 2.9: Non-dimensional (by (ND)) time-averaged flow magnitude profile plot: (**a**) vertical at r/T = 0.226. (**b**) vertical at r/T = 0.452. (**c**) horizontal at z/H = 0.780.

Alternatively, this overlapping pattern suggests a shift in momentum that could be due to a change in the direction of the axial flow in that region rather than a local dominance, confirming that the presence of particles does not affect the flow magnitude itself, but somehow modifies the structure. A possible explanation for this shift could be attributed to slight alterations in the effective viscosity of the suspension (at α_p = 3 v%). At such concentrations, the presence of particles in the jet stream may divert the liquid flow direction upward and toward the wall. Hence, this can lead to the modest relocation of the recirculation centerline observed in Figure 2.8. The same behavior is reported by Unadkat et al. [25] in axial flow with the addition of particles, where the center of the loop shifted, resulting in a 50% increase near the tank wall, for volume fractions above 0.2 v%. The authors explained that this increase is due to the change in direction of the axial flow from downwards to upwards in the wall jet.

To further investigate the influence of the presence of particles and their concentration on local averages, the non-dimensional mean velocity magnitude averaged over the two areas of interest depicted in Figure 2.7 is plotted as a function of the PMMA particle volume fraction (see Figure 2.10). The first area of interest (box_1) is located in the impeller discharge near the tip, and the second (box_2) is located near the wall at the beginning of the upward part of the recirculation loop. In both zones, the averaged magnitude of the mean flow is rather constant as a function of particle volume fraction, except in box_2 near the wall where a sudden increase in velocity magnitude (around 7.5%) is observed between 2.5 and 3 v%. This is likely an artifact due to a shift in the centreline of the recirculation loop rather than a true increase in wall-jet velocity.

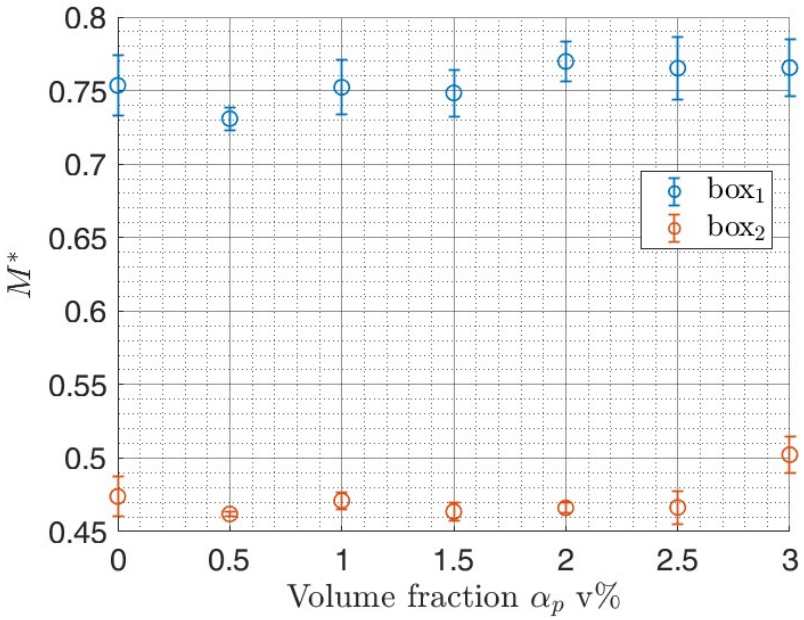

Figure 2.10: Non-dimensional (by (ND)) flow velocity magnitude M^* in the zones of interest for different volume fractions α_p.

Aside from the change in structure, the influence of the addition of particles on the mean flow appears to be overall negligible in magnitude. This is in agreement with the Stokes number ($St = 0.078 \ll 1$), which indicates that the particles closely follow the liquid flow. In addition, near-density matching between the phases also contributes to this outcome.

Other authors have reported negligible variations of the mean liquid flow field due to the presence of solids in stirred tank reactors. Montante et al. [28] used glass particles with different sizes (115–774 µm) up to fractions $\alpha_p = 0.2$ v% and density ratio $\rho_f/\rho_p = 0.4 \ll 1$; Gabriele et al. [26] used PMMA spheres of relatively large 1.5 mm size suspended in p-cymene solution up to 5 v% and $\rho_f/\rho_p = 0.4 \ll 1$; Guiraud et al. [34] examined glass spheres of 253 µm size at concentrations of $\alpha_p = 0.5$ v% suspended in a medium of $\rho_f/\rho_p = 0.45 \ll 1$. These studies did not find alterations in either the radial or axial components of the carrier-phase flow, despite the high density mismatches. Interestingly, the overall

fluid flow field as well as the circulating patterns were altered by a dampening effect of 30% as noted by Li et al. [29] at α_p = 5 v% with 7 mm particles and $\rho_f/\rho_p = 0.45 \ll 1$. In other flow geometries, the addition of particles can impact the mean carrier flow values in different ways, as demonstrated by Fornari et al. [56] in a turbulent particle-laden channel flow with finite-size particles, who found that at concentrations of 5 v% and near density-matched phases, the mean fluid velocity slightly lower near the wall and slightly higher at the center of the channel compared with single-phase flow.

Turbulent Kinetic Energy

The turbulent kinetic energy k^* from Equation (2.9) is represented in Figure 2.11 for the single-phase flow (a) and two-phase flow at α_p = 3 v% (b). As expected, the TKE values are the highest in the flow discharge area and gradually diminish toward the wall side. The upper part of the recirculation, above the impeller, contains lower fluctuations.

Figure 2.11 shows a decrease in TKE in the impeller discharge from single-phase (a) to PMMA at α_p = 3 v% (b), with a maximum of $0.33(ND)^2 \approx 0.033V_{tip}^2$ and $0.27(ND)^2 \approx 0.027V_{tip}^2$ reached, respectively. One can argue that the experimental errors are also the highest in this region (see Figure 2.6b). Nonetheless, the corresponding variations are around $0.02(ND)^2 \approx 0.002V_{tip}^2$ and $0.04(ND)^2 \approx 0.004V_{tip}^2$, which are far inferior compared to the TKE values of single-phase and α_p = 3 v%, respectively. In the rest of the tank, the values of TKE are rather similar with and without particles at 3 v%.

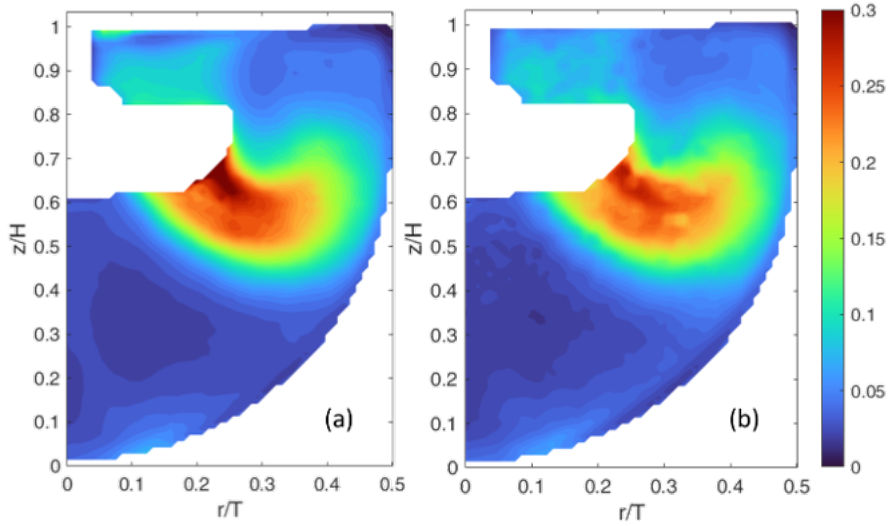

Figure 2.11: Non-dimensional (by $(ND)^2$) time-averaged TKE k^*: (**a**) single-phase α_p= 0 v% (**b**) α_p= 3 v% PMMA

The non-dimensional TKE profiles are presented in Figure 2.12a–c at r/T = 0.226, r/T = 0.452 (axial profiles), and z/H = 0.78 (radial profile), respectively . At r/T = 0.226 (Figure 2.12a), the turbulence level for single-phase flow and α_p = 3 v% follows closely

except in the impeller discharge (0.6 < z/H < 0.7), where a decrease in TKE is noted when the particles are present, as seen in the contour plot as well. The drop in TKE reaches 20% at the peak. This is recognizable relative to the experimental errors at that location, particularly for 2.5 v% and 3 v%. Despite this dampening effect, it is limited locally to 0.6 < z/H < 0.7.

At r/T = 0.452 near the wall (Figure 2.12b), TKE values with α_p = 3 v% are slightly higher than the single-phase values, with a maximum difference of 10% observed at the peak corresponding to z/H = 0.6. Similarly, higher values of TKE are observed in the presence of particles on the horizontal profile (Figure 2.12c) up to 10% as well. The differences are within the observed experimental deviations of TKE up to $0.02(ND)^2 \approx 0.002V_{tip}^2$ and therefore can be considered trivial. Additionally, it merits attention that across all the TKE profiles, these differences are limited to small local regions and neither phase dominates.

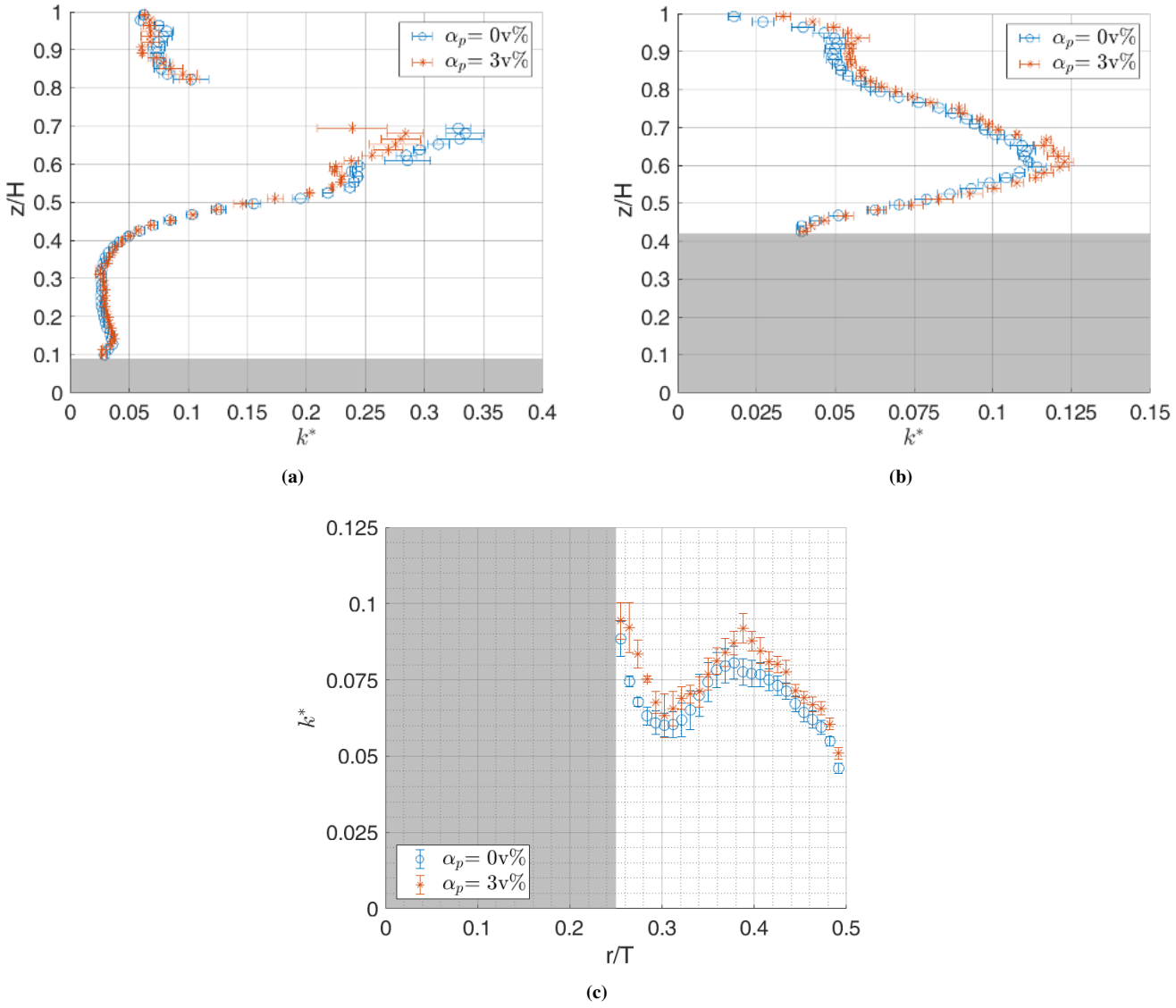

Figure 2.12: Non-dimensional (by $(ND)^2$) time-averaged TKE profile plot: (**a**) vertical at r/T = 0.226. (**b**) vertical at r/T = 0.452. (**c**) horizontal at z/H = 0.780.

To examine the extent of the change in TKE produced by the particles on the liquid phase in the very specific regions observed, the locally averaged TKE values computed in the two areas of interest are plotted in Figure 2.13 as a function of the particle volume fraction. In the impeller discharge area (box_1), TKE levels slightly increase by 5% for α_p = 0.5 v%, then from 0.5 to 2.5 v% vary around the TKE value of the single-phase flow, and finally a small drop of around 7% is observed for α_p = 3 v%. Near the wall (box_2), TKE values are rather constant between 0 and 1 v% and appear to slightly increase from 1.5 up to 3 v%. Yet, in both areas, the differences in TKE values as a function of the volume fraction fall within the experimental uncertainties computed for the same areas. For that reason, the influence of the particles on the locally averaged liquid phase turbulence is trivial. The differences seen on the profile plots are reduced after spatial averaging over the region where a potential effect was suspected. The slight decrease and increase in TKE for box_1 and box_2 at 3 v%, respectively, is rather inconsequential compared to those observed in some sections of the profile plots (<10%).

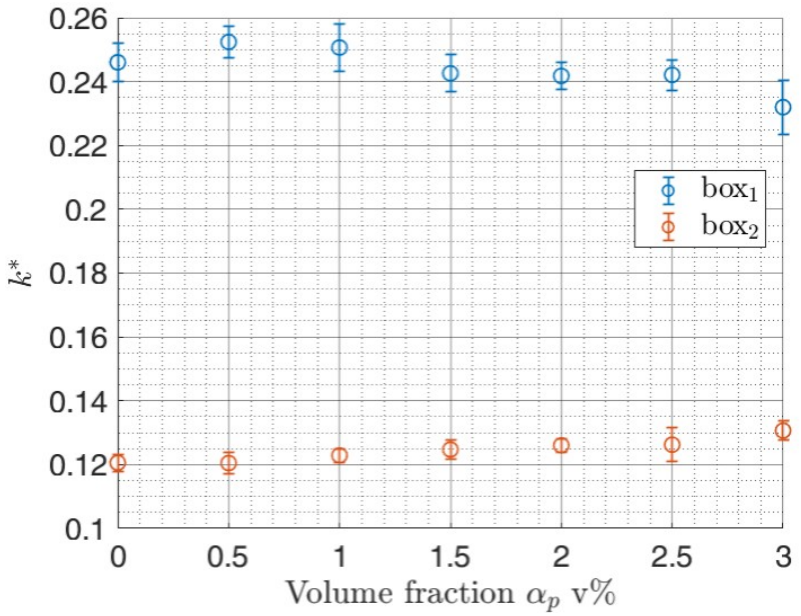

Figure 2.13: Non-dimensional (by $(ND)^2$) TKE k^* in the zones of interest for different volume fractions α_p.

As already pointed out, the literature on the influence of the presence of particles on the flow in stirred tank reactors is scarce. Virdung and Rasmuson [33, 24] found an increase of 45% in r.m.s. velocities even in the impeller jet zone with particle sizes ten times larger than those of the PMMA used in this work. Micheletti and Yianneskis [32] reported a significant decrease in turbulence (r.m.s.) levels of 50% at just α_p = 0.2 v% with the same particle size as the PMMA used here, but at much higher Reynolds numbers (Re = 20 000). However, it did not drop any further for concentrations above 1 v%, indicating that interparticle interactions no longer governed turbulence suppression.

In previous studies, some attempts were dedicated to model the modification in turbulence.

Gore and Crowe [57] postulated the attenuation of turbulence if the ratio of particle diameter to integral length scale $d_p/L < 0.1$, with augmentation occurring for the opposite sense. In this work, the average integral length scale was estimated based on $L = k^{3/2}/\varepsilon \approx 7.4$ mm ($0.12D$), and thus the value obtained $d_p/L = 0.023$ would anticipate turbulence attenuation. Since the model deals with a global (domain-averaged) integral length scale, the impact is not necessarily evident. Previous authors noted the contradiction between this suggestion and their experimental findings [32, 25], knowing that Unadkat et al, [25] estimated the integral length scales by integrating the autocorrelation functions, and these scales did not change with particle addition (0.5 v%). Certainly, the model does not account for other influential parameters of the domain, e.g., Stokes and Reynolds numbers, particle-to-fluid density ratio, and solid concentration [58, 59].

In the present study, the system operates at relatively moderate Re and low St numbers, with very close liquid and solid densities and very small particles, which corresponds to a system where solids are often considered to have minimal impact on the liquid flow field. However, previous studies showed that even at $St \ll 1$, particle addition could modify turbulent structures. Sommer et al. [35] demonstrated that in the impeller region, turbulent fluctuations were damped for $\alpha_p = 0.025$ v%, whereas for $\alpha_p = 0.075$ v% they were enhanced compared to single-phase. This effect was held for both glass and polyethylene particles of $\rho_f/\rho_p = 0.4$ and 0.91, respectively, with a diameter range of 63–450 µm and St range of $1.9\times10^{-4} - 7.9$. A larger impact for the heavier glass particles was also reported. Further, particle diameter imposed different effects on the turbulent fluctuations. For $d_p \geq 400$ µm, PE particles suppressed the turbulence whereas the glass particles enhanced the turbulence. In general, independently of particle diameter and material, turbulence was reduced for all cases except for the glass particles of $d_p \geq 400$ µm.

Also at the local level, specifically in the impeller region, a previous work by Delafosse et al [60] on axial mixing in a stirred tank showed that TKE dissipation rate estimations could vary from 15 to 50 times the mean dissipation rate computed from the mean power input. In that study, special attention was paid to the acquired spatial resolution. This ultimately induced lower local Kolmogorov scales (100–135 µm) in the impeller zone which are smaller than the microcarrier size ($d_p \approx 200$ µm). Thus, the cells attached to microcarriers passing through this region might be damaged. Moreover, Maillot et al. [18] demonstrated that MSC growth is greatly impacted by particle addition and that certain quality attributes were progressively degraded when taking into account the physical characteristics of the domain. Authors who investigated similar cases of particle-laden flow in stirred tanks reported either attenuation or augmentation in turbulence. More attention is required for the type of solid–liquid system used in stirred tanks—which can operate across a wide range of geometries and parameters—to acquire more data before a decisive conclusion can be drawn [61].

2.4 Conclusions

The aim of this work was to characterize, using Particle Image Velocimetry (PIV), the influence of adding microcarriers (i.e., microparticles) to the continuous phase (liquid phase) in the specific application of stem cell expansion on microcarriers suspended in stirred tank bioreactors. PIV for multiphase flow is often challenging. Typically, microcarriers possess poor optical properties (opaque) and are quite small in size (d_p= 150–300 µm), thus it is not possible to acquire PIV measurements at solid volume fractions usually used in MSC cultures (α_p = 2–3 v%). To overcome this limitation, a solid–liquid, refractive index matching (RIM) system was specifically selected for the PIV setup. It consists of PMMA microparticles suspended in a 61 wt% ammonium thiocyanate solution (NH_4SCN). This RIM solid–liquid system closely mimics the properties of the original microcarrier-culture medium system in terms of particle diameter, density difference, and even liquid viscosity.

The experimental investigation shows that the presence of microparticles has no impact on the mean velocity magnitude values of the continuous phase. This applies globally and locally, in the impeller discharge and near the wall areas. However, the impact appears as an ambiguous shift in the structure and direction of the recirculation loop at 3 v% concentrations.

Likewise, the examination of turbulent kinetic energy of the liquid phase reveals trivial impact due to microparticle addition. In fact, the analysis near the impeller and wall zones shows no evident influence as the differences between single-phase and 3 v% particles concentration are <10% on the locally averaged level, of the same order as the experimental uncertainties. Except for a limited location near the impeller where the TKE is dampened by 20% at r/T = 0.226.

As pointed out, the mechanism of turbulence modulation is highly complex. It depends on dimensionless parameters such as the Stokes St and Reynolds Re numbers, particle-to-fluid density ratio, solid concentration, and particle-to-turbulence length scales ratio. Tanaka and Eaton [58] mapped out 30 experimental databases from the open literature with different values of Re and St to propose a new model. The present work is an effort to provide necessary insights to account for turbulence modulation in a very direct application to MSC culture. More studies are also needed on matched-density systems between the continuous and suspended phases with low Stokes number (St $\ll$ 1). Besides, measurements of the solid phase hydrodynamics are also required to further understand the solid–liquid interactions, which will be the next step in our investigations. Such experimental measurements, both on the liquid and solid phase, are essential to help develop reliable CFD modeling approaches for two-phase flow with such specific characteristics (small particle diameter, close density

match, low Reynolds number, etc.) as encountered in stem cell (or more generally animal cell) cultures.

Bibliography

[1] D. E. Rodríguez-Fuentes, L. E. Fernández-Garza, J. A. Samia-Meza, S. A. Barrera-Barrera, A. I. Caplan, and H. A. Barrera-Saldaña, "Mesenchymal stem cells current clinical applications: a systematic review," *Archives of medical research*, vol. 52, no. 1, pp. 93–101, 2021.

[2] N. Beyer Nardi and L. da Silva Meirelles, "Mesenchymal Stem Cells: Isolation, In Vitro Expansion and Characterization," in *Stem Cells* (A. M. Wobus and K. R. Boheler, eds.), Handbook of Experimental Pharmacology, pp. 249–282, Berlin, Heidelberg: Springer, 2006.

[3] S. Frauenschuh, E. Reichmann, Y. Ibold, P. M. Goetz, M. Sittinger, and J. Ringe, "A Microcarrier-Based Cultivation System for Expansion of Primary Mesenchymal Stem Cells," *Biotechnology Progress*, vol. 23, no. 1, pp. 187–193, 2007. _eprint: https://onlinelibrary.wiley.com/doi/pdf/10.1021/bp060155w.

[4] D. Schop, F. W. Janssen, E. Borgart, J. D. de Bruijn, and R. van Dijkhuizen-Radersma, "Expansion of mesenchymal stem cells using a microcarrier-based cultivation system: growth and metabolism," *Journal of Tissue Engineering and Regenerative Medicine*, vol. 2, no. 2-3, pp. 126–135, 2008. https://doi.org/10.1002/term.73.

[5] Q. A. Rafiq, K. M. Brosnan, K. Coopman, A. W. Nienow, and C. J. Hewitt, "Culture of human mesenchymal stem cells on microcarriers in a 5 l stirred-tank bioreactor," *Biotechnology Letters*, vol. 35, pp. 1233–1245, Aug. 2013.

[6] M. S. Croughan, J.-F. P. Hamel, and D. I. C. Wang, "Effects of microcarrier concentration in animal cell culture," *Biotechnology and Bioengineering*, vol. 32, no. 8, pp. 975–982, 1988. _eprint: https://onlinelibrary.wiley.com/doi/pdf/10.1002/bit.260320805.

[7] T. M. Maul, D. W. Chew, A. Nieponice, and D. A. Vorp, "Mechanical stimuli differentially control stem cell behavior: morphology, proliferation, and differentiation," *Biomechanics and Modeling in Mechanobiology*, vol. 10, pp. 939–953, Dec. 2011.

[8] A. W. Nienow, "Reactor engineering in large scale animal cell culture," *Cytotechnology*, vol. 50, no. 1-3, pp. 9–33, 2006.

[9] P. Godara, C. McFarland, and R. Nordon, "Design of bioreactors for mesenchymal stem cell tissue engineering," *Journal of Chemical Technology and Biotechnology*, vol. 83, pp. 408–420, Apr. 2008.

[10] V. Jossen, R. Pörtner, S. C. Kaiser, M. Kraume, D. Eibl, R. Eibl, V. Jossen, R. Pörtner, S. C. Kaiser, M. Kraume, D. Eibl, and R. Eibl, "Mass Production of Mesenchymal Stem Cells — Impact of Bioreactor Design and Flow Conditions on Proliferation and

Differentiation," in *Cells and Biomaterials in Regenerative Medicine*, IntechOpen, Nov. 2014.

[11] D. W. Hutmacher and H. Singh, "Computational fluid dynamics for improved bioreactor design and 3d culture," *Trends in biotechnology*, vol. 26, no. 4, pp. 166–172, 2008.

[12] Q. A. Rafiq, K. Coopman, A. W. Nienow, and C. J. Hewitt, "Systematic microcarrier screening and agitated culture conditions improves human mesenchymal stem cell yield in bioreactors," *Biotechnology Journal*, vol. 11, pp. 473–486, Apr. 2016.

[13] M.-L. Collignon, A. Delafosse, S. Calvo, C. Martin, A. Marc, D. Toye, and E. Olmos, "Large-eddy simulations of microcarrier exposure to potentially damaging eddies inside mini-bioreactors," *Biochemical engineering journal*, vol. 108, pp. 30–43, 2016.

[14] C. Loubière, A. Delafosse, E. Guedon, I. Chevalot, D. Toye, and E. Olmos, "Dimensional analysis and CFD simulations of microcarrier 'just-suspended' state in mesenchymal stromal cells bioreactors," *Chemical Engineering Science*, vol. 203, pp. 464–474, Aug. 2019.

[15] E. Olmos, K. Loubiere, C. Martin, G. Delaplace, and A. Marc, "Critical agitation for microcarrier suspension in orbital shaken bioreactors: Experimental study and dimensional analysis," *Chemical Engineering Science*, vol. 122, pp. 545–554, 2015.

[16] A. Delafosse, C. Loubière, S. Calvo, D. Toye, and E. Olmos, "Solid-liquid suspension of microcarriers in stirred tank bioreactor – Experimental and numerical analysis," *Chemical Engineering Science*, vol. 180, pp. 52–63, Apr. 2018.

[17] C. Loubière, C. Sion, N. De Isla, L. Reppel, E. Guedon, I. Chevalot, and E. Olmos, "Impact of the type of microcarrier and agitation modes on the expansion performances of mesenchymal stem cells derived from umbilical cord," *Biotechnology Progress*, vol. 35, no. 6, p. e2887, 2019. _eprint: https://onlinelibrary.wiley.com/doi/pdf/10.1002/btpr.2887.

[18] C. Maillot, N. De Isla, C. Loubiere, D. Toye, and E. Olmos, "Impact of microcarrier concentration on mesenchymal stem cell growth and death: Experiments and modeling," *Biotechnology and Bioengineering*, vol. 119, no. 12, pp. 3537–3548, 2022. _eprint: https://onlinelibrary.wiley.com/doi/pdf/10.1002/bit.28228.

[19] C. J. Hewitt, K. Lee, A. W. Nienow, R. J. Thomas, M. Smith, and C. R. Thomas, "Expansion of human mesenchymal stem cells on microcarriers," *Biotechnology Letters*, vol. 33, pp. 2325–2335, Nov. 2011.

[20] M. A. Northrup, T. J. Kulp, and S. M. Angel, "Fluorescent particle image velocimetry: application to flow measurement in refractive index-matched porous media," *Applied optics*, vol. 30, no. 21, pp. 3034–3040, 1991.

[21] L. Hopkins, J. Kelly, A. Wexler, and A. Prasad, "Particle image velocimetry measurements in complex geometries," *Experiments in Fluids*, vol. 29, pp. 91–95, 2000.

[22] R. G. Morgan, C. N. Markides, I. Zadrazil, and G. F. Hewitt, "Characteristics of horizontal liquid–liquid flows in a circular pipe using simultaneous high-speed laser-induced fluorescence and particle velocimetry," *International journal of multiphase flow*, vol. 49, pp. 99–118, 2013.

[23] A. M. Bluestein and D. Bohl, "Development and validation of a PIV processing routine for two-phase index-matched flows," *Journal of Visualization*, vol. 23, pp. 951–970, Dec. 2020.

[24] T. Virdung and A. Rasmuson, "Solid–Liquid Flow at Dilute Concentrations in an Axially Stirred Vessel Investigated Using Particle Image Velocimetry," *Chemical Engineering Communications*, vol. 195, pp. 18–34, Jan. 2008.

[25] H. Unadkat, C. D. Rielly, G. K. Hargrave, and Z. K. Nagy, "Application of fluorescent PIV and digital image analysis to measure turbulence properties of solid–liquid stirred suspensions," *Chemical Engineering Research and Design*, vol. 87, pp. 573–586, Apr. 2009.

[26] A. Gabriele, A. N. Tsoligkas, I. N. Kings, and M. J. H. Simmons, "Use of PIV to measure turbulence modulation in a high throughput stirred vessel with the addition of high Stokes number particles for both up- and down-pumping configurations," *Chemical Engineering Science*, vol. 66, pp. 5862–5874, Dec. 2011.

[27] J. Smagorinsky, "General circulation experiments with the primitive equations: I. the basic experiment," *Monthly weather review*, vol. 91, no. 3, pp. 99–164, 1963.

[28] G. Montante, A. Paglianti, and F. Magelli, "Analysis of dilute solid–liquid suspensions in turbulent stirred tanks," *Chemical Engineering Research and Design*, vol. 90, pp. 1448–1456, Oct. 2012.

[29] G. Li, Z. Gao, Z. Li, J. Wang, and J. Derksen, "Particle-resolved piv experiments of solid-liquid mixing in a turbulent stirred tank," *AIChE Journal*, vol. 64, no. 1, pp. 389–402, 2018.

[30] J. Nouri and J. Whitelaw, "Particle velocity characteristics of dilute to moderately dense suspension flows in stirred reactors," *International journal of multiphase flow*, vol. 18, no. 1, pp. 21–33, 1992.

[31] C. Kohnen and M. Bohnet, "Measurement and simulation of fluid flow in agitated solid/liquid suspensions," *Chemical Engineering & Technology: Industrial Chemistry-Plant Equipment-Process Engineering-Biotechnology*, vol. 24, no. 6, pp. 639–643, 2001.

[32] M. Micheletti and M. Yianneskis, "Study of Fluid Velocity Characteristics in Stirred Solid–Liquid Suspensions With a Refractive Index Matching Technique," *Proceedings of The Institution of Mechanical Engineers Part E-journal of Process Mechanical Engineering - PROC INST MECH ENG E-J P M E*, vol. 218, pp. 191–204, Nov. 2004.

[33] T. Virdung and A. Rasmuson, "Measurements of continuous phase velocities in solid–liquid flow at elevated concentrations in a stirred vessel using ldv," *Chemical Engineering Research and Design*, vol. 85, no. 2, pp. 193–200, 2007.

[34] P. Guiraud, J. Costes, and J. Bertrand, "Local measurements of fluid and particle velocities in a stirred suspension," *Chemical Engineering Journal*, vol. 68, no. 2-3, pp. 75–86, 1997.

[35] A.-E. Sommer, H. Rox, P. Shi, K. Eckert, and R. Rzehak, "Solid-liquid flow in stirred tanks:"cfd-grade" experimental investigation," *Chemical Engineering Science*, vol. 245, p. 116743, 2021.

[36] A. Ferrante and S. Elghobashi, "On the physical mechanisms of two-way coupling in particle-laden isotropic turbulence," *Physics of fluids*, vol. 15, no. 2, pp. 315–329, 2003.

[37] D. Borrero-Echeverry and B. C. A. Morrison, "Aqueous ammonium thiocyanate solutions as refractive index-matching fluids with low density and viscosity," *Experiments in Fluids*, vol. 57, p. 123, July 2016.

[38] R. Budwig, "Refractive index matching methods for liquid flow investigations," *Experiments in Fluids*, vol. 17, pp. 350–355, Sept. 1994.

[39] S. F. Wright, I. Zadrazil, and C. N. Markides, "A review of solid–fluid selection options for optical-based measurements in single-phase liquid, two-phase liquid–liquid and multiphase solid–liquid flows," *Experiments in Fluids*, vol. 58, p. 108, Sept. 2017.

[40] C. Sion, D. Ghannoum, B. Ebel, F. Gallo, N. de Isla, E. Guedon, I. Chevalot, and E. Olmos, "A new perfusion mode of culture for wj-mscs expansion in a stirred and online monitored bioreactor," *Biotechnology and Bioengineering*, vol. 118, no. 11, pp. 4453–4464, 2021.

[41] S. Wiederseiner, N. Andreini, G. Epely-Chauvin, and C. Ancey, "Refractive-index and density matching in concentrated particle suspensions: a review," *Experiments in fluids*, vol. 50, pp. 1183–1206, 2011.

[42] R. J. Adrian, "Image shifting technique to resolve directional ambiguity in double-pulsed velocimetry," *Applied optics*, vol. 25, no. 21, pp. 3855–3858, 1986.

[43] J. Chéron, C. Loubière, S. Delaunay, A.-G. Guezennec, and E. Olmos, "Cfd numerical simulation of particle suspension and hydromechanical stress in various designs of multi-stage bioleaching reactors," *Hydrometallurgy*, vol. 197, p. 105490, 2020.

[44] S. B. Pope, "Turbulent flows," *Measurement Science and Technology*, vol. 12, no. 11, pp. 2020–2021, 2001.

[45] E. Simon, F. Augier, J. Morchain, J.-L. Pierson, and A. Liné, "Investigation of the local apparent viscosity in a stirred tank with a shear-thinning fluid through particle image velocimetry," *Chemical Engineering Research and Design*, vol. 206, pp. 378–385, 2024.

[46] P. Saarenrinne, M. Piirto, and H. Eloranta, "Experiences of turbulence measurement with piv," *Measurement Science and Technology*, vol. 12, no. 11, p. 1904, 2001.

[47] S. Baldi and M. Yianneskis, "On the quantification of energy dissipation in the impeller stream of a stirred vessel from fluctuating velocity gradient measurements," *Chemical Engineering Science*, vol. 59, no. 13, pp. 2659–2671, 2004.

[48] S. Elghobashi, "On predicting particle-laden turbulent flows," *Applied Scientific Research*, vol. 52, pp. 309–329, June 1994.

[49] P. Owen, "Turbulent flow and particle deposition in the trachea," in *Ciba Foundation Symposium-Circulatory and Respiratory Mass Transport*, pp. 236–255, Wiley Online Library, 1969.

[50] S. Scharnowski and C. J. Kähler, "Particle image velocimetry-classical operating rules from today's perspective," *Optics and Lasers in Engineering*, vol. 135, p. 106185, 2020.

[51] A. Gabriele, A. Nienow, and M. Simmons, "Use of angle resolved piv to estimate local specific energy dissipation rates for up-and down-pumping pitched blade agitators in a stirred tank," *Chemical Engineering Science*, vol. 64, no. 1, pp. 126–143, 2009.

[52] N. Liu, W. Wang, J. Han, M. Zhang, P. Angeli, C. Wu, and J. Gong, "A piv investigation of the effect of disperse phase fraction on the turbulence characteristics of liquid–liquid mixing in a stirred tank," *Chemical Engineering Science*, vol. 152, pp. 528–546, 2016.

[53] R. Escudié and A. Liné, "Experimental analysis of hydrodynamics in a radially agitated tank," *AIChE Journal*, vol. 49, no. 3, pp. 585–603, 2003.

[54] F. R. Khan, C. D. Rielly, and D. A. R. Brown, "Angle-resolved stereo-PIV measurements close to a down-pumping pitched-blade turbine," *Chemical Engineering Science*, vol. 61, pp. 2799–2806, May 2006.

[55] K. H. K. Chung, M. Barigou, and M. J. H. Simmons, "Reconstruction of 3-D Flow Field Inside Miniature Stirred Vessels Using a 2-D PIV Technique," *Chemical Engineering Research and Design*, vol. 85, pp. 560–567, Jan. 2007.

[56] W. Fornari, A. Formenti, F. Picano, and L. Brandt, "The effect of particle density in turbulent channel flow laden with finite size particles in semi-dilute conditions," *Physics of Fluids*, vol. 28, no. 3, 2016.

[57] R. Gore and C. Crowe, "Effect of particle size on modulating turbulent intensity," *International Journal of Multiphase Flow*, vol. 15, pp. 279–285, Apr. 1989.

[58] T. Tanaka and J. K. Eaton, "Classification of Turbulence Modification by Dispersed Spheres Using a Novel Dimensionless Number," *Physical Review Letters*, vol. 101, p. 114502, Sept. 2008. Publisher: American Physical Society.

[59] J. D. Tsuji, M. Schwarzkopf, Y. Sommerfeld, and C. T. Crowe, *Multiphase Flows with Droplets and Particles*. Boca Raton: CRC Press, 2 ed., Sept. 2011.

[60] A. Delafosse, M.-L. Collignon, M. Crine, and D. Toye, "Estimation of the turbulent kinetic energy dissipation rate from 2d-piv measurements in a vessel stirred by an axial mixel ttp impeller," *Chemical Engineering Science*, vol. 66, no. 8, pp. 1728–1737, 2011.

[61] G. Gai, A. Hadjadj, S. Kudriakov, and O. Thomine, "Particles-induced turbulence: A critical review of physical concepts, numerical modelings and experimental investigations," *Theoretical and Applied Mechanics Letters*, vol. 10, pp. 241–248, Apr. 2020.

Appendix

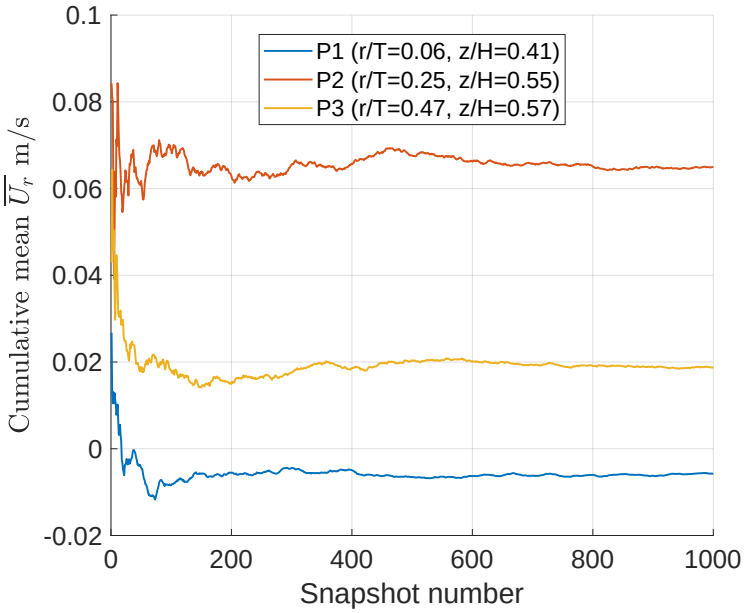

Figure A.2.1: Statistical convergence of mean radial velocity component (m/s) at three different positions for α_p = 3 v%. P1: bulk (under the impeller), P2: impeller region, and P3: wall region.

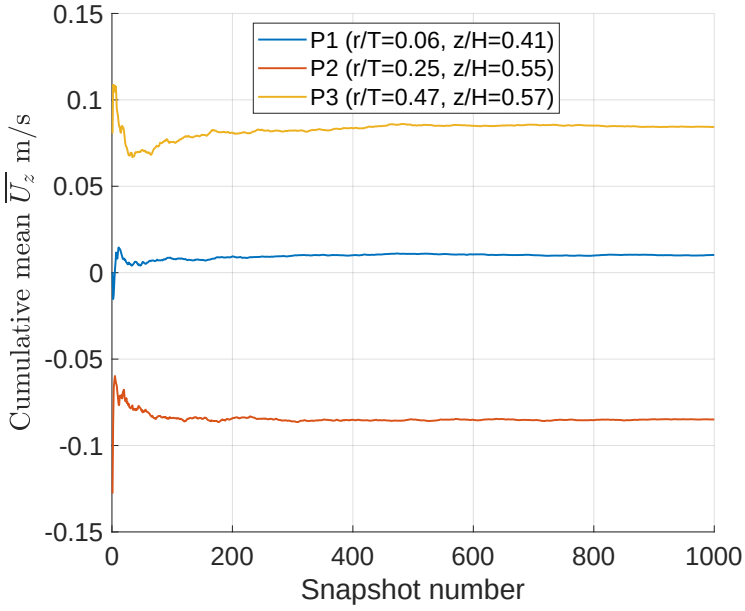

Figure A.2.2: Statistical convergence of mean axial velocity component (m/s) at three different positions for α_p = 3 v%. P1: bulk (under the impeller), P2: impeller region, and P3: wall region.

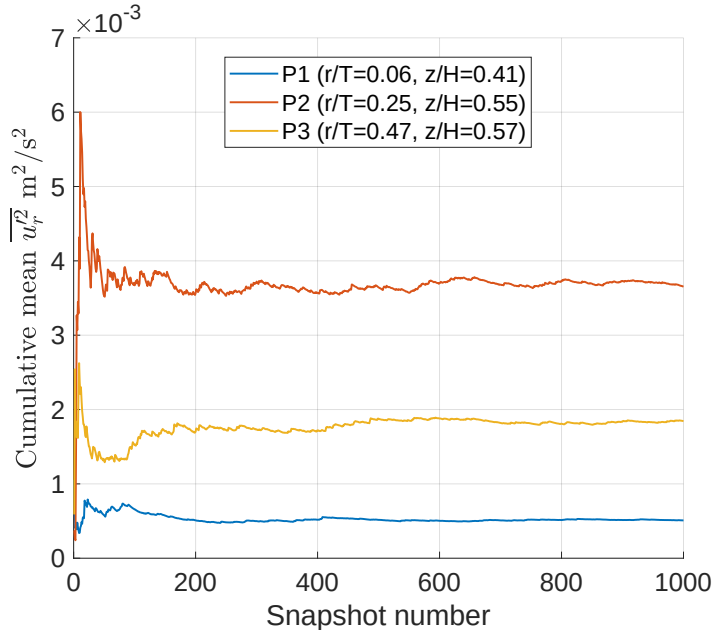

Figure A.2.3: Statistical convergence of mean fluctuating radial velocity component (m^2/s^2) at three different positions for α_p = 3 v%. P1: bulk (under the impeller), P2: impeller region, and P3: wall region.

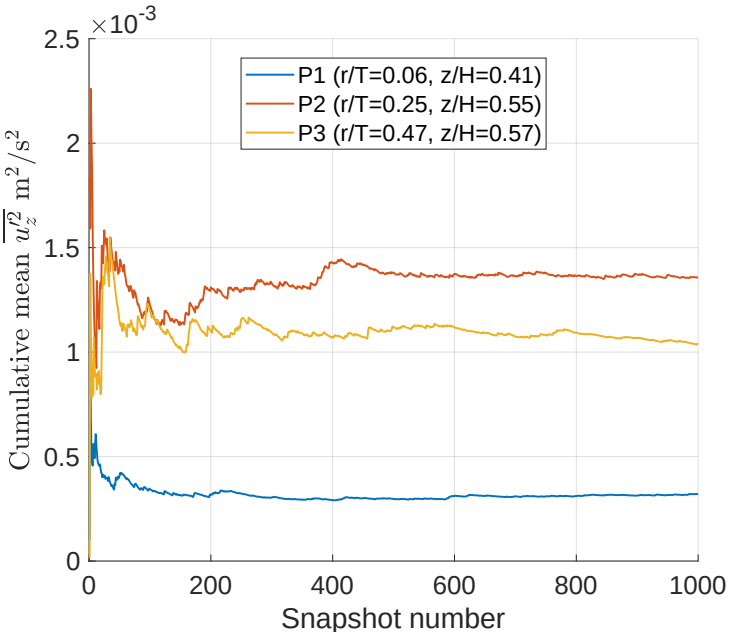

Figure A.2.4: Statistical convergence of mean fluctuating axial velocity component (m^2/s^2) at three different positions for α_p = 3 v%. P1: bulk (under the impeller), P2: impeller region, and P3: wall region.

Chapter 3

Solid–liquid Flow Behaviour and Interfacial Interactions: Two-Phase PIV

Abstract

Solid–liquid stirred tanks are widely used in multiphase processes, including bioreactors for mesenchymal stem cell (MSC) culture, yet simultaneous experimental data for both dispersed and carrier phases remain limited. Here, a refractive index-matched (RIM) suspension of PMMA microparticles ($d_p = 168\,\mu m$, $\rho_f/\rho_p \approx 0.96$) in an NH_4SCN solution is studied at an intermediate Reynolds number ($Re \approx 5000$), low Stokes number ($St = 0.078$), and particle volume fractions $0.1 \leq \alpha_p \leq 0.5$ v%. This system was previously established and studied for the effect of addition of particles on the carrier phase. In this work, a dual-camera PIV set-up provides simultaneous velocity fields of the liquid and particle phases in a stirred tank equipped with a three-blade down-pumping HTPGD impeller. The liquid mean flow and circulation loop remained essentially unchanged with particle loading, whereas particle mean velocities were lower than single-phase and liquid-phase values in the impeller discharge. Turbulence levels diverged between phases: liquid-phase turbulent kinetic energy (TKE) in the impeller region increased modestly with α_p, while solid-phase TKE was attenuated. Slip velocity maps showed that particles lagged the fluid in the impeller jet and deviated faster from the wall in the upward flow, with slip magnitudes increasing with α_p. An approximate axial force balance indicated that drag dominates over lift in the impeller and wall regions, while the balance is approximately satisfied in the tank bulk, providing an experimental benchmark for refining drag and lift models in this class of stirred tanks.

3.1 Introduction

Multiphase flows occur in nature and in an abundance of industrial processes, such as aerospace [1], metallurgy [2], and chemical engineering. Within the world of chemical engineering, examples include crude oil recovery [3], catalysts in chemical reactors [4], and food production [5]. Dispersed multiphase systems consist of small particles, bubbles, or droplets that are suspended in a continuous medium. The continuous phase generally acts as a carrier, often demonstrating turbulent flow, while the dispersed phase can influence the behavior of this carrier flow [6].

The presence of a dispersed phase in a continuous carrier flow adds challenges to the experimental characterization, which is essential to understand the interactions between both phases. The interactions would affect the properties and behavior of the discrete/dispersed phase and those of the carrier flow. The impacts include alterations on local flow velocities, local volume fractions distribution of rigid particles, size distribution of droplets/bubbles, and local residence time of dispersed phases. The presence of the dispersed phase could also introduce particle–particle interactions as well as coalescence–rupture of bubbles/droplets that add complexities to the flow. Other impacts on system performance could be on the global scheme of things, such as mass and heat transfer rates and power consumption. Over the years, researchers have developed and tested computational tools to model interfacial phenomena and interactions [7, 8]. However, to validate the numerical tools and inspire the principal models, recording and collecting experimental data are a must. Hence, in all cases, developing experimental techniques is essential to inspect and optimize the process. Several measurement techniques, in addition to modeling approaches, have been established and documented [6, 9].

To list a few, these experimental techniques could be in the form of intrusive probes, such as hot wire and electrical impedance probes or nonintrusive like imaging and laser-driven methods. Hot wire anemometry utilizes constant temperature Wheatstone bridge that exploits the differences in heat transfer due to phase density, eventually allowing for the detection of phase interfaces. Consequently, it accurately captures bubble or droplet sizes, volume (void) fractions, and velocities of both phases [10, 11]. Electrical impedance probes rely on resistive or capacitive contrasts—by inserting needle-like electrodes into the flow—to measure local or bulk multiphase properties and detect phase boundaries [12, 13]. Multi-point arrangements including wire mesh sensors, enable 2D/3D mapping of volume fractions and velocity fields [14, 15]. Nevertheless, the presence of such probes is invasive, as interfaces could be deformed by the probe and the path of the dispersed phases may deviate as they encounter the probe, which further results in local flow disturbances and eventually inducing excessed biased errors [16, 17].

On the other hand, nonintrusive imaging methods are another way of characterizing multiphase flows as in shadowgraphy. It is a backlit imaging technique that uses a collimated (parallel) light beam to provide volumetric illumination with an effectively infinite depth of field, so that the apparent size of an object does not depend on its position within the measurement volume [18]. This setup is ideal for sizing objects in dilute multiphase flows and can be used for 3D particle tracking with reduced calibration requirements [19, 20]. The major drawbacks for shadowgraphy are the fixed working distance and magnification of the telecentric lens, the demands of long optical benches, and large-aperture collimating optics [21]. Moreover, only droplets/particles lying in the focal depth are sharply captured; those located closer or farther than this zone appear increasingly blurred and could overestimate the statistics [22].

When shadowgraphy is limited by optical density or depth-of-field, researchers often shift to tomographic approaches. Tomographic technology involves the acquisition of measurement signals from sensors located on the periphery of an object, then reconstructing cross-sectional images from these data obtained [23, 24]. There are several tomographic techniques such as X-ray, γ-ray, and electrical capacitance. X-ray hard-field imaging positions a source behind the test section; the transmitted beam is converted to visible light by a scintillator and captured by a camera. High spatial resolution is provided that is capable of mapping void fractions or particle concentrations for dense multiphase flows where optical access is limited [25, 26]. However, its high cost and safety requirements make it largely confined to specialized facilities, which means that the experimental set-up must be moved and often indicates limited space and access. Equally important, the technique generates massive data loads that impose intensive computations for processing, reconstruction, and analysis [27]. In contrast to X-rays, γ-rays have higher photon energies that provide better penetration through thick steel or concrete, making the method suitable for packed columns, risers, and dense-walled containment vessels [28, 29]. With regard to technique constraints, gamma rays can interact with matter through various processes, including scattering and absorption, making it sometimes difficult to reconstruct the flow structure [30], as well as the expensive cost of the system [31]. In terms of low-cost electrical tomography, it is similar in principle to electrical probes, but the sensors are rather arranged around the measurement domain to obtain tomographic reconstructions of resistance, capacitance, or impedance data [32, 33]. Overall, electrical tomography techniques provide coarse spatial resolution, struggling to resolve fine details of the phase distribution [34]. The soft-field nature, i.e. the non-linearity of the electric field, adds also complications for image reconstruction [35, 36].

Since tomography primarily yields phase-distribution maps, high-resolution flow hydrodynamics are usually captured with laser-based techniques. Laser-based methods are commonly used such as PIV and PTV for instance. Particle Image Velocimetry (PIV) and

Particle Tracking Velocimetry (PTV) rely on laser light scattering by particles or absorption/emission of fluorescence tracers to measure the velocities of dispersed and continuous carrier phases. Often associated together to measure multiphase flows (PIV/PTV), phase discrimination is a must to differentiate both phases. The approach involves digital image processing [37], wavelength-based optical separation [38], or correlation peak analysis [39]. Various applications and geometries have thus been studied, covering pipe flows [40], open channels [41], turbulent jets [42], sprays [43], grid turbulence [44] and stirred tanks [45]. Villafañe et al. [46] recently presented a more consolidated review of the developments and research of experimental multiphase flows.

Stirred tanks have been numerously investigated so far, but the turbulent characteristics of the multiphase flow inside the tank are still open for debate [47]. A typical flow type is a solid–liquid one where particles of different sizes are suspended inside the tank. Only few studies were conducted to simultaneously measure the dispersed and carrier phases in stirred tanks via PIV. Most studies focused on the effect of the dispersed phase (addition of particles) on the carrier phase as summarized by Madani et al. [48], i.e., data on the liquid phase only. In the following, research related to the measurements of both phases is outlined. A first PIV use in this context was performed by Virdung and Rasmuson [49] who used glass beads 1 mm in diameter that matched the refractive index of Benzyl alcohol/Ethanol mixture up to 1.5 v% volume fractions, suspended by the means of a pitched-blade impeller with a corresponding Reynolds number of Re = 7500. They showed that the r.m.s. velocities for both phases increased, whereas the velocity fields decreased overall with increasing particle concentrations. In addition, analysis of the mean axial slip velocity showed that particles lead the continuous phase in the impeller jet area and lag behind in the vertical stream close to the wall. Another study by Unakdat et al. [50] also used glass sphere particles of a size of 1 mm, suspended in water and thus without matching the liquid refractive index, reaching a dilute volumetric fraction of 0.5 v% operating at Re = 30,800. Consequently, the two phases were then separated by a phase discrimination technique based on the geometrical characteristics of the particles [51]. Results showed that particle turbulence levels measured at 0.5% were lower than the corresponding continuous phase without reports on the slip velocity. Further, Montante et al. [45] investigated the dilute suspension of 0.2 v% glass particles of sizes 115 and 774 µm in diameter without RIM (refractive index matching) of the liquid phase, at Re = 88,000 corresponding to a fully turbulent system. Phase separation was based on optical filters mounted on the cameras. Continuous-phase turbulence was found to reduce the values of particle settling velocity for the bigger particles, which was also reinforced by the approximate analysis of the force balance equation of the particles. A recent experimental study on this manner was communicated by Sommer et al. [52] that dealt with glass and polyethylene particles with a diameter range of 63–450 and various solid volume fractions. The camera

used for the dispersed particle phase was based on shadowgraphy approach. The axial velocity of the glass beads, that possessed the highest inertia, was lower than the liquid mean flow velocity above and below the impeller. Comparisons also revealed that the axial turbulent fluctuations in the solid phase were lower than in the liquid phase, and this could be attributed to the huge difference between the depth of field (DOF) of the shadowgraphy camera (solid) and that of the PIV (liquid). The authors did not disclose any slip velocity analysis.

It is important to mention that Laser Doppler Velocimetry LDV is also a laser-based option for simultaneous data collection on solid and liquid flows in stirred tanks. Nouri and Whitelaw [53] used Diakon particles up to 2.5 v% concentration with size ranging from 590 to 730 µm to match the refractive index of Tetraline and Turpentine oil mixture and glass particles with water at dilute concentrations. The experiments were applied to different geometric set-ups and Re numbers. As a result, turbulence levels in the impeller stream were lower than the single-phase values (13–15%), with heavier particles exhibiting lower turbulence levels compared to lighter ones. Additionally, as particle concentration increased, the axial and radial particle mean velocities dropped by up to 5% in the impeller stream and 10% in the bulk of the flow. Since the measurement of liquid phase velocities in the presence of particles was not possible, the apparent relative velocity—which is the difference between particle velocity and that of the single phase—was discussed. They found that the apparent relative velocities of the glass particles were larger than those of the Diakon particles by factors of 2 and 2.5 in the impeller stream and in the bulk region, respectively. Guiraud et al. [54] analyzed the suspension of glass particles in water at low volume fraction 0.5 v% and diameter of 253 µm inside a stirred tank. Consequently, the r.m.s. axial particle velocities were always greater than those measured for the continuous phase, and the slip velocities were of the same order of magnitude as the terminal velocity evaluated by classical correlations.

As a reminder, the stirred tank in this work—dedicated for the mesenchymal stem cell MSC culture—has already been used to investigate practical aspects such as spatial distribution of microcarriers, just-suspended impeller speed, and the effect of particle loading on liquid-phase hydrodynamics [48]. Here, the simultaneous data acquisition of the solid–liquid flow of both phases inside the tank was obtained. That means that the system consists of microparticles whose density is very close to that of the liquid phase $\rho_f/\rho_p \approx 0.96$, a low-viscosity liquid, intermediate Reynolds numbers $Re \approx 5000$ and a low Stokes number ($St - 0.078 < 1$). By the means of two-camera PIV, suspension of an RIM solid–liquid system was characterized to evaluate the velocities of the particles and the liquid phase, simultaneously, at various volume fractions ($0.1 < \alpha_p < 0.5$ v%). The interactions between both phases in terms of turbulence, slip velocities, and eventually interfacial forces were thus analyzed and discussed.

3.2 Materials and Methods

3.2.1 Experimental Set-Up

The investigated solid–liquid flow properties are exactly the same as those used to characterize the fluid phase previously [48], i.e., the effect of particle addition on the liquid phase up to α_p = 3 v%. It is composed of PMMA microparticles (Cospheric) of d_p = 168 µm and ρ_p = 1185 kg/m^3 and Ammonium Thiocyanate NH_4SCN solution of 61 wt% corresponding to ρ_l = 1139.2 ± 0.1 kg/m^3 and μ_l = 1.94 ± 0.01 mPa.s. The solution was carefully filtered to remove any insoluble impurities (solid residues). Both phases were matched for a refractive index $RI \approx 1.491$. The volume fraction of the particles was systematically increased until it reached α_p = 0.5 v% where significant noise made it impractical to treat images afterward despite the matching indices of both phases. The noise is evidently related to the images of particles in this case and not to the liquid phase. The maximum number of particles would thus be limited, around 1.4 million inside the tank.

As for the stirred tank (see Figure 3.1), it is made of borosilicate glass with a cylindrical body and hemispherical bottom shape, a diameter T = 0.12 m and a height of H = 0.082 m (H/T = 0.68). The impeller used is a three-blade axial-down-pumping mode HTPGD (Pierre Guerin [55]) with diameter D positioned at an off-bottom clearance C being $C/T = D/T = 0.5$. The tank is unbaffled but equipped with four dip tubes resembling the necessary sensors (temperature, pH, etc.), which play the same role as baffles and prevent the swirling phenomenon (See also Figures S1-S3 in the Supplementary Materials section). The working volume of the fluid phase is $V = 0.7L$ agitated at N = 150 rpm which corresponds to a full homogeneous suspension of PMMA microparticles. It is higher than the just-suspended state for all concentrations used as established by Delafosse et al. [56] on a solid–liquid system with the same properties. The resulting Reynolds number is around $Re \approx 5000$, indicating a relatively turbulent regime.

In addition, the stirred tank was held in an aquarium filled with paraffin oil of RI ≈ 1.468 (Fauth) to match the wall of the tank refractive index and thus limit the diffraction in the laser sheet due to the curvature of the body and the bottom side. The temperature was controlled by the means of an air conditioner inside the operating room (22–23 °C).

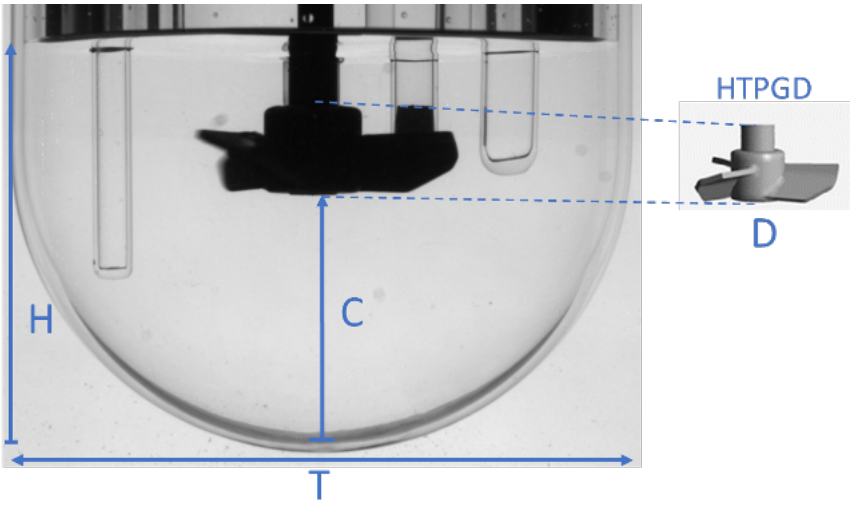

Figure 3.1: Geometrical configuration of the tank used equipped with HTPG down-pumping axial impeller. T = 0.12 m, H = 0.082 m. C/T = D/T = 0.5.

3.2.2 Simultaneous Two-Camera PIV

PIV technique was applied to simultaneously capture the continuous/carrier- and dispersed-phase flow fields in the vertical z-r plane at the center of the tank (measurement plane as seen in the green area in Figure 3.2 Left). The field of view captured thus corresponds to 80×60 mm which is half of the tank in the z-r plane. The system represented in Figure 3.2 was equipped with two CMOS cameras (FlowSense EO 4M), each with a 16 Hz maximum acquisition frequency and a 2048×2048 pixel resolution. To capture flow images separately, the cameras were mounted with wavelength-based optical filters. The illumination was provided by Nd:YAG double pulse laser of 532 nm wavelength operating at 50 mJ. A prism was located between the two cameras at 45° that allowed a straight vision of the tank for the "liquid" camera and acted as a mirror for the "solids" camera.

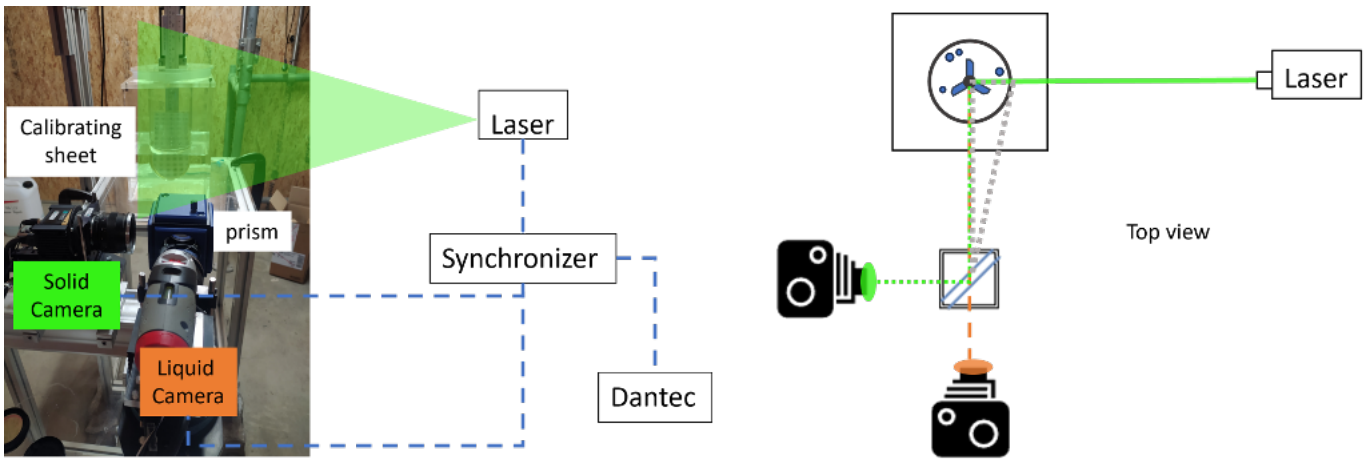

Figure 3.2: (**Left**): Simultaneous PIV set-up associated with a calibration sheet. (**Right**): Top view of the PIV set-up with the stirred tank. Liquid camera is equipped with an orange filter (>570 nm). Solids camera is equipped with a green filter (=530 nm). Laser sheet illuminates the center of the tank right at the shaft. The gray-dotted lines indicate the measurement plane perceived by the imaging system.

The two-phase flow was seeded with 20 µL Rhodamine-coated-PMMA fluorescent tracers (0.25 g/mL initial concentration, Dantec Dynamics v7.3), neutrally buoyant, with emission wavelength ≈ 590 nm, tracer diameter size of $d \approx 10$ µm and density of $\rho = 1190$ kg/m^3. That being said, phase separation for images relied on the optical filters as mentioned above: the camera for the continuous liquid phase was fitted with a 570 nm orange filter that cuts off emissions below this wavelength, whereas the camera for the dispersed solid phase was equipped with a 530 nm green filter that reflects the laser sheet. Despite the RIM technique, PMMA microparticles are solely detected due to the presence of slight mismatches at the interface (between the dispersed phase and the liquid phase) that permit the high-intensity laser to be scattered by the particles. This point is heavily discussed in a previous study [48]. Moreover, the particles camera aperture was adjusted accordingly as a first step to minimize noise capture. The noise treatment is discussed in detail in the following section. With the time interval between two laser pulses fixed at $\Delta t = 1500$ µs—limiting tracer displacement in the impeller region to roughly one-quarter of the interrogation area—the two cameras, synchronized by an encoder, acquired images at the same instant. A set of 1100 image pairs was finally captured at an acquisition rate of 15.8 Hz and saved in the Dantec Dynamics software v7.3 for each case to ensure the statistical convergence of mean velocities and turbulent fluctuations.

3.2.3 Noise and PIV Treatments

When dealing with two-phase flows, optical separation is not enough for analysis. Noise treatment is crucial and essential prior to the application of cross-correlations to obtain vector maps. A step that is sometimes ignored or not shown in the research could support the reliability of the PIV raw images. First, the efficiency of optical filters was assessed by comparing images taken with the solid camera with and without fluorescent tracers (Figure 3.3). As one may notice, the tracers did not interfere or appear in the solid camera, as the emission was at a higher wavelength. This is an important check to verify that the particles tracked during the increase in volume fractions are PMMA particles per se and not tracers. Furthermore, considerable impurities can be present in salt solutions (NH_4SCN in this case) and can further alter image clarity and ultimately bias dispersed phase velocities; therefore, filtering the solution is a paramount checkpoint.

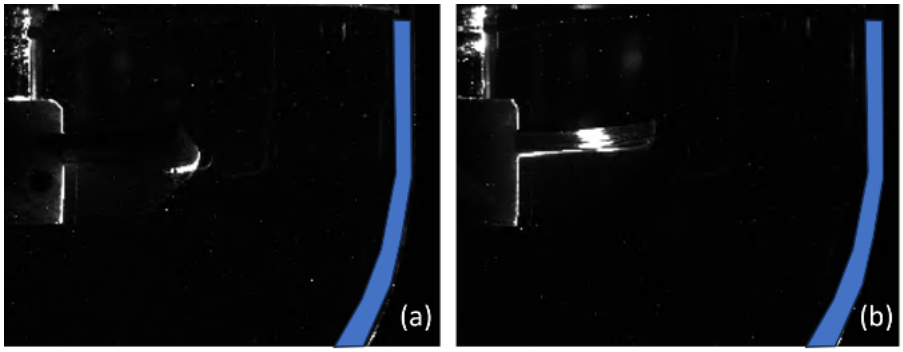

Figure 3.3: Solids camera snap-shot: (**a**) Without tracer particles. (**b**) With tracer particles.

Subsequently, the images registered for each camera were treated differently but with the same concept of creating a background image that represents noise and then subtracting the generated background from the raw images. The liquid-phase images followed the same approach as used before, by computing the minimum power mean grayscale values from the set of images (also known as a generalized mean) to form a unified background image. Insignificant noise was found at $\alpha_p = 0.5$ v%, as the presence of PMMA particles at these levels did not deteriorate the quality of the image, thanks to RIM between both phases. As previously mentioned, this was validated in a previous study [48]. On the other hand, for particle-phase images, a background needs to be created for every image. Since PMMA microparticles were added accordingly up to $\alpha_p = 0.5$ v%, noise propagated with increasing particle concentration, resulting in either high bright spots or gray areas in the images. An example is shown in Figure 3.4 where the generated background is subtracted from the raw image to eliminate as much noise as possible. The background creation was based on a sequence of image processing operations: a median filter, an erosion followed by a dilation, and finally a shock filter, each applied with a 5×5 pixel window (Dantec Dynamics v7.3). Noticeably, near the tank wall, where the laser first hits, low noise from PMMA microparticles is found, which is confirmed by the black area from the background image (Figure 3.4b) in that region. As the laser beam travels farther into the medium, PMMA-induced noise becomes increasingly prominent, but the four-stage image processing tool effectively removes this noise.

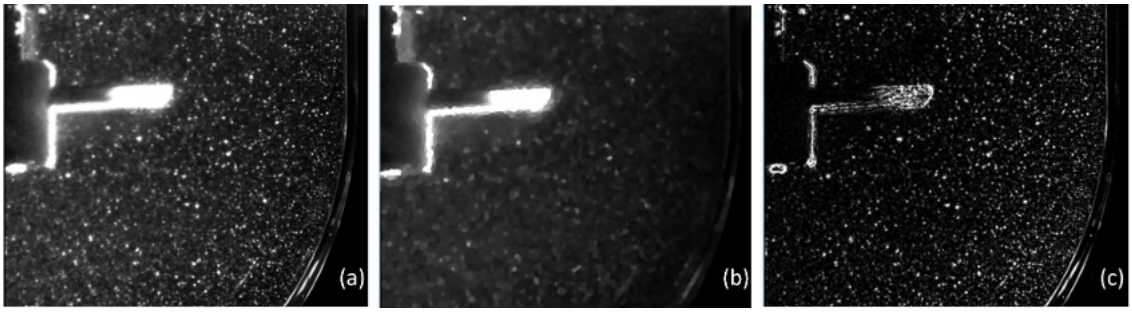

Figure 3.4: Instantaneous PIV images from solids camera at $\alpha_p = 0.5$ v%: (**a**) Raw image. (**b**) Generated background filter. (**c**) Treated image. The impeller is evidently masked prior to obtaining vector maps.

After the image treatment step, the instantaneous velocity maps were obtained for both phases using the open-source PIVLab toolbox (v3.02) [57, 58]. Since the emergence of this tool, it has been extensively used and validated in various applications [59, 60, 61, 62]. Multipass FFT window deformation scheme was used with a final window size of 32×32 pixel and 50% overlap, corresponding to a spatial resolution of $L_{IA} = 1.1$ mm. The ratio of spatial resolution to particle diameter is $L_{IA}/d_p = 6.5$, which means that it is large enough to acquire velocity vectors of PMMA particles that appear in the entire IA. Eventually, spurious vectors would emerge, and a validation step is necessary. For the liquid phase, the standard deviation (σ) of each vector map was computed; subsequently, any vectors that deviate from the mean by more than $3{\cdot}\sigma$ were disposed. With regard to dispersed phase, slightly more spurious vectors arose compared to the liquid phase, and the local median filter approach was thus utilized. Each velocity vector was compared with the median of the eight neighbours in a 3×3 window. This difference was then divided by the median of the eight differences inside the window to form a normalized residual k. Vectors that exceeded $3 \cdot k$ were then removed and considered invalid. More than 99% of the vectors passed the validation step for the liquid phase and around 97.5–98% for the particle phase, indicating a high-quality vector field. The results obtained were then post-processed in MATLAB (R2023b) for further analysis.

3.2.4 Flow Properties

One way to characterize turbulent levels inside the stirred tank is by estimating the turbulent kinetic energy TKE. It depends on the fluctuating velocity terms that could be evaluated using classical Reynolds decomposition $u' = u - \overline{U}$, where u is the instantaneous velocity and $\overline{U}$ is the time-averaged velocity, i.e., the ensemble-average of the 1100 set of the velocity fields. The mean velocity magnitude of the flow is defined as the square root of the sum of the squared velocity terms $M = \sqrt{\overline{U_r}^2 + \overline{U_z}^2}$. The subscripts r and z denote the radial and axial terms, respectively, with positive r directed to the right and positive z directed upward. The origin of the axis is located at the center of the tank bottom.

Note that the fluctuations contain periodic ones produced by the impeller, which can be isolated using an angle-resolved measurement. This study did not attempt to produce such information, which could be tackled in future work. In addition, Escudié and Liné [63] showed that the dissipation rates of mean and periodic kinetic energy were negligible compared to the dissipation rate of turbulent kinetic energy, so the use of classical decomposition is sufficient when angle-resolved technique is unavailable. Theoretically, TKE is half of the trace of the Reynolds stress tensor, which means knowledge of the three terms of the fluctuating velocity components (radial, axial and tangential), whereas the experimental set-up employed here is a 2D PIV system. In this case, where the tangential

component is unknown, a pseudo-isotropic scheme may be applied [64, 65, 50] so that TKE $k = \frac{3}{4}\left(\overline{u_r'^2} + \overline{u_z'^2}\right) = \frac{3}{4}\left(\overline{Urms_r}^2 + \overline{Urms_z}^2\right)$. The root mean square r.m.s. velocity $\overline{Urms} = \sqrt{\overline{u'^2}}$ also gives a single representative magnitude of these fluctuations. Additional comments on the Kolmogorov scale and the Taylor microscale could be found in [48].

Lastly, the velocity and turbulent kinetic energy terms are non-dimensionalized by (ND) and $(ND)^2$, respectively. The non-dimensional terms are denoted by a '*' as in $M^* = M/(ND)$ and $k^* = k/(ND)^2$ for instance. Note that this scaling is different from normalizing by the maximum tangential blade-tip velocity, $V_{tip} = \pi ND$, which introduces a factor of π.

Acquiring data at the same instant with unified spatial resolution opens the door for further analysis of the flow, specifically the particle–fluid slip velocity. It is the difference between the velocity of the particle phase and that of the liquid phase on either axis, that is, the velocity of the particle relative to the local fluid velocity, associated with a directional term, $u_s = (u_p - u_l)\ \frac{u_p}{|u_p|}$. The directional vector is added to govern the sign of the momentum transfer between phases [49]. Slip velocities are negative for areas where the continuous phase leads the dispersed phase and vice versa. The subscripts p and l are denoted for particles and liquid, respectively; e.g., $u_{p,z}$ is the instantaneous axial velocity for the particles. Using the terminal velocity experiments of PMMA particles, established previously in a still liquid, the axial slip velocity can be normalized by the terminal velocity, u_s/u_t.

3.3 Results and Discussions

First, several instantaneous superimposed vector maps of both particles (red) and liquid phases (blue) are shown in Figure 3.5, where one may notice that the velocity vectors are not perfectly matched, yet not completely diverted. The main difference that could be spotted is not only the magnitude, but also the orientation of the vectors, i.e., the angle between the velocity vectors, especially in the impeller region. The extent of such variations will be further discussed in the slip velocity Section 3.3.2.

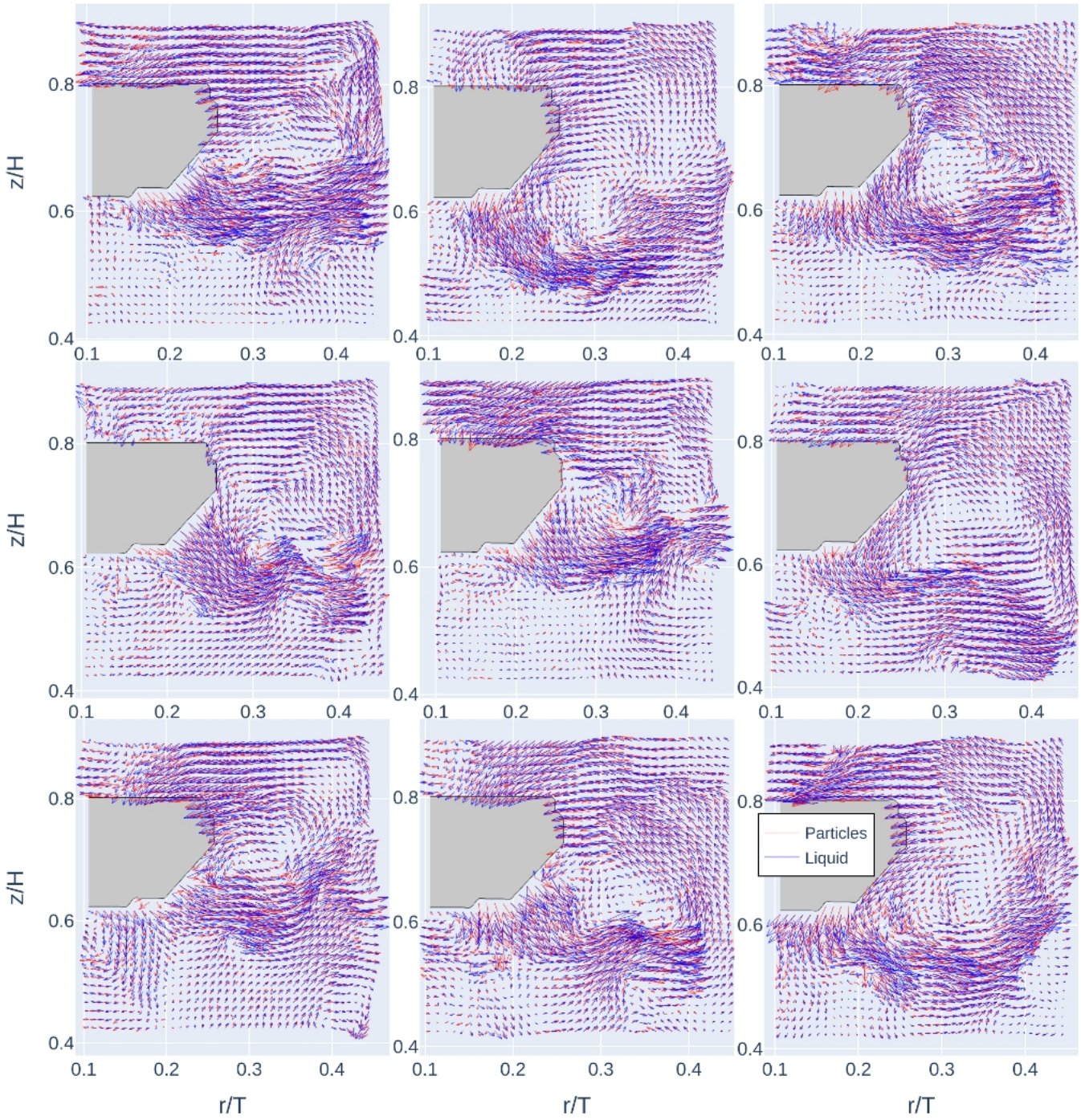

Figure 3.5: Case α_p = 0.5 v%: Superimposed instantaneous velocity vectors of particles (red) and liquid (blue) phases for different snap-shots. Geometry is limited here to the impeller region for a clear view of velocity vectors.

The scheme presented in Figure 3.6 is used as a reference in the following sections. It shows the axial/vertical profiles at r/T = 0.22 and 0.48, as well as an area of 10 × 10 mm, located at 0.57 < z/H < 0.67 and 0.22 < r/T < 0.32, in the impeller discharge region. The first vertical profile at r/T = 0.22 passes through the impeller to cover the discharge flow and the ending phase of the recirculation loop. The second vertical profile at r/T = 0.48,

near the wall, covers the other half of the loop where the up-flow part takes place and where low-to-moderate values of the properties investigated (e.g., velocity, turbulence) are observed. These profiles and values locally averaged on the square area will be used for the analysis in the upcoming sections.

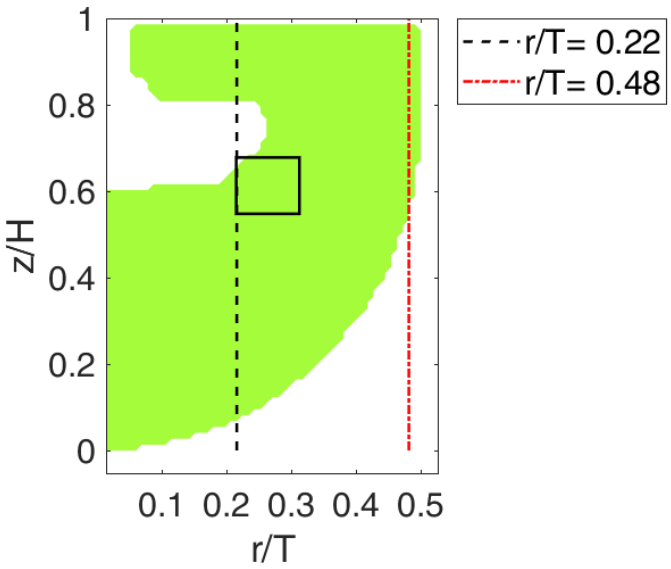

Figure 3.6: Scheme showing relative cross sections/profile cuts and local area (box) positions for further analysis. The area/box is located at 0.57 < z/H < 0.67 and 0.22 < r/T < 0.32.

3.3.1 Flow and Turbulence Analysis

Contour plots in Figure 3.7 show that the liquid mean velocity is essentially unchanged from α_p = 0 to 0.5 v% (panels a–b, respectively), whereas the solid phase mean velocity at α_p = 0.5 v% (panel c) is reduced in the impeller discharge region. Both the fluid velocity contours (with and without particles) and the particle velocity contours exhibit the same down-pumping axial flow in the measured plane. The resulting circulating loop starts at the lower side of the impeller tip and extends toward the wall where the flow changes its direction upward to finally close the loop at the upper side of the impeller tip. It is apparent that the values of the mean velocity at the end of the loop above the impeller tip are consistently higher than those near the wall. This difference arises from the impeller pushing the flow, which entrains fluid and particles from the upper region as it sweeps through the volume. The center of the loop is located between 0.3 < r/T < 0.4 and 0.65 < z/H < 0.75. Under the impeller, there is a region of almost stagnant flow in the measurement plane, where the unmeasured off-plane tangential flow is predominant. The maximum velocity magnitude in the impeller discharge is around $1.1ND = 0.35V_{tip}$ for both liquid phases. On the other hand, the contour plot of the mean velocity of the solid phase at α_p = 0.5 v% possesses lower values in the impeller stream (Figure 3.7c) around $0.85ND = 0.27V_{tip}$ compared to the former contours. Note that the mean velocity vectors

(white) of each corresponding case are also plotted in the contour images.

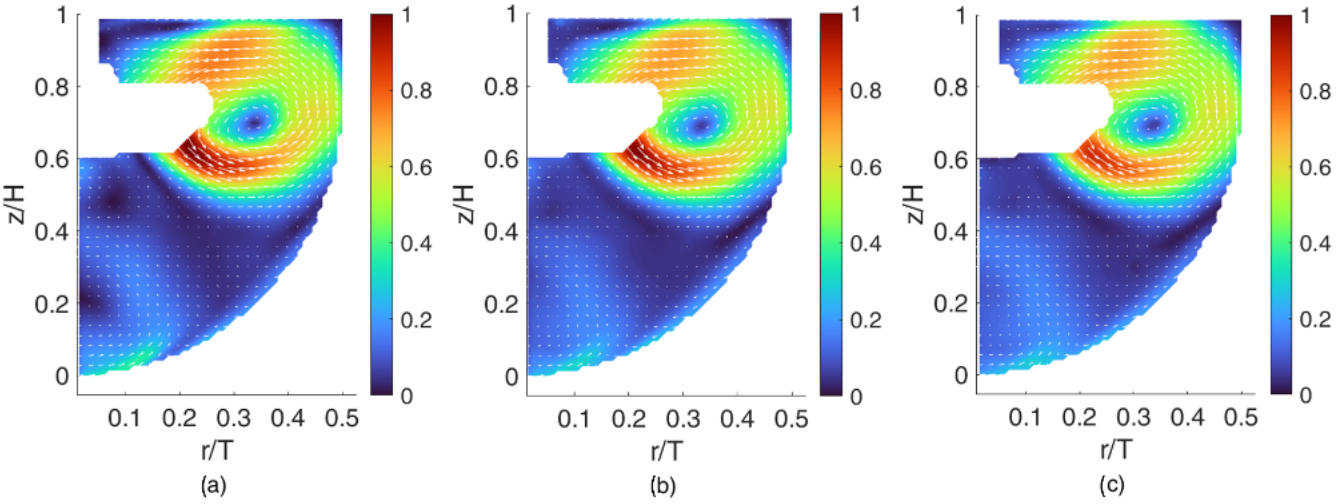

Figure 3.7: Non-dimensional mean velocity magnitude of the flow M^*, scaled by (ND): (**a**) Single-phase flow, (**b**) liquid phase for α_p = 0.5 v%, (**c**) solid phase for α_p = 0.5 v%. The corresponding mean velocity vectors are added to each contour plot. Color-bar: $M^* = M/(ND)$.

For a more detailed, quantitative comparison, the velocity profiles are shown in Figures 3.8 and 3.9, arranged according to the scheme presented previously in Figure 3.6. The evaluation is between single phase (without particles) on one hand, and liquid phase and solid phase at the maximum solid concentration reached α_p = 0.5 v% on the other hand. Figure 3.8 shows the mean radial (Figure 3.8 Left) and axial (Figure 3.8 Center) velocities, $\overline{U}_r^*$ and $\overline{U}_z^*$, respectively, as well as the velocity magnitude (Figure 3.8 Right) M^* along the vertical profile at r/T = 0.22. As mentioned above, this profile passes through the impeller jet stream. For the mean radial velocity, negligible variations are found for the liquid phase with α_p = 0.5 v% and without particles. The solid phase at α_p = 0.5 v% also exhibits the same behavior except for the impeller discharge at 0.6 < z/H < 0.65, where mean radial values drop by 12%. Moving to the mean axial velocity, at 0.6 < z/H < 0.65, single phase carries higher mean axial values than that of liquid phase at α_p = 0.5 v% with a drop of 13%, whereas the particles' mean axial velocity at the same concentration hold even lower values in the same region, with 11% decrease from that of the liquid phase and a maximum of 20% decrease from that of the single phase. Otherwise, the three examined cases are almost identical elsewhere in the profile plot. The combination of radial and axial terms into mean velocity magnitude further demonstrates the differences observed between solid and liquid phases in the same region 0.6 < z/H < 0.65, with a maximum damping of 18%. Aside from the impeller region, the local velocity magnitudes remain essentially unchanged by the addition of particles.

Near the wall, at r/T= 0.48, where lower velocities are present, small differences can be

noticed on Figure 3.9. For the mean radial velocity term $\overline{U}_r^*$ (Figure 3.9 Left), liquid phase at α_p = 0.5 v% is slightly greater than that of single phase and dispersed phase by ≈ 12% along the z-axis at 0.6 < z/H < 0.65 and 0.8 < z/H < 0.9. However, for the mean axial velocity term (Figure 3.9 Center) and velocity magnitude (Figure 3.9 Right), particles lead the liquid phase without and with α_p = 0.5 v% fractions along the z-axis by ≈ 10%. Although the variations at r/T = 0.48 are considered not as significant as those at r/T = 0.22, one may notice that the behavior near the wall is opposite to that in the impeller region, where the particles lead in the zone near the wall and lagged behind in the impeller vicinity. Note that a radial plot is reported in Appendix in Figure A.3.1.

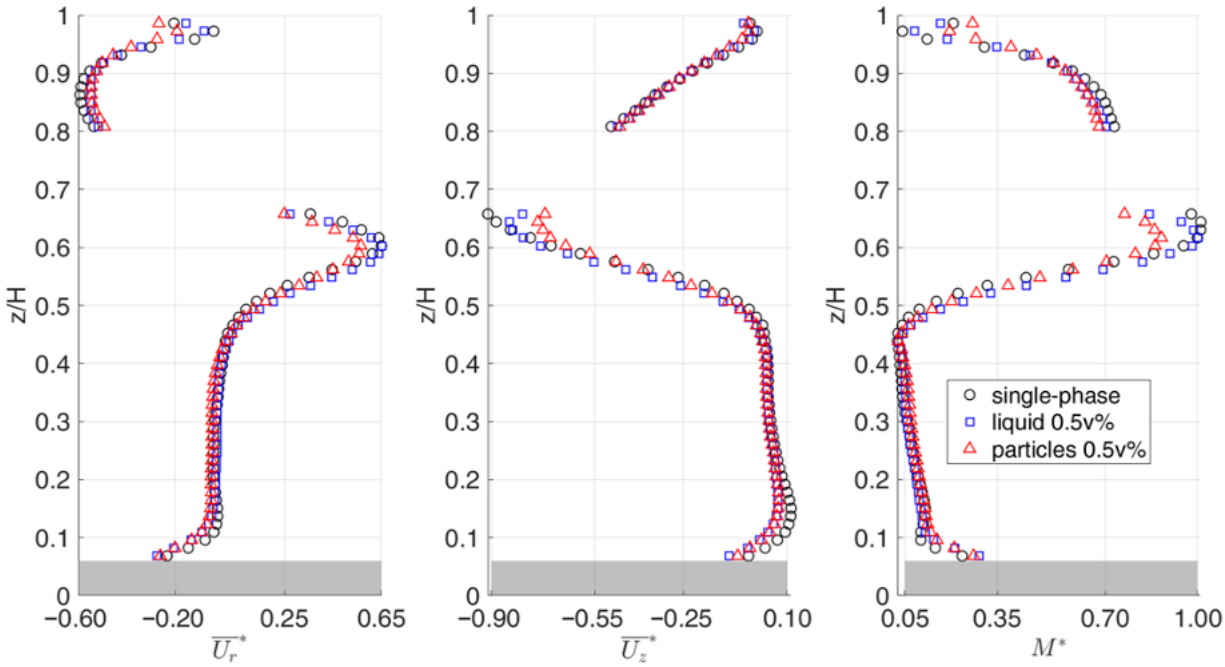

Figure 3.8: Non-dimensional mean velocity profile plots at r/T = 0.22, scaled by (ND): (**Left**) Mean radial velocity $\overline{U}_r^*$. (**Center**) Mean axial velocity $\overline{U}_z^*$. (**Right**) Mean velocity magnitude M^*. ◯: Single phase, □: Liquid phase at α_p = 0.5 v%, △: Solid phase at α_p = 0.5 v%. Gray-shaded area corresponds to tank edge; outside the measurement plane.

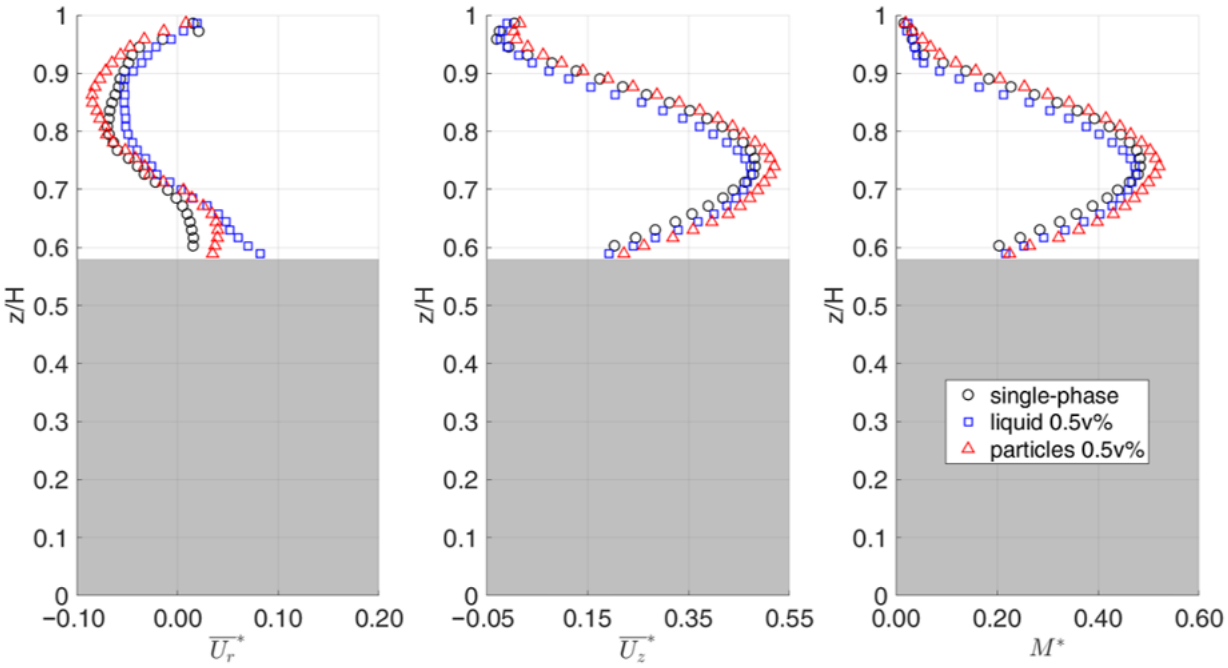

Figure 3.9: Non-dimensional mean velocity profile plot at r/T = 0.48, scaled by (ND): (**Left**) Mean radial velocity $\overline{U}_r^*$. (**Center**) Mean axial velocity $\overline{U}_z^*$. (**Right**) Mean velocity magnitude M^*. ○: Single phase, □: Liquid phase at α_p = 0.5 v%, △: Solid phase at α_p = 0.5 v%. Gray-shaded area edge; outside the measurement plane.

Moving on to the turbulence levels, more clear and obvious differences are spotted in the contour plots of Figure 3.10. The figure shows the mean turbulent kinetic energy TKE k^* of the single-phase flow (Figure 3.10a), liquid phase at α_p = 0.5 v% (Figure 3.10b) and solid phase (Figure 3.10c) at the same particle volume fraction. The TKE attains its maximum value in the flow discharge region and progressively decreases toward the wall, as expected. This covers the bottom-half of the flow circulating loop. In the last phase of the circulating loop, above the impeller, low quantities of turbulence are also depicted. When comparing the liquid phases with and without particles, the TKE just at the blade tip is consistent with a maximum value reaching $k_l^* = 0.3(ND)^2 \approx 0.03V_{tip}^2$, while in the area around it, liquid-phase turbulence with α_p = 0.5 v% has slightly higher magnitudes. As for the solid-phase turbulence at α_p = 0.5 v%, the behavior is clearly different, where TKE is much lower in the impeller vicinity compared to both liquid cases, averaging around $k_p^* = 0.2(ND)^2 \approx 0.02V_{tip}^2$, that is, 1.5 times lower than the corresponding liquid-phase peak, highlighting a visible damping effect of particle addition on solid-phase turbulence.

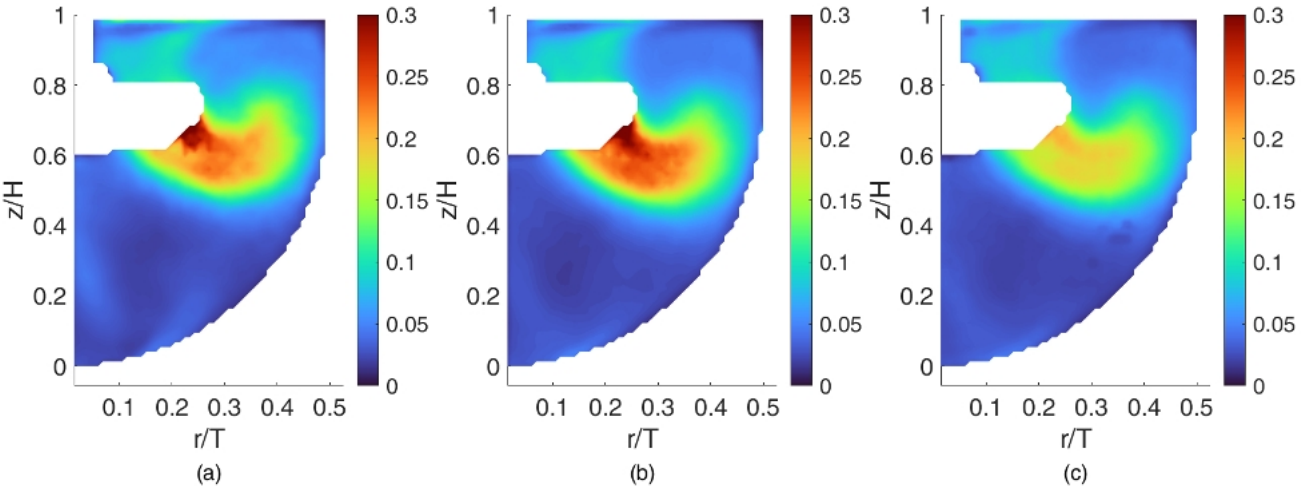

Figure 3.10: Non-dimensional mean turbulent kinetic energy TKE k^*, scaled by $(ND)^2$: (**a**) Single-phase flow, (**b**) liquid phase for α_p = 0.5 v%, (**c**) solid phase for α_p = 0.5 v%. Color-bar: $k^* = k/(ND)^2$.

In order to further analyze the observed phenomenon in the contour plots, the same approach as the flow velocity is used to compare the profile cuts at the positions mentioned previously in the scheme of Figure 3.6. These profiles are depicted in Figure 3.11 and Figure 3.12 at r/T = 0.22 and r/T = 0.48, respectively. Recall that at r/T = 0.22 is the axial cut that passes through the impeller region; Figure 3.11 shows the root mean square r.m.s. velocities of the radial (Figure 3.11 Left) and axial (Figure 3.11 Center) terms, $\overline{Urms}_r^*$ and $\overline{Urms}_z^*$, respectively, as well as the turbulent kinetic energy TKE (Figure 3.11 Right) k^*. Generally, the liquid-phase turbulence levels slightly edge over the single phase and solid phase at 0.5 < z/H < 0.65 in all examined terms. For the radial term), differences reach 12%, whereas for the axial term, liquid phase with and without particles plots are relatively coincided, and the recorded differences are around 15% higher than the solid phase. Eventually, the drop in turbulence levels between liquid phase and solid phase at α_p = 0.5 v% increases up to 30% for TKE plot in the same region 0.5 < z/H < 0.65. A minor damp is also observed for the single phase by around 10% at that position; this was observed in the contour plot of Figure 3.10 and previously established by another work [48].

On the wall side, where low levels of turbulence appear, a profile cut at r/T = 0.48 is covered in Figure 3.12. The radial r.m.s. velocity plot $\overline{Urms}_r^*$ (Figure 3.12 Left) highlights that the solid phase values at α_p = 0.5 v% surpass those of the single phase and liquid phase at the same concentration by 28%. This effect is drastically diminished for the axial term $\overline{Urms}_z^*$ (Figure 3.12 Center), where the three plots are almost overlapping. At last, the resulting TKE (Figure 3.12 Right) k^* reveals a 15% increase for the solid phase near the wall; however, the values at that position are very low, and thus, the difference could be considered insignificant.

To examine the extent of the change in turbulence levels in the impeller region, a local average area is outlined. The idea is to spatially average the TKE in that region of interest, instead of showing several profile plots. This allows us to trace any possible effect over the particle volume fractions examined. The position of this area/box is depicted in Figure 3.6. The results shown in Figure 3.13 are the locally averaged TKE k^* values as a function of particle loading α_p for both carrier and dispersed phases. As previously reported, a 10% increase in turbulence is noticed for the liquid phase, from particle-free to α_p = 0.5 v%. This slight augmentation starts at α_p = 0.4 v%, while it is the same levels of turbulence for other cases. Conversely, TKE values decline substantially between α_p = 0.1 v% and 0.5 v% by 25% in the impeller region. Upon comparing both phases, it is noticeable that at α_p = 0.1 v%, particle turbulence is marginally higher than that of the liquid part, within the experimental deviations. Increasing the volume fractions to α_p = 0.2–0.3 v% diminishes any variations, while from α_p = 0.4–0.5 v%, the liquid phase possesses higher values, as seen previously, with differences being 12% and 30%, respectively, in that region.

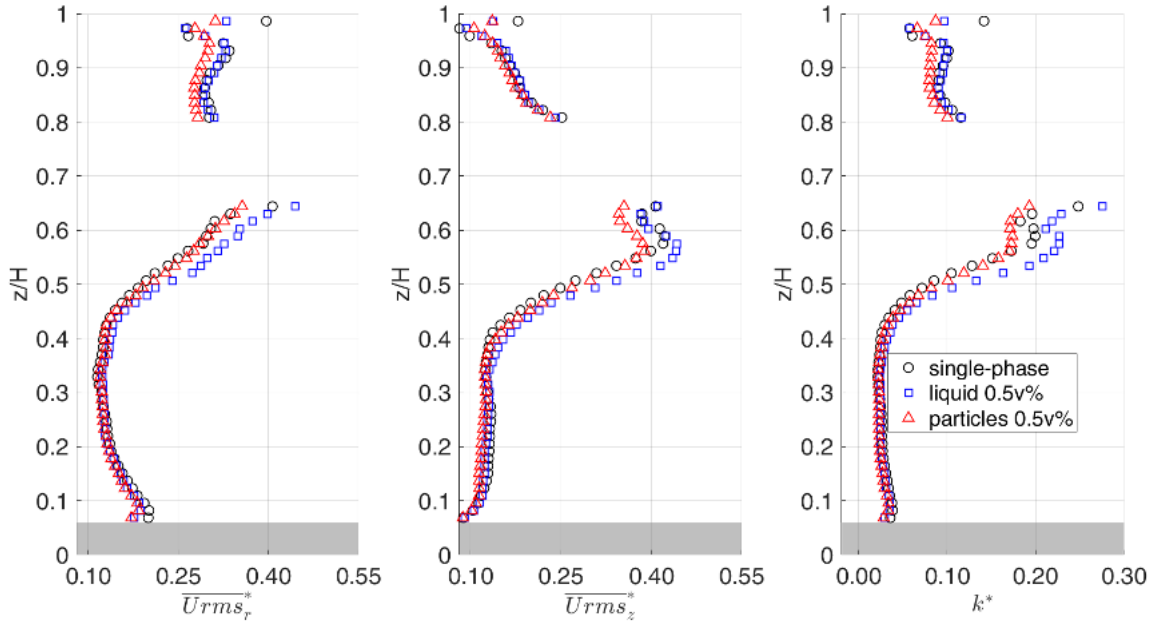

Figure 3.11: Non-dimensional turbulence terms profile plots at r/T = 0.22, scaled by $(ND)^2$: (**Left**) Mean radial r.m.s. velocity $\overline{Urms}^*_r$. (**Center**) Mean axial r.m.s. velocity $\overline{Urms}^*_z$. (**Right**) Turbulent kinetic energy TKE k^*. ◯: Single phase, □: Liquid phase at α_p = 0.5 v%, △: Solid phase at α_p = 0.5 v%. Gray-shaded area corresponds to tank edge; outside the measurement plane.

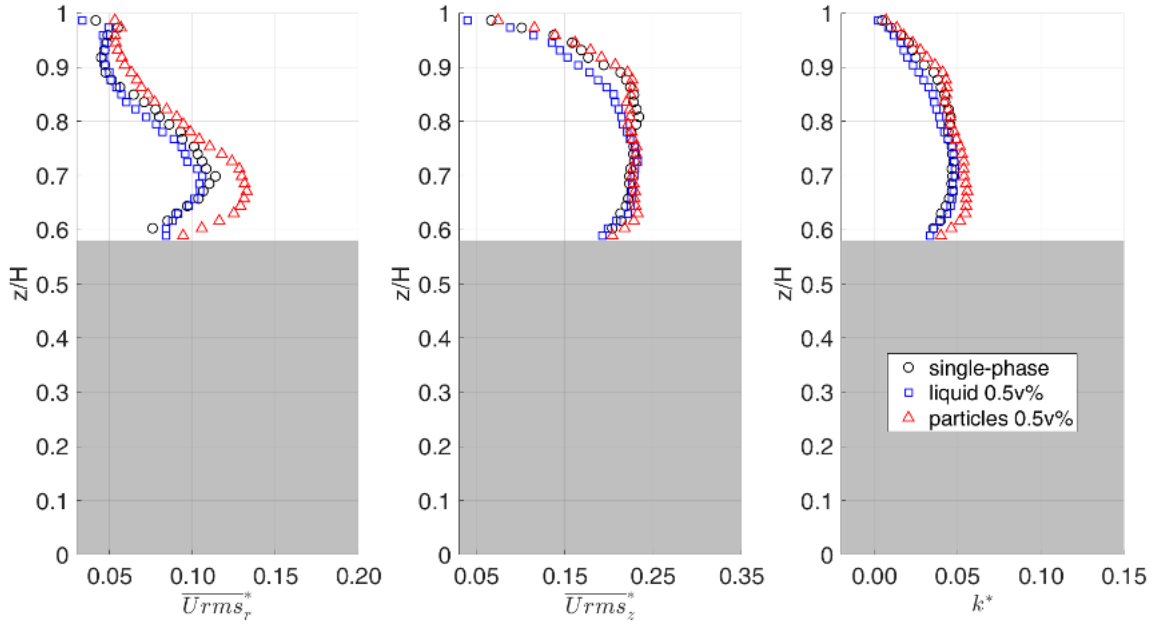

Figure 3.12: Non-dimensional turbulence terms profile plot at r/T = 0.48, scaled by $(ND)^2$: (**Left**) Mean radial r.m.s. velocity $\overline{Urms}^*_r$. (**Center**) Mean axial r.m.s. velocity $\overline{Urms}^*_z$. (**Right**) Turbulent kinetic energy TKE k^*. ◯: Single phase, □: Liquid phase at α_p = 0.5 v%, △: Solid phase at α_p = 0.5 v%. Gray-shaded area corresponds to tank edge; outside the measurement plane.

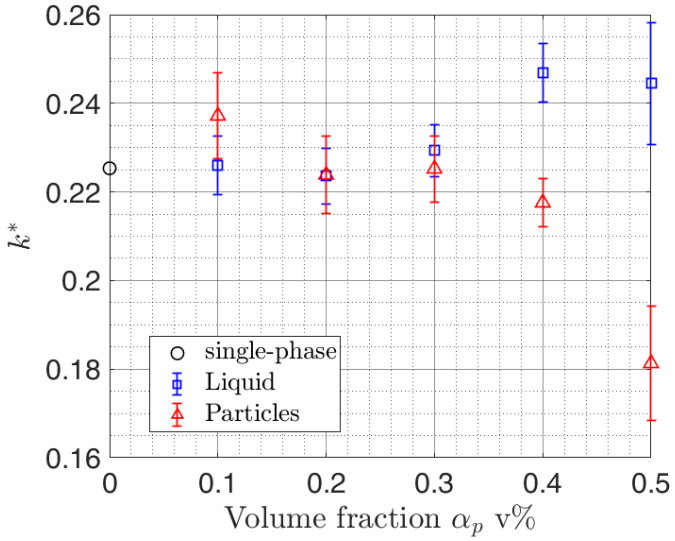

Figure 3.13: Local average of non-dimensional turbulent kinetic energy TKE k^* scaled by $(ND)^2$; it is averaged in the area/box depicted in Figure 3.6 in the impeller region, as a function of different volume fractions α_p v%. ◯: Single phase, □: Liquid phase, △: Solid phase.

Interestingly, one can replot a comparative axial profile cut at r/T = 0.22 between the standout cases. Figure 3.14 reveals the ratio of TKE of the solid phase to that of the liquid phase k^*_p/k^*_l for α_p = 0.1, 0.4 and 0.5 v%. For reference, a solid vertical line is also shown as a unity. For α_p = 0.1 v%, the ratio k^*_p/k^*_l is generally higher than 1, and it could reach 1.2–1.4 times in the impeller stream, only to drop to 0.95 at 0.4 < z/H < 0.6. However,

at α_p = 0.4 and 0.5 v%, the ratio k_p^*/k_l^* is always lower than 1, varying around 0.85. At 0.4 < z/H < 0.6, the TKE ratio drops even lower for α_p = 0.5 v% to reach 0.5. This means that TKE of the dispersed phase drops 50% compared to that of the liquid phase in this segment. Few researchers revealed the same response of particles in terms of turbulence levels. Unakdat et al. [50] noticed a drop in r.m.s. intensities with increasing volume fractions (at α_p = 0.5 v%). Sommer et al. [52] also reported a drop in the turbulence levels of the solid phase, with values always lower than that of the liquid phase (at α_p = 0.1 v%), whereas Virdung and Rasmuson [49] observed an opposite pattern, where turbulence levels for both solid and liquid phases increased with the addition of particles (at α_p = 1.5 v%).

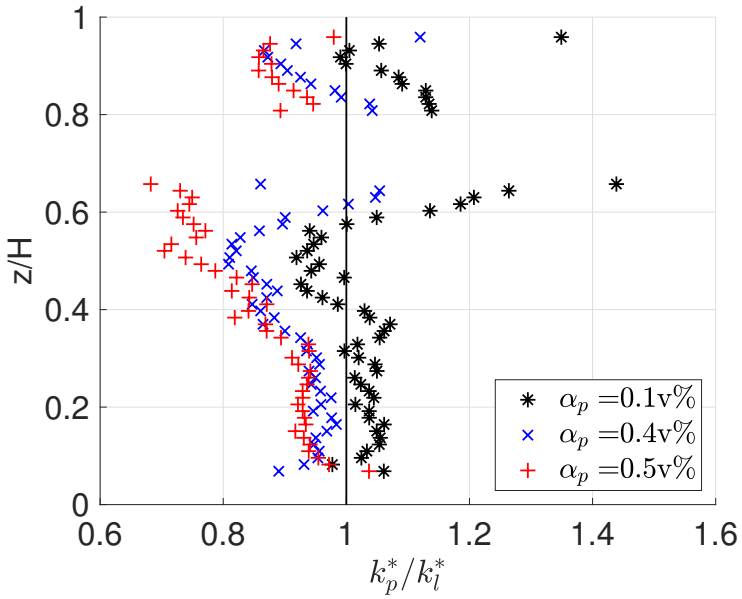

Figure 3.14: Ratio of particle-to-liquid turbulent kinetic energy TKE k_p^*/k_l^* profile plot at r/T = 0.22. ∗: α_p = 0.1 v%, ×: α_p = 0.4 v%, +: α_p = 0.5 v%.

3.3.2 Slip Velocity

As discussed previously, the slip velocity quantifies the relative motion between the dispersed particles and the carrier fluid. In this section, we present the differences in slip velocity values, which could be further influenced by the vector orientation of each phase in the 2D vertical plane. In some areas, mainly in the impeller, wall, and bottom regions, few distinctions are noticed in terms of angle deviations between the velocity vectors of each phase, which can be referred to in Figures A.3.2 and A.3.3 (see Appendix). In Figure 3.15, the slip velocity divided by the terminal velocity of particles in still liquid U_s/U_t is shown as a contour plot. The first row represents the case α_p = 0.1 v%, while the second corresponds to the case α_p = 0.5 v%. Column-wise, from left to right, the contours are listed as radial, axial, and magnitude, respectively. The effect of increasing the particle loading is then discussed for each term. Note that the value of U_t is estimated from independent settling

experiments following Delafosse et al. [56]; the resulting value is around 6.5×10^{-4} m/s.

For the radial term, an interesting behavior is noticed in the impeller region, from $\alpha_p = 0.1$ v% (Figure 3.15a) to $\alpha_p = 0.5$ v% (Figure 3.15d). In Figure 3.15a, in the impeller region, specifically at 0.5 < z/H < 0.7 and 0.2 < r/T < 0.3, radial slip velocity is split into a positive sign reaching $10U_t$ in the upper area and a negative sign in the lower area around $-5U_t$. Recall that the biggest impact is near the center of the circulating loop, where lower velocities exist (Figure 3.7). Nevertheless, the particle leads radially in that region toward the wall and lags behind the liquid phase below that area. Regarding Figure 3.15d, the phenomenon is almost diminished; the positive sign region near the center of the loop drops to $1.5U_t$, whereas in the region corresponding to the flow stream, the radial slip velocity increases to $-10U_t$. It is worth mentioning that near the surface, at z/H $\approx$ 1, high radial slip velocities are found, which could be attributed to some experimental deviations there. Globally, for both cases, the radial slip velocity varies between $-U_t$ and U_t.

Concerning axial slip velocities for $\alpha_p = 0.1$ v% and 0.5 v%, the corresponding contour plots are shown in Figure 3.15b and Figure 3.15e, respectively. Visually, the effect of rising particles concentration is clearer in the impeller stream zone. An increase in axial slip velocity is observed up to $-10U_t$, as well as an increase in the area. That is, the axial slip also increased with increasing particle concentration. Markedly, the negative sign means that particles are slower in the impeller flow stream than the carrier fluid. In contrast, near the wall where upward flow takes place, particles deviate faster from the wall to the domain than the fluid, especially with $\alpha_p = 0.5$ v%. A further discussion on this matter follows shortly thereafter. Overall, similar to the case of the radial term, the axial slip velocities shift between $-U_t$ and U_t.

In Figure 3.15c and Figure 3.15f, the slip velocity magnitude is displayed, which combines both axial and radial slip terms, for $\alpha_p = 0.1$ v% and 0.5 v%, respectively. An increase in the mean slip velocity is noticed with the increase in particle volume fractions, specifically in the impeller and wall zones. This is in agreement with Sardeshpande et al. [66] who demonstrated the same trend of slip velocity data as a function of particle concentration.

Arguably, some studies detected an inverse behavior to the one reported by our study, where particles lead the fluid phase in the downward-accelerating flow and lag behind in the upward stage, such as Nouri and Whitelaw [53], Virdung and Rasmuson [49], and Montante et al. [45] in their experimental point of view, as well as Ljungqvist and Rasmuson [67] who mentioned that the computational model always predicts that the particles move downwards more rapidly and upwards more slowly than the fluid phase. The possible explanation for this could be due to the inertia of particles. However, in their experimental data, Ljungqvist and Rasmuson [68] also mentioned that the opposite situation occurs in some parts of the tank. Other authors who reported that the particles are slower

in the downward flow and faster in the upward flow with respect to the fluid phase are Giraud et al. [69], Sardeshpande et al. [66], and Sommer et al. [52], who noticed that the particle axial velocity was lower than the liquid mean flow velocity above and below the impeller. Since the particles were not fully suspended in the system, the overall decrease in particle axial velocity could be attributed to the sedimentation of particles. It should be noted that for all the studies mentioned, the particle size used is on average 4–9 times greater than the PMMA microparticle size, and the density ratio between both phases is $\rho_p/\rho_l \gg 1$ much greater than $\rho_p/\rho_l \approx 1$ used in this study.

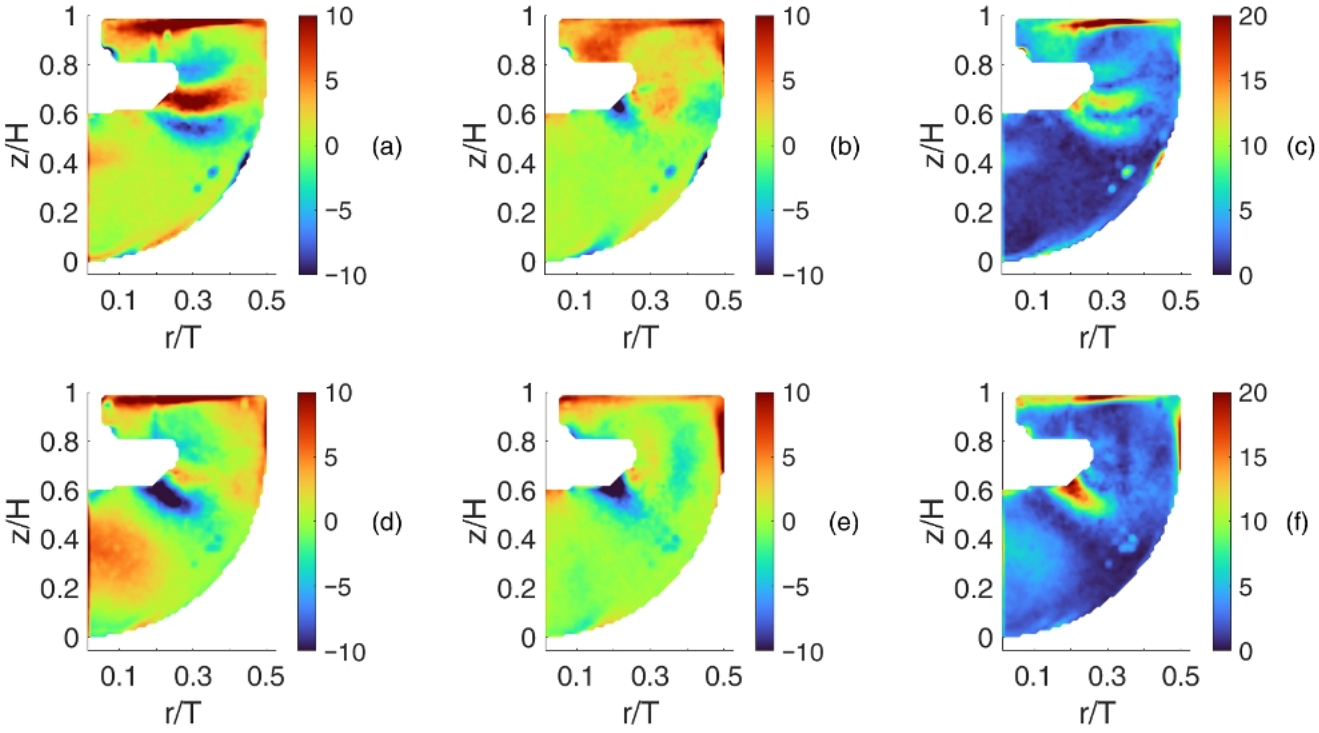

Figure 3.15: Non-dimensional mean slip velocity data scaled by terminal velocity U_s/U_t for $\alpha_p = 0.1$ v% (1st row) and $\alpha_p = 0.5$ v% (2nd row). Column-wise: 1st column: Mean radial slip velocity $U_{s,r}/U_t$ (**a**) $\alpha_p = 0.1$ v%, (**d**) $\alpha_p = 0.5$ v%. 2nd column: Mean axial slip velocity $U_{s,z}/U_t$ (**b**) $\alpha_p = 0.1$ v%, (**e**) $\alpha_p = 0.5$ v%. 3rd column: Mean slip velocity magnitude U_s/U_t (**c**) $\alpha_p = 0.1$ v%, (**f**) $\alpha_p = 0.5$ v%. Color-bar: U_s/U_t.

Accordingly, additional comparisons with correlations from the literature are invoked for a more valid analysis. One is the correlation previously demonstrated by Pinelli et al. [70] and a suggested modification by Fajner et al. [71] to include the effect of the density difference between the dispersed and carrier phases and some adjustments to the correcting terms

$$\frac{U_s}{U_t} = 0.6 + 0.32 \tanh\left[19 \frac{\eta}{d_p}\left(\frac{\rho_p - \rho_l}{\rho_l}\right)^{0.5} - 1\right] \tag{3.1}$$

where η is the Kolmogorov length scale, and U_s and U_t are the settling velocities in turbulent and quiescent fluids of the empirical model, respectively. Note that U_s in definition, is

referred to as the slip velocity, which is essentially the effective settling velocity of the particle in a turbulent fluid. Another correlation proposed by Lane et al. [72] where the effect of turbulence on the drag coefficient was correlated in terms of Stokes number

$$\frac{U_s}{U_t} = 1 - 1.4\, St^{0.7} \exp(-0.6\, St) \tag{3.2}$$

The Stokes number St used in their model relates the particle relaxation time to the integral time scale of the carrier fluid and not to the Kolmogorov time scale. The key parameter between the two models is that Equation (3.1) depends on the length scale ratio (η/d_p) of the domain, whereas Equation (3.2) contains the time scale ratio (St), which permits more valid comparisons. Note that the required characteristic scales of the system, i.e., the Kolmogorov length scale and the integral time scale, were estimated from the mean power dissipation based on the impeller power number (Np = 0.67 [73]).

Aside from the impeller and wall regions where high differences appeared, both radial and axial slip velocities are in good agreement with the proposed correlations. The spatial average for the radial and axial slip velocities divided by the terminal velocity U_s/U_t of the experiments leads to 0.7 and 0.85, respectively, for both α_p = 0.1 v% and 0.5 v%. Even when the domain is averaged, including the high-slip-velocity zones, the total average increases to U_s/U_t = 0.9 and 1.1 for radial and axial terms, respectively. On the other hand, the correlations would predict 0.92 and 0.96 for Equation (3.1) and Equation (3.2), respectively. This suggests that U_s/U_t, on average, is less than unity. Taking into account exclusively the impeller zone, the slip velocity is higher than the values predicted by the literature, which could be attributed to the acceleration phase experienced by the particles.

Previous authors reported high slip velocities in the impeller region for different radial and axial flow geometries. In the experiments of Montante et al. [45], they noticed the same order of slip velocity in the high-accelerating-flow zone $U_s/U_t > 10$. Within the realm of CFD work and validation, Derksen [74] observed a dominance of high slip velocity in the impeller zone, and all drag models used were able to capture this behavior. Ljungqvist and Rasmuson [67] found that the enhanced drag model utilized [75], which accounts for free-stream turbulence, resulted in a severe underestimation of radial and tangential slip velocities and overestimation of the axial slip, whereas Sardeshpande et al. [66] indicated that drag correlation proposed by Brucato et al. [75] overpredicted experimental axial slip velocity near the impeller region. Consequently, it was more appropriate to use the measured local slip velocity to evaluate and modify different interphase drag correlations.

3.3.3 Contributing Forces

Furthermore, the slip velocity data obtained from the experiments are incorporated into the force balance equation (Equation (3.3)) of a single spherical particle, suspended in an unsteady and non-uniform flow field [76, 77]. The tentative evaluation of the contributing forces was only approached experimentally by Montante et al. [45]. As the authors explained, various assumptions were made: the contribution of the tangential velocity component, wall interactions, shear rate forces, and the effect of the rotation of particles are not considered. Thus, the scalar force balance equation in the vertical direction z using the mean velocity data can be approximated as follows:

$$-\rho_p \overline{U}_{p,z} \frac{d\overline{U}_{p,z}}{dz} + \rho_l \overline{U}_{l,z} \frac{d\overline{U}_{l,z}}{dz} - F_M - F_L - F_D - \left(\rho_p - \rho_l\right) g = 0 \tag{3.3}$$

$$\begin{cases} F_M = \rho_l C_M \left(\overline{U}_{p,z} \dfrac{d\overline{U}_{p,z}}{dz} - \overline{U}_{l,z} \dfrac{d\overline{U}_{l,z}}{dz} \right), \\ F_L = \rho_l C_L \left(\overline{U}_{p,r} - \overline{U}_{l,r} \right) \left(\dfrac{d\overline{U}_{l,r}}{dz} - \dfrac{d\overline{U}_{l,z}}{dr} \right), \\ F_D = \dfrac{3}{4} \rho_l \dfrac{C_D}{d_p} \left(\overline{U}_{p,z} - \overline{U}_{l,z} \right) \left| \overline{U}_{p,z} - \overline{U}_{l,z} \right| \end{cases}$$

From left to right, the contributing forces are particle inertia, liquid pressure gradient, virtual added mass, lift, drag, and finally the combination of gravity and buoyancy forces. The equation is divided by the unit volume of a single particle; thus, the unit of forces is N/m^3. The coefficients C_M, C_L and C_D represent the added mass, lift, and drag, respectively. The particle lift coefficient is based on Saffman correlation only, since PIV cannot provide information on the rotation of particles, while particle drag coefficient is based on the Oseen model [78]. The various estimated terms of the force balance equation are approximate, yet valuable insights are obtained for a better understanding of the system.

Figure 3.16 shows the contributions of the different forces in the approximate scalar equation for the case $\alpha_p = 0.5$ v%. The terms are listed as in (Equation (3.3)), starting with particle inertia, then fluid pressure gradient, added mass, and lift force. These terms are found in the first row of the figure as they share the same scale. In the second row, the drag force, which is higher than the rest, is found alongside the total sum of the forces, i.e., Equation (3.3) per se. Note that the sign of each term in the equation (+ve or −ve) is also added to the graphs.

Regarding particle inertia and fluid pressure gradient presented in Figure 3.16a and Figure 3.16b, respectively, they are closely identical. The significance of these two terms

is spotted in the four phases of the circulating loop: acceleration phase in the impeller vicinity, the start of the upward movement near the wall, the second phase of the upward flow, and the end phase on top of the impeller. The values are around 1000 and −1000 N/m^3, which is three times less than lift force effect.

The virtual mass force (added mass) shown in Figure 3.16c has no contribution to the domain, as the map is almost nil everywhere. This phenomenon is expected, especially for a system with microparticle size and density that is highly close to the carrier fluid.

As for the lift force depicted in Figure 3.16d, it is dominant in the impeller and wall regions, where vorticity and radial slip velocity act mainly. Note that the lift term could be highly approximated, since the tangential component is unknown; this leads to the approximation of the vorticity term and eventually only the axial lift force is evaluated. In addition, there is no information on the rotation of microparticles, i.e., particle angular velocity, which is impossible to measure using PIV. This information would further contribute to the lift force (Magnus force [74]). The effect of lift and added mass is often ignored and reported to have no considerable contribution to solid–liquid hydrodynamics in stirred tanks, with a positive constant coefficient used, which is $C_L = 0.5$, and the lift force is much smaller than the drag force [67, 79, 80]. This coefficient value is valid for free-slip spheres, but likely inapplicable for no-slip surfaces, as the lift generation mechanisms are fundamentally different [81]. Moreover, Derksen [74] mentioned that the flow in a stirred tank is very inhomogeneous, making it difficult to estimate a priori if forces, such as lift, play an important role. That being said, the assessed lift force, using the Saffman coefficient C_L, is three times higher than that of particle inertia and fluid pressure gradient, varying between −2000 and 3000 N/m^3.

On the other hand, the estimated drag force is 3–5 times higher than that of the lift force, as can be seen in Figure 3.16e. This effect was noticed by Montante et al. [45], but with one order of magnitude higher than the lift force. Note that the authors estimated the drag force using the Schiller and Naumann standard base drag model [82], which was in turn modified by adapting the average of Equation (3.1). For that reason, and since the particle Reynolds number in this work is $\mathrm{Re}_p < 3$ (Figure A.3.4 in Appendix), the choice of Oseen's drag coefficient is adapted [78] instead of Schiller and Naumann (for $\mathrm{Re}_p < 1000$). The main regions of drag are in the impeller region and near the wall, where the high axial slip velocity dominates, ranging between −10,000 and 10,000 N/m^3.

The total sum of the forces of Equation (3.3) in the axial direction is finally presented in Figure 3.16f. Noticeably, the sum is far from nil in the impeller discharge and the wall region, where turbulent dispersion forces and wall interactions are missing from the equation, which are important for modeling multiphase flows, and, hence, the evaluated drag force prevails, whereas in the bulk of the tank, the sum varies around zero and the

equation is satisfied. For flows near the wall region, Sommerfeld et al. [83] reported that a drag enhancement may occur in that region and another study by Shi and Rzehak [84] found that a wall-lift force effect was presented and directed away from the wall. It is important to bear in mind that the equation remains a tentative approximation, as the absence of data on the tangential term, as well as the hypothesis of steady flow, further contribute to the mismatches. Montante et al. [45] also reported the same phenomenon in their experimental attempt, also stating that the scalar Eulerian information was adopted for the estimate of Lagrangian terms.

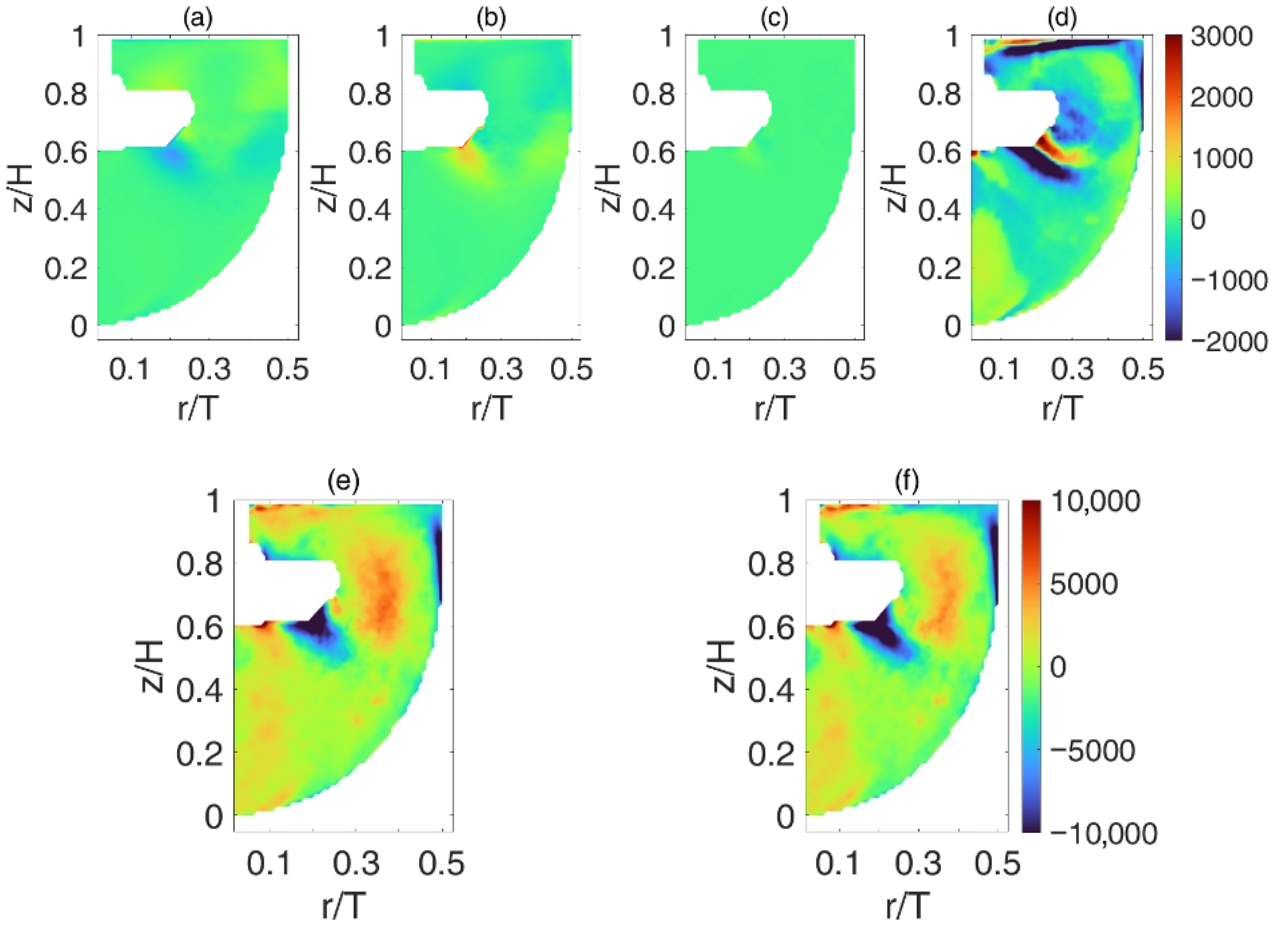

Figure 3.16: Contour plot of the axial force balance terms and the total sum of Equation (3.3) for α_p = 0.5 v%. 1st row: Unified scale/color-bar (**a**) inertia (**b**), pressure gradient (**c**), added mass (**d**), lift force. 2nd row: Unified scale/color-bar (**e**) drag force (**f**), total sum of Equation (3.3). The associated sign of each term (−ve or +ve) inside the balance equation is embedded within the contour plot. Color-bar: N/m^3

Drag models have been extensively studied in the literature and embedded in computational tools, where it has been proven necessary to include the effect of turbulence on the modeling of drag force in stirred tanks [85]. The appreciable effect of turbulence on the mean drag force resulted in various correlations that depend on the characteristic time and length scales of the domain. The review by Balachandar and Eaton [86] indicates that multiple mechanisms operate and various phenomena emerge under particular conditions;

nevertheless, a full comprehensive understanding has not yet been reached. Equations (3.1) and (3.2) are examples, and several others can be found in the review by Shah et al. [85]. Since PIV resolution cannot provide information on the Kolmogorov scales, the use of some empirical drag models is only limited to the mean dissipation from power number equation, and, thus, only averaged values are resolved instead of local maps, as approached by Montante et al. [45].

The debate on which correlation adequately fits the slip data could be rather treated with CFD as a future endeavor, as approached by Sardeshpande et al. [66]. Since the ratio of $U_s/U_t > 10$ in the impeller discharge zone, it is important to pay attention to the turbulence intensity quantified there. Recently, Shi and Rzehak [87] highlighted that the use of the drag modification factor from Lane et al. (Equation (3.2)) resulted in a significant impact of the lift force on the results. Hence, for any CFD validation, a complete model is suggested to account for possible effects of lift, virtual mass, turbulent dispersion, and any modified drag force.

3.4 Conclusions

A dual-camera particle image velocimetry PIV (2D-2C) technique has been used to map the hydrodynamics of microparticles PMMA suspension of $0.1 \leq \alpha_p \leq 0.5$ v% in an axial mixing stirred tank. The tank is a physical analog of the bioreactor used to culture stem cells within the imposed configuration [88]. Thus, the system has unique specific properties that match the world of stem cell culture: microparticles of microcarrier size $d_p = 168$ µm and a highly close density between the dispersed and carrier phases $\rho_p/\rho_l \approx 0.96$. The simultaneous measurements of both phases allow one to track the effect of particle loading on mean flow, turbulence, slip velocities, and a tentative evaluation of interfacial forces.

The mean flow remained quasi-invariant with the addition of particles, with a slight 10% shift in momentum between single phase and $\alpha_p = 0.5$ v% of the liquid phase. However, solid-phase velocities were slower than those of single phase and carrier phase at the same concentration $\alpha_p = 0.5$ v% (approximately 20% in the impeller discharge zone). It was also noticed that, for solid phase, mean flow structure (circulating loop) differed between $\alpha_p = 0.1$ v% and 0.5 v%.

Turbulence levels were found to diverge sharply between both phases. In the impeller discharge, liquid-phase turbulent kinetic energy TKE rose modestly (10%) from single phase to $\alpha_p = 0.5$ v%, while the solid-phase TKE fell by 25% in that region, and reached up to 50% at maximum levels. The TKE ratio between particles and liquid phases revealed that for $\alpha_p = 0.1$ v%, particles possess slightly higher turbulence. The ratio then decreased

drastically at α_p = 0.5 v% so that the liquid-phase turbulence was 50% higher than that of the solid phase. Near the wall, where turbulence levels are low, the radial r.m.s velocities of the solids were approximately 30% higher than those of the liquid phase, but the differences became marginal on the TKE side.

Analysis of the slip velocities showed that the particles lag behind the carrier phase in the impeller stream and deviate faster in the wall region. In addition, the slip velocities increased with the increase in the volume fraction of particles. Comparisons with correlations from the literature indicate good agreement, which confirms the modification of settling velocity due to the turbulence of the liquid phase, especially in the bulk of the tank. In the impeller and wall regions, slip velocities are much higher than in the bulk. Both experimental investigations [45] and numerical simulations [74] proved the extent of the high slip velocities in these regions.

In contrast to CFD tools, slip velocities were used directly to approximately evaluate the force balance equation of the particles. Using the Oseen drag coefficient, the drag force was 3–5 times higher than the lift force. Drag and lift forces were dominant in the impeller discharge and wall regions, where slip velocities are high. In the tank bulk, the tentative force balance of the particles is approximately satisfied; i.e., the sum of forces varied around zero. The review by Balachandar and Eaton [86] demonstrated that drag, lift and turbulent dispersion all vary with local strain and vortex topology. Hence, a CFD approach is necessary to compare with the present maps, by adjusting and modifying drag–lift–dispersion models [66]. This will be the next step within this research group in developing and validating further insights into the hydrodynamics for this type of stirred tank including angle-resolved measurements using a high-speed camera to enable direct comparison with the present time-averaged fields.

Supporting Information

The following supporting information can be downloaded at: https://www.mdpi.com/article/10.3390/fluids11010017/s1. Figure S1: Back-side of the tank, opposite to camera view. Dip tubes (sensors analogue) are highlighted; Figure S2: A video of the tank under N=150 rpm with PMMA microparticles. The video (gif format) is captured from the same side of the laser sheet (perpendicular to the camera field); Figure S3: Tank under N= 150 rpm with PMMA particles and laser on.

Bibliography

[1] V. Kumar, K. Nigam, *et al.*, "Multiphase fluid flow and heat transfer characteristics in microchannels," *Chemical Engineering Science*, vol. 169, pp. 34–66, 2017.

[2] J.-s. Zhang, B.-m. Qin, Y.-h. Liu, Q.-h. Li, X.-t. Zuo, C. Wang, S.-f. Yang, and Q. Liu, "Multiphase flow inside a four-strand continuous casting tundish using three types of ladle shrouds," *Journal of Iron and Steel Research International*, vol. 30, no. 6, pp. 1171–1181, 2023.

[3] Y. Zhou, D. Yin, Y. Li, J. He, and C. Zhang, "A review of crude oil emulsification and multiphase flows in chemical flooding," *Energy Science & Engineering*, vol. 11, no. 4, pp. 1484–1500, 2023.

[4] J. Kim, J. Yu, S. Lee, A. Tahmasebi, C.-H. Jeon, and J. Lucas, "Advances in catalytic hydrogen combustion research: Catalysts, mechanism, kinetics, and reactor designs," *International Journal of Hydrogen Energy*, vol. 46, no. 80, pp. 40073–40104, 2021.

[5] D. I. Wilson and Y. M. J. Chew, "Fluid mechanics in food engineering," *Current Opinion in Food Science*, vol. 51, p. 101038, 2023.

[6] S. Balachandar, *Fundamentals of dispersed multiphase flows*. Cambridge University Press, 2024.

[7] A. Prosperetti and G. Tryggvason, *Computational methods for multiphase flow*. Cambridge university press, 2009.

[8] G. H. Yeoh and J. Tu, *Computational techniques for multiphase flows*. Butterworth-Heinemann, 2019.

[9] S. Subramaniam, "Multiphase flows: Rich physics, challenging theory, and big simulations," *Physical Review Fluids*, vol. 5, no. 11, p. 110520, 2020.

[10] B. Farrar, A. Samways, J. Ali, and H. Bruun, "A computer-based hot-film technique for two-phase flow measurements," *Measurement Science and Technology*, vol. 6, no. 10, p. 1528, 1995.

[11] R. Zenit, D. L. Koch, and A. S. Sangani, "Measurements of the average properties of a suspension of bubbles rising in a vertical channel," *Journal of Fluid Mechanics*, vol. 429, pp. 307–342, 2001.

[12] S. Ceccio and D. George, "A review of electrical impedance techniques for the measurement of multiphase flows," *Fluids Engineering*, vol. 118, pp. 391–399, 1996.

[13] D. L. George, C. O. Iyer, and S. L. Ceccio, "Measurement of the bubbly flow beneath partial attached cavities using electrical impedance probes," *J. Fluids Eng.*, vol. 122, no. 1, pp. 151–155, 2000.

[14] H.-M. Prasser, D. Scholz, and C. Zippe, "Bubble size measurement using wire-mesh sensors," *Flow measurement and Instrumentation*, vol. 12, no. 4, pp. 299–312, 2001.

[15] C. Tompkins, H.-M. Prasser, and M. Corradini, "Wire-mesh sensors: A review of methods and uncertainty in multiphase flows relative to other measurement techniques," *Nuclear Engineering and Design*, vol. 337, pp. 205–220, 2018.

[16] J. Vejražka, M. Večeř, S. Orvalho, P. Sechet, M. C. Ruzicka, and A. Cartellier, "Measurement accuracy of a mono-fiber optical probe in a bubbly flow," *International Journal of Multiphase Flow*, vol. 36, no. 7, pp. 533–548, 2010.

[17] B. Hohermuth, M. Kramer, S. Felder, and D. Valero, "Velocity bias in intrusive gas-liquid flow measurements," *Nature communications*, vol. 12, no. 1, p. 4123, 2021.

[18] C. Tropea, A. L. Yarin, J. F. Foss, *et al.*, *Springer handbook of experimental fluid mechanics*, vol. 1. Springer, 2007.

[19] N. Fdida and J.-B. Blaisot, "Drop size distribution measured by imaging: determination of the measurement volume by the calibration of the point spread function," *Measurement Science and Technology*, vol. 21, no. 2, p. 025501, 2009.

[20] P. Huck, N. Machicoane, and R. Volk, "A cost-efficient shadow particle tracking velocimetry setup suitable for tracking small objects in a large volume," *Procedia IUTAM*, vol. 20, pp. 175–182, 2017.

[21] M. A. Erinin, B. Néel, M. T. Mazzatenta, J. H. Duncan, and L. Deike, "Comparison between shadow imaging and in-line holography for measuring droplet size distributions," *Experiments in Fluids*, vol. 64, no. 5, p. 96, 2023.

[22] D. Jasikova, M. Kotek, B. Kysela, R. Sulc, and V. Kopecky, "Experimental study of two-phase flow using shadowgraphy and ipi technique," *International Journal of Theoretical and Applied Mechanics*, vol. 2, 2017.

[23] M. S. Beck and R. A. Williams, "Process tomography: a european innovation and its applications," *Measurement Science and Technology*, vol. 7, no. 3, p. 215, 1996.

[24] J. Jamaludin, M. Z. Zawahir, R. A. Rahim, F. R. M. Yunus, N. M. N. Ayob, N. S. Fadzil, Z. Zakaria, M. H. F. Rahiman, *et al.*, "A review of tomography system," *Jurnal Teknologi (Sciences & Engineering)*, vol. 64, no. 5, 2013.

[25] D. Toye, P. Marchot, M. Crine, and G. L'Homme, "Modelling of multiphase flow in packed beds by computer-assisted x-ray tomography," *Measurement Science and Technology*, vol. 7, no. 3, p. 436, 1996.

[26] T. J. Heindel, "X-ray imaging techniques to quantify spray characteristics in the near field," *Atomization and Sprays*, vol. 28, no. 11, 2018.

[27] T. T. J. Heindel, "X-ray flow visualization: Techniques and applications," *Journal of Fluids Engineering*, vol. 146, no. 1, p. 010801, 2024.

[28] H. Jin, S. Yang, Z. Guo, G. He, and Z. Tong, "The axial distribution of holdups in an industrial-scale bubble column with evaluated pressure using γ-ray attenuation approach," *Chemical Engineering Journal*, vol. 115, no. 1-2, pp. 45–50, 2005.

[29] A. Shaikh, M. M. Taha, and M. H. Al-Dahhan, "Phase distribution in fischer-tropsch mimicked slurry bubble column via computed tomography," *Chemical Engineering Science*, vol. 231, p. 116278, 2021.

[30] W. Salgado, R. Dam, and C. Salgado, "Optimization of a flow regime identification system and prediction of volume fractions in three-phase systems using gamma-rays and artificial neural network," *Applied Radiation and Isotopes*, vol. 169, p. 109552, 2021.

[31] I. TECDOC, "1589, industrial process gamma tomography, final report of a coordinated research project 2003–2007," *International Atomic Energy Agency, Austria*, 2008.

[32] Z. Cui, Q. Zhang, K. Gao, Z. Xia, and H. Wang, "Electrical impedance sensors for multi-phase flow measurement: A review," *IEEE Sensors Journal*, vol. 21, no. 24, pp. 27252–27267, 2021.

[33] R. K. Rasel, S. M. Chowdhury, Q. M. Marashdeh, and F. L. Teixeira, "Review of selected advances in electrical capacitance volume tomography for multiphase flow monitoring," *Energies*, vol. 15, no. 14, p. 5285, 2022.

[34] S. Ren and F. Dong, "Interface and permittivity simultaneous reconstruction in electrical capacitance tomography based on boundary and finite-elements coupling method," *Philosophical Transactions of the Royal Society A: Mathematical, Physical and Engineering Sciences*, vol. 374, no. 2070, p. 20150333, 2016.

[35] W. Yang, "Design of electrical capacitance tomography sensors," *Measurement science and technology*, vol. 21, no. 4, p. 042001, 2010.

[36] Z. Cui, Q. Wang, Q. Xue, W. Fan, L. Zhang, Z. Cao, B. Sun, H. Wang, and W. Yang, "A review on image reconstruction algorithms for electrical capacitance/resistance tomography," *Sensor Review*, vol. 36, no. 4, pp. 429–445, 2016.

[37] K. Kiger and C. Pan, "Piv technique for the simultaneous measurement of dilute two-phase flows," *J. Fluids Eng.*, vol. 122, no. 4, pp. 811–818, 2000.

[38] W. Kosiwczuk, A. Cessou, M. Trinite, and B. Lecordier, "Simultaneous velocity field measurements in two-phase flows for turbulent mixing of sprays by means of two-phase piv," *Experiments in fluids*, vol. 39, no. 5, pp. 895–908, 2005.

[39] G. Rottenkolber, J. Gindele, J. Raposo, K. Dullenkopf, W. Hentschel, S. Wittig, U. Spicher, and W. Merzkirch, "Spray analysis of a gasoline direct injector by means of two-phase piv," *Experiments in Fluids*, vol. 32, pp. 710–721, 2002.

[40] J. Borowsky and T. Wei, "Simultaneous velocimetry/accelerometry measurements in a turbulent two-phase pipe flow," *Experiments in fluids*, vol. 41, pp. 13–20, 2006.

[41] T. Ohmoto, H. Une, and K. Adachi, "A fundamental study on the interaction between driftwood and free-surface flow in an open channel," in *International Conference on Civil, Structural and Transportation Engineering*, 2022.

[42] F. Shaffer, E. Ibarra, and Ö. Savaş, "Visualization of submerged turbulent jets using particle tracking velocimetry," *Journal of Visualization*, vol. 24, pp. 699–710, 2021.

[43] M. Zhang, M. Xu, and D. L. Hung, "Simultaneous two-phase flow measurement of spray mixing process by means of high-speed two-color piv," *Measurement Science and Technology*, vol. 25, no. 9, p. 095204, 2014.

[44] M. Elhimer, O. Praud, M. Marchal, S. Cazin, and R. Bazile, "Simultaneous piv/ptv velocimetry technique in a turbulent particle-laden flow," *Journal of Visualization*, vol. 20, pp. 289–304, 2017.

[45] G. Montante, A. Paglianti, and F. Magelli, "Analysis of dilute solid–liquid suspensions in turbulent stirred tanks," *Chemical Engineering Research and Design*, vol. 90, no. 10, pp. 1448–1456, 2012.

[46] L. Villafañe, A. Aliseda, S. Ceccio, P. DiMarco, N. Machicoane, and T. J. Heindel, "50 years of international journal of multiphase flow: Experimental methods for dispersed multiphase flows," *International Journal of Multiphase Flow*, p. 105239, 2025.

[47] M. Micheletti and M. Yianneskis, "Study of fluid velocity characteristics in stirred solid-liquid suspensions with a refractive index matching technique," *Proceedings*

of the Institution of Mechanical Engineers, Part E: Journal of Process Mechanical Engineering, vol. 218, no. 4, pp. 191–204, 2004.

[48] M. Madani, A. Delafosse, S. Calvo, and D. Toye, "Rim-piv measurements of solid–liquid flow in a stirred tank used for mesenchymal stem cell culture.," *Fluids*, vol. 10, no. 10, 2025.

[49] T. Virdung and A. Rasmuson, "Solid-liquid flow at dilute concentrations in an axially stirred vessel investigated using particle image velocimetry," *Chemical Engineering Communications*, vol. 195, no. 1, pp. 18–34, 2007.

[50] H. Unadkat, C. D. Rielly, G. K. Hargrave, and Z. K. Nagy, "Application of fluorescent piv and digital image analysis to measure turbulence properties of solid–liquid stirred suspensions," *Chemical Engineering Research and Design*, vol. 87, no. 4, pp. 573–586, 2009.

[51] D. Khalitov and E. K. Longmire, "Simultaneous two-phase piv by two-parameter phase discrimination," *Experiments in fluids*, vol. 32, no. 2, pp. 252–268, 2002.

[52] A.-E. Sommer, H. Rox, P. Shi, K. Eckert, and R. Rzehak, "Solid-liquid flow in stirred tanks:"cfd-grade" experimental investigation," *Chemical Engineering Science*, vol. 245, p. 116743, 2021.

[53] J. Nouri and J. Whitelaw, "Particle velocity characteristics of dilute to moderately dense suspension flows in stirred reactors," *International journal of multiphase flow*, vol. 18, no. 1, pp. 21–33, 1992.

[54] P. Guiraud, J. Costes, and J. Bertrand, "Local measurements of fluid and particle velocities in a stirred suspension," *Chemical Engineering Journal*, vol. 68, no. 2-3, pp. 75–86, 1997.

[55] C. Loubière, A. Delafosse, E. Guedon, I. Chevalot, D. Toye, and E. Olmos, "Dimensional analysis and cfd simulations of microcarrier 'just-suspended'state in mesenchymal stromal cells bioreactors," *Chemical Engineering Science*, vol. 203, pp. 464–474, 2019.

[56] A. Delafosse, C. Loubière, S. Calvo, D. Toye, and E. Olmos, "Solid-liquid suspension of microcarriers in stirred tank bioreactor–experimental and numerical analysis," *Chemical Engineering Science*, vol. 180, pp. 52–63, 2018.

[57] E. Stamhuis and W. Thielicke, "Pivlab–towards user-friendly, affordable and accurate digital particle image velocimetry in matlab," *Journal of open research software*, vol. 2, no. 1, p. 30, 2014.

[58] W. Thielicke and R. Sonntag, "Particle image velocimetry for matlab: Accuracy and enhanced algorithms in pivlab," *Journal of Open Research Software*, vol. 9, no. 1, 2021.

[59] S. A. Stanier, J. Blaber, W. A. Take, and D. White, "Improved image-based deformation measurement for geotechnical applications," *Canadian Geotechnical Journal*, vol. 53, no. 5, pp. 727–739, 2016.

[60] L. Sarno, A. Carravetta, Y.-C. Tai, R. Martino, M. Papa, and C.-Y. Kuo, "Measuring the velocity fields of granular flows–employment of a multi-pass two-dimensional particle image velocimetry (2d-piv) approach," *Advanced Powder Technology*, vol. 29, no. 12, pp. 3107–3123, 2018.

[61] S. Ly, A. M. Rubenchik, S. A. Khairallah, G. Guss, and M. J. Matthews, "Metal vapor micro-jet controls material redistribution in laser powder bed fusion additive manufacturing," *Scientific reports*, vol. 7, no. 1, p. 4085, 2017.

[62] U. Arya, W. Peterson, F. Sadeghi, A. Meinel, and H. Grillenberger, "Investigation of oil flow in a ball bearing using bubble image velocimetry and cfd modeling," *Tribology International*, vol. 177, p. 107968, 2023.

[63] R. Escudié and A. Liné, "Experimental analysis of hydrodynamics in a radially agitated tank," *AIChE Journal*, vol. 49, no. 3, pp. 585–603, 2003.

[64] J. Sheng, H. Meng, and R. Fox, "A large eddy piv method for turbulence dissipation rate estimation," *Chemical engineering science*, vol. 55, no. 20, pp. 4423–4434, 2000.

[65] F. Khan, C. Rielly, and D. Brown, "Angle-resolved stereo-piv measurements close to a down-pumping pitched-blade turbine," *Chemical Engineering Science*, vol. 61, no. 9, pp. 2799–2806, 2006.

[66] M. V. Sardeshpande, V. Juvekar, and V. V. Ranade, "Solid suspension in stirred tanks: Uvp measurements and cfd simulations," *The Canadian Journal of Chemical Engineering*, vol. 89, no. 5, pp. 1112–1121, 2011.

[67] M. Ljungqvist and A. Rasmuson, "Numerical simulation of the two-phase flow in an axially stirred vessel," *Chemical Engineering Research and Design*, vol. 79, no. 5, pp. 533–546, 2001.

[68] M. Ljungqvist and A. Rasmuson, "The two-phase flow in an axially stirred vessel investigated using phase-doppler anemometry," *The Canadian Journal of Chemical Engineering*, vol. 82, no. 2, pp. 275–288, 2004.

[69] P. Guiraud, J. Costes, J. Bertrand, and J. Bousquet, "Local measurements of liquid and solid velocities and of particle sizes in stirred suspensions with a phase doppler particle

analyser," in *Fluid Mechanics of Mixing: Modelling, Operations and Experimental Techniques*, pp. 145–152, Springer, 1992.

[70] D. Pinelli, M. Nocentini, and F. Magelli, "Solids distribution in stirred slurry reactors: influence of some mixer configurations and limits to the applicability of a simple model for predictions," *Chemical Engineering Communications*, vol. 188, no. 1, pp. 91–107, 2001.

[71] D. Fajner, D. Pinelli, R. Ghadge, G. Montante, A. Paglianti, and F. Magelli, "Solids distribution and rising velocity of buoyant solid particles in a vessel stirred with multiple impellers," *Chemical Engineering Science*, vol. 63, no. 24, pp. 5876–5882, 2008.

[72] G. Lane, M. Schwarz, and G. M. Evans, "Numerical modelling of gas–liquid flow in stirred tanks," *Chemical Engineering Science*, vol. 60, no. 8-9, pp. 2203–2214, 2005.

[73] J. Chéron, C. Loubière, S. Delaunay, A.-G. Guezennec, and E. Olmos, "Cfd numerical simulation of particle suspension and hydromechanical stress in various designs of multi-stage bioleaching reactors," *Hydrometallurgy*, vol. 197, p. 105490, 2020.

[74] J. Derksen, "Numerical simulation of solids suspension in a stirred tank," *AIChE Journal*, vol. 49, no. 11, pp. 2700–2714, 2003.

[75] A. Brucato, F. Grisafi, and G. Montante, "Particle drag coefficients in turbulent fluids," *Chemical Engineering Science*, vol. 53, no. 18, pp. 3295–3314, 1998.

[76] J. O. Hinze, "Turbulence 2d ed., new york," 1975.

[77] C. Crowe, J. Schwarzkopf, M. Sommerfeld, and Y. Tsuji, *Multiphase Flows with Droplets and Particles, Second Edition*. Taylor & Francis, 2011.

[78] W. Sobieski, "Drag coefficient in solid–fluid system modeling with the eulerian multiphase model," *Drying Technology*, vol. 29, no. 1, pp. 111–125, 2010.

[79] A. Ochieng and A. E. Lewis, "Nickel solids concentration distribution in a stirred tank," *Minerals Engineering*, vol. 19, no. 2, pp. 180–189, 2006.

[80] A. Khopkar, A. Rammohan, V. Ranade, and M. Dudukovic, "Gas–liquid flow generated by a rushton turbine in stirred vessel: Carpt/ct measurements and cfd simulations," *Chemical Engineering Science*, vol. 60, no. 8-9, pp. 2215–2229, 2005.

[81] D. Legendre and J. Magnaudet, "The lift force on a spherical bubble in a viscous linear shear flow," *Journal of Fluid Mechanics*, vol. 368, pp. 81–126, 1998.

[82] V. L. Schiller, "Uber die grundlegenden berechnungen bei der schwerkraftaufbereitung," *Z. Vereines Deutscher Inge.*, vol. 77, pp. 318–321, 1933.

[83] M. Sommerfeld, *Best practice guidelines for computational fluid dynamics of dispersed multiphase flows*. Ercoftac, 2008.

[84] P. Shi and R. Rzehak, "Lift forces on solid spherical particles in wall-bounded flows," *Chemical Engineering Science*, vol. 211, p. 115264, 2020.

[85] R. S. S. Raja Ehsan Shah, B. Sajjadi, A. A. Abdul Raman, and S. Ibrahim, "Solid-liquid mixing analysis in stirred vessels," *Reviews in Chemical Engineering*, vol. 31, no. 2, pp. 119–147, 2015.

[86] S. Balachandar and J. K. Eaton, "Turbulent dispersed multiphase flow," *Annual review of fluid mechanics*, vol. 42, no. 1, pp. 111–133, 2010.

[87] P. Shi and R. Rzehak, "Solid-liquid flow in stirred tanks: Euler-euler/rans modeling," *Chemical Engineering Science*, vol. 227, p. 115875, 2020.

[88] C. Sion, D. Ghannoum, B. Ebel, F. Gallo, N. de Isla, E. Guedon, I. Chevalot, and E. Olmos, "A new perfusion mode of culture for wj-mscs expansion in a stirred and online monitored bioreactor," *Biotechnology and Bioengineering*, vol. 118, no. 11, pp. 4453–4464, 2021.

Appendix

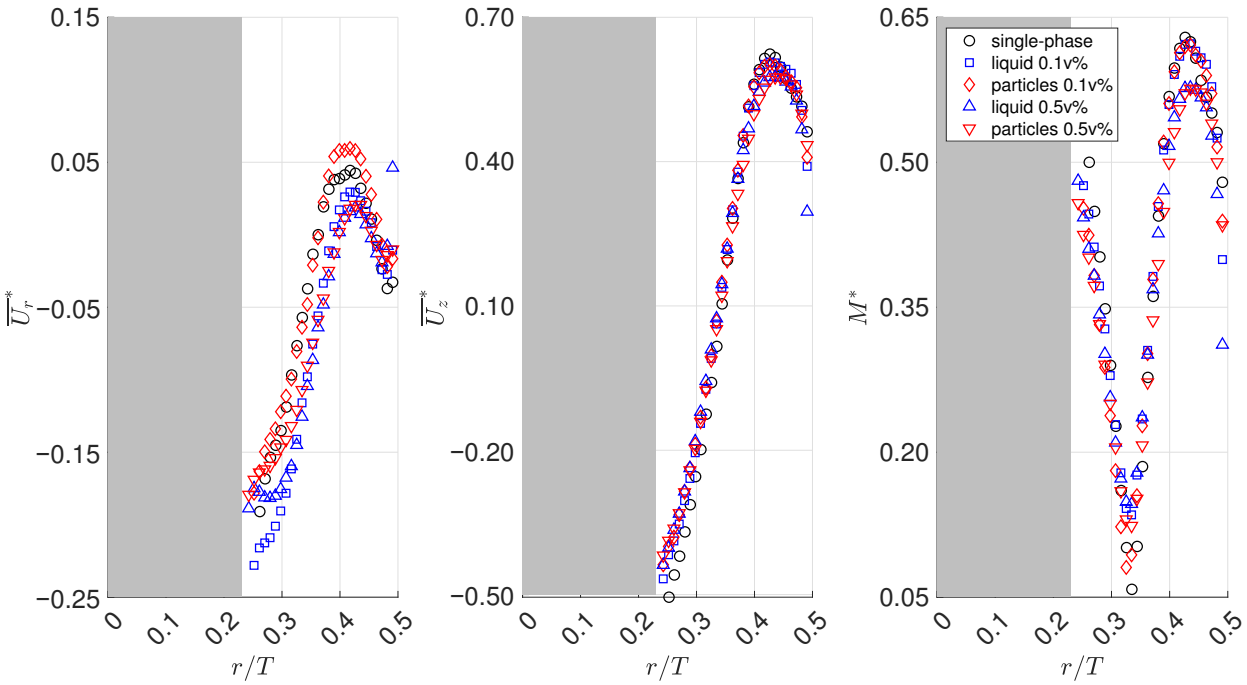

Figure A.3.1: Non-dimensional mean velocity profile plots at z/H = 0.7, scaled by (ND): (**Left**) Mean radial velocity $\overline{U}_r^*$. (**Center**) Mean axial velocity $\overline{U}_z^*$. (**Right**) Mean velocity magnitude M^*. ◯: Single phase, □: Liquid phase at α_p = 0.1 v%, ◊: Solid phase at α_p = 0.1 v%, △: Liquid phase at α_p = 0.5 v%, ∇: Solid phase at α_p = 0.5 v%. Gray-shaded area corresponds to impeller; outside the measurement plane.

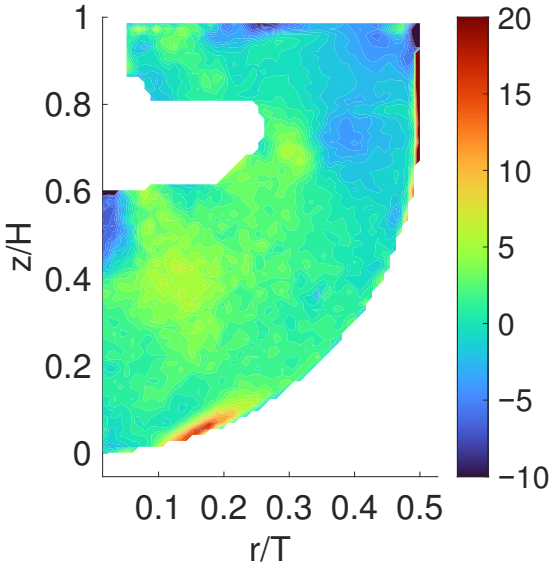

Figure A.3.2: Contour plot of mean/average angle deviations between solids and liquid velocity vectors $\Delta\theta$ in degrees °. solid-phase vectors act as a reference. +ve angle: Particle velocity vector is oriented counter-clock-wise CCW from liquid velocity vectors ↺. −ve angle: Particle velocity vector is oriented clock-wise CW from liquid velocity vectors ↻. Color-bar: $\Delta\theta$ in degrees °.

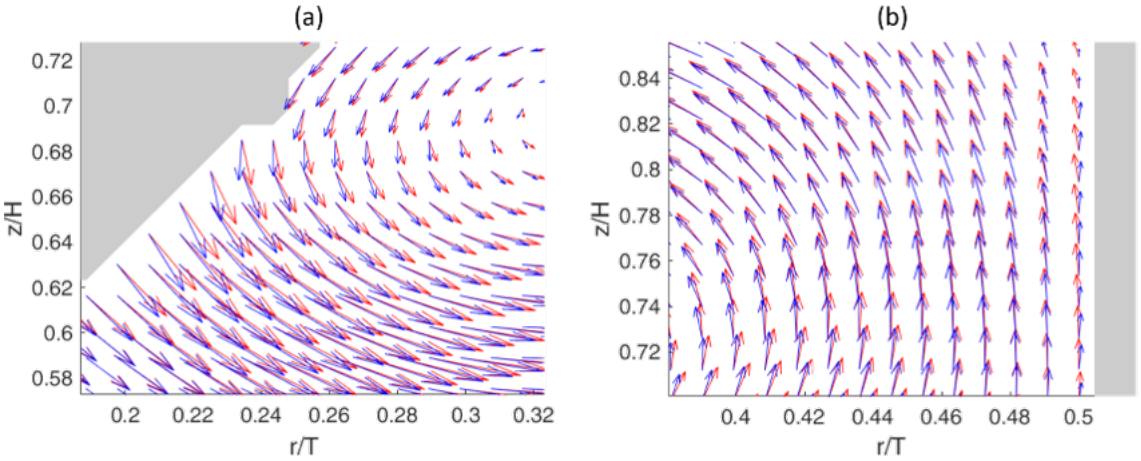

Figure A.3.3: Superimposed mean velocity vectors of solid phase (red) and liquid phase (blue): (**a**) Impeller region, (**b**) near the wall region. Case α_p = 0.5 v%.

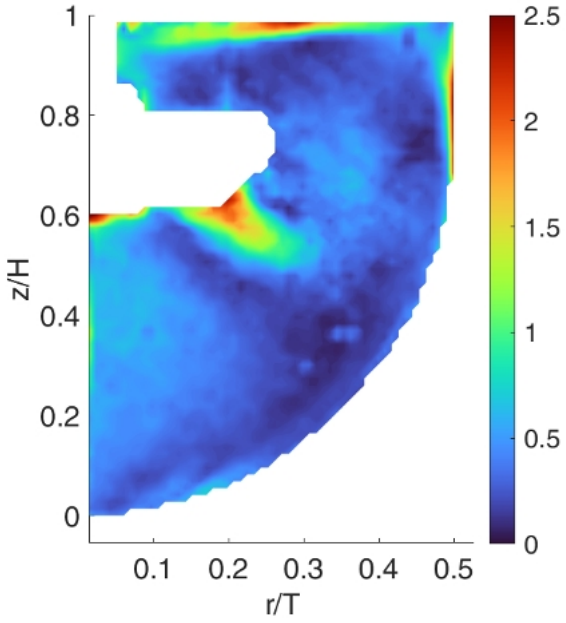

Figure A.3.4: Contour plot of particle Reynolds number Re_p at α_p = 0.5 v%.

Chapter 4

Solid-Phase Tracking and Collisions Quantification: One-Phase PTV

Abstract

In this work, the impact of inter-particle collisions as a subprocess is discussed, within a stirred tank designed and dedicated to stem cell culture. Inter-particle collisions in microcarrier-based stem cell culture are often invoked as a potential source of mechanical damage, yet they remain unquantified experimentally in stirred tanks. Here, 2D particle tracking velocimetry (PTV) is used to resolve Lagrangian trajectories of PMMA particles of diameter $d_p = 0.55$ mm suspended in a refractive index matched (RIM) Ammonium Thiocyanate solution at $N = 150$ rpm ($Re \approx 5000$). A post-processing workflow was developed to identify interacting and colliding particle pairs and to reduce ambiguities associated with 2D tracking in a 3D flow. The resulting collision database provides, for the first time in this configuration, locally resolved statistics of collision rate and frequency across various particle volume fractions $0.1 \leq \alpha_p \leq 0.7$ v%. In addition, the impact and intensity of collisions are estimated in terms of exchanged kinetic energy and collision severity. These measurements offer direct experimental insight into the collision environment in stirred tanks beyond global estimates.

4.1 Introduction

Over the past century, the study of multiphase flows represented a challenging yet fruitful area of endeavour for scientists and engineers, who, keen to model and quantify turbulence and its influence on mass, momentum, and energy transfer, have encountered manifold difficulties and ongoing debates. Briefly, multiphase flow is in principle composed of a dispersed phase and a continuous carrier fluid, which could take the forms of gas–liquid,

solid–liquid, solid–gas, liquid–liquid, and three-phase flows as gas–solid–liquid flows. It is well known that the presence of a dispersed phase influences the behaviour of the carrier fluid [1]. However, the extent of such an impact directly depends on the mass/volume/void fractions of the dispersed-phase. The increase in the load of the dispersed-phase increases the interactions with the carrier-phase. Elghobashi [2] has demonstrated that for volume fractions $\alpha_p > 0.1$v%, the momentum transfer of the dispersed-phase is not only large enough to alter the turbulence structures, but also to induce interactions among the dispersed-phase elements adding more stresses and modifications to the medium (four-way coupling). The interactions at this stage are thus of great importance for the multiphase problem. Table 4.1 illustrates the different coupling states within the multiphase elements in relation to the volume fractions [3]. Note that the "particle" term denotes solid particles, droplets, or bubbles, and particle-to-particle interactions could be in the form of collision, aggregation/flocculation, coalescence, or rupture depending on the state of the dispersed-phase.

Table 4.1: Continuous and dispersed phase interactions. Table adapted from [3].

Particle motion	**Coupling**	**Volume fraction**	**Interaction**
	One-way	Sparse $\alpha_p < 10^{-4}$v%	Continuous fluid affects particles.
			+
	Two-way	Dilute 10^{-4}v% $< \alpha_p < 10^{-1}$v%	Particles affect fluid motion.
			+
	Three-way	10^{-1}v% $< \alpha_p <$ 1v%	Fluid disturbance by a particle affects other particles locally.
			+
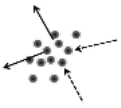	Four-way	Collision-dominated 1v% $< \alpha_p <$ 10v%	Particle collisions influence individual particle motion.
			+
	Four-way	Dense contact-dominated $\alpha_p >$ 10v%	Particles frequently remain in contact.

Collisions play a key-role in a wide range of natural occurring as well as industrial processes. For example, planetary formation based on the aggregation of dust in protoplanetary disks [4, 5] and the growth of raindrops in atmospheric clouds [6, 7], are two natural phenomena where the expression of collisions is required to understand and describe such evolutions.

Collisions are also relevant for numerous industrial applications. The aggregation of solid particles (solid–gas flow) such as the formation of soot in plug flow reactors [8, 9] and the effects of these models on optimizing the methane pyrolysis process [10], the coalescence/rupture of bubbles (gas–liquid) [11, 12] or droplets (liquid–gas or liquid–liquid) [13, 14], the efficiency of collision rates in froth flotation [15], the treatment of waste materials in clarifiers [16], in addition to food processing, and ink technologies to name a few.

Hence, researchers over the years were fully dedicated to modelling the different collisions exhibited in the various multiphase flows mentioned. These models attempt to resolve and anticipate collision rates or frequencies within the investigated medium, often referred to as collision kernels (β), i.e., number of collisions per unit volume per time. Moreover, collisions could be classified into different modes or mechanisms depending on the Stokes number St and flow regime. Starting with perikinetic (Brownian-driven), collisions are due to random Brownian motion of particles of size < 1 µm suspended in laminar flow. Smoluchowski [17] developed a collision kernel for this case assuming that diffusion dominates over convection and particle size is limited to 1 µm, while ignoring inter-particle forces and hydrodynamic interactions. Another mode is orthokinetic (shear-induced) collision, where particles of $St \ll 1$ and size limited to flow Kolmogorov scale, follow streamlines and collide due to different positions within shear flow, which could range from laminar to turbulent regimes (Figure 4.1a). The models that investigated this mechanism are those of Saffman and Turner [18], who presented a kernel based on homogeneous isotropic turbulence, and Kramer and Clark [19], who introduced the absolute strain rate field. Next, the accelerative-correlated and preferential concentration (inertial clustering) mechanisms are considered, which are similar, in which particle size is roughly matched to the Kolmogorov scale and $St \approx 1$. This means that bigger inertial particles might centrifuge out of vortices and gather in high strain rate zones (Figure 4.1b). For this, Saffman and Turner [18] extended their analysis to include particle relaxation time in the kernel to bridge shear and inertia. Subsequently, Williams and Crane [20] expressed a kernel in terms of relative fluctuating particle velocity. Sundaram and Collins [21] developed a kernel based on radial distribution function and cylindrical formulation, while Wang et al. [22] improved the latter model, considered as erroneous, using a spherical approach. Last but not least, in highly vigorous turbulent flows, large dense particles decorrelate from the fluid and each other causing collision as they are randomly projected from eddy to eddy, which is known as accelerative-independent form (Figure 4.1c). Under these circumstances, Abrahamson [23] assumed classic kinetic gas theory to establish a collision kernel based on Gaussian velocity statistics. Further discussions, limitations, and model expressions are heavily treated by Meyer and Deglon [24] in addition to the review by Shah et al. [3] who also included some comments on the models.

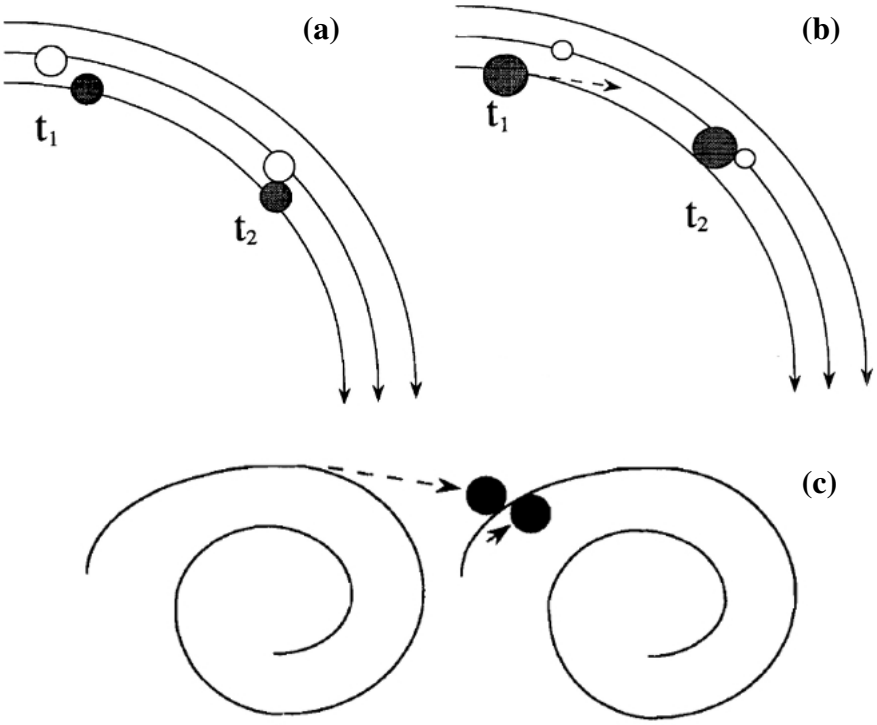

Figure 4.1: Collision mechanisms of particles. **a)** Shear-induced effect. **b)** Accelerative-correlated, inertial effect. **c)** Accelerative-independent, highly turbulent effect. The assemble of figures is adapted from [25].

In any case, the researchers mentioned above, who attempted to develop a so-called universal collision model over the entire range of particle inertias, have relied almost entirely on DNS rather than experimental data. More importantly, the models cover nearly exclusively the agglomeration of particles. That is to say, particles (solids, droplets, or bubbles) collide within the flow to form aggregates of different sizes, larger than those prior to collision. Essentially, this does not take into account rigid particle-particle collisions where particles bounce or slide against each other, and size remains basically the same. The rigid inter-particle collisions have been approached numerically (via discrete element method DEM) with two key differences to be handled. A hard-sphere approach, which is based on instantaneous momentum exchange upon contact between a pair of particles resulting in an elastic collision. The model accounts only for binary collisions with elasticity as an approximation, while ignoring attractive forces. This is considered useful for dilute granular flows with low computational demands [26]. Whereas for the soft-sphere model, particles may overlap and deform during contact, introducing a contact force that depends on material properties (stiffness and damping; spring-dashpot model) [27]. A more consolidated review on these models is reported by Deen et al. [28] on fluidized beds. Another dense review on discrete particle simulations is communicated by Zhu et al. [29], which lists extensively the progress of the numerical approach for various applications. In addition to fluidized beds, applications could be in the form of channel flow for the study of fuel-rich/lean burner [30], rotating drum/mill [31], and stirred tanks by means of a

mechanically agitating impeller [32].

In the world of stirred tanks, numerical simulations that used the discrete method to model the dispersed phase are also numerous; however, collisions are generally not the core of the study. In most cases, the use of the computationally expensive discrete method is to have a better description of the hydrodynamics of the multiphase flow to analyse the impact on mixing [33], suspension and spatial distribution of particles [34, 35], mass transfer [36] or heat transfer [37], for instance. As for models dedicated to quantifying collisions in stirred tanks, the studies are rather scarce. Derksen [38] was one of the first to report direct information and statistics on collisions in his large eddy simulation LES, where the intensity of particle-particle and particle-impeller collisions was quite comparable, while the frequency of the former was much higher than the latter. The particles were glass beads of size 0.3 and 0.47 mm with volume fractions up to α_p= 3.6 v% suspended by a Rushton turbine impeller. Particles with larger sizes had higher collisional intensities than the smaller ones due to differences in inertia. Kazemzadeh et al. [39] studied the mixing hydrodynamics of a highly dense slurry α_p> 40v% for a variety of particle sizes of $2-5$ mm in a stirred tank using electrical resistance tomography ERT and CFD. They mentioned that an increase in inter-particle and particle-equipment collisions was attained with the decrease of the off-bottom clearance C, which eventually led to higher energy loss. However, the authors did not include any collision quantification on the matter. Recently, Shuai et al. [32] modelled a continuous flow inside a stirred tank equipped with 3 impellers where coal particles of 0.25 mm size were fed at a rate of 3.73 g/s. The results show that there is a significant interrelationship between the total number of collisions and the total number of particles simulated on the basis of a proposed fitting equation. The average collision duration was longer away from the inlet, where the velocities are lower in that region. They also mentioned that the particles collided strongly with the baffles inside the mixing tank. Kang et al. [40] studied the drawdown process of floating particles inside a turbulent stirred tank for up-pumping and down-pumping bitched blade impellers via DEM-VOF method. The particle diameter ranged from 0.5 to 1.5 mm with volume fractions up to α_p= 6.5v%. Increasing the particle number (volume fractions) and particle diameter resulted in an increase in the number of particle–particle collisions, with up-pumping mode inducing more collisions. Additionally, it was found that particle-particle collisions led to a shorter drawdown time.

The use of numerical models is inherently linked to validation against experimental data, which promotes exploration and refinement of the models under study in an effort to optimize the process. However, acquiring experimental data depends on the property to be measured, which often represents a challenge in multiphase flows. Several measurement techniques were listed and discussed in Chapter three [41]. Although, Eulerian techniques like PIV are established for characterizing general flow fields, they are often insufficient

for quantifying discrete particle–particle interactions. Consequently, particle tracking velocimetry PTV is considered a useful, low-cost, and safe-to-operate tool. PTV has been widely used and established to characterize flow, in a Lagrangian field, for wide applications, including impinging jets [42], pipe flows [43, 44], flows through porous media [45], fluidized beds [46, 47] and stirred tanks [48, 49, 50]. Nevertheless, such characterizations are limited to flow velocity and turbulence in the case of stirred tanks, e.g., average flow field, fluctuating components, shear rate, and energy dissipation, where validations and comparisons with the PIV technique are studied. The need for a comparison between both techniques arises from the fact that most of the quantities mentioned are Eulerian-based [49]. It is worth noting that the tracked particles in these cases are the tracers representing the carrier-phase and not the dispersed-phase particles. Whereas in other flow applications, such as pipe flows [44] and fluidized beds [46, 47], studies were dedicated to quantifying collisions. The main constraint in stirred tanks is the complexity of the flow, as the agitation provided by the impeller (whether axial, radial, or mixed flow) makes it difficult to follow the dispersed particles to account for collisions as opposed to the flow mechanism in pipes or fluidized beds (mainly 2D).

Beyond that, previous research used positron emission particle tracking (PEPT) as well as computer automated radioactive particle tracking (CARPT) techniques to obtain the Lagrangian flow field in a stirred tank. PEPT is mostly used for opaque flows and involves labelled tracer that emits back-to-back gamma rays γ, a positron camera and a location algorithm to compute the tracer location [51]. Examples include the determination of two-phase flow field, spatial phase distributions, and slip velocities for high slurry concentrations (>20v%) [52, 53], or in-depth validation with laser techniques (PIV, LDA) [54]. Similarly, CARPT utilizes gamma rays γ from a buoyant tracer and an array of external detectors to reconstruct 3D velocity fields and turbulence statistics in opaque multiphase systems. Guha et al. [55] studied the flow field of particles in dense solid–liquid suspensions (2.5 – 19 v% concentration) inside a stirred tank using CARPT method.

Despite these advances in Lagrangian and Eulerian measurement techniques, their application in stirred tanks has primarily focused on bulk flow characteristics, as mentioned earlier, rather than discrete inter-particle collision events. Consequently, these collisions still depend on foundational global frameworks to estimate their impact. Notably, Cherry and Papoutsakis [56] provided a model that accounts for the energy of collisions in association with the collision frequency described as turbulent collision severity TCS. This quantity has always been used as an approximation by using global estimations of the system due to flow complexities and absence of local experimental statistics.

Hence, a PTV technique is set to capture the Lagrangian information of PMMA particles suspended in Ammonium Thiocyanate NH_4SCN 61 wt% solution as a carrier fluid inside

a stirred tank using a high-speed camera. To account for the 2D nature of the data, a unique code is developed to filter collision events based on a change in the threshold angle $\theta_{threshold}$ between colliding particles, that is, the relative angle between the trajectories and the effective diameter d_{eff}, which is the separation distance between the particles. For the first time, the resolved local Lagrangian statistics provided a direct experimental insight into the collision environment. Specifically, the collision rate, frequency, and impact are evaluated and quantified across various particle volume fractions $0.1 < \alpha_p < 0.7$v%.

4.2 Materials and methods

4.2.1 Experimental set-up

Following the same experimental set-up and solid–liquid flow previously used [57, 41], the apparatus and geometrical configuration are represented in Figure 4.2. The stirred tank, found in Figure 4.2a, is a cylinder made of borosilicate glass with a hemispherical bottom. The diameter of the tank is $T = 0.12$ m which is filled with fluid to a height $H = 0.082$ m ($H/T = 0.68$), corresponding to a total volume of $V = 0.7$ L. The agitation inside is driven by the HTPGD impeller (Pierre Guerin), a three-blade axial impeller with a down-pumping functionality, of diameter $D = 0.06$ m ($D/T = 0.5$). The impeller is placed at an off-bottom clearance $C = 0.06$ m ($C/T = 0.5$). The tank is unbaffled; however, four dip tubes representing the required sensors for MSC culture (temperature, pH, etc.) behave as baffles and prevent swirl formation at the surface near the shaft. The rotational speed is set to $N = 150$ rpm, insuring homogeneous suspension of the dispersed-phase, while avoiding the air bubbles entrapment from the free surface. For all concentrations used, the agitation, resulting in a Reynolds number $Re \approx 5000$, is much higher than the just-suspension speed N_{js} [57]. A high-speed camera is set perpendicular to the laser sheet to capture the field of view. Figure 4.2b shows the top-view of the tank, where the vertical measurement plane illuminated by the laser is located at the center of the tank. Note that the vessel is rotated so that the dip tubes do not block the field of view. Furthermore, the stirred tank is installed in an aquarium that is filled with paraffin oil as seen in Figure 4.2c, so that the diffractions in the laser sheet traversing the set-up, due to the curvature of the vessel, are minimized. The temperature inside the operating room is regulated around 22 – 23 °C using an air conditioner.

The carrier fluid used in the experiments is Ammonium Thiocyanate NH_4SCN solution with 61 wt% which corresponds to a refractive index RI= 1.491. The density and dynamic viscosity of the fluid flow would then be $\rho_f = 1139$ kg/m^3 and $\mu_f = 1.94$ mPa.s, respectively. The solution is carefully filtered to remove any insoluble impurities (solid residues). PMMA particles (Cospheric) are chosen to represent the dispersed phase, with a

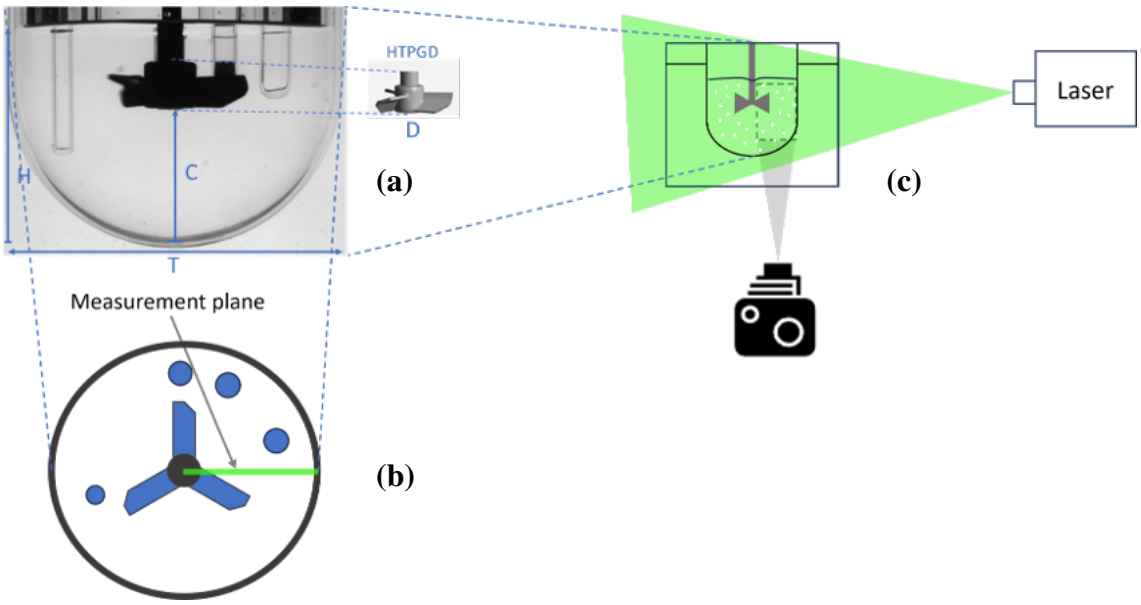

Figure 4.2: PTV setup. **a)** camera-view of the stirred tank equipped with HTPG down-pumping axial impeller. T = 0.12 m, H = 0.082 m, C/T = D/T = 0.5. **b)** Top-view of the stirred tank with the location of the dipped tubes. Laser sheet illuminates the center of the tank right at the shaft. **c)** Stirred tank installation in an aquarium. The gray area indicates the measurement plane perceived by the imaging system.

refractive index RI≈ 1.49, a diameter d_p= 0.55 mm, and a density ρ_p = 1185 kg/m^3. The associated resulting Stokes number is around St = 0.8. Here, it should be noted that the set-up configuration and methodology are consistent with those used previously to mimic MSC culture systems [57, 41]. The only difference in the present work is the particle size, which is slightly larger to allow their detection on PTV images.

4.2.2 PTV processing

PTV technique critically depends on a high-speed camera, a continuous laser source and tracking algorithms to obtain particle trajectories. For that, a SpeedSense VEO 440 camera (Dantec Dynamics) with a 2560 × 1600 resolution and a maximum frame rate 1000 Hz is used, equipped with a 530 nm green-filter that reflects the incident laser light. The camera view captures the vertical z-r plane at the center of the tank where a continuous laser sheet of 3 – 4 mm thickness illuminates that region using a coherent Genesis CX-532 STM-Series laser. The wavelength of the laser is 532 nm with a maximum output power of 5 W. Since tracking is 2D in a 3D environment, having enough thickness to capture the particles is mandatory, especially in the impeller region where the highest velocities prevail. A set of 10,000 image is then captured for each particle concentration at a frequency of 500 Hz with a resulting scale factor SF= 46.5 µm/pixel. After that, the time-resolved 2D PTV analysis, provided by Dantec Dynamics software v7.3, is used to obtain particle trajectories. Prior to this step, an image processing step is applied so every gray value below a threshold fixed to 1% is clamped to 0. It is crucial as it clears out the noise generated by particles

outside the laser sheet and hence enhances the detection algorithm. The effect of such is shown in Figure 4.3, where a) is the raw image and b) is the image treated by the mentioned threshold at the maximum particle volume fraction measured $\alpha_p = 0.7$ v%. Clearly, the black background is ameliorated and the white shining spots represent the particles on the laser sheet. As a result, a data-sheet is generated which contains particle IDs, and, for each ID, the corresponding frame numbers, equivalent durations, positions, and velocities. These data are exported to MATLAB (R2023a) to post-process for collision analysis.

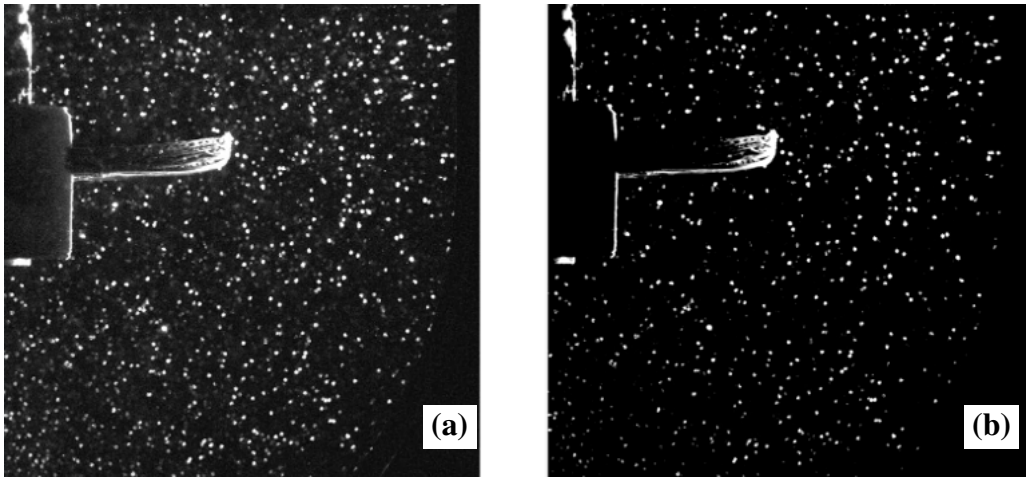

Figure 4.3: Noise elimination at $\alpha_p = 0.7$ v% concentration. **a)** Instantaneous raw PTV image without treatment. **b)** Instantaneous raw PTV image with 1% threshold treatment.

4.2.3 Post-processing of collisions

To quantify particle-particle interactions, special care is paid to the post-process phase on MATLAB, where trajectories are treated in two main stages. Before that, a mask was applied to hide the impeller and the shaft and to eliminate trajectories in the region under the impeller. In this region, the tangential velocity term (off-plane 3^{rd} component) is dominant, and thus the particles leave the laser sheet quickly, resulting in a short trajectory. Moreover, the trajectory is perpendicular to the laser sheet, so it is practically impossible to account for collisions in that region unless a 3D tracking approach is used, requiring two high-speed cameras, which is beyond the scope of this study. Hence, the zone under the impeller is masked in post-processing. Then, trajectories with a duration shorter than 10 ms, i.e. 5 frames, were also discarded, because they likely reflect transient appearances in the laser sheet or particles grazing its edges, which do not contribute to the interaction analysis. Furthermore, some main assumptions concerning the interactions of particles are summarized as follows: (i) the particles are spherical and rigid with a uniform size and density; (ii) the shape is unchanged during agitation and collisions, and thus deformation is not considered; (iii) rotational motion of the particles is ignored.

The first stage of analysis aims at eliminating overlapped or stacked particles while

registering pairs that are within a separating threshold distance. The threshold distance between a particle pair is defined as $2.5d_p$ from center-to-center which is equal to $1.5d_p$ that separates the edges of two particles, as the PTV algorithm provides position information on the centroids of the particles. This criterion is selected to mark the pairs as colliding candidates. The principle of which is explained in the flow diagram presented in Figure 4.4. For each frame, the particles data detected on this frame is loaded, and the distances for neighbouring particles within $2.5d_p$ are collected while avoiding self-counting. A key/identifier is then generated for every satisfied pair based on their ID number. If this pair, e.g., 512 – 831 pair, has been already registered before, it passes a check to ensure that the separating distance is higher than d_p, otherwise the pair has overlapped overtime and is hence discarded and completely removed as no collision/interaction incident would occur, i.e. passive particles. If the pair is detected for the first time, a double check on the overlapping/stacking condition is also imposed ($>d_p$) and a new record is registered. Ultimately, pairs that are skipped or removed have the chance to be re-engaged with other particles. In this way, pairs with trajectories separated by $2.5d_p$ are registered for the next step. Note that throughout this study, all inter-particle separation distances are defined on a center-to-center basis.

Since tracking is achieved in 2D, eliminating overlapped particles is not sufficient to regard as a collision incident. Particles could appear within the $2.5d_p$ threshold distance in 2D, but in reality the separation could be $\gg 2.5d_p$ due to the laser sheet depth. In addition, it is important to realize that the exact moment of collision is beyond reach; this has also been reported by Jiang et al. [47] even at 1000 Hz acquisition rate with manual estimation of collision duration. Furthermore, in the present work, it is mainly because the two phases have close densities $\rho_f/\rho_p \approx 0.96$ so the fluid pressure prevents a direct impact. Hence, a more dynamic and flexible approach must be used to detect a possible interaction.

Consequently, implementing a detection of the angular change between the paths of a particle pair has been identified as the optimal way to verify possible collision or interaction between these particles. For each pair of particles gathered in step 1, frames are collected as long as they satisfy a separating distance $<1.5d_p$, to be considered as a duration of collision. Choosing the minimum separating distance, d_p is impractical since (i) it would not necessarily reflect the exact moment of collision as explained earlier, and (ii) applying "the change in angle" condition also becomes inconvenient as to how long it takes a particle to change its direction (collision duration), which is rather specific and unique to each particle case, and relies on the high- or low-speed zones, for instance. Hence, instead of using a fixed frame number, the angle change threshold is dynamically implemented for each pair based on the $1.5d_p$ separation condition. The relative angle between the paths of two particles is calculated in the first and last satisfying frames and the difference is compared to the defined angle threshold $\theta_{threshold} = 25°$. Any change $> \theta_{threshold} = 25°$

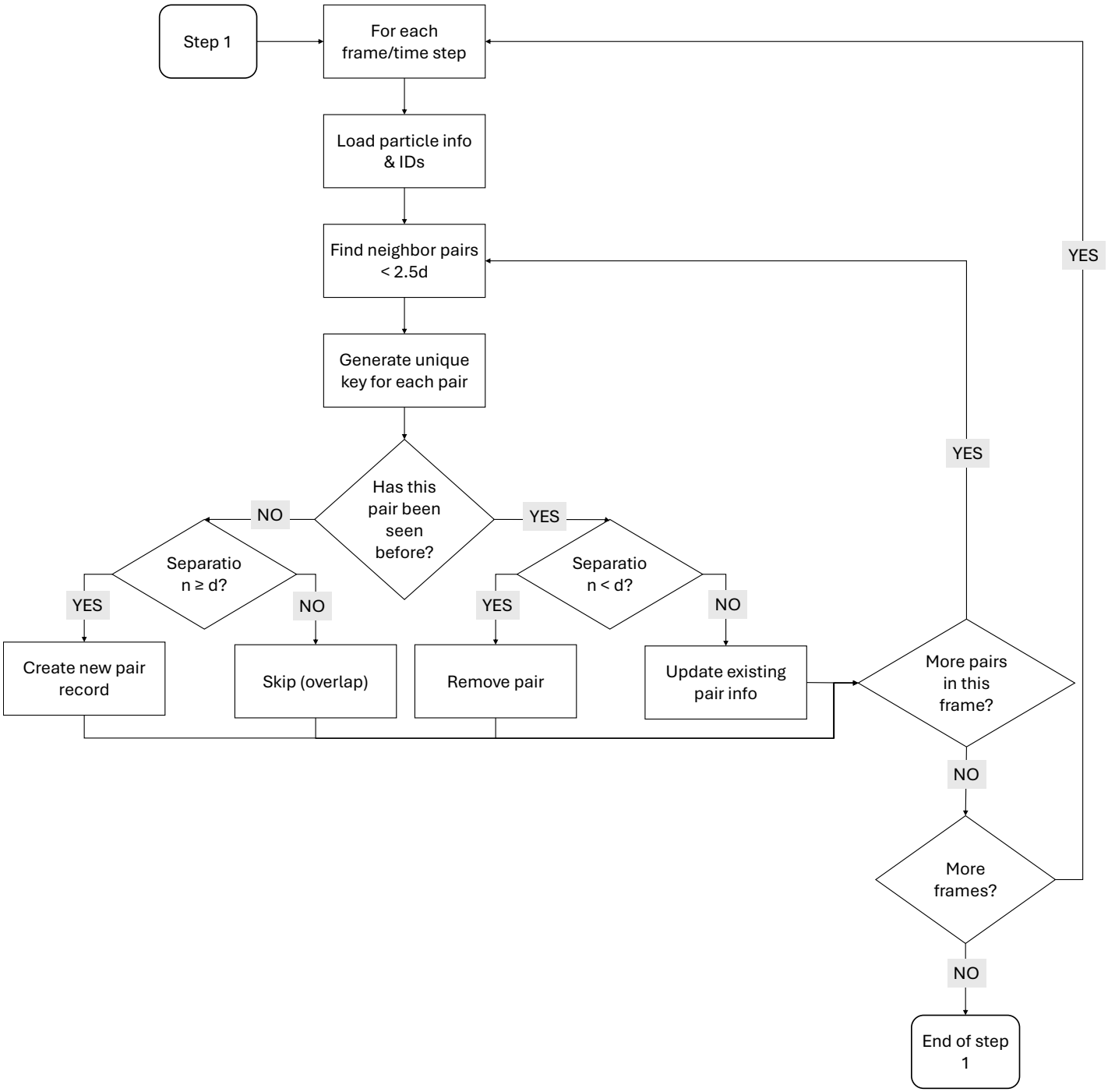

Figure 4.4: Step 1 of PTV data post-processing - Detection of potentially colliding pairs. d here is the particle diameter d_p

would mean that the particles in a pair have encountered an interaction. The complete itinerary of step 2 is shown in Figure 4.5. Ultimately, the pairs of step 1 are then updated based on step 2 and the results are: "interactive" pairs with prolonged duration separated by $2.5d_p$ and "collisional" pairs separated by $1.5d_p$. Evidently, the pairs who fail the test are completely removed. This can be visualized in the scheme of Figure 4.6, where the pair who passed the angle threshold test is stored in the collision pairs and the interactive pairs pools with the corresponding duration.

The angle of each particle path is calculated on the basis of the velocity components as

$$\theta_p = arctan\left(\frac{u_z}{u_r}\right) \tag{4.1}$$

The relative angle between paths of the two particles in a pair is simply referred to as $\theta = \theta_{P_1} - \theta_{P_2}$, where P_1 and P_2 are the two members of the pair. Then the relative angle θ is accompanied by a subscript i to mark the frame or instant (θ_3 at instant t_3), as can be seen in the scheme of Figure 4.6. Definitely, the difference between two relative angles is in absolute form $\mid \theta_f - \theta_i \mid \geq \theta_{threshold}$, where i and f denote the first and last frames satisfying the separating condition $<1.5d_p$, respectively.

It is worth noting that, in most of the models discussed in the literature that deal with collision predictions, the imaginary contact distance is at the heart of the assumptions, often of a separating distance of $3d_p$ [21] or $2d_p$ [18]. The imaginary contact assumption, indeed alongside other factors, simply says that the pair is most likely going to collide. Also, at such distances, more dominant forces arise such as lubrication forces. This force, within a flow of Stokes number $St = 0.8$, further supports the approach proposed to detect collisions, which acts as a layer against direct impact. Additional details can be found in section 4.3.2.

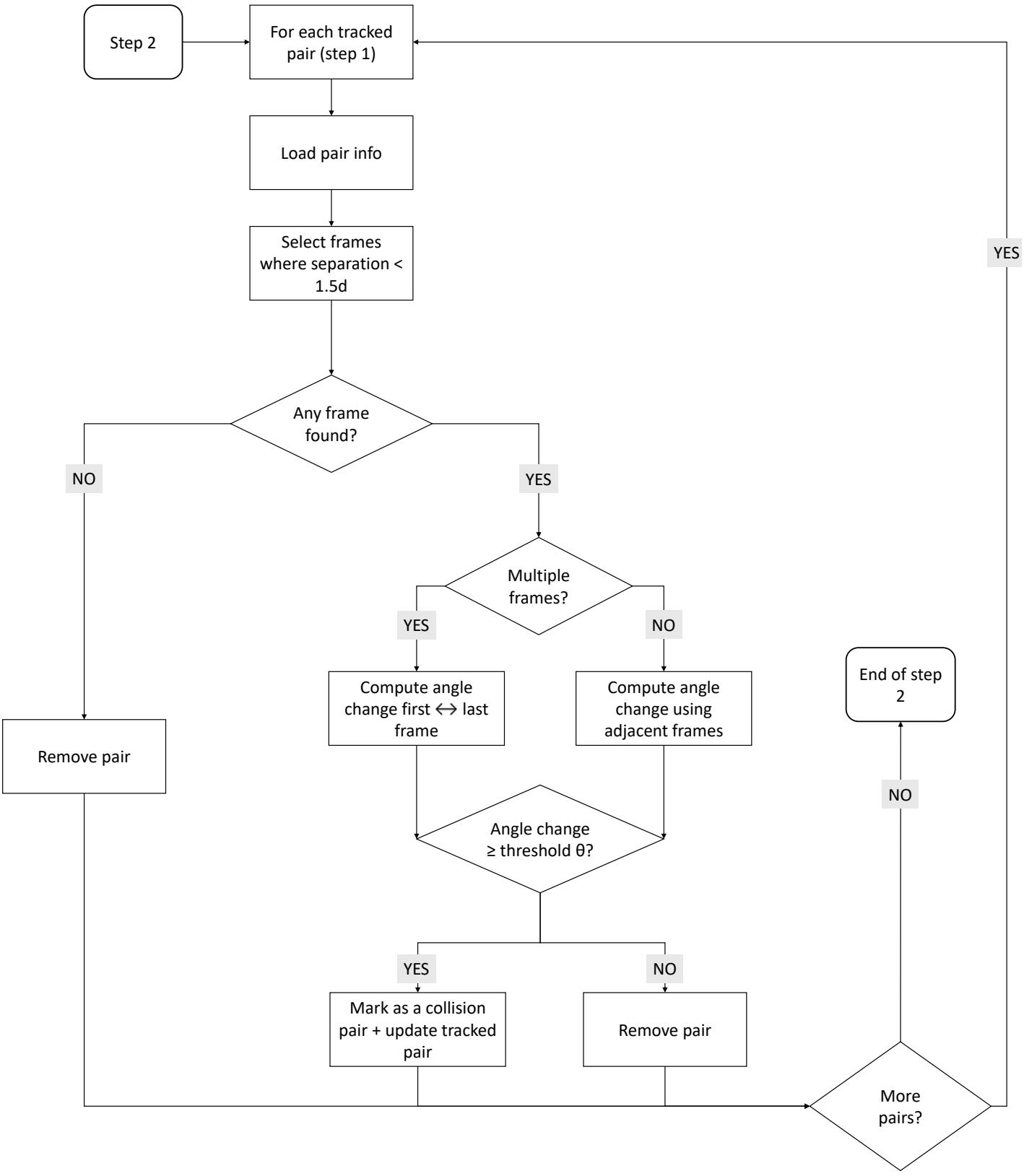

Figure 4.5: Step 2 of PTV data post-processing: Detection of angle change based on the data of step 1, which is updated simultaneously with step 2. d here is the particle diameter d_p

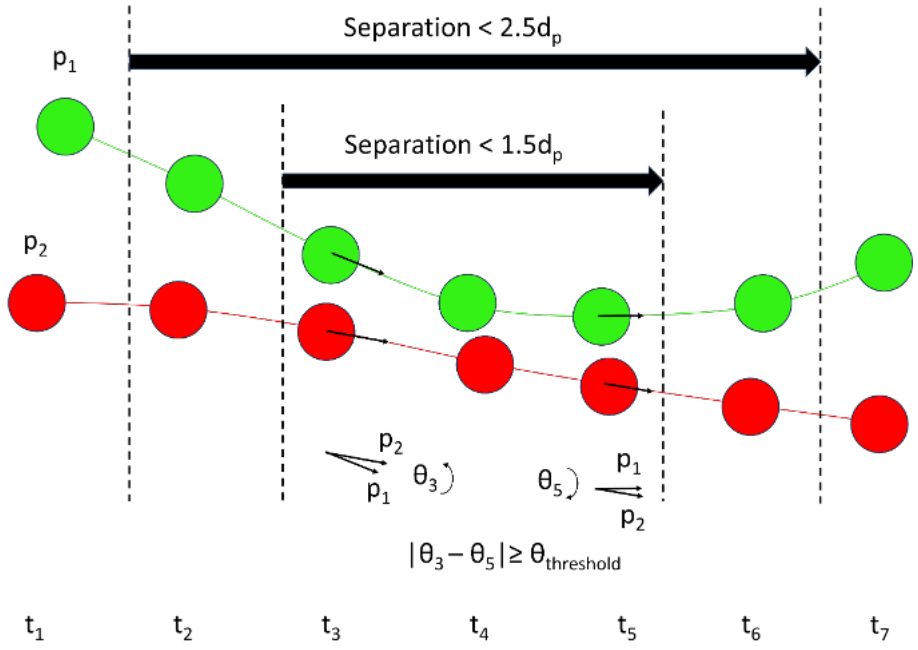

Figure 4.6: Collision illustration scheme as a result of Step 1 & 2. $d_{eff} \leq 2.5$ corresponds to "interactive" period. $d_{eff} \leq 1.5$ corresponds "collision" period. The change in path relative angle is based on the first and last frames satisfying $d_{eff} \leq 1.5$.

4.2.4 Properties

Since the data provided by the PTV experiments are solely focused on the particles of the dispersed-phase, with the absence of fluid velocity information (external impact), and in addition to the 2D nature of the results, evaluating and approximating forces during interaction/collision duration depends on Newton's second law as a total sum of forces, without considering deformation, as

$$m_p \frac{du_p}{dt} = \sum F_{total} \tag{4.2}$$

The high temporal resolution used would allow the evaluation of the left-hand side, whereas the exploration of the forces for the collected pairs is not attained due to the reasons mentioned. One can re-write the equation of motion during the interaction of a pair of particles as a momentum exchange

$$J = m_p \Delta u_{rel} = \Delta t \cdot F_{total} \tag{4.3}$$

$$F_{total} = F_{P1,hyd} - F_{P2,hyd} + 2F_c \tag{4.4}$$

where $u_{rel} = u_{P_1} - u_{P_2}$ is the relative velocity between the members of the pair at an instant t, and Δu_{rel} is then the difference between two relative velocities over a time step Δt. The

total force F_{total} includes inter-particle interaction force F_c, and the difference in external hydrodynamic forces between the two particles $F_{P1,hyd} - F_{P2,hyd}$ acted by the fluid such as drag, lift, fluid pressure, etc. The factor 2 for the contact force arises from Newton's 3^{rd} law, where $F_{P1,c} = -F_{P2,c} = F_c$. Note that some works neglect the particle-fluid interactions during collision with an effective diameter equal to particle diameter $d_{eff} = d_p$ and therefore the contributing force is only due to contact [58].

During interactions, particles can still be subjected to acceleration from the carrier fluid. To account for sudden changes in the velocities of particles, the strategy consists of collecting consecutive frames that correspond only to a decreasing relative velocity u_{rel} during interaction ($< 2.5d_p$) or collision ($< 1.5d_p$). In other words, data collected from steps 1 & 2 are used to compute relative velocities, where this condition is applied. Consequently, pairs with one frame are eliminated. On this basis, the "interactive" pairs gathered are used to compute the momentum exchange and the total estimated force mentioned above (Equation 4.3). Meanwhile, the "collisional" pairs pathway allows one to estimate the collision kinetic energy exchanged, known as

$$\Delta KE = \frac{1}{2} m_p \left(\Delta u_i^2 - \Delta u_f^2 \right) \tag{4.5}$$

so that it represents the loss in energy between the members of the particle pair prior to and after the collision ($\Delta KE > 0$). Such an evaluation is paramount for the turbulent collision severity TCS developed and discussed by Cherry and Papoutsakis [56] which is defined as

$$TCS = KE \cdot f \tag{4.6}$$

where f is the collision frequency defined as the collision rate per particle number density. The collision rate r is a measure of collision events over time in the volume of measurement, and the particle number density n is the relevant number of particles in the volume of measurement. Hence, the collision frequency f accounts for how often a particle collides, i.e. the number of collisions per particle per time $f = 2r/n$. In other words, the collision frequency is a normalization of the collision rate by the corresponding number of particles rather than the volume of measurement. Note that the particle number density n can be expressed as $n = \alpha_p / V_p$, where V_p is the volume of a single particle.

In an effort to attempt and adapt a model from the list discussed by Meyer and Deglon [24], the collision mechanism in our system is believed to be a mix between shear-induced and accelerative-correlated in connection with the evaluated $Re = 5000$ and $St = 0.8$. This indicates that as a turbulent regime with a high shear rate, particles have moderate inertia ($St = 0.1 - 1$) to deviate from stream lines and collide. However, in all the models

developed, the density difference or ratio between the dispersed- and carrier-phases was barely considered, which plays an important role in the collision process. Thus, the collision dynamics in this system is predominantly attributed to shearing (orthokinetic). Kramer and Clark model [19] is one interesting model that refers to the strain rate in principle, specifically the absolute maximum strain rate $\dot{\gamma}_{max}$ as a scalar value, as the main motive for collision, with

$$r_{KC} = \frac{n^2}{2}\frac{4\pi}{3}|\dot{\gamma}_{max}|d_{eff}^3 \tag{4.7}$$

where n is the particle number density. The major obstacle is that a detailed knowledge of the flow field near the smallest scales is required to evaluate the quantity $\dot{\gamma}_{max}$. In a previous work done on the same type of stirred tank with axial agitation, Delafosse et al. [59] established that the maximum dissipation rate generated by the impeller is at least 50 times higher than the overall dissipation rate estimated from the power number equation $\varepsilon_{max} \approx 50\langle\varepsilon\rangle$. The mean dissipation rate is estimated from the power number of the HTPG impeller $P_0 = 0.67$ [60] as

$$\langle\varepsilon\rangle = \frac{P_0 N^3 D^5}{V} \tag{4.8}$$

where N is the impeller rotational speed, D is the impeller diameter, and V is the volume of the fluid used. The missing maximum scalar shear rate values in Equation 4.7 would then be estimated as

$$\dot{\gamma}_{max} = \sqrt{\frac{\varepsilon_{max}}{\nu}} \tag{4.9}$$

where ν is the dynamic viscosity of the fluid. For the sake of comparison and to support the Kramer and Clark model that best describes the flow in this study, another model is also presented below according to Wang et al. [22].

$$r_w = n^2\pi d_{eff}^2\, g(d)\, \langle|w_r|\rangle \tag{4.10}$$

where g(d) is the radial distribution function that serves as a correction to the particle number density at contact due to the non-uniform particle distribution, and w_r is the radial relative velocity which represents the speed at which two particles move toward each other along the imaginary line connecting their centers. For a complete description of the model, the reader is invited to check the work of Chen [61]. The results of such evaluation are shown in section 4.3.4.

In summary, Table 4.2 below recaps each criterion and post-processing stage with its associated property. Statistics related to collisions are strictly treated with step 2 data, while the properties discussed in this section are further treated with the decreasing relative velocity condition prior to evaluation.

Table 4.2: Recap of post-processing stages, the evaluated statistics and properties associated with each stage.

	Name	d_{eff}	Statistics	Relative velocities		Properties
Step 1	"Interactive pairs"	2.5	–	✓	⇒	Exchanged impulse
Step 2	"Collisional pairs"	1.5	Rate & Frequency	✓	⇒	Exchanged KE

4.3 Results and discussions

4.3.1 RIM system

The choice of quasi refractive index matching of the particles and liquid phases could be justified in Figure 4.7, where a α_p = 0.4 v% dispersion of PMMA particles in a 19 wt% NaCl solution a) is compared to the same dispersion in a 61 wt% NH_4SCN solution b). The NaCl solution has the same properties as NH_4SCN except for the refractive index (ρ_f = 1137 kg/m^3, μ_f = 1.91 mPa.s, and RI=1.365). For the NaCl case, the laser power was adjusted to 0.25 W, which is half the intensity used for NH_4SCN case 0.5 W. Clearly, at volume fractions α_p = 0.4 v%, PMMA particles with NaCl solution almost saturated the images, where the noise is impractical to treat even at lower laser power. The blurring effect is due to the fact that particles outside the laser sheet deteriorate and interfere with imaging. In contrast, the quasi-RIM NH_4SCN image exhibits significantly enhanced background even though the laser power is higher (0.5 W), which further supports the use of a close refractive indices. A quasi index matching is required as the mismatch is enough to distinguish particles from the liquid in the measurement plane, while minimising the blurring effect induced by out-of-plane particles. Hence, the 61 wt% NH_4SCN option was the optimal choice to reach a higher concentration of particles. Similarly, Aguilar-Corona et al. [46] benefited from slight mismatches in refractive indices to track collisions in a fluidized bed. The maximum volume fractions of the PMMA solid-phase is α_p = 0.7 v%, beyond which it could be demanding for the PTV algorithm.

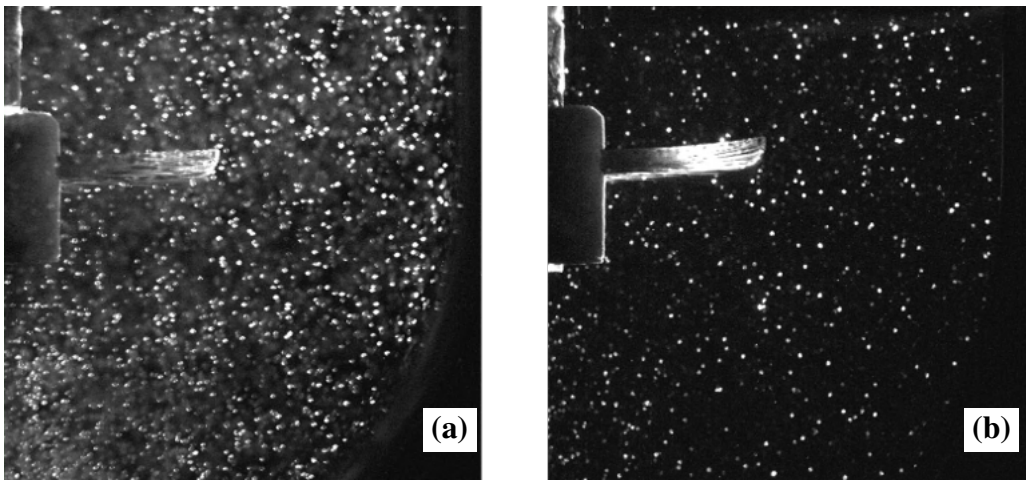

Figure 4.7: PTV Raw images comparison for $\alpha_p = 0.4$v% volume fraction. **a)** 19 wt% NaCl liquid solution, without RIM. **b)** 61 wt% NH_4SCN liquid solution, with RIM.

It is well demonstrated that for an optimal PTV function, a typical seeding density would be around 0.01 particles per pixel ppp [62]. The seeding here is referred to as the tracers used to characterize a carrier flow (liquid or gas) of a size $< 20\,\mu m$. Nonetheless, the maximum concentration of particles reached $\alpha_p = 0.7$v% would account for 0.0083 ppp, which is considered sufficient for an efficient detection while avoiding biased errors observed in densely seeded flows [63].

4.3.2 Qualitative analysis

Figure 4.8 and Figure 4.9 which present two particles coming close together in the flow to interact/collide, show qualitative examples of collision taken from sequential raw camera snap-shots. The colliding particles are colored red (top-side particle) and green (bottom-side particle). As explained previously, two phenomena are emphasized: (i) the exact moment of collision is ambiguous, with the closest gap being between t_4 and t_7 for Figure 4.8 and t_5 and t_7 for Figure 4.9. It is noticeable that in both examples the particles rather graze against each other for a short amount of time instead of having a direct impact, due to (ii) the fluid pressure in the thin layer between the two particles (lubricating force) that builds up at nearly-contact separation, in addition to tangential resistance due to viscous shear as well. This further explains and supports the choice of $\theta_{threshold} = 25°$ in such a system ($St = 0.8$), where slightly higher angle values may result in a severe decrease of detected collisions (see Appendix Figure A.4.1). Another important marked behaviour is the change in direction before and after impact, which is one of the main approaches used in the analysis (step 2). In Figure 4.8, the red particle (top-side) progressively leaves the laser sheet after the interaction ($t_{10} \rightarrow t_{12}$), the same also happens with the green particle (bottom-side) in Figure 4.9 ($t_{11} \rightarrow t_{14}$). Whereas the blue dashed circle in Figure 4.8 ($t_8 \rightarrow t_{12}$) labels overlapped particle pairs, where two particles passed in front of each

other to appear as a merged body in the 2D format. These are the pairs eliminated in step 1.

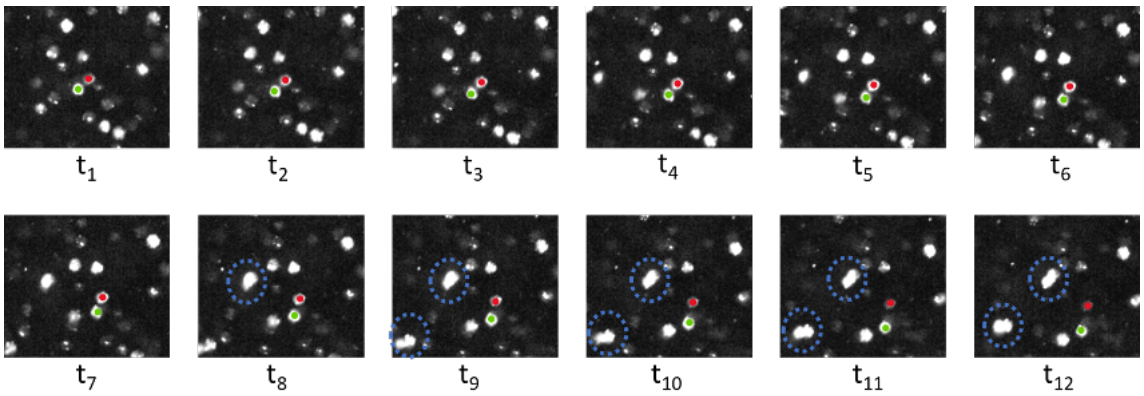

Figure 4.8: A collision example from raw PTV snapshots. The time step t is 2 ms (500 Hz acquisition) with a total duration of 22 ms. The colliding particles are marked with red and green. The dashed blue circles spot different overlapping particles.

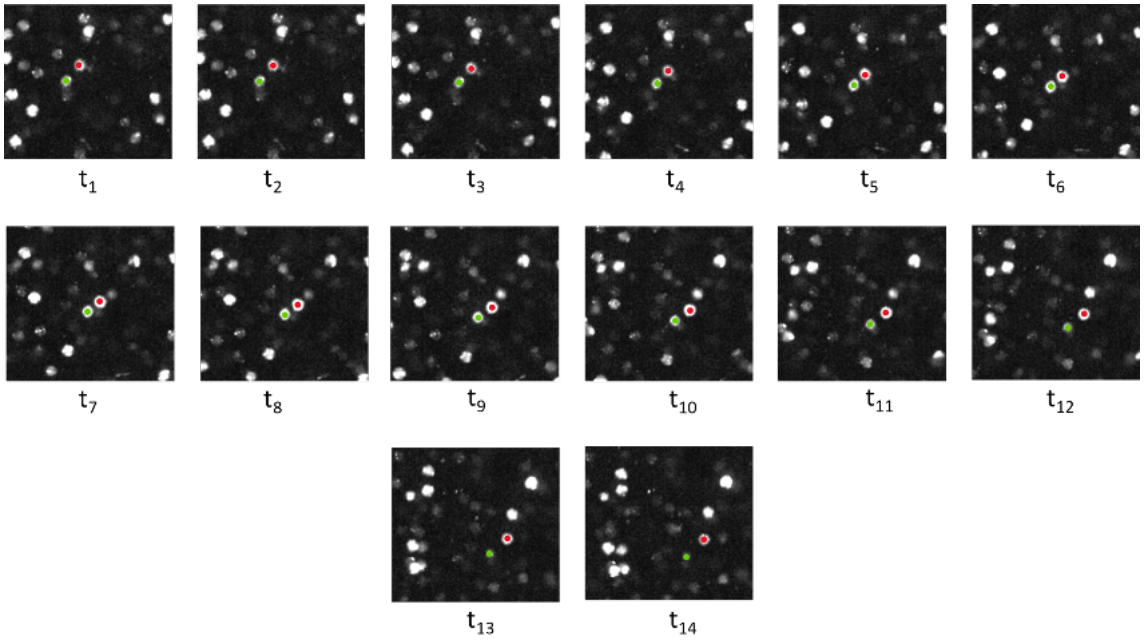

Figure 4.9: A collision example from raw PTV snapshots. The time step t is 2 ms (500 Hz acquisition) with a total duration of 26 ms. The colliding particles are marked with red and green.

4.3.3 Collision quantification

First, in Figure 4.10, all the trajectories provided by the PTV algorithm for $\alpha_p = 0.7$ v% case are shown with the mean velocity of each particle: a) stacks the trajectories over time (10000 frames) on the z-axis of the plot, while b) represents the top-view of a) that is just collapsing the trajectories into the z-r plane. The mean average velocity magnitude of each corresponding trajectory $M = \sqrt{u_z^2 + u_r^2}$ is non-dimensionalized by ND. Clearly, the flow pattern of the particles is attained, which is an axial circulating loop, and further demonstrates that with $St = 0.8$, the great majority follows the streamlines of the fluid

flow; this is in qualitative agreement with previous PIV measurements on PMMA particles with size $d_p = 0.168$ mm [57]. The high speed paths are majorly located in the impeller discharge ($M/ND \approx 1 \approx 0.32V_{tip}$) and decay progressively in the bulk and near the surface. As mentioned earlier, the region below the impeller is masked where the off-plane tangential velocity component is dominant, to enhance collision detection.

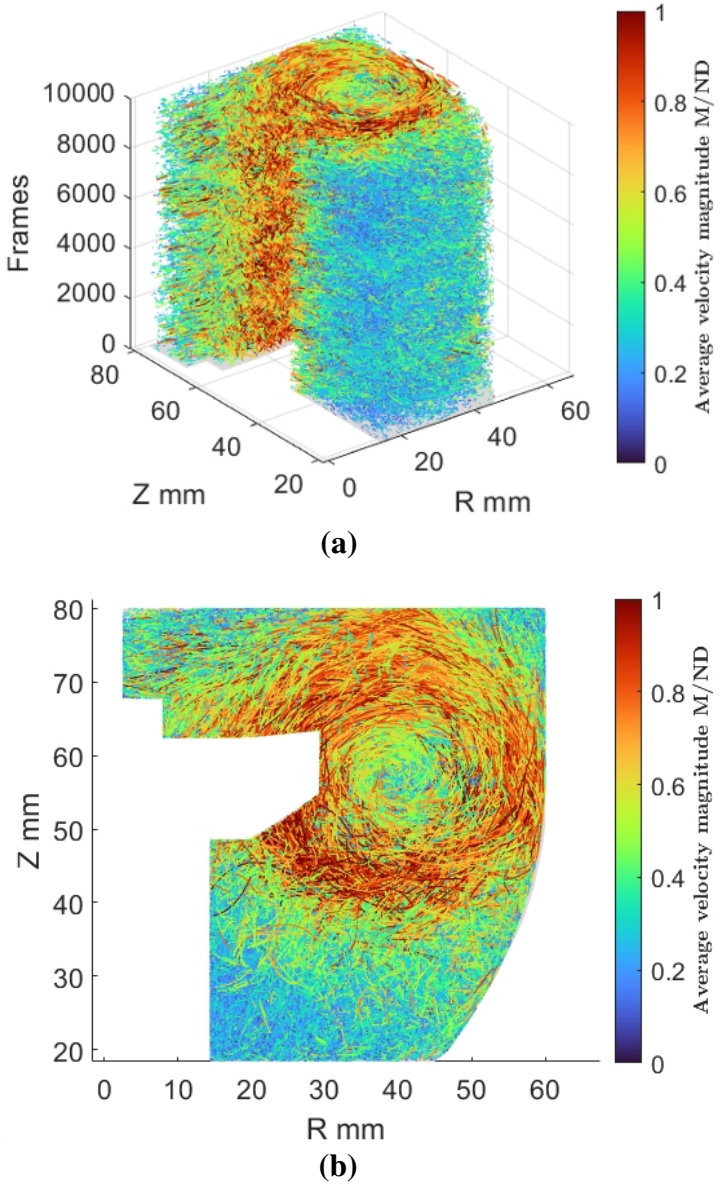

Figure 4.10: Total tracked particle trajectories for $\alpha_p = 0.7$ v% volume fraction. **a)** 3D plot over total duration of 20 s (500 Hz acquisition equivalent to 10 000 total frames). **b)** 2D plot (top view). Each trajectory is traced with the corresponding mean velocity magnitude M followed by the color-bar:M/ND (on the right).

The result of processing the trajectories of particles via steps 1 and 2 is shown in Figure 4.11a for $\alpha_p = 0.7$ v% case, with all the collided particle pairs over their respective measured duration. The measured volume appears more clearly in this plot as a gray

background in the r-z plane. The total number of collisions detected is 4399 events. Zoomed-in subplot versions are shown in Figure 4.11b-d from different times and regions. In these zoomed plots, few tweaks, rotations, and zoom levels are made so that particle pairs are easily addressed and do not appear over-stack or members are miss-identified with faulty ones. Moreover, on these images, a circle with the same particle size $d_p = 0.55$ mm is overlaid on trajectories every three frames to better visualize the relative approach and interaction. Each binary event is marked as a red–blue pair, while black highlights particles that experienced multiple collisions with red/blue indicating their partners. One should note that this is the first time that multiple collisions have been considered and accounted for experimentally, thanks to the ID assignment by the PTV algorithm provided by Dantec.

4.3.4 Collision rate and frequency

In this section, the previously established collisional pairs are further processed to evaluate the rate of collision events for the different concentrations examined. Basically, each pair has to be considered as a single collision event, and since storage is based on $d_{eff} < 1.5$, the minimal distance reached between each pair in the corresponding frame is set to count as an event per frame. The number of particles present in each frame is counted as well, where the evolution is presented in the Appendix (see Figure A.4.4), indicating a fairly constant count with each concentration. The per frame data are then averaged over 1 second (over 500 frames), and the results are presented in Figure 4.12a) and b) for collision rate and collision frequency for different volume fractions examined, respectively. As expected, the collision rate increases with the increase in particle concentrations. However, it does not increase monotonically, where the collision rates between $0.3 \leq \alpha_p \leq 0.5$v% are highly close. Regarding collision frequency (Figure 4.12b), where the rates are normalized by the corresponding number of particles detected by the algorithm, the trend does not change drastically. In fact, the gap observed in the collision rate plot from one concentration to another narrows slightly, yet the increasing trend is still pronounced. The statistical convergence is shown in the Appendix (Figure A.4.2). The evolution of these trends over time also reveals some fluctuations. Such scatterings are related to the number of particles detected for each volume fraction case; at reduced volume fractions, lower particle counts are detected which lead to sharper and stochastic fluctuations. The intermittency of particles entering and exiting the laser sheet is also correlated with the blade passage, i.e. flow behaviour. These fluctuations are gradually enhanced with the increasing volume fraction until $\alpha_p = 0.7$ v%. This is more evident with the KE results later on.

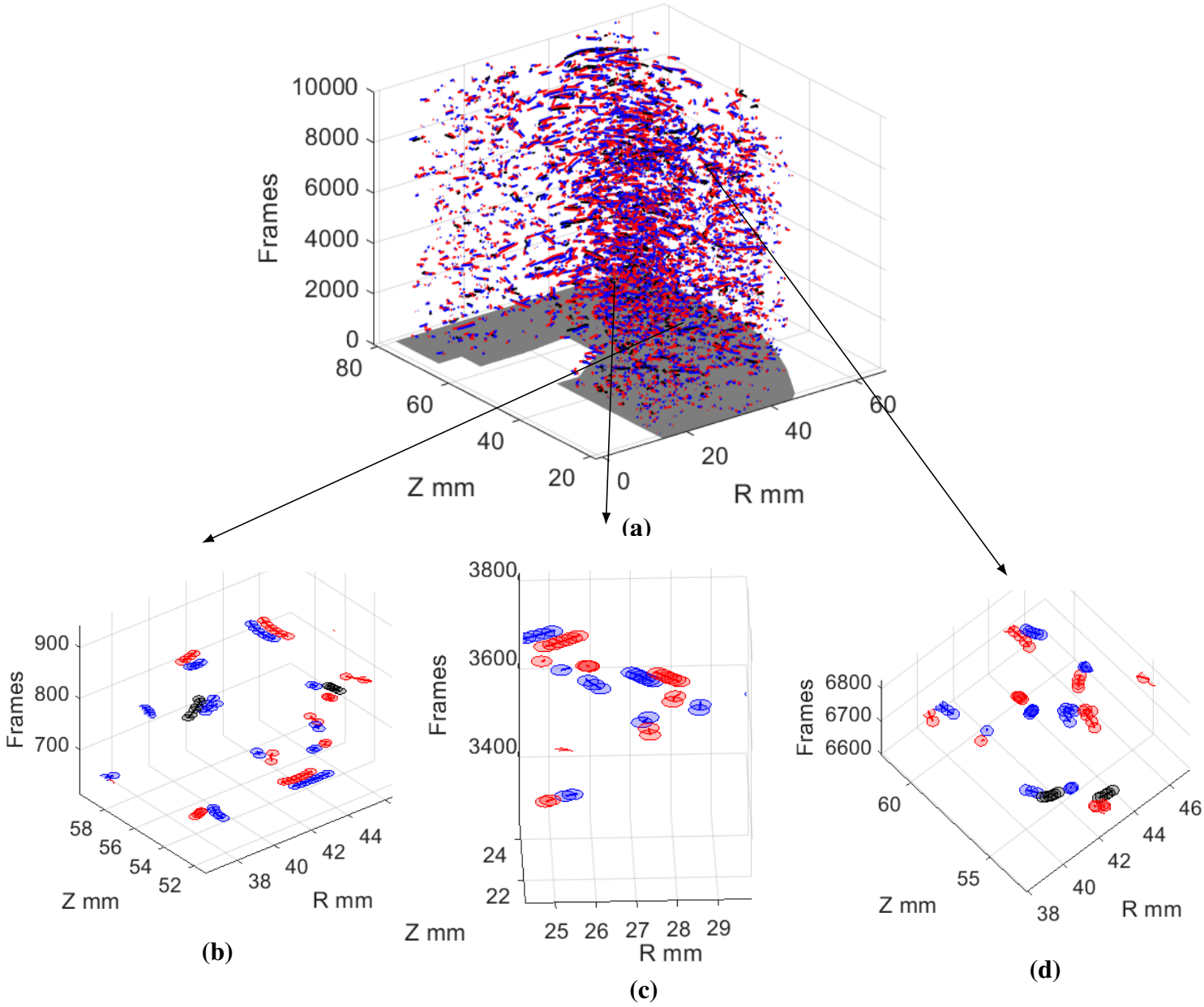

Figure 4.11: **a)** Total trajectories of the colliding pairs for α_p = 0.7v% volume fraction. **b, c & d)** Zoomed plots from different positions and durations. Particle shape-like is plotted every 3 frames. Viewing angles and zoom levels are adjusted for legibility so pair members remain visually distinct. Blue and red circles are assigned for two colliding particles. Black circles are assigned for particles that undergo multiple collisions.

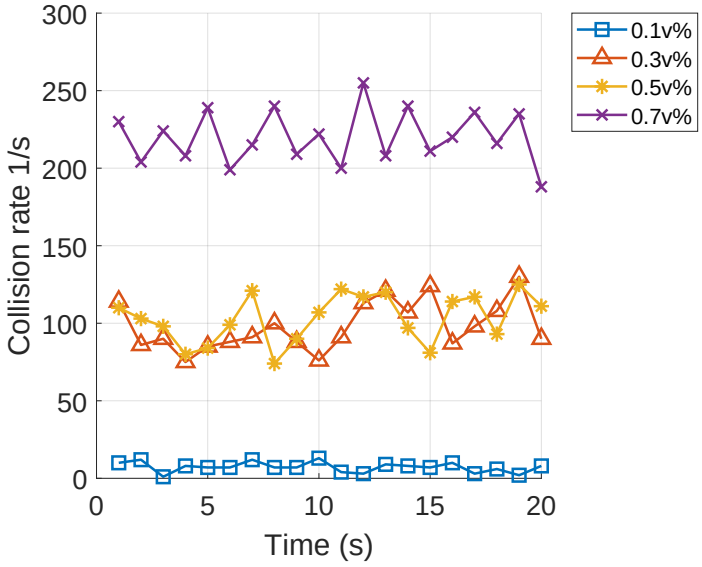

(a)

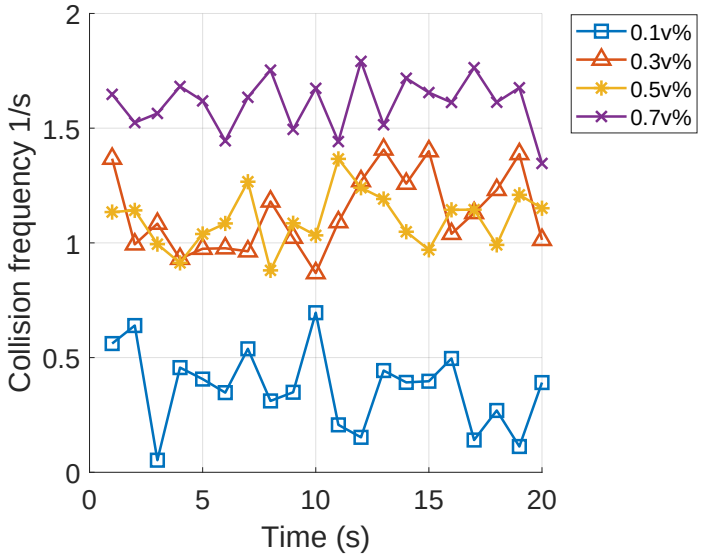

(b)

Figure 4.12: Evolution of collision statistics with time for different volume fractions. **a)** Collision rate r averaged over 1 second interval (s^{-1}). **b)** Collision frequency f averaged over 1 second interval (s^{-1}). □: 0.1 v%; △: 0.3 v%; ∗: 0.5 v%; ×: 0.7 v%.

To further investigate the trends, collision rates and frequencies are subsequently averaged over the duration of the entire experiment, the plot of which is found in Figure 4.13. The standard deviation of each case is therefore computed and is shown as an error bar in the plot.

Additionally, the model proposed by Kramer and Clark for the collision rate r_{KC} is also plotted (Equation 4.7) alongside the model proposed by Wang et al. r_W (Equation 4.10), where $\dot{\gamma}_{max}$ is estimated to be 600 s^{-1} (Equation 4.9) and $g(d) = 1.45$ according to [22, 61]. The collision rate information is read using the left axis (blue), while the frequency is

read using the right axis (red). The collision rate is found to increase steeply from 10 to 100 s^{-1} when the particle concentration increases from $\alpha_p = 0.1$ to 0.3 v% respectively. Then it stays consistent before it resumes the increasing trend at $\alpha_p = 0.6$ v% to reach a collision rate of 220 s^{-1} at $\alpha_p = 0.7$ v%. The two increasing phases are preserved for collision frequency with a slower slope in the second phase (from 0.5 to 0.7v%), which means that the strong rise in total collision events is driven primarily by the larger number of interacting particles ($\propto n^2$). The addition of particles from 0.1 to 0.7 v% has resulted in a 4-times higher collision frequency from 0.4 to 1.6 s^{-1}, respectively.

Regarding the Kramer and Clark model (Equation 4.7), although it purely relies on shear effects, it fairly predicts the rise while generally underestimating the measured collision rate. This gap becomes more pronounced as the concentration increases. Specifically, a consistent ratio of approximately $\frac{4}{3} \approx 1.33$ is observed between the estimated collision rate r and the Kramer and Clark model r_{KC}. The ratio implies that the measured collisions are roughly 33% more frequent than those predicted by shear alone, suggesting that additional mechanisms beyond shear effect become increasingly prominent for concentrations higher than 0.5v%. This ratio is replotted as $r_{KC_{mod}} = \frac{4}{3} r_{KC}$, which clearly and adequately captures the trend of the experimental collision rate. Nevertheless, among the models discussed for collisions, Kramer and Clark is the closest to predict the evaluated results, as can be compared with the model of Wang et al. r_W which falls further back by a ratio of around 7 from the estimated collision rate.

Moreover, for each concentration, the percentage of particles that have undergone multiple collisions from all colliding particles is presented in Table 4.3. Within the processing code, the percentage of particles that collided more than once did not reach 10% with the maximum being 8.8% at $\alpha_p = 0.7$v%. Ideally, with an increasing number of particles, the chances of multiple collisions are evidently higher. Here, the cases that are found to divert correspond to the plateau observed in Figure 4.13, namely $\alpha_p = 0.3 - 0.5$ v%. This further supports the stable phenomenon of collisions at such concentrations, which could be related to the transition mechanism toward four-way coupling (Table 4.1).

Table 4.3: Multiple collisions percentage evaluated for each volume fraction.

α_p v%	0.1	0.2	0.3	0.4	0.5	0.6	0.7
Multiple collisions %	5.5	7.7	8.1	6.9	6.4	7.3	8.8

Knowing that the flow is complex in stirred tanks, a spatial distribution of the collision events could be an interesting examination. Figure 4.14 reveals the spatial distribution of the average collision rate at $\alpha_p = 0.7$v% inside the domain of measurement, which can be referred to as collision density. The domain is discretized into a 1.4×1.4 mm bin

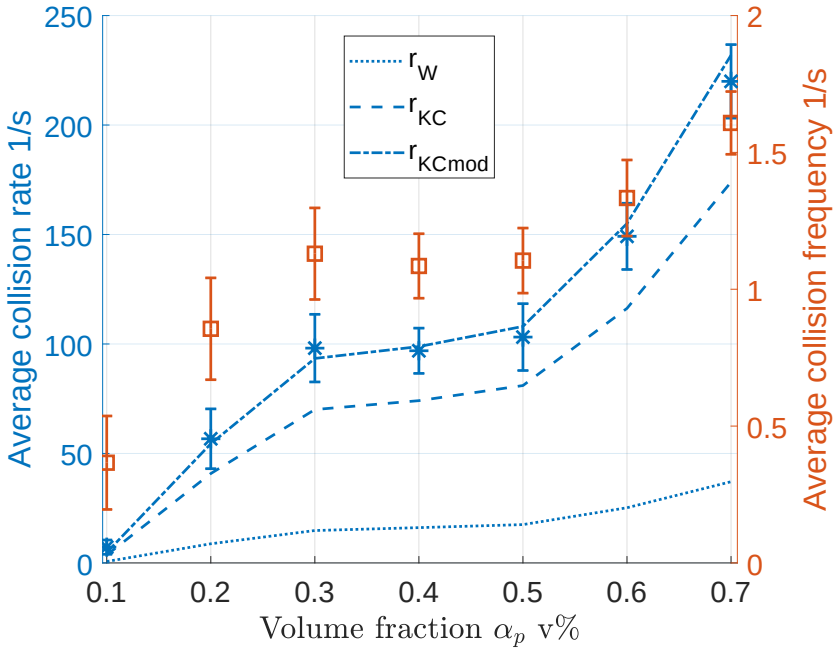

Figure 4.13: Global average of collision statistics over the entire experimental time for all volume fractions in comparison with relevant models. **Left, blue**) Average collision rate r (s^{-1}). **Right, red**) Average collision frequency f (s^{-1}). $*$: experimental collision rate r; $\square$: experimental collision frequency f; $\cdots$: Wang et al collision rate model r_W (Equation 4.10); $--$: Kramer and Clark collision rate model r_{KC} (Equation 4.7); $-\cdot$: modified Kramer and Clark collision rate model $r_{KC_{mod}} = \frac{4}{3} r_{KC}$.

where collision events are reassigned into the corresponding locations, based on the known positions of particle pairs. Collisions are strongly localized in two major zones: one just near the center of the circulating flow loop ($40 < R < 45$ mm, $50 < Z < 55$ mm) and another just below the strong discharge zone of the flow ($20 < Z < 30$ mm, $35 < Z < 40$ mm), accounting for a collision rate of $0.8 - 1$ s^{-1}. This signifies two facts: (i) in the first zone near the center of the circulating loop, particles are brought together via the trailing vortices and high shear rates produced by the impeller to converge into the low speed zone and collide repeatedly (accumulated collisions), while (ii) in the second lower zone, after the transportation of particles from the jet of the impeller, they frequently collide with the particles coming from the tangential circulating loop. In other words, the collision density map reflects how shear-driven transport of particles leads to collisions occurring at the periphery of the shearing zone rather than within the zone of high shear (impeller discharge).

In his simulations, Derksen [38] showed that particle-particle collisions happen mainly in the impeller stream, below the impeller region, and near the wall. However, the impeller was a rushton turbine that induces a radial flow, with particle of size $d_p = 0.47$ mm used, volume fractions up to 3.6 v%, density fraction $\rho_p/\rho_f = 2.5$, and a resulting Reynolds number $Re = 10^5$. At that speed, with high density differences between the dispersed- and carrier-phases, particles can decorrelate from streamlines and collide even in the high-speed

zones. Furthermore, the simulated collision rate was normalized by the model provided by Smoluchowski [17] (please refer to Meyer and Deglon [24] for a detailed description of the models), and was found to be 9 times higher than the theoretical prediction. In this work and as a preliminary estimation, the experimental collision rate is 30 times higher than the model proposed by Smoluchowski. In essence, both the work mentioned and the normalizing model are based on simulations (DNS; two-way coupling), while the data presented here are experimental and do not specifically tackle Smoluchowski's model, which further explains the discrepancies.

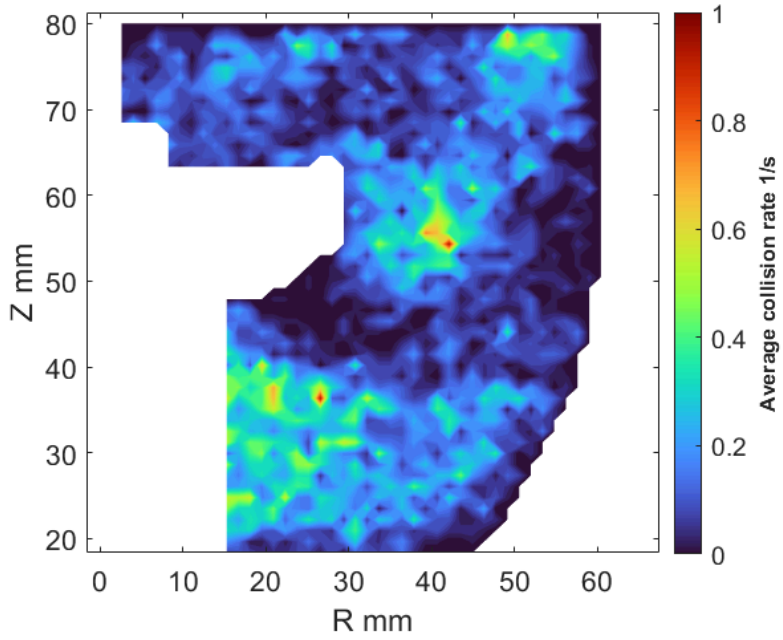

Figure 4.14: Spatial distribution of the average collision rate r for 0.7 v% volume fraction inside the stirred tank. Bin size is 1.4×1.4 mm; Color-bar: average collision rate r s^{-1}.

4.3.5 Collision stresses

In addition to the rate at which particles collide, it is important to attempt to characterize the impact and intensity of such interactions. Figure 4.15a) and b) shows the collision kinetic energy exchanged (Equation 4.5) in g cm^2/s^2 and the collision severity (Equation 4.6) in g cm^2/s^3 for different volume fractions, respectively, as a function of the measurement duration. The data shown are averaged for a 1 s interval. Across the 20 s window, the kinetic energy exchanged at $\alpha_p = 0.1$ v% appears to be the lowest, while the remaining cases possess a higher energy but overlap around the same level. Two distinct peaks are noticed for $\alpha_p = 0.1$ v% at $t = 10$ s and $t = 13$ s, which could be associated with the high relative collision rate at these instants (Figure 4.12). Another assumption is that at this diluted concentration, collisions detected are much lower than the $\alpha_p = 0.7$ v% case, for instance, and hence variations are more significant per 1 s interval average, related to

the lower particles detected on the laser sheet as explained earlier. It is worth noting that the statistical convergence is demonstrated in the Appendix (Figure A.4.3), confirming that all cases are converged. On the other hand, for collision severity, the variations in values between concentration cases are more pronounced due to the increase in collision frequency, which evidently indicates higher collision severity with the addition of particles. Both the collision frequency and the kinetic energy exchanged during collision contribute to the elevated severity, with the former being the predominant.

The global average of both properties over the duration of the experiment for all concentrations is presented in Figure 4.16. The standard deviation for each property is also shown as an error bar. The average collision kinetic energy (left, blue axis) rises from 3×10^{-4} g cm^2/s^2 at $\alpha_p = 0.1$ v% to roughly 5×10^{-4} g cm^2/s^2 and flats around it for all remaining volume fractions. In contrast, the collision severity (red, right axis) increases, with the same trend as the collision frequency, by a factor of 8 to reach 8×10^{-4} g cm^2/s^3 at $\alpha_p = 0.7$ v%. This further demonstrates that the average kinetic energy exchanged in collisions is nearly concentration-independent beyond $\alpha_p = 0.2$ v%, and that the steep increase in collision severity is primarily a reflection of collision frequency. In the case of stem cell culture in stirred tanks, typically attached to particles with smaller size ($d_p = 0.1 - 0.2$ mm), cells endure much higher collision events with particle addition, rather than higher impact/intensity at collision, resulting in repetitive damage to cells. For particle concentrations $\alpha_p < 0.2$ v%, the collision severity is an effect of both contributing terms.

In their work, Cherry and Papoutsakis [56] estimated the TCS to be around 3.45×10^{-7} and 0.85×10^{-6} for both $\alpha_p = 0.2$ and 0.6 v%, respectively. The size of particles was 160 µm with the system operating at just suspended speed N_{js} (75 rpm, MSC conditions). Obviously, the operating conditions are different from those in this work (3.5 times lower particle size and 2 times lower agitation speed). Importantly, the estimated TCS was based on global estimations and assumptions of inter-particle collisions with some dimensional analysis as well (correlated with global terms of the system); whereas the efforts in this work aim to statistically evaluate these assumptions.

Lastly, the impulse calculated from Equation 4.3 is distributed against the relative corresponding durations for each pair, and the results are reported in Figure 4.17 for $\alpha_p = 0.7$ v%. Both variables, impulse exchanged and duration, are discretized in 21×7 bins on the x and y axes, respectively. The impulse values are rounded to the first decimal, whereas the duration values are deliberately kept at the 2 ms interval, i.e., the actual temporal resolution of the acquisition system, and any finer discretization would be inconsistent with the frame period. To focus on the behaviour and avoid influence of extreme outliers, the covered ranges are restricted to the $5 - 95^{th}$ percentile for both quantities before binning. The total

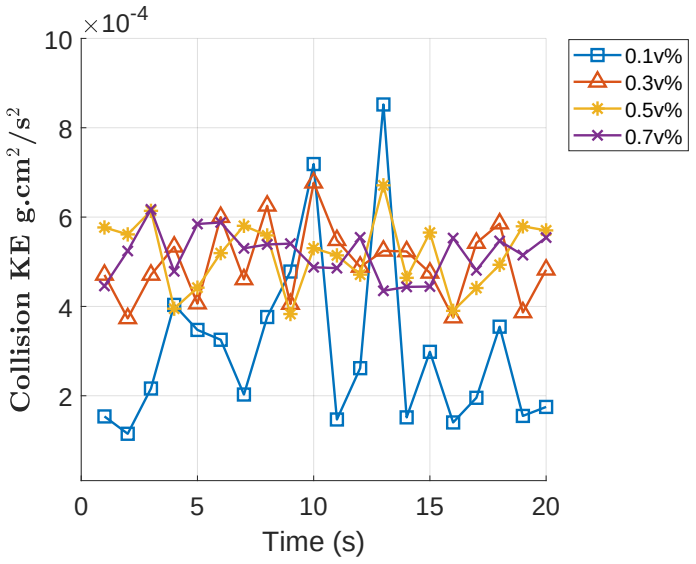

(a)

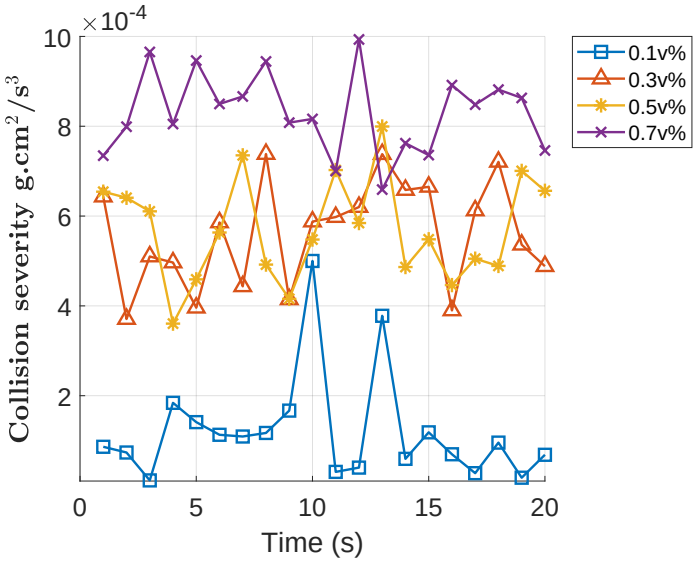

(b)

Figure 4.15: Evolution of collision impact metrics with time for different volume fractions. **a)** Collision kinetic energy exchanged KE (Equation 4.5) averaged over 1 second interval ($\mathrm{g\,cm^2/s^2}$). **b)** Collision severity TCS (Equation 4.6) averaged over 1 second interval ($\mathrm{g\,cm^2/s^3}$). □: 0.1 v%; △: 0.3 v%; ∗: 0.5 v%; ×: 0.7 v%.

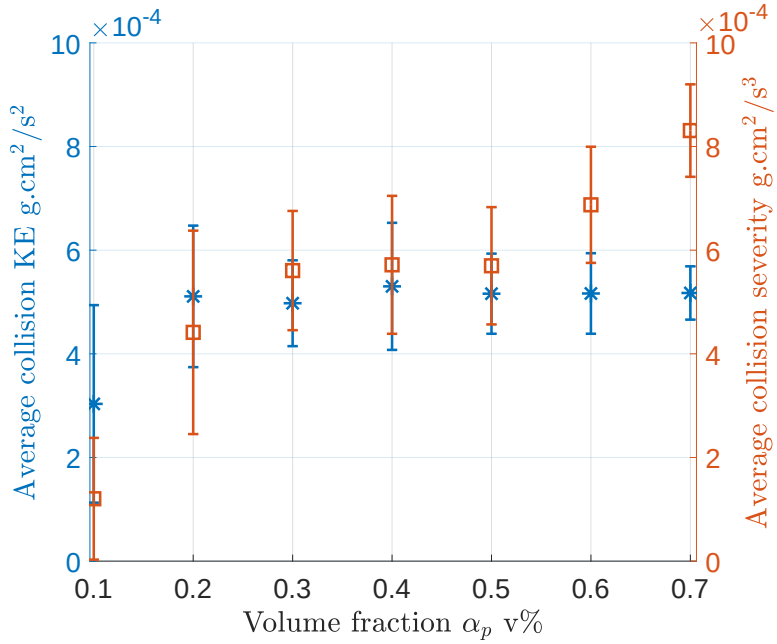

Figure 4.16: Global average of collision impact metrics over the entire experimental time for all volume fractions in comparison with relevant models. **Left, blue**) Average collision kinetic energy KE ($\mathrm{g\,cm^2/s^2}$). **Right, red**) Average collision severity TCS ($\mathrm{g\,cm^2/s^3}$). $*$: collision kinetic energy KE (Equation 4.5); □: collision severity TCS (Equation 4.6).

distributed counts of impulses and durations after outlier removal is thus 4139 compared to the original 4399 total collision counts (94%). The z-axis and the colour-bar correspond to the percentage of these counts (occurrences) for each associated bin. Panel a) represents the 3D view while panel b) compacts the view into a 2D (top-view), which could be regarded as a heat-map. Hence, the total sum of the 3D bars (a) or areas (b) accumulates to 100%. As an example, the bin corresponding to the $0.4 - 0.6 \times 10^{-4}$ g cm/s impulse exchanged and $2 - 4$ ms duration contains roughly 4.5% of the distributed events. Recall that for each interactive pair: $d_{eff} < 2.5 d_p$ (see Table 4.2).

Although the majority of the distributions are concentrated around $2 - 6$ ms durations and $0.4 - 2.2 \times 10^{-4}$ g cm/s impulses, the rest could not be neglected a priori. By estimating the skewness and kurtosis statistical properties for binned impulses, it is found that the distribution is right-tailed ($skew > 0$) where most events are on the lower impulse side, with a tail of larger values spreading to the other side and that the tail is heavy ($kurt > 3$), meaning that small fractions of events exchange much larger momentum. Hence, the distribution is heterogeneous, with the tail carrying a disproportionate share of the total exchanged momentum: the median is around 1.5×10^{-4} g cm/s lower than the mean that is pushed up by the sparse fractions on the right side (tail) to 2 g cm/s. Overall, it is evident that the small fractions dispersed at high impulses $2.6 - 5 \times 10^{-4}$ g cm/s also contain longer durations $10 - 16$ ms (sustained interactions). This is further interpreted by investigating

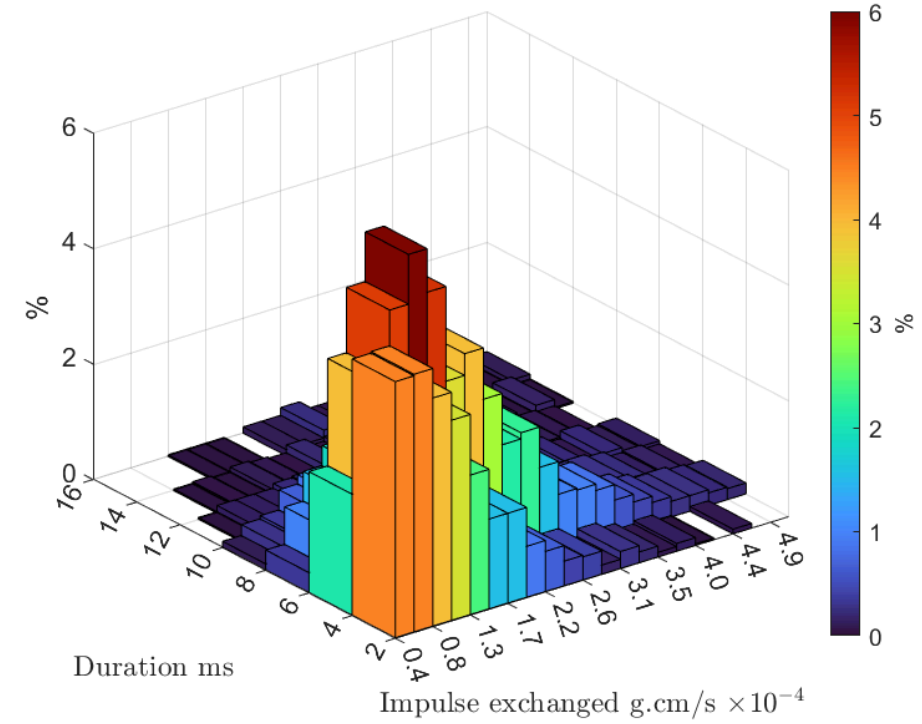

(a)

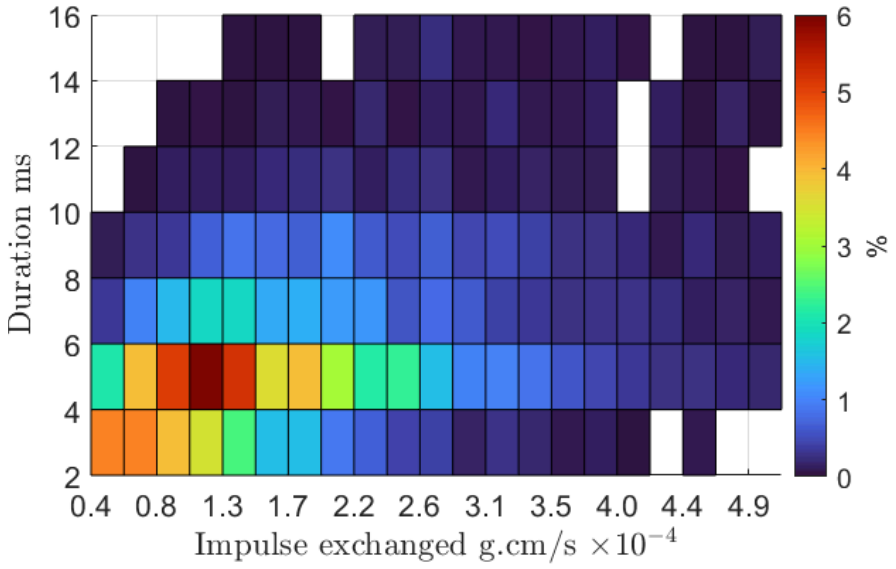

(b)

Figure 4.17: Distribution of impulse exchanged of J (g cm/s) of interactive pairs against the corresponding lasting durations (ms) for $\alpha_p = 0.7$ v%. **a)** 3D view. **b)** 2D view (top-view). z axis and colour-bar correspond counts percentage of events (%). Duration binning is limited to the acquisition rate (500 Hz = 2 ms).

bin-wise profiles.

For each duration bin, impulse events are gathered and the median and mean are computed. This is shown in Figure 4.18a) where the x axis represents the duration bins and within each bin the horizontal sum of all impulses percent counts is displayed as yellow bars (right y axis), i.e., the overall duration distributions of the interactive pairs. The median and mean values of the impulses exchanged that fall within every duration bin are also plotted (left y axis), except for the bins beyond 12 ms where the median and mean are not computed simply because the events contribute to $< 1\%$ and thus it is insufficient to make a reasonable averaging. The plot is indeed a complementary to the previous figure as it reveals how impulses evolve with time, and further demonstrates the asymmetry of the distribution. In Figure 4.18a), 90% of the events are heavily concentrated at short durations ($2 - 8$ ms); the bar heights fall steeply thereafter and contribute to $< 1\%$ from 14 ms and above. As a reminder, this distribution is in accordance with the fact that the minimum quantization is 2 ms which corresponds to a 500 Hz acquisition. Nevertheless, one may notice an increase in the median and mean impulses by a factor of 4 between 2 and 12 ms, which means that longer contacts tend to exchange more momentum. Moreover, the mean impulse is always higher than the median value for each corresponding duration bin, highlighting the heavy right tail. Note that a full statistical distribution of the impulses is reported in the Appendix in Figure A.4.5 as a box plot.

From impulses and durations of events, one can estimate the total force exerted during the interaction using (Equation 4.3). Figure 4.18b) reveals the mean and median estimated forces at different event durations. Forces are scaled by the volume of a single particle F_{total}/V_p and expressed in N/m^3. The mean and median forces are not constant and decrease, indicating that the impulse does not scale linearly with interaction duration. So, even if particles exchange higher impulses at longer contact durations, this does not correspond to higher impact intensities, as the force decreases with impact duration. Specifically, while the interaction period increases by a factor of 6 between shorter and longer durations, the impulse only increases by a factor of 4, leading to a decrease of forces by a factor of ≈ 1.5. In other words, while prolonged contacts promote greater cumulative momentum exchange, the maximum mechanical load is significantly higher during short-duration, high-intensity interactions. Ultimately, regardless of contact dynamics, the magnitudes of these estimated forces represent a significant and persistent physical impact that acts on the particles within the flow field. Such values are comparable to the fluid pressure force estimated by Montante et al. [64] for particles of 0.774 mm in size and to the lift force estimated by Madani et al. [41] for particles of 0.168 mm in size.

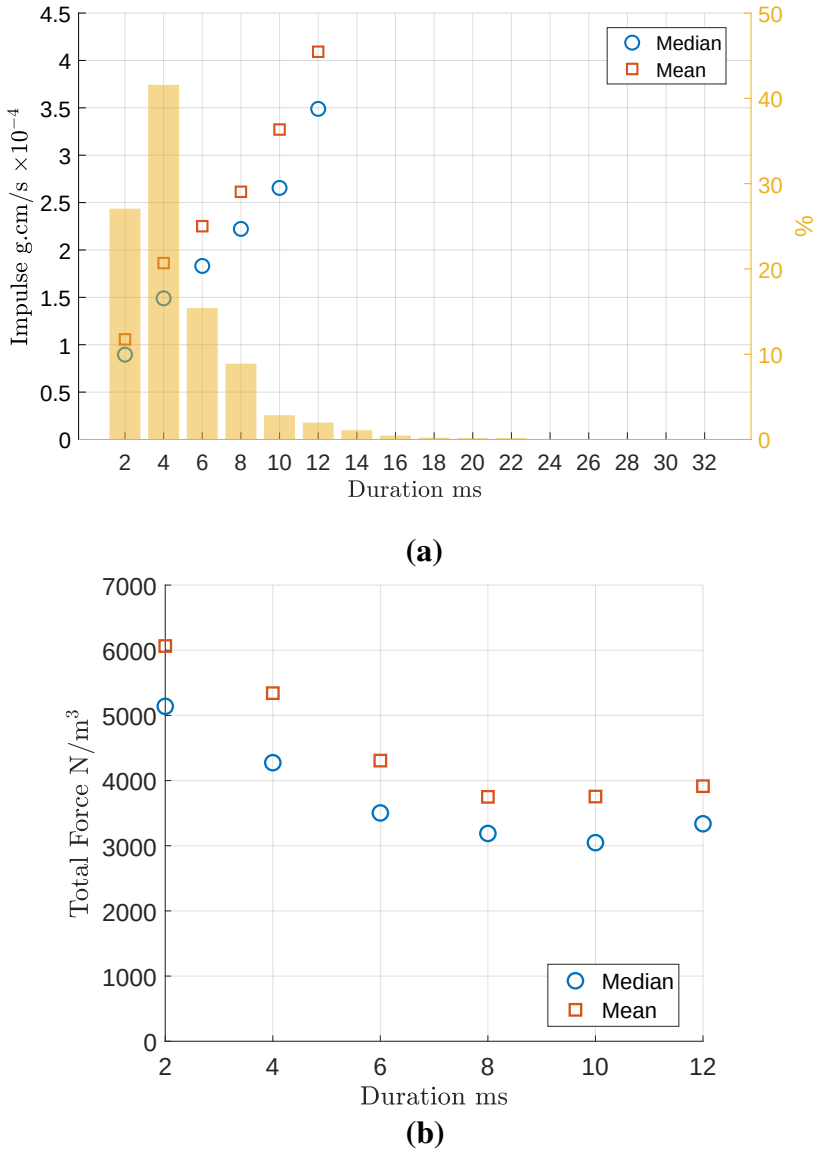

Figure 4.18: a) (Right) Distribution of the lasting durations (ms) of the interactive pairs for $\alpha_p = 0.7$ v%. (%) represent the percent of events of the duration distribution. **(Left)** The evolution of mean and median Impulse exchanged J (g cm/s) of each corresponding duration. Mean and median Impulse values are ignored for $t \geq 14$ s due to low event counts. **b)** The evolution of total force F_{total} (N/m^3) estimated from interactive pairs against the duration of interaction (ms). □: Mean value; ◯: Median value.

4.4 Conclusions

This study quantified particle–particle interactions in a stirred tank relevant to stem cell culture using 2D PTV in a refractive index matched system (PMMA/NH_4SCN). A two-step post-processing method was applied to address the limitations of 2D tracking in a 3D flow and to filter out the colliding particles from PTV trajectories. Candidate pairs were first detected using a distance criterion and overlapped/stacked detections were removed. Collision events were then validated using a path-change criterion based on a relative angle threshold during interaction, with multiple collisions being addressed for the first time. The resulting database was used to compute collision statistics and impact-related metrics for different volume fractions $0.1 \leq \alpha_p \leq 0.7$ v%.

As a result, the average collision rate increased with particle concentration and reached values of the order of 200 s^{-1} at 0.7 v%. The average collision frequency increased by approximately a factor of 4 between $\alpha_p = 0.1$ and 0.7 v% to reach 1.6 s^{-1}. As one may expect, this indicates that the increase in total collision activity is mainly due to the increase in the number of particle pairs available for interaction.

Compared with global collision models from the literature, Kramer and Clark [19] shear-based model reproduced the trend of the measured collision rate, but underestimated its magnitude by a factor of $\frac{4}{3} \approx 1.33$; applying this factor to the model improved agreement with the experimental values. On the other hand, Wang et al. [22] model underestimated the measured rates more severely by a factor of 7.

Taking into account impact-related metrics, the mean kinetic energy exchanged during collisions increased between $\alpha_p = 0.1$ and $\alpha_p = 0.2$ v% and then remained approximately constant within the tested range. In contrast, the collision severity proposed by Cherry and Papoutsakis [56] increased with concentration, as it mainly followed the trend of the collision frequency.

The impulse exchanged during interaction was statistically distributed against the corresponding duration of each particle pair and was found to be heavily right-tailed. Most events occurred at short durations (2–8 ms) with lower impulses, and a smaller fraction of events contributed higher impulses at longer interactions. Although bin-wise analysis showed that the mean and median impulse increased with duration, the estimated force values actually decreased with longer durations.

Future work should include a more comprehensive and quantitative comparison with PIV to further assess and validate the flow generated with PTV. In addition, a 3D tracking could also be implemented to resolve the collision environment, combined with measurements of the liquid phase to separate fluid hydrodynamic contributions from inter-particle interaction

effects. This database offers a more comprehensive understanding to support the choice, validation, and refinement of numerical models (CFD) for stirred tank bioreactors. It also opens the door for a more detailed comparative analysis with experiments featuring higher time resolution, which would allow for a rigorous characterization of specific collision dynamics.

Bibliography

[1] S. Balachandar, *Fundamentals of dispersed multiphase flows*. Cambridge University Press, 2024.

[2] S. Elghobashi, "On predicting particle-laden turbulent flows," *Applied scientific research*, vol. 52, no. 4, pp. 309–329, 1994.

[3] R. S. S. R. E. Shah, B. Sajjadi, A. A. A. Raman, and S. Ibrahim, "Solid-liquid mixing analysis in stirred vessels," *Reviews in Chemical Engineering*, vol. 31, no. 2, pp. 119–147, 2015.

[4] J. M. Champney, A. R. Dobrovolskis, and J. N. Cuzzi, "A numerical turbulence model for multiphase flows in the protoplanetary nebula," *Physics of Fluids*, vol. 7, no. 7, pp. 1703–1711, 1995.

[5] C. Dominik, J. Blum, J. Cuzzi, and G. Wurm, "Growth of dust as the initial step toward planet formation," *arXiv preprint astro-ph/0602617*, 2006.

[6] M. Pinsky, A. Khain, and M. Shapiro, "Stochastic effects of cloud droplet hydrodynamic interaction in a turbulent flow," *Atmospheric research*, vol. 53, no. 1-3, pp. 131–169, 2000.

[7] R. A. Shaw, "Particle-turbulence interactions in atmospheric clouds," *Annual Review of Fluid Mechanics*, vol. 35, no. 1, pp. 183–227, 2003.

[8] M. Balthasar, F. Mauss, A. Knobel, and M. Kraft, "Detailed modeling of soot formation in a partially stirred plug flow reactor," *Combustion and Flame*, vol. 128, no. 4, pp. 395–409, 2002.

[9] J. Z. Wen, M. Thomson, S. Park, S. Rogak, and M. Lightstone, "Study of soot growth in a plug flow reactor using a moving sectional model," *Proceedings of the Combustion Institute*, vol. 30, no. 1, pp. 1477–1484, 2005.

[10] M. Mokashi, A. B. Shirsath, A. Çelik, P. Lott, H. Müller, S. Tischer, L. Maier, J. Bode, D. Schlereth, F. Scheiff, *et al.*, "Methane pyrolysis in packed bed reactors: kinetic modeling, numerical simulations, and experimental insights," *Chemical Engineering Journal*, vol. 485, p. 149684, 2024.

[11] H. A. Jakobsen, H. Lindborg, and C. A. Dorao, "Modeling of bubble column reactors: progress and limitations," *Industrial & engineering chemistry research*, vol. 44, no. 14, pp. 5107–5151, 2005.

[12] T. Wang, J. Wang, and Y. Jin, "Population balance model for gas- liquid flows: Influence of bubble coalescence and breakup models," *Industrial & engineering chemistry research*, vol. 44, no. 19, pp. 7540–7549, 2005.

[13] J. Qian and C. K. Law, "Regimes of coalescence and separation in droplet collision," *Journal of fluid mechanics*, vol. 331, pp. 59–80, 1997.

[14] L. Rekvig and D. Frenkel, "Molecular simulations of droplet coalescence in oil/water/surfactant systems," *The Journal of chemical physics*, vol. 127, no. 13, 2007.

[15] P. Koh and M. Schwarz, "Cfd modelling of bubble–particle collision rates and efficiencies in a flotation cell," *Minerals Engineering*, vol. 16, no. 11, pp. 1055–1059, 2003.

[16] H. Jiao, W. Chen, A. Wu, Y. Yu, Z. Ruan, R. Honaker, X. Chen, and J. Yu, "Flocculated unclassified tailings settling efficiency improvement by particle collision optimization in the feedwell," *International Journal of Minerals, Metallurgy and Materials*, vol. 29, no. 12, pp. 2126–2135, 2022.

[17] M. v. Smoluchowski, "Versuch einer mathematischen theorie der koagulationskinetik kolloider lösungen," *Zeitschrift für physikalische Chemie*, vol. 92, no. 1, pp. 129–168, 1918.

[18] P. Saffman and J. Turner, "On the collision of drops in turbulent clouds," *Journal of Fluid Mechanics*, vol. 1, no. 1, pp. 16–30, 1956.

[19] T. A. Kramer and M. M. Clark, "Influence of strain-rate on coagulation kinetics," *Journal of Environmental Engineering*, vol. 123, no. 5, pp. 444–452, 1997.

[20] J. Williams and R. Crane, "Particle collision rate in turbulent flow," *International Journal of Multiphase Flow*, vol. 9, no. 4, pp. 421–435, 1983.

[21] S. Sundaram and L. R. Collins, "Collision statistics in an isotropic particle-laden turbulent suspension. part 1. direct numerical simulations," *Journal of Fluid Mechanics*, vol. 335, pp. 75–109, 1997.

[22] L.-P. Wang, A. S. Wexler, and Y. Zhou, "Statistical mechanical description and modelling of turbulent collision of inertial particles," *Journal of Fluid Mechanics*, vol. 415, pp. 117–153, 2000.

[23] J. Abrahamson, "Collision rates of small particles in a vigorously turbulent fluid," *Chemical Engineering Science*, vol. 30, no. 11, pp. 1371–1379, 1975.

[24] C. Meyer and D. Deglon, "Particle collision modeling–a review," *Minerals Engineering*, vol. 24, no. 8, pp. 719–730, 2011.

[25] F. Kruis and K. Kusters, "The collision rate of particles in turbulent flow," *Chemical Engineering Communications*, vol. 158, no. 1, pp. 201–230, 1997.

[26] B. Hoomans, J. Kuipers, W. J. Briels, and W. P. M. van Swaaij, "Discrete particle simulation of bubble and slug formation in a two-dimensional gas-fluidised bed: a hard-sphere approach," *Chemical Engineering Science*, vol. 51, no. 1, pp. 99–118, 1996.

[27] J. Shäfer, S. Dippel, and D. Wolf, "Force schemes in simulations of granular materials," *Journal de physique I*, vol. 6, no. 1, pp. 5–20, 1996.

[28] N. Deen, M. V. S. Annaland, M. A. Van der Hoef, and J. Kuipers, "Review of discrete particle modeling of fluidized beds," *Chemical engineering science*, vol. 62, no. 1-2, pp. 28–44, 2007.

[29] H. Zhu, Z. Zhou, R. Yang, and A. Yu, "Discrete particle simulation of particulate systems: a review of major applications and findings," *Chemical Engineering Science*, vol. 63, no. 23, pp. 5728–5770, 2008.

[30] H. Zhou, G. Mo, J. Zhao, and K. Cen, "Dem–cfd simulation of the particle dispersion in a gas–solid two-phase flow for a fuel-rich/lean burner," *Fuel*, vol. 90, no. 4, pp. 1584–1590, 2011.

[31] J. Jin, S.-Y. Shi, G.-L. Liu, Q.-H. Zhang, and W. Cong, "Numerical simulation of flow and particle collision in a rotating-drum bioreactor," *Chemical engineering & technology*, vol. 35, no. 2, pp. 287–293, 2012.

[32] L. Shuai, Y. Runquan, W. Caili, S. Yang, and W. Huaifa, "Simulation of the solid particles behavior in 3d stirred tank using cfd-dem coupling approach," *Particulate Science and Technology*, vol. 40, no. 8, pp. 911–921, 2022.

[33] B. Blais, M. Lassaigne, C. Goniva, L. Fradette, and F. Bertrand, "Development of an unresolved cfd–dem model for the flow of viscous suspensions and its application to solid–liquid mixing," *Journal of Computational Physics*, vol. 318, pp. 201–221, 2016.

[34] D. Wadnerkar, M. O. Tade, V. K. Pareek, and R. P. Utikar, "Cfd simulation of solid–liquid stirred tanks for low to dense solid loading systems," *Particuology*, vol. 29, pp. 16–33, 2016.

[35] L. Xie and Z.-H. Luo, "Modeling and simulation of the influences of particle-particle interactions on dense solid–liquid suspensions in stirred vessels," *Chemical Engineering Science*, vol. 176, pp. 439–453, 2018.

[36] L. Li, Z. Gu, W. Xu, Y. Tan, X. Fan, and D. Tan, "Mixing mass transfer mechanism and dynamic control of gas-liquid-solid multiphase flow based on vof-dem coupling," *Energy*, vol. 272, p. 127015, 2023.

[37] X. Luo, J. Yu, B. Wang, and J. Wang, "Heat transfer and hydrodynamics in stirred tanks with liquid-solid flow studied by cfd–dem method," *Processes*, vol. 9, no. 5, p. 849, 2021.

[38] J. Derksen, "Numerical simulation of solids suspension in a stirred tank," *AIChE Journal*, vol. 49, no. 11, pp. 2700–2714, 2003.

[39] A. Kazemzadeh, F. Ein-Mozaffari, and A. Lohi, "Hydrodynamics of solid and liquid phases in a mixing tank containing high solid loading slurry of large particles via tomography and computational fluid dynamics," *Powder Technology*, vol. 360, pp. 635–648, 2020.

[40] Q. Kang, X. Feng, C. Yang, and J. Wang, "DEM-VOF simulations on the drawdown mechanisms of floating particles at free surface in turbulent stirred tanks," *Chemical Engineering Journal*, vol. 431, p. 133275, 2022.

[41] M. Madani, A. Delafosse, S. Calvo, and D. Toye, "Solid–liquid flow analysis using simultaneous two-phase piv in a stirred tank bioreactor," *Fluids*, vol. 11, no. 1, p. 17, 2026.

[42] T. Hwang, D. Doh, H. Jo, M. Tsubokura, B. Piao, S. Kuroda, T. Kobayashi, K. Tanaka, and M. Takei, "Analysis of fluid–elastic-structure interactions in an impinging jet with a dynamic 3d-ptv and non-contact 6d-motion tracking system," *Chemical Engineering Journal*, vol. 130, no. 2, pp. 153–164, 2007.

[43] J. Oliveira, C. Van der Geld, and J. G. Kuerten, "Lagrangian velocity and acceleration statistics of fluid and inertial particles measured in pipe flow with 3d particle tracking velocimetry," *International journal of multiphase flow*, vol. 73, pp. 97–107, 2015.

[44] R. Shokri, S. Ghaemi, D. Nobes, and R. Sanders, "Investigation of particle-laden turbulent pipe flow at high-reynolds-number using particle image/tracking velocimetry (piv/ptv)," *International Journal of Multiphase Flow*, vol. 89, pp. 136–149, 2017.

[45] M. Monica, J. H. Cushman, and A. Cenedese, "Application of photogrammetric 3d-ptv technique to track particles in porous media," *Transport in porous media*, vol. 79, no. 1, pp. 43–65, 2009.

[46] A. Aguilar-Corona, R. Zenit, and O. Masbernat, "Collisions in a liquid fluidized bed," *International journal of multiphase flow*, vol. 37, no. 7, pp. 695–705, 2011.

[47] Z. Jiang, T. Hagemeier, A. Bueck, and E. Tsotsas, "Experimental measurements of particle collision dynamics in a pseudo-2d gas-solid fluidized bed," *Chemical Engineering Science*, vol. 167, pp. 297–316, 2017.

[48] F. Alberini, L. Liu, E. Stitt, and M. Simmons, "Comparison between 3-d-ptv and 2-d-piv for determination of hydrodynamics of complex fluids in a stirred vessel," *Chemical Engineering Science*, vol. 171, pp. 189–203, 2017.

[49] M. Romano, F. Alberini, L. Liu, M. Simmons, and E. Stitt, "Development and application of 3d-ptv measurements to lab-scale stirred vessel flows," *Chemical Engineering Research and Design*, vol. 172, pp. 71–83, 2021.

[50] Q. Laine, T. Randriamanantena, F. Lamadie, and E. Olmos, "Experimental study of velocity and turbulence fields in a square mixer-settler tank: Comparison of shake the box ptv and 2d2c piv," *Chemical Engineering Science*, vol. 275, p. 118636, 2023.

[51] M. Barigou, "Particle tracking in opaque mixing systems: An overview of the capabilities of pet and pept," *Chemical Engineering Research and Design*, vol. 82, no. 9, pp. 1258–1267, 2004.

[52] A. Guida, A. W. Nienow, and M. Barigou, "Pept measurements of solid–liquid flow field and spatial phase distribution in concentrated monodisperse stirred suspensions," *Chemical Engineering Science*, vol. 65, no. 6, pp. 1905–1914, 2010.

[53] L. Liu and M. Barigou, "Lagrangian particle tracking in mechanically agitated polydisperse suspensions: Multi-component hydrodynamics and spatial distribution," *International Journal of Multiphase Flow*, vol. 73, pp. 80–89, 2015.

[54] F. Chiti, S. Bakalis, W. Bujalski, M. Barigou, A. Eaglesham, and A. W. Nienow, "Using positron emission particle tracking (pept) to study the turbulent flow in a baffled vessel agitated by a rushton turbine: Improving data treatment and validation," *Chemical Engineering Research and Design*, vol. 89, no. 10, pp. 1947–1960, 2011.

[55] D. Guha, P. Ramachandran, and M. Dudukovic, "Flow field of suspended solids in a stirred tank reactor by lagrangian tracking," *Chemical Engineering Science*, vol. 62, no. 22, pp. 6143–6154, 2007.

[56] R. S. Cherry and E. T. Papoutsakis, "Physical mechanisms of cell damage in microcarrier cell culture bioreactors," *Biotechnology and bioengineering*, vol. 32, no. 8, pp. 1001–1014, 1988.

[57] M. Madani, A. Delafosse, S. Calvo, and D. Toye, "Rim-piv measurements of solid–liquid flow in a stirred tank used for mesenchymal stem cell culture," *Fluids*, vol. 10, no. 10, p. 272, 2025.

[58] Y. Yao, C. S. Criddle, and O. B. Fringer, "Competing flow and collision effects in a monodispersed liquid–solid fluidized bed at a moderate archimedes number," *Journal of Fluid Mechanics*, vol. 927, p. A28, 2021.

[59] A. Delafosse, M.-L. Collignon, M. Crine, and D. Toye, "Estimation of the turbulent kinetic energy dissipation rate from 2d-piv measurements in a vessel stirred by an axial mixel ttp impeller," *Chemical Engineering Science*, vol. 66, no. 8, pp. 1728–1737, 2011.

[60] J. Chéron, C. Loubière, S. Delaunay, A.-G. Guezennec, and E. Olmos, "Cfd numerical simulation of particle suspension and hydromechanical stress in various designs of multi-stage bioleaching reactors," *Hydrometallurgy*, vol. 197, p. 105490, 2020.

[61] S. Chen, P.-Y. Passaggia, and B. L. White, "Particle radial velocity and concentration kernels estimation in isotropic grid turbulence experiments of inertialess particles at small separation distances," *Journal of Fluid Mechanics*, vol. 942, p. A39, 2022.

[62] S. Bhattacharya and P. P. Vlachos, "Volumetric particle tracking velocimetry (ptv) uncertainty quantification," *Experiments in Fluids*, vol. 61, no. 9, p. 197, 2020.

[63] D. Schanz, S. Gesemann, and A. Schröder, "Shake-the-box: Lagrangian particle tracking at high particle image densities," *Experiments in fluids*, vol. 57, no. 5, p. 70, 2016.

[64] G. Montante, A. Paglianti, and F. Magelli, "Analysis of dilute solid–liquid suspensions in turbulent stirred tanks," *Chemical Engineering Research and Design*, vol. 90, no. 10, pp. 1448–1456, 2012.

[65] K. Grayson, C. De Silva, N. Hutchins, and I. Marusic, "Impact of mismatched and misaligned laser light sheet profiles on piv performance," *Experiments in Fluids*, vol. 59, no. 1, p. 2, 2018.

Appendix

The particle number density for each concentration α_p is estimated from the PTV analysis by counting the number of unique particles present in each frame and then reversely used to estimate the depth (thickness) w of the laser sheet. The idea is based on the fact that all particles are homogeneously suspended at 150 rpm and hence uniform volume fractions are dispersed in the field of view. From each frame, the particles are counted and the total volume of particles is used to estimate the total volume of the measured sheet for each volume fraction α_p v%. As a result, the laser depth w is computed by dividing the total estimated volume of the domain by the total area. The total area is simply the sum of the pixels multiplied by the square of the scale factor SF that represents the real size. The laser depth estimation for each volume fraction case is shown in Table A.4.1. The evaluations are fairly consistent with a mean of $w = 3.51$ mm which is in agreement with the measured laser thickness 3 – 4 mm. Note that it is notoriously difficult and challenging to experimentally measure the laser sheet thickness [65].

Table A.4.1: Estimated laser depth w (mm) for different particle volume fractions

α_p v%	0.1	0.2	0.3	0.4	0.5	0.6	0.7
Laser depth w mm	3.588	3.677	3.361	3.368	3.351	3.560	3.627

In Figure A.4.1, the drop in the counts of collisions detected at $\alpha_p = 0.7$ v% with $\theta_{threshold} = 37°$ reaches 93% compared to $\theta_{threshold} = 25°$ (from 4399 to around 300 collision count). This also worsens with lower volume fractions with approximately no collisions detected at $\theta_{threshold} = 37°$.

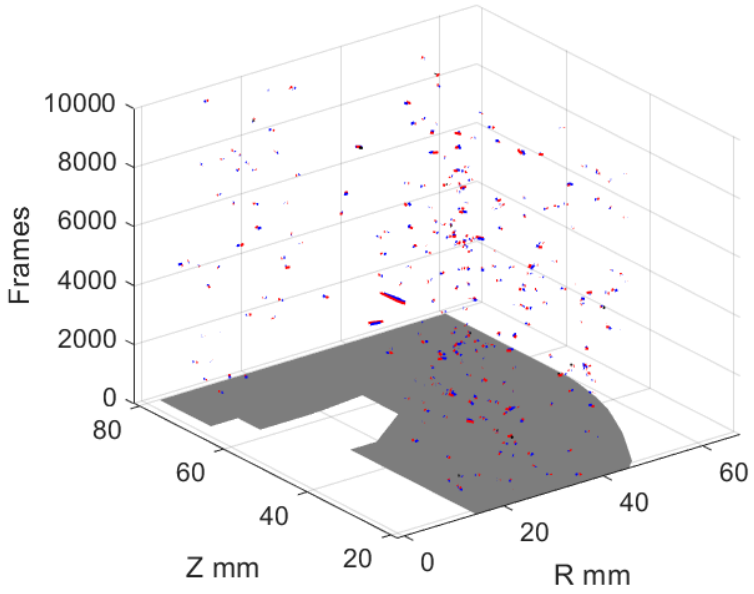

Figure A.4.1: Collisions detected with threshold angle $\theta = 37°$ for $\alpha_p = 0.7$v%. Total collisions counted are approximately 300.

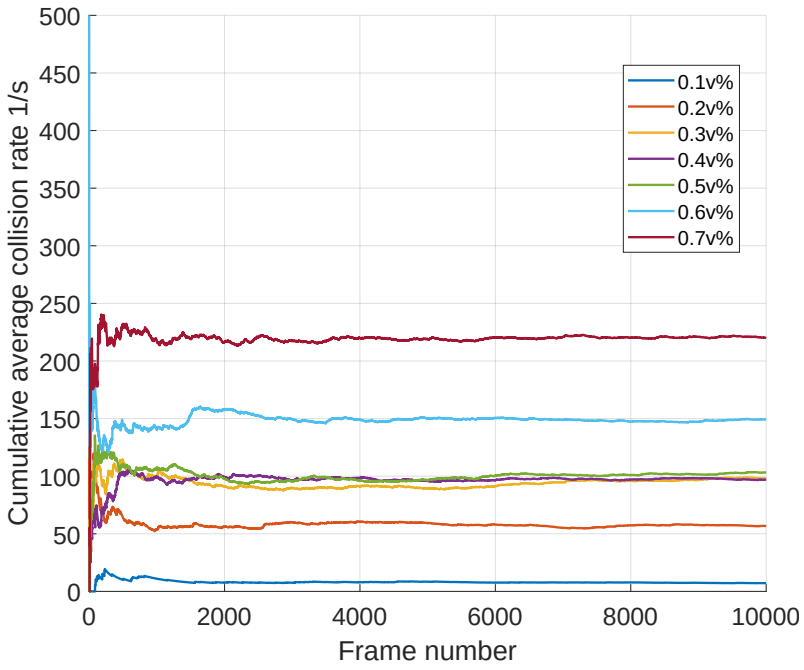

Figure A.4.2: Statistical convergence of collision rate r for all volume fractions measured.

In Figure A.4.3, at $\alpha_p = 0.1$ v%, the convergence is reached less rapidly (requiring more recording time). This is due to the fact that low particles are detected on the laser sheet, which results in lower detected collisions. The latter also follows the decreasing relative

velocity condition and hence the convergence of KE data occurred after frame number 6000 (t= 12 s).

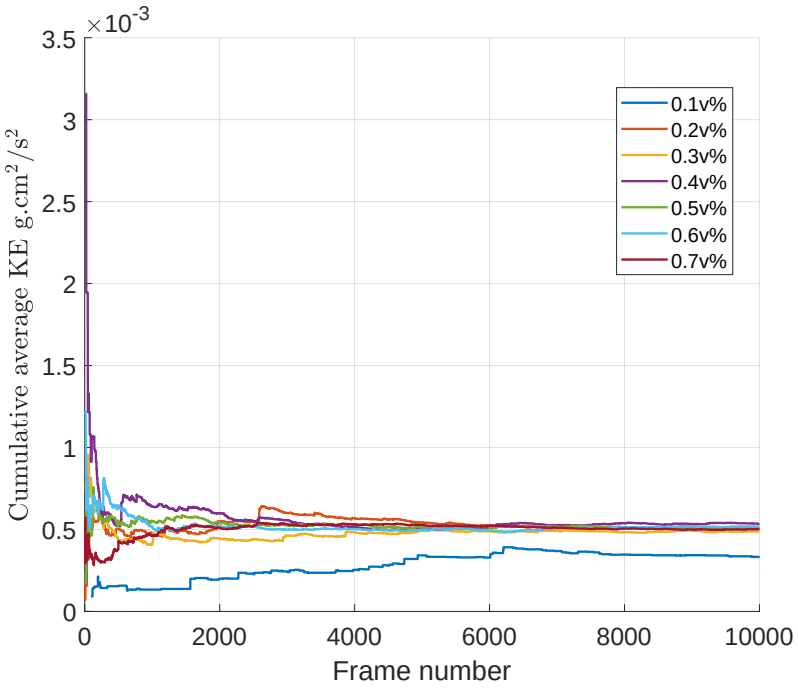

Figure A.4.3: Statistical convergence of KE for all volume fractions measured.

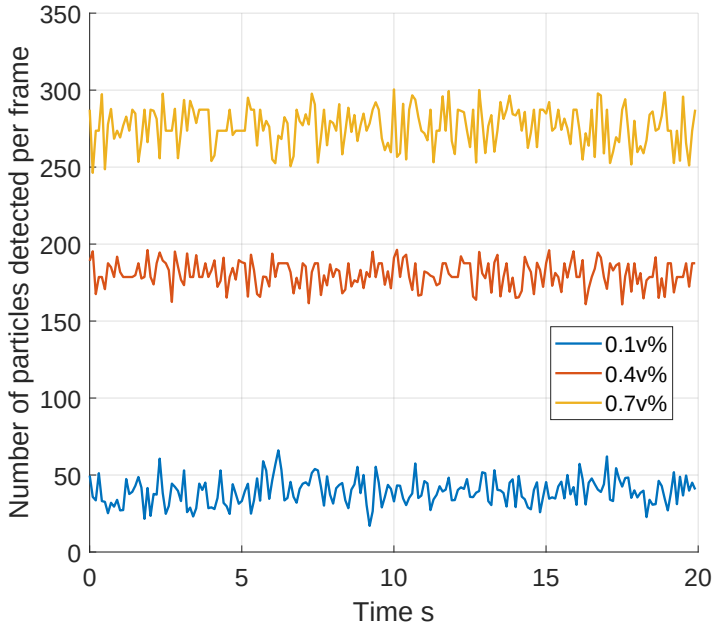

Figure A.4.4: The evolution of the number of particles detected per frame, from raw PTV results, with experimental recording time for different volume fractions.

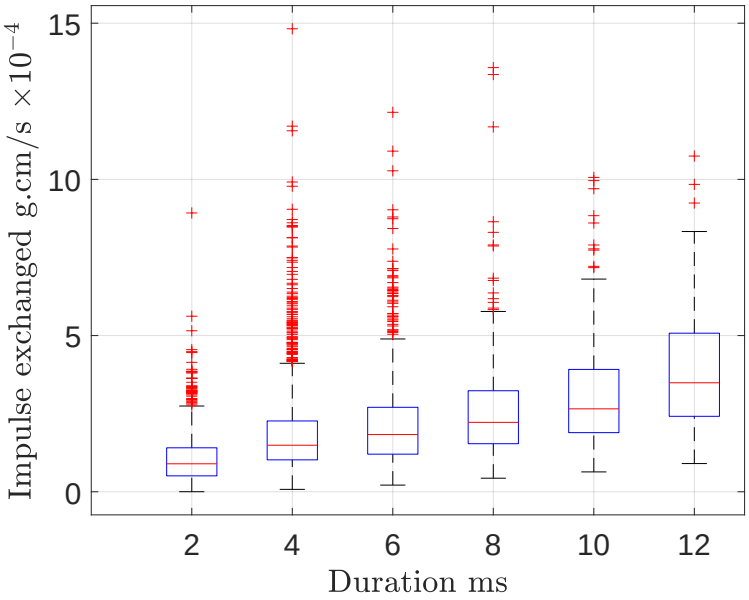

Figure A.4.5: Statistical distribution (box plot) of the impulse exchanged J for each corresponding duration. at α_p = 0.7 v%.

Chapter 5

Conclusions and Perspectives

5.1 Concluding Remarks

This thesis established and explored a refractive index matched (RIM) solid–liquid system to enable quantitative optical measurements in a stirred tank configuration relevant to microcarrier-based stem cell bioreactors, generally of specific characteristics: microparticles of microcarrier size $d_p = 100 - 300$ µm, volume fractions in the range $0.1 \leq \alpha_p \leq 3$ v%, a highly close density between the dispersed and carrier phases $\rho_f/\rho_p \approx 0.96 - 0.97$, and agitation at the just suspended state N_{js}, which is critical for mitigating hydro-mechanical stresses while ensuring expansion quality and quantity. In particular, this work addressed turbulence modulation, solid–liquid interactions, and interparticle collisions. First, a PMMA/NH_4SCN system was selected after a comparative assessment of candidate materials and fluids, with emphasis on maintaining representative particle size, low viscosity range, and, critically, a close density match. The analysis showed that candidates with a larger density mismatch lead to substantially higher settling velocities and just-suspension speeds, and are therefore not representative of the targeted suspension conditions. On this basis, PMMA/NH_4SCN was retained as a suitable surrogate for Cytodex-1/water and was used consistently throughout the experimental chapters.

In chapter two, one-phase 2D PIV was used to quantify how microparticle addition affects liquid-phase hydrodynamics. Over the investigated range, particle loading had no clear impact on the mean liquid velocity magnitude, both globally and locally, including the impeller discharge and near-wall regions. The main observable change was a slight shift in the recirculation pattern at the 0.5 and 3 v% concentration. The liquid-phase turbulence levels, quantified through turbulent kinetic energy TKE, were also only weakly affected; differences between single-phase and particle-laden cases at local-average level were generally within experimental uncertainty ($\approx 10\%$), with the exception of localized

damping effect near the impeller region (≈ 20%). Overall, this is the first time that turbulence modulation has been addressed for this specific solid–liquid properties at such concentrations. A benchmark dataset was thus obtained to support further understanding of turbulence modulation.

In chapter three, simultaneous two-phase 2D PIV provided solid–liquid measurements of mean flow, turbulence, and slip in the same tank configuration but up to $\alpha_p = 0.5$ v% volume fraction. The mean liquid flow remained close to the single-phase reference as established in chapter two, whereas the solid phase exhibited lower velocities (≈ 20%), particularly in the impeller discharge zone, and a concentration-dependent modification of the solid-phase circulating loop structure. Turbulence levels were found to diverge between phases: liquid-phase turbulent kinetic energy TKE increased modestly with particle loading in the impeller discharge, while solid-phase TKE decreased substantially in the same region, to reach 50% at $\alpha_p = 0.5$ v%. The simultaneous acquisition and the same spatial resolution also enabled direct slip velocity maps, showing particle lag in the impeller stream and larger deviations near the wall, with slip velocities increasing with concentration. An approximate force balance based on measured slip velocities indicated that drag dominated lift under the present conditions, and that it is globally satisfied in the tank bulk. The analysis lastly highlighted the need for CFD-based modelling to account for missing local strain and vortex topology effects.

In chapter four, 2D PTV was used to quantify particle-particle interactions in the same RIM system but for 3 times larger PMMA particles at various loadings $0.1 \leq \alpha_p \leq 0.7$ v%. A dedicated two-step post-processing scheme was developed on MATLAB (2023a) to filter-out colliding pairs from a planar tracking in a three-dimensional flow. Candidate pairs were detected using a distance criterion with removal of overlapped/stacked detections, and collision events were then validated using a path-change criterion based on a relative angle threshold during interaction. The resulting database provided direct experimental collision statistics and impact-related metrics. The collision rate increased with concentration and reached values of the order of 200 s^{-1} at $\alpha_p = 0.7$ v%, while the collision frequency increased by approximately a factor of four over the tested range. Comparison with global collision models showed that the Kramer and Clark shear-based model reproduced the measured trend but underestimated the magnitude by a factor of $\frac{4}{3}$, and applying this factor improved agreement with the experimental results; the Wang et al. model underestimated the rates more strongly. The mean kinetic energy exchanged during collisions increased from $\alpha_p = 0.1$ to 0.2 v% and then remained approximately constant, whereas collision severity increased primarily with collision frequency. Finally, the impulse–duration analysis revealed a strongly right-tailed distribution: most events occurred at short durations with lower impulses, while a smaller fraction contributed higher impulses and longer interactions; although impulse increased with duration, the estimated force decreased with increasing

duration.

Overall, the thesis provides an experimental RIM strategy suitable for two-phase optical measurements in a 2D plane and at steady state. These results act as a consistent experimental basis for the selection and validation of numerical approaches, while also extending the analysis to additional conditions and cases.

5.2 Perspectives

First, to achieve a more comprehensive characterization of the interactions, the research scope must be broadened to include the boundary effects (wall region) of the tank. The methodology used in chapter four for particle-particle collisions could be extended as well to detect particle-wall collisions. In this case, more information related to the rate, frequency and impact is provided, which could be compared with the statistics of particle-particle interactions. However, to access such information, more attention is needed to enhance the spatial resolution near the wall, especially with the curvature body of the tank. This means that another experimental set-up is required with the camera being focused on a region of interest near the wall accomplished at higher spatial resolution. Thus, a more detailed understanding of the dominant behaviour and intensity of each type (particle-particle and particle-wall interactions) could then be compared and evaluated.

Building upon the findings in this work, there is an opportunity to perform simultaneous measurements of the liquid and solid phases at high temporal resolution in a region of interest. The present datasets indicate that slip and collision activity are spatially different, which motivates a targeted measurement strategy that focuses on the location where shear effects are dominant and collision interactions are largest: near the periphery of the impeller discharge (shear effect) and the center of the circulating loop (high collisions). High-speed imaging with increased spatial resolution, combined with simultaneous PIV (liquid phase) and PTV (solid particles) in such a field of view, would enable direct evaluation of local strain rate, interfacial forces, and collision impact during interaction events. This approach can be initially implemented in 2D to establish the methodology before extending it to 3D.

Beyond that, an important next step is the transition from planar measurements to three-dimensional experimental characterization. Both two-phase PIV and PTV remain affected by out-of-plane motion when performed in a laser sheet, particularly in regions of strong tangential effects. Implementing 3D measurements would reduce the dependence on planar assumptions and improve the interpretation of both phase coupling and collision events. For the liquid phase, stereo-PIV or tomographic PIV could provide three-component 3D velocity fields, which permits the evaluation of vortex-structures relevant for interfacial forces. Whereas for the dispersed phase, a multi-camera system 3D PTV would enable

reconstruction of particle trajectories in a measurement volume. Such a configuration would allow the identification of collisions based on 3D distances to validate the assumptions made and the model developed in 2D PTV.

Further work of the RIM concept could also examine a broader operating range, including different agitation speeds and particle properties. Varying agitation rate and particle size (within experimental detectability) would broaden the ranges of Reynolds and Stokes numbers and support the generalization of trends. In chapters two & three, the rotational speed N was fixed for a complete homogeneous suspension, while the analysis at the N_{js} of each concentration case could be investigated. Different particle sizes may be used to enhance the understanding of turbulence modulation and interfacial interactions. For this matter, some issues arise concerning the spatial distribution of particles, as zones with higher concentrations of particles (typically at the bottom of the tank) may saturate the images and induce measurement uncertainties, whereas zones with lower concentrations of particles (top side of the tank) might not be sufficient to capture representative data.

Another major concern is the hydrodynamic analysis during the transient state (related to set-up restart), in which the flow and particle distribution (concentration) evolve until a statistically steady state is reached. The acquisition of experimental measurements of two-phase flow in this state in stirred tanks, using optical techniques, is still to be addressed in research. High-speed imaging with a stereo approach could be used in a certain region of interest where the resuspension of particles is critical. A full extended version of the stirred tank is bounded by the applicability of a dynamic masking of the particle bed presented at the bottom. In any case, measurements are only possible after the acceleration period of the impeller ends (speed increases gradually before reaching the desired target), since it is directly related to the image acquisition frequency and hence the lack of tools and accessibility to fully capture the transient state is still of an exploratory nature, requiring further methodological advancements.

On the other hand, systematic validation of CFD models against the obtained experimental database is necessary. The PIV results provide rigorous validation targets for mean fields, turbulence statistics, and slip distributions. Future numerical work should prioritize reproducing the measured slip maps and the observed divergence between liquid and solid phase turbulence. This requires careful selection and assessment of closures for drag, lift, turbulent dispersion. The experimental results can be used to compare and select models by checking their predictions both overall and locally, including impeller discharge, wall region, and tank bulk.

In combination with the choice of closure models, tracking collision dynamics is another important aspect. For rigid particles in stirred tanks, a natural modelling route is the CFD–DEM approach, as suggested by Jiang et al. [1] in the conclusion for a fluidized

bed set-up. The DEM resolves the particle contacts and the duration of collisions, while the CFD resolves the surrounding flow field. Another simulation option would be direct numerical simulation DNS, as suggested by Chen et al. [2] for their grid turbulence experiments, but it is well-known to be computationally demanding. In any case, the trends in collision rate and frequency, the spatial distribution of collision activity, and the impact metrics reported in this thesis provide quantitative targets for the validation of such coupled simulations. Beyond mean values, a useful criterion for model assessment is the ability to reproduce local collision environments that are not accessible experimentally, including blade vicinity regions for instance. By correlating these hydromechanical metrics with the biological response/behaviour of stem cells (MSCs), these validated numerical models will ultimately serve as predictive tools to optimize bioreactor design, operation, and subsequently support scale-up.

Bibliography

[1] Z. Jiang, T. Hagemeier, A. Bueck, and E. Tsotsas, "Experimental measurements of particle collision dynamics in a pseudo-2d gas-solid fluidized bed," *Chemical Engineering Science*, vol. 167, pp. 297–316, 2017.

[2] S. Chen, P.-Y. Passaggia, and B. L. White, "Particle radial velocity and concentration kernels estimation in isotropic grid turbulence experiments of inertialess particles at small separation distances," *Journal of Fluid Mechanics*, vol. 942, p. A39, 2022.